

# **Synthesis and Chemical Modification of Poly(phenylene vinylene) and Polystyrene Systems for Energy Applications**

A thesis submitted to the

**SAVITRIBAI PHULE PUNE UNIVERSITY**

For the degree of

**DOCTOR OF PHILOSOPHY**

in

**CHEMISTRY**

by

**Shraddha Yashwant Chhatre**

**Dr. Prakash.P. Wadgaonkar (Research Guide)  
Dr. Satishchandra B. Ogale (Research Co-Guide)**

**Polymers and Advanced Materials Laboratory,  
Polymer Science and Engineering Division,  
CSIR-National Chemical Laboratory,  
PUNE 411 008 INDIA**

**October 2015**



# सीएसआयआर-राष्ट्रीय रासायनिक प्रयोगशाला

(वैज्ञानिक तथा औद्योगिक अनुसंधान परिषद)

डॉ. होमी भाभा मार्ग, पुणे - 411 008. भारत



## CSIR-NATIONAL CHEMICAL LABORATORY

(Council of Scientific & Industrial Research)

Dr. Homi Bhabha Road, Pune - 411008. India

### Certificate

This is to certify that the work presented in the thesis titled **“Synthesis and Chemical Modification of Poly(phenylene vinylene) and Polystyrene Systems for Energy Applications”** by **Shraddha Yashwant Chhatre**, submitted for the degree of **Doctor of Philosophy in Chemistry** was carried out under our supervision at the Polymer Science and Engineering Division and Physical and Materials Chemistry Division, CSIR-National Chemical Laboratory, Pune. All the materials obtained from other sources have been duly acknowledged in this thesis.

**Prakash P. Wadgaonkar**

**(Guide)**

Chief Scientist,

Polymer Science & Engineering Division,

CSIR-National Chemical Laboratory,

Pune- 411008, India

Date:

**Satishchandra B. Ogale**

**(Co-Guide)**

Chief Scientist,

Physical and Materials Chemistry Division,

CSIR-National Chemical Laboratory,

Pune – 411008, India

Date:



Communications  
Channels

NCL Level DID : 2590  
NCL Board No. : +91-20-25902000  
Four PRI Lines : +91-20-25902000

FAX

Director's Office : +91-20-25902601  
COA's Office : +91-20-25902660  
SPO's Office : +91 20 25902664

WEBSITE

[www.ncl-india.org](http://www.ncl-india.org)



## DECLARATION

I, **Ms. Shraddha Yashwant Chhatre**, hereby declare that the work incorporated in my thesis entitled “**Synthesis and Chemical Modification of Poly(phenylene Vinylene) and Polystyrene Systems for Energy Applications**” was carried out by me, for the degree of **Doctor of Philosophy**, under the guidance of **Dr. Prakash P. Wadgaonkar** (Polymer Science and Engineering Division, CSIR-National Chemical Laboratory, Pune) and **Dr. Satishchandra B. Ogale** (Physical and Materials Chemistry Division, CSIR-National Chemical Laboratory, Pune). This work has not been previously submitted to this University or any other University for the degree of Ph.D. or any other degree. All the materials that are obtained from other sources are duly acknowledged in this thesis.

**Date:**

**Shraddha Yashwant Chhatre**

**Place: Pune**

**(Research Student)**

*Dedicated to my family, friends and teachers...*



## *Acknowledgements*

*I take this opportunity to thank and to express my gratitude to all those who have been with me throughout the completion of my PhD research and thesis.*

*I express my foremost and sincere gratitude to my supervisor, Dr. Prakash P. Wadgaonkar for his constant support and guidance during my Ph.D. research. I would like to thank him for the immense help, kindness, encouragement and believing in me and making things happen. He gave me the resourceful space and freedom for the research work of my choice. He is a passionate and visionary scientist and also, most importantly a kind person. He has built my confidence from beginning to end with most valuable discussions; he has given the liberty to work independently, which will definitely be useful throughout my career. I take this opportunity to thank him for everything.*

*I would like to express my deepest gratitude to my research co-guide Dr. Satishchandra B. Ogale for giving me the opportunity to work under his guidance. His enthusiastic, inspiring and positive nature made me to think positive in all situations. His guidance has always been inspiring in our scientific endeavours. His general approach to overcome any difficult situation and philosophy towards life and people has also helped me grow as a human being. The idea of him to conduct weekly group meetings and seminars was helpful to me to grow in all aspects and to gain knowledge in diverse fields*

*I would like to acknowledge CSIR funding (JRF-SRF) during my PhD study period. I also take this opportunity to express my gratitude to Dr. S. Sivaram (former Director, CSIR-NCL), Dr. Sourav Pal (former Director, CSIR-NCL), Dr. Vijayamohanan Pillai (Director, CSIR-NCL), Dr. A. J. Varma and Dr. M. G. Kulkarni (former Head, Polymer Science and Engineering Division), Dr. Ashish Lele (Head, Polymer Science and Engineering Division), Dr. Anil Kumar (Head of Physical and Materials Chemistry Division) for providing the infrastructure and advanced facilities for research at CSIR-NCL. I acknowledge CSIR-NCL staff from student academic office, Accounts/bills section, Glass blowing section, Library, engineering sections and DIRC for their co-operation.*

*I wish to thank Professor Neil Robertson for giving an opportunity to visit University of Edinburgh, Scotland, UK and for providing me a space to work in his laboratory for 3 months under Indo-UK “Advancing the Efficiency and*

*Production Potential of Excitonic Solar cells” (APEX) program. I am also thankful to all labmates Ioanna, Emily, Miquel, Tracy, Nina, Max, Alex, Luca, Chun-Cheng, Martina, Yoko, Georg and John for helping me. I thank Manisha tai, Yogita tai, Prasad dada, Kunal and Dr. Sandeep Pathak for their help during my stay in UK.*

*I also would like to thank Professor Andreas F. M. Kilbinger, University of Fribourg, Switzerland, for giving me an opportunity to work in his laboratory for five months as an academic student visitor. I also thank University of Fribourg for funding. I express my special thanks to Mahesh, Amit, Ujjwala, Swanand, Mohit, Aniket, Animesh and Swati for making my stay memorable. I thank all labmates there Nils, Christof, Mark, Maren, Michael N., Michael B. and Maja for help during visit.*

*I thank all the journal editors, reviewers of our published articles and the editors, authors who have allowed us to reprint their published material in this thesis.*

*I extend my thankfulness towards Mr. Shamal Menon, Mr. Anandrao Patil, Dr. Ashutoosh Ambade, Dr. S. K. Asha, Dr. K. Krishnamoorthy, Dr. K. Sreekumar, Dr. B. L. V. Prasad, Dr. Pankaj Poddar, Dr. Rajmohanan, Dr. Manohar Badiger, Mr. Saroj, Mrs. Poorvi, Mrs. Deepa Dhoble, Dr. Rahul Banerjee for their guidance and help. I thank external expert of my yearly assessments Dr. Chetan Bhongale and internal experts Dr. Jyoti Jog and C. V. Avadhani. I thank Dr. Mahendra More and Kashmira Harpale, Department of Physics, Savitribai Phule Pune University, for field emission measurements, Dr. Aravindan and Dr. Madhavi, NTU, Singapore, for Li-HEC measurements.*

*I acknowledge the help and support from my laboratory seniors/friends in SBO group Tushar, Rajesh Hyam, Sarfaraj, Vivek, Subas, Abhimanyu, Anup, Sarika, Arif, Parvez, Vivek, Harish Gholap, Ashish Yangantiwar, Prasad, Shruti, Supriya, Meenal, Rohan, Lily, Mandakini, Abhik, Onkar, Rupali, Nilima (all PhDs from group), Aniruddha, Rounak, Pradeep, Satish, Yogesh, Wahid, Umesh, Golu, Sambhaji, Reshma, Divya, Dipti, Pooja, Mukta, Ketaki, Aparna, Shital, Srashti, Ishita, Poonam. I am grateful to Dattakumar Mhamane, Anil Suryawanshi, Vishal Thakare, and Dhanya P. for their help, constant support and encouragement.*

*I would like to thank my labmates/friends in PPW group Dr. Arun Kulkarni, Dr. Arvind More, Dr. Ankush Mane, Dr. Pandurang Honkhambe, Dr. Prakash Sane, Dr. Sharad Pasale, Dr. Bhausahab Tawade, Dr. Savita Kumari, Dr. Aarati Shedge, Dr. Nilakshi Sadavarte, Dr. Vivek Kodgire, Dr. Mahesh Biyani, Dr. Nagendra Bhairamdgi, Kishor Kumbhar, Parimal, Indravadan, Naganath, Nagedra, Samadhan, Sachin Patil, Sachin Kuhire, Nitin Basutkar, Deepak, Dr. Shyambho, Dr. Murugesan, Vikas, Uday, Sachin Basutkar, Nitin Valsange, Durgaprasad, Jagdish, Bharat, Abhijit, Kavita, Deepshikha, Rajeshwari, Sayali, Rupali and Ashwini for their help and support.*

*I specially thank my friends Satyawan and Amol for their constant help and support. I thank Rajashree for helping me for CV measurements. I thank Shrikant for his help for special NMR measurements and Sharath for BET measurements. I also thank, Aaditya, Manik, Chinmay, Satej, Chayanika, Neeta, Amruta, Megha, Swapnil, Shekhar and Nisha for their help.*

*I must say a special thanks to my best friend Shivangi and Alok for keeping faith in me and encouraging me constantly. I wish to thank my friends, Kashmira, Yashashree, Rima, Tejashree, Mayuri, Harshal, Shyam, Sonal and Ameya.*

*I wish to thank my family, Aai, Baba, Harshada, and Pranali for their absolute love, support, care and comfort without whom this work would not have been successful. My parent's constant emphasis on the importance of education has always been a guiding path for me. Special thanks are also due to all my relatives and my grandparents for their constant encouragement.*

*Finally, I thank the almighty God for being with me all the time.*

***Shraddha Yashwant Chhatre***

---

## Table of Contents

Description	Page No.
▪ Abstract	i
▪ Abbreviations	iv
▪ List of Figures	vii
▪ List of Schemes	xii
▪ List of Tables	xiii

---

---

### Chapter 1: Introduction

---

---

1.1. Grand Challenges for the Modern Society	2
1.2. Energy: The Central Factor	3
1.2.1. Usage of Energy and Related Consequences	3
1.2.2. Renewable Energy	5
1.2.2.1. Biomass	5
1.2.2.2. Wind Energy	7
1.2.2.3. Hydro Energy	8
1.2.2.4. Geothermal Energy	9
1.2.2.5. Solar Energy	9
1.3. Solar Energy Conversion	11
1.4. Photovoltaics: Solar Cell	11
1.4.1. Distinctive Generations of Solar Cell	12
1.4.1.1. Classical Silicon Solar Cells	13
1.4.1.2. Thin Film Solar Cells	14
1.4.1.3. Organic/Hybrid Solar Cells	15
1.5. Dye Sensitized Solar Cell (DSSC)	16
1.5.1. Various Components of DSSC	17
1.5.2. Working Principle of DSSC	26
1.5.3. Kinetics	27
1.5.4. Parameters Governing the DSSC Performance	29
1.6. Storage of Energy	32
1.6.1. Supercapacitors	33

---

---



1.6.1.1. Parameters for Device Characterization	35
1.6.2. Electrical Double Layer Capacitance (EDLC)	35
1.6.2.1. List of Factors Affecting the Performance of EDLC	36
1.6.3. Pseudocapacitor	37
1.6.4. Hybrid Supercapacitors	37
1.6.5. Lithium-Ion Battery (LIB)	37
1.6.6. Materials/ Components of the Device	38
1.6.7. Electrode Materials	38
1.6.8. Electrolytes	38
1.6.8.1. Electrolyte Parameters	39
1.7. Energy Conservation	39
1.7.1. Field Emission Display	40
1.7.1.1. The Field Emission Phenomenon	40
1.7.1.2. Fowler- Nordheim Theory	41
1.7.2. F-N Theory for Semiconductors	45
1.8. Polymers	45
1.9. Polymers for Energy Applications	47
1.9.1. Polymers in Solar Cells	48
1.9.2. Polymers in Energy Conservation	48
1.9.2.1. Conjugated Polymers	49
1.9.2.2. Band Theory for Conjugated Systems	51
1.9.2.3. Challenges in Conjugated Polymers	52
1.9.3. Poly (p-phenylene vinylene) (PPV)	52
1.9.3.1. Synthesis Routes for PPV	53
1.9.3.2. Properties of PPV	56
1.9.4. Polymers in Energy Storage	58
Outline of the Thesis	60
References	61

---

---

## **Chapter 2: Experimental Methods and Characterization Techniques**

---

---

2.1. Synthesis/ Deposition Techniques	73
2.1.1. DSSC Device Fabrication	73

2.1.2. High Temperature Pyrolysis	74
2.2. Techniques for Materials Characterization	74
2.2.1. Nuclear Magnetic Resonance Spectroscopy (NMR)	74
2.2.2. UV-Vis Spectroscopy	76
2.2.3. Photoluminescence (PL) Spectroscopy	77
2.2.4. Fourier Transform Infrared Spectroscopy (FT-IR)	78
2.2.5. Raman Spectroscopy	80
2.2.6. X-Ray Diffraction (XRD)	81
2.2.7. X-ray Photoelectron Spectroscopy (XPS)	82
2.2.8. Field Emission Scanning Electron Microscope (FESEM)	83
2.2.9. Energy Dispersive X-ray Analysis (EDAX)	85
2.2.10. Transmission Electron Microscope (TEM)	85
2.2.11. Atomic Force Microscopy (AFM)	86
2.2.12. Thermogravimetric Analysis (TGA)	88
2.2.13. Gel Permeation Chromatography (GPC)	88
2.2.14. Surface Area: BET Analysis	89
2.2.15. Electrochemical Measurements	91
2.2.15.1. Cyclic Voltammetry (CV)	91
2.2.15.2. Galvanostatic Charging-Discharging Measurements	92
2.2.15.3. Electrochemical Impedance Spectroscopy (EIS)	93
2.16. Solar Simulator	93
2.17. Field Emission Study	94
References	96

---

---

### **Chapter 3: Carboxyl-Modified Conjugated Polymer Sensitizer for Dye Sensitized Solar Cells: Significant Efficiency Enhancement**

---

---

3.1. Introduction	99
3.2. Experimental Section	100
3.2.1. Synthesis	100
3.2.1.1. Vilsmeier–Haack formylation of <b>BEHP-co-MEH-PPV</b> <b>(PPV A)</b>	100
3.2.1.2. Knoevenagel Condensation of <b>BEHP-co-MEH-PPV</b> -aldehyde	

---

---

( <b>PPV-CHO</b> )	101
3.2.2. Characterization of Physical Properties	101
3.2.3. Fabrication and Testing of DSSCs	102
3.3. Results and Discussion	102
3.3.1. Synthesis of Acid Derivative of <b>BEHP-co-MEH-PPV</b> Starting from <b>BEHP-co-MEH-PPV</b>	102
3.3.2. UV-Visible Spectroscopy	104
3.3.3. Diffuse Reflectance Spectra (DRS)	105
3.3.4. Photoluminescence Spectroscopy (PL)	106
3.3.5. Infrared Spectroscopy (FTIR study)	107
3.3.6. Band Alignment of Polymer with TiO <sub>2</sub>	107
3.3.7. J–V Characterization and IPCE Measurements	108
3.3.8. Atomic Force Microscopy (AFM) and Scanning Tunneling Microscopy (STM) Studies on Bare and <b>PPV-acid</b> dye Loaded TiO <sub>2</sub> Thin Film	112
3.3.9. Thermogravimetric Analysis of <b>PPV-A</b> and <b>PPV-acid</b>	114
3.3.10. Thermal Stability of the <b>PPV acid</b> polymeric dye	115
3.4. Conclusion	116
References	117

---

---

## **Chapter 4: High Surface Area Porous Carbon for Ultracapacitor Application by Pyrolysis of Polystyrene Containing Pendent Carboxylic Acid Groups Prepared *via* Click Chemistry**

---

---

4.1. Introduction	120
4.2. Experimental Section	125
4.2.1. Synthesis of Polymer Precursor:	125
4.2.1.1. Synthesis of Polymer <b>P1</b> : Polymerization of 4-chloromethyl styrene	125
4.2.1.2. Synthesis of Polymer <b>P2</b> : Conversion of chloro (-Cl) to azido (-N <sub>3</sub> )	125
4.2.1.3. Synthesis of polymer <b>P3</b> : Azide-alkyne click reaction	126
4.2.1.4. Synthesis of <b>P3K</b> : Preparation of Potassium Salt of	

---

Carboxylic Acid	126
4.2.2. Synthesis of Porous Carbon ( <b>P3KC</b> ): Carbon Obtained by Pyrolysis of <b>P3K</b>	126
4.2.3. Structural Characterization	127
4.2.4. Electrochemical Testing:	128
4.2.4.1. Electrode Preparation for EDLC	128
4.2.4.2. Electrode Preparation for Li-HEC	128
4.3. Results and Discussion	129
4.3.1. Synthesis of Polymer Precursor <b>P3K</b>	130
4.3.2. FTIR Spectra of Polymers <b>P1</b> , <b>P2</b> and <b>P3</b>	131
4.3.3. NMR Spectra of Polymers <b>P1</b> , <b>P2</b> and <b>P3</b>	131
4.3.4. XRD and Raman	133
4.3.5. FESEM and TEM of <b>P3KC</b>	135
4.3.6. XPS of <b>P3KC</b>	137
4.3.7. Surface Area Analysis	138
4.3.8. Electrochemical Testing	140
4.3.8.1. Electrochemical Measurements of <b>P3KC</b> in an Aqueous System: 1M H <sub>2</sub> SO <sub>4</sub>	140
4.3.8.2. Electrochemical Measurements in 1M TEABF <sub>4</sub> in Propylene Carbonate (Pc) Electrolyte	141
4.3.8.3. Impedance Measurements	143
4.3.8.4. Electrochemical Capacitance (Li-HEC) Measurements	144
4.4. Conclusion	147
References	148

---

---

## **Chapter 5: Phenazine Containing Poly (phenylene vinylene): Synthesis, Characterization and Application to Field Emission**

---

---

5.1. Introduction	153
5.2. Experimental	154
5.2.1. Synthesis	155
5.2.1.1. Synthesis of 5,10-dihydrophenazine (1)	155
5.2.1.2. Synthesis of [5,10-dioctyl-5,10-dihydrophenazine] (2)	155

---

5.2.1.3. Synthesis of [5,10-dioctyl-5,10-dihydrophenazine-2,7-dicarbaldehyde] (3)	155
5.2.1.4. Synthesis of [1,4-bis((2-ethylhexyl)oxy)benzene] (4)	156
5.2.1.5. Synthesis of [1,4-bis(bromomethyl)-2,5-bis((2-ethylhexyl)oxy)benzene] (5)	156
5.2.1.6. Synthesis of [tetraethyl ((2,5-bis((2-ethylhexyl)oxy)-1,4 phenylene) bis(methylene))bis(phosphonate)] (6)	157
5.2.1.7. Synthesis of phenazine containing poly(phenylene vinylene) ( <b>PHN-PPV</b> )	157
5.2.2. Characterization	158
5.2.3. Preparation of the Polymer Film for Field Emission Study Using Spray Coating	158
5.2.4 Field Emission Studies	159
5.3. Results and Discussion	159
5.3.1. Polymer Design and Synthesis	159
5.3.2. <sup>1</sup> H NMR Spectra of Monomers	161
5.3.3. <sup>1</sup> H NMR Spectra of Monomer (3)	163
5.3.4. MALDI Characterizations of Monomers (3) and (6)	165
5.3.5. <sup>1</sup> H NMR spectrum of <b>PHN-PPV</b>	166
5.3.6. UV-Vis and Photoluminescence Spectroscopy	167
5.3.7. Electrochemical Properties	168
5.3.8. Thermogravimetric Analysis (TGA)	169
5.3.9. Theoretical Studies	169
5.3.10. Mott-Schottky and Conductivity Measurements	170
5.3.11. Field Emission Studies	171
5.3.12. Field Emission Scanning Electron Microscopy (FESEM)	173
5.3.13. Field Emission Images	174
5.4 Conclusions	175
References	177

---

---

**Chapter 6: Summary and Future Scope**

---

---

6.1. Summary	182
6.2 Future Scope	184
Synopsis	188
List of publications	198



## Abstract

There is an exponential growth in the development of world today and improvement in the lifestyle of the human beings. This change in developing countries is the cause of problems regarding the scarcity of the energy resources. The growing population and development makes the human beings to think about the renewable sources of energy. The nature has provided many renewable resources to our world like sun, water, wind, etc. The objective is now to use those resources in the proper way for the betterment of the mankind. However, the renewable resources are not ready to use energy sources. These resources require specific directional efforts to make them into usable form of energy, eg. electricity.

The foremost focus of the present thesis is on the design and development of the polymeric systems for the demonstration of the applications in the areas of energy conversion, storage and conservation. The work deals with making use of simpler chemistry reactions tools and strategies for synthesizing the required polymeric structures. Herein the potential of the polymers in the energy field has been presented. The two classes of polymers *viz.* poly(phenylene vinylene) and polystyrene were explored for the energy applications. Conjugated polymers *viz.* PPV derivatives were used for the energy conversion and conservation. Polystyrene derivative was explored for energy storage.

**Chapter 1** describes the progression of non-renewable energy sources to renewable energy sources; their need and developments. It also reviews in detail the theoretical concepts of each aspect i.e. energy conversion: solar cells, energy storage: supercapacitors and energy conservation: field emission display. The chapter also deals with the materials used for the energy applications; especially about the polymeric systems.

**Chapter 2** deals with the description of the techniques used for the characterization of the materials. The chapter describes basic principles and the application of the characterization tools.

**Chapter 3** describes use of the polymer sensitizer for Dye Sensitized Solar Cell application. The chapter deals with the chemical modification of conjugated polymer (poly {[2-[2',5'-bis(2''-ethylhexyloxy)phenyl]-1,4-phenylenevinylene]-co-[2-methoxy-5-(2'-ethylhexyloxy)-1,4-phenylenevinylene]}) (**BEHP-co-MEH PPV**) for introducing carboxylic acid group on the polymer for the attachment of polymer sensitizer on the surface of TiO<sub>2</sub>. Modified (**BEHP-co-MEH PPV**) was characterized using spectroscopic tools *viz.* <sup>1</sup>H NMR and IR. Polymeric dye (**BEHP-co-MEH PPV**) was adsorbed on the TiO<sub>2</sub> film. The device was tested and the power conversion efficiency of 3 % was achieved. The work evidences the role of anchoring group for the performance of DSSC. The device was observed to be stable up to 90 °C.

**Chapter 4** demonstrates the potential of polymeric system for the charge storage application. Polystyrene derivative containing potassium salt of carboxylic acid was synthesized using “click chemistry” approach. The polymer was then subjected to pyrolysis in order to get the functionalized porous, high surface area carbon (**P3KC**). The carbon was found to possess high surface area of 1860 m<sup>2</sup> g<sup>-1</sup>. The performance of the carbon was investigated for electrical double layer capacitor (EDLC) as well as lithium ion hybrid capacitor (Li-HEC). EDLC showed the specific capacitance of 137 F g<sup>-1</sup> at the applied current density of 0.5 A g<sup>-1</sup>. For Li-HEC measurements **P3KC** exhibited the maximum energy density of 61 Wh k g<sup>-1</sup> and maximum power density value of 10015 W k g<sup>-1</sup>. Approximately 70 % capacitance retention was observed after 2000 cycles.

**Chapter 5** demonstrates the synthesis of phenazine containing derivative of a conjugated polymer poly phenylenevinylene (**PHN-PPV**) and its performance was studied for field emission. Field emission display devices are low power devices that have performance similar to traditional system with lower power consumption. Molecular weight (M<sub>n</sub>) of **PHN-PPV** was observed to be 6 \*10<sup>3</sup>. The polymer **PHN-PPV** showed reversible redox properties with lower oxidation onset of ~0.2 V. The field emission measurements depicted the lower turn on voltage of 1.68 V/μm for 1 μA/cm<sup>2</sup>. At the applied field of 3.6 V/μm, the maximum current density of ~4.9 mA/cm<sup>2</sup> was achieved.

**Chapter 6** condenses the results of the current dissertation along with the future scope of the work.

**List of Abbreviations**

<b>Abbreviation</b>	<b>Name</b>
AM	Air Mass
AC	Alternating Current
AIBN	2, 2'-Azobis (isobutyronitrile)
AFM	Atomic force microscopy
BEHP-co-MEH-PPV	Poly {[2-[2',5'-bis(2''-ethylhexyloxy)phenyl]-1,4-phenylenevin-ylene]-co-[2-methoxy-5-(2' -ethylhexyloxy)-1,4- phenylenevin-ylene]}
BHJ	Bulk Heterojunction Solar cells
CPs	Conjugated Polymers
CV	Cyclic Voltammetry
CVD	Chemical Vapour Deposition
DRS	Diffuse Reflectance Spectroscopy
DSSCs	Dye Sensitized Solar Cells
DMF	N,N-Dimethyl Formamide
DCM	Dichloromethane
DMC	Dimethyl Carbonate
DFT	Density Functional Theory
EDLC	Electrical Double Layer Capacitor
EC	Ethylene Carbonate
FE SEM	Field Emission Scanning Electron Microscopy
FED	Field Emission Display
FTO	Fluorine doped Tin Oxide
FF	Fill Factor
FTIR	Fourier Transform Infrared Spectroscopy
GPC	Gel permeation chromatography
HRTEM	High resolution transmission electron microscopy
HOMO	Highest Occupied Molecular Orbital
HTM	Hole Transport Materials
ITO	Indium doped Tin Oxide
IPCE	Incident Photon-to-Current conversion Efficiency
ITO	Indium doped Tin Oxide

Jsc	Short Circuit Current Density
KOH	Potassium Hydroxide
K <sub>2</sub> CO <sub>3</sub>	Potassium Carbonate
KBr	Potassium Bromide
LCD	Liquid Crystal Display
LHE ( $\lambda$ )	Light Harvesting Efficiency at wavelength $\lambda$
LUMO	Lowest Unoccupied Molecular Orbital
LED	Light Emitting Diodes
Li-HEC	Lithium ion Hybrid Electrochemical Capacitor
LiPF <sub>6</sub>	Lithium Hexafluorophosphate
MALDI	Matrix Assisted Laser Desorption Ionization
NMR	Nuclear Magnetic Resonance
NMP	N-Methyl-2-Pyrrolidone
OLED	Organic Light Emitting Diode
OPV	Organic Photovoltaics
PL	Photoluminescence
PDI	Poludispersity Index
PLD	Pulsed Laser Deposition
PCE	Power Conversion Efficiency
Pmax	Maximum power
PPV	Poly phenylenevinylene
PHN	Phenazine
P <sub>3</sub> HT	Poly(3-hexylthiophene)
PET	Polyethylene terephthalate
PTFE	Poly tetrafluoroethylene
PPP	Polyphenylne
PVDF	Poly vinylidene fluoride
PC	Propylene Carbonate
POCl <sub>3</sub>	Phosphorus (V) oxychloride
ROMP	Ring-Opening Metathesis Polymerization
SEM	Scanning Electron Microscopy
STM	Scanning Tunneling Microscopy
TCO	Transparent Conducting Oxide

TBAB	Tetrabutyl Ammonium bromide
TEM	Transmission Electron Microscopy
TGA	Thermogravimetric analysis
TEABF <sub>4</sub>	Tetraethyl Ammonium Tetrafluoroborate
UV	Ultraviolet
V <sub>oc</sub>	Open Circuit Voltage
QD	Quantum Dot
XPS	X-Ray Photoelectron Spectroscopy
XRD	X-Ray Diffraction



## List of Figures

No.	Description	Page no.
	Figure 1.1: Global grand challenges .....	2
	Figure 1.2: World energy consumption (a) by sector and (b) by population .....	3
	Figure 1.3: Total world energy consumption .....	4
	Figure 1.4: Health effects of air pollution. ....	5
	Figure 1.5: Biomass to bioenergy .....	6
	Figure 1.6: Methods to convert biomass into various products .....	7
	Figure 1.7: Wind energy to electricity .....	7
	Figure 1.8: Hydro power .....	8
	Figure 1.9: Geothermal Energy .....	9
	Figure 1.10: Comparison of solar energy with other energy forms .....	10
	Figure 1.11: A p-n junction and depletion region .....	12
	Figure 1.12: Different types and generations of solar cell .....	13
	Figure 1.13: Classic silicon solar cells- (a) Monocrystalline solar cell (b) polycrystalline solar cell .....	13
	Figure 1.14: Thin film solar cell .....	14
	Figure 1.15: Organic solar cell .....	15
	Figure 1.16: DSSC device architecture .....	18
	Figure 1.17: Evolution of different types of sensitizers. ....	19
	Figure 1.18: Commercially available ruthenium dyes .....	20
	Figure 1.19: Structure of organic dyes exhibiting high efficiency. ....	21
	Figure 1.20: Working principle of DSSC .....	26
	Figure 1.21: Kinetics involved in each step of DSSC .....	28
	Figure 1.22: IV parameters of solar cell. ....	29
	Figure 1.23: The Ragone plot .....	33
	Figure 1.24: Double layer capacitors .....	34
	Figure 1.25: Classification of supercapacitors .....	35
	Figure 1.26: Mechanisms for (a) double layer, (b) pseudocapacitor and (c) Li- battery .....	36
	Figure 1.27: Potential energy of an electron as a function of distance x .....	42

---

Figure 1.28: Variety of architectures of polymers.....	46
Figure 1.29: Applications of polymers .....	46
Figure 1.30: Polymers for various energy applications.....	47
Figure 1.31: Few representative examples of conjugated polymers.....	49
Figure 1.32: Conjugated polymers: perspective .....	50
Figure 1.33: Representation of the band gap modulation with the increasing number of repeating units.....	51
Figure 1.34: Basic structure of PPV .....	53
Figure 1.35: Gilch polymerization approach.....	53
Figure 1.36: Chemical vapor deposition for synthesis of PPV.....	54
Figure 1.37: Olefin metathesis polymerizations for synthesis of PPV.....	55
Figure 1.38: Wittig type polymerization methods for synthesis of PPV.....	55
Figure 1.39: Palladium catalyzed reactions for synthesis of PPV.....	56
Figure 1.40: Overview of the use of polymers in energy storage systems.....	58
Figure 2.1: DSSC device fabrication.....	73
Figure 2.2: Schematic representation of NMR spectroscopy system.....	75
Figure 2.3: Schematic description of UV-Vis setup.....	76
Figure 2.4: Photoluminescence Spectroscopy- schematic representation.....	78
Figure 2.5: Schematic diagram of FTIR system.....	79
Figure 2.6: Raman spectroscopy diagram .....	80
Figure 2.7: Mechanism of X-ray diffraction.....	81
Figure 2.8: Schematic illustration of XPS .....	83
Figure 2.9: SEM instrument and mechanism .....	84
Figure 2.10: TEM setup.....	86
Figure 2.11: Schematic representation of AFM .....	87
Figure 2.12: TGA diagrammatic representation.....	88
Figure 2.13: GPC setup.....	89
Figure 2.14: BET analysis instrument .....	90
Figure 2.15: A typical cyclic voltammogram .....	92
Figure 2.16: CV potential waveform.....	92
Figure 2.17: (a) Schematic representation of solar simulator, (b) Instrument photograph of solar simulator at CSIR-National Chemical Laboratory.....	94
Figure 2.18: (a) Configuration of planer diode system, (b) Field emission	

---

---

setup.....	95
Figure 3.1: $^1\text{H}$ NMR spectra of <b>PPV A</b> , <b>PPV CHO</b> and <b>PPV acid</b> .....	104
Figure 3.2: UV-Vis spectra of <b>PPV A</b> and <b>PPV acid</b> .....	105
Figure 3.3: DRS spectra of <b>PPV A</b> and <b>PPV acid</b> .....	106
Figure 3.4: Photoluminescence spectra of (a) <b>PPV A</b> and (b) <b>PPV acid</b> .....	106
Figure 3.5: FTIR spectra of <b>PPV A</b> , <b>PPV CHO</b> and <b>PPV acid</b> (inset showing expanded portion of carbonyl region).....	107
Figure 3.6: Band alignment of <b>PPV A</b> and <b>PPV acid</b> with $\text{TiO}_2$ .....	108
Figure 3.7: J-V characterization for (a) <b>PPV A</b> and <b>PPV acid</b> , (b) comparison of J-V curves for <b>PPV A</b> , <b>PPV CHO</b> and <b>PPV acid</b> .....	109
Figure 3.8: ( <i>Top</i> ) $\text{TiO}_2$ films sensitized with <b>PPV A</b> , <b>PPV CHO</b> and <b>PPV acid</b> by dipping in their chloroform solutions ( <i>Below</i> ).....	110
Figure 3.9: IPCE measurements of <b>PPV A</b> and <b>PPV acid</b> dye loaded $\text{TiO}_2$ films.....	111
Figure 3.10: Force-distance curves taken at four different locations on bare and <b>PPV acid</b> dye-loaded $\text{TiO}_2$ surface.....	112
Figure 3.11: STM Spectra taken on bare $\text{TiO}_2$ and <b>PPV acid</b> dye loaded $\text{TiO}_2$ .....	113
Figure 3.12: STM Topography and line scan on bare $\text{TiO}_2$ and <b>PPV acid</b> dye loaded $\text{TiO}_2$ .....	114
Figure 3.13: TG curves of <b>PPV A</b> and <b>PPV acid</b> .....	114
Figure 3.14: Solar conversion efficiency with respect to cell processing temperature.....	115
Figure 4.1: Representation and mechanism of click reaction.....	123
Figure 4.2: (a) Illustration of the strategic design of the precursor structure, (b) molecular representation of <b>P3K</b> in 3D (Element ID: grey small ball C, grey big ball K, white ball H, blue ball N and red ball O).....	129
Figure 4.3: FTIR spectra of polymers <b>P1</b> , <b>P2</b> and <b>P3</b> .....	131
Figure 4.4: (a) $^1\text{H}$ NMR spectrum of <b>P1</b> [poly(4-chloromethylstyrene)] , (b) $^1\text{H}$ NMR spectrum of <b>P2</b> [poly(4-azidomethylstyrene)] and (c) $^1\text{H}$ NMR spectrum of <b>P3</b> [carboxylic acid functionalized triazole ring-containing polystyrene].....	133
Figure 4.5: (a) Powder XRD pattern of <b>P3KC</b> , (b) Raman spectrum of <b>P3KC</b> .....	134
Figure 4.6: Raman Spectra of (a) <b>P1C</b> and (c) <b>P3C</b> , Powder X-ray diffraction pattern of (b) <b>P1C</b> and (d) <b>P3C</b> .....	134

---

---

Figure 4.7: (a) and (b) FESEM images of <b>P3KC</b> at different scales.....	135
Figure 4.8: (a), (b) and (c): HRTEM images of <b>P3KC</b> at different scales, (d) lattice fringes pattern obtained for <b>P3KC</b> .....	136
Figure 4.9: XPS of <b>P3KC</b> : (a) C1s, (b) O 1s, (c) N1s.....	137
Figure 4.10: (a): Pore size distribution of <b>P3KC</b> acquired from DFT calculations, (inset- cumulative pore volume) (b) N <sub>2</sub> adsorption- desorption isotherm for <b>P3KC</b> . .....	138
Figure 4.11: (a) Cyclic voltammogram (CV) of <b>P3KC</b> in 1M H <sub>2</sub> SO <sub>4</sub> as electrolyte at the scan rate of 100 mV s <sup>-1</sup> , (b) Galvanostatic charging-discharging data for <b>P3KC</b> at the current density of 1 Ag <sup>-1</sup> .....	141
Figure 4.12: (a) CV of <b>P3KC</b> in TEABF <sub>4</sub> as electrolyte at different scan rates in the potential range of 0-2.7 V, (b) Galvanostatic charging- discharging data for <b>P3KC</b> at the various current densities.....	141
Figure 4.13: (a) Specific capacitance measured from charging-discharging at different current densities, (b) Ragone plot.....	142
Figure 4.14: Cyclic stability data of organic EDLC measurements for <b>P3KC</b> case in the coin-cell assembly.....	143
Figure 4.15: Comparison of impedance measurements (Nyquist plot) between coin cell and Swagelok cell assembly for <b>P3KC</b> .....	144
Figure 4.16: (a) Typical charging-discharging curves for Li/ <b>P3KC</b> half-cell, (b) half cell cyclic stability from 3 V to 4.6 V at the current density of 100 mA g <sup>-1</sup> , (c) Galvanostatic charging-discharging curves for <b>P3KC</b> / Li <sub>4</sub> Ti <sub>5</sub> O <sub>12</sub> Li-HEC at different current densities between 1V to 3V, (d) Ragone plot of <b>P3KC</b> / Li <sub>4</sub> Ti <sub>5</sub> O <sub>12</sub> and commercial AC/ Li <sub>4</sub> Ti <sub>5</sub> O <sub>12</sub> , (e) Cyclic stability of <b>P3KC</b> / Li <sub>4</sub> Ti <sub>5</sub> O <sub>12</sub> at the current density of 2 A g <sup>-1</sup> .....	145
Figure 5.1: Polymer film preparation .....	158
Figure 5.2: <sup>1</sup> H spectrum of 5,10-dioctyl-5,10-dihydrophenazine.....	162
Figure 5.3: <sup>1</sup> H NMR spectrum of 5,10-dioctyl-5,10-dihydrophenazine-2,7- dicarbaldehyde recorded in CDCl <sub>3</sub> .....	162
Figure 5.4: <sup>1</sup> H NMR spectrum of tetraethyl ((2,5-bis((2-ethylhexyl) oxy)-1,4 phenylene) bis(methylene))bis(phosphonate) recorded in CDCl <sub>3</sub> ....	163
Figure 5.5: <sup>13</sup> C spectrum of 5,10-dioctyl-5,10-dihydrophenazine recorded in	

---

---

Benzene d <sub>6</sub> .....	164
Figure 5.6: <sup>13</sup> C NMR spectrum of 5,10-dioctyl-5,10-dihydrophenazine-2,7-dicarbaldehyde recorded in Benzene d <sub>6</sub> .....	164
Figure 5.7: MALDI spectrum of monomer (3) 5,10-dioctyl-5,10-dihydrophenazine-2,7-dicarbaldehyde.....	165
Figure 5.8: MALDI spectrum of monomer (6) - tetraethyl ((2,5-bis((2-ethylhexyl) oxy)-1,4 phenylene) bis(methylene))bis(phosphonate)..	166
Figure 5.9: <sup>1</sup> H NMR spectrum polymer <b>PHN-PPV</b> .....	167
Figure 5.10: (a) UV visible spectrum of the <b>PHN-PPV</b> in chloroform solution, (b) Photoluminescence spectrum of <b>PHN-PPV</b> in chloroform solution. ....	167
Figure 5.11: Cyclic voltammetry for <b>PHN-PPV</b> at the scan rate of 100 mV/s...	168
Figure 5.12: TG curve of <b>PHN-PPV</b> in the nitrogen atmosphere.....	169
Figure 5.13: HOMO and LUMO levels of the monomer of <b>PHN-PPV</b> .....	170
Figure 5.14: (a) Mott-Schottky measurements, (b) AC conductivity measurements .....	170
Figure 5.15: (a) Emission Current density versus applied electric field (J-E) plot, (b) F-N plot.....	172
Figure 5.16: Stability of the field emitter over the duration of 6 hrs.....	173
Figure 5.17: SEM images of the film before (a) and after (b) the FE measurement.....	173
Figure 5.18: Field emission images .....	174
Figure 6.1: Donor-acceptor conjugated polymers for organic solar cells .....	184
Figure 6.2: PPV derivatives for LED applications .....	185
Figure 6.3: Representative structure of polymer for hole transport material application.....	186

---

**List of Schemes**

---

No.	Description	Page no.
	Scheme 3.1: Synthesis of <b>PPV acid</b>	103
	Scheme 4.1: Synthesis of polystyrene derivative-a polymeric precursor ( <b>P3K</b> ) for porous carbon.	130
	Scheme 5.1: Synthesis of monomers ( <b>3</b> ) and ( <b>6</b> )	160
	Scheme 5.2: Synthesis of <b>PHN-PPV</b>	160



---

**List of Tables**

---

No.	Description	Page no.
Table 1.1:	List of polymers used as sensitizers in DSSC	22
Table 1.2:	Lifetime of each process within DSSC	28
Table 1.3:	Derivatives of PPV used for various applications	57
Table 1.4:	List of different polymer derived carbon for various applications.	59
Table 3.1:	Table Optimization of TiO <sub>2</sub> type and polymeric dye concentration.	108
Table 3.2:	Thickness optimization of TiO <sub>2</sub> film.	109
Table 3.3:	Comparison of <b>PPV A</b> , <b>PPV-CHO</b> and <b>PPV acid</b> dyes on the optimized films.	110
Table 3.4:	Solar cell parameters for <b>PPV A</b> and <b>PPV acid</b> .	110
Table 3.5:	Efficiency of <b>PPV-acid</b> and <b>N719</b> dye with increasing temperature	115
Table 4.1:	Literature review table for carbon obtained by polymer pyrolysis	122
Table 4.2:	Representative examples for post polymerization modification by click chemistry.	124
Table 4.3:	I <sub>D</sub> /I <sub>G</sub> ratio in case of <b>P1C</b> and <b>P3C</b>	135
Table 4.4:	Comparison of <b>P1C</b> , <b>P3C</b> and <b>P3KC</b> morphology and surface area	139
Table 5.1:	Turn on field and maximum current density values of the different conducting polymer.	175

## Chapter 1

### Introduction

The current chapter deals with the introduction to energy needs and demands of the growing world. The course of the depletion of non-renewable energy resources and the necessity of the renewable sources is included herein. The dissertation is mainly focused on the synthesis of polymeric systems for energy applications and thus the contents include detailed discussion regarding the mechanism and theory of energy conversion, energy storage and energy conservation devices. Here we have focused on polymeric systems hence, the chapter encompasses the detailed discussion about polymers and their properties.

## 1.1 Grand Challenges for the Modern Society

The present era is of great innovations and discovery-driven developments, and there have been spectacular advances in the globalization of industrial sector with stupendous progress in the fields of transportation, communication and information technologies. The lifestyle of the modern society is changing rapidly with remarkable advances and growing demands on the quality of life. Thus, this era is also facing many new challenges on different fronts. The global village, as the modern society is termed in different contexts, has identified several grand challenges in the areas such as food, water, energy, environment, security, education, global health, poverty etc.<sup>1</sup> as depicted in **Figure 1.1**.



**Figure 1.1:** Global grand challenges

(<http://zezantam.com/2013/07/02/week-two/>)

These various challenges not only are independently very important to be addressed but are also intertwined in various ways and hence have to be addressed and possibly resolved simultaneously. For example, health depends on climatic conditions, pollution, surroundings, and circumstances, which are deeply influenced by the sectors of the quality of environment, water and food. To address environmental issues, education is the most important pathway to walk on. To deal with the global health issues economics needs to be considered along with environment, education, etc. The increase in population is driving more attention to look into these grand challenges. According to an estimate, the population has increased exponentially in the last few decades and it will grow even further. Therefore, there is a necessity to understand the demands of the rising population and their requirements. It is thus imperative to focus on the above global grand challenges of the modern society on an urgent basis to fulfill

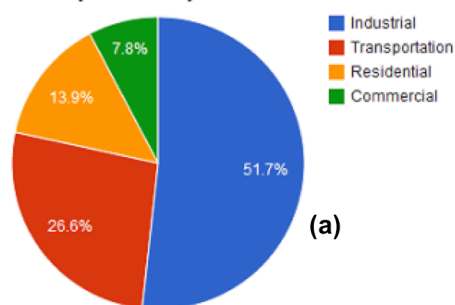
the demands and requirements of the increasing population and thereby enhancing the quality of life for all.

## 1.2 Energy: The Central Factor

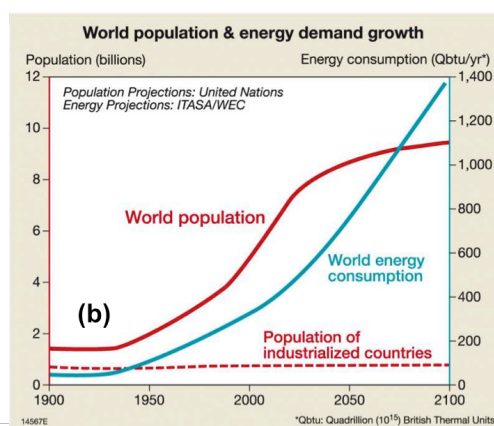
Interestingly, while the grand challenges are braided with each other, all of them are connected to the energy sector in one way or the other, directly or indirectly. Hence energy is the most important sector that we must deal with.

### 1.2.1 Usage of Energy and Related Consequences

**World Energy Consumption by Sector, 2012 (EIA Data)**



(a)



(b)

**Figure 1.2:** World energy consumption (a) by sector and (b) by population

((a)<http://earthzine.org/2014/07/08/vermont-law-school-the-ethical-dimensions-of-energy-policy/>, (b) <http://www.diercke.com/kartenansicht.xtp?artId=978-3-14-100790-9&seite=190&id=17702&kartennr=2>)

**Figures 1.2 (a)** and **(b)** describe the world energy consumption by the sector and by population, respectively. The energy utilization for the development is exponentially increasing. In the year 1980, the total primary energy consumption was 284 Quadrillion Btu<sup>2</sup> and it is predicted to rise above 600 Quadrillion Btu by 2050, which is huge. The major volume (approximately 52%) of available energy source is required for the industrial purpose. Transportation is one of the biggest users with ~ 26% and is also one of the main contributors to pollution. From these studies it is clear that modern civilization and globalization needs tremendous amount of energy in various forms. **Figure 1.3** depicts the scenario of the total world energy consumption categorized by the available sources.

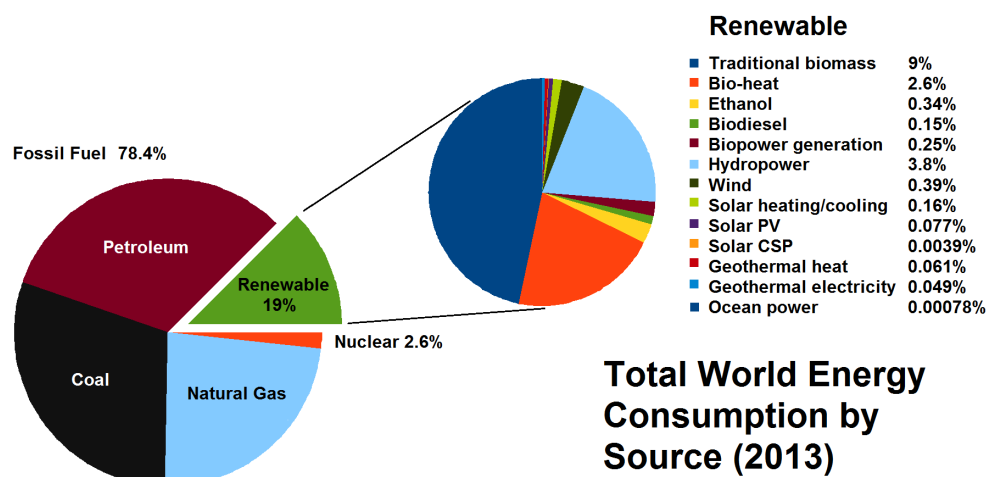


**Figure 1.3:** Total world energy consumption

([https://commons.wikimedia.org/wiki/File:Total\\_World\\_Energy\\_Consumption\\_by\\_Source\\_2013.png](https://commons.wikimedia.org/wiki/File:Total_World_Energy_Consumption_by_Source_2013.png))

Amongst the available forms, till date the largest amount of energy is derived from non-renewable resources like coal, natural gas, oil, petroleum resources, etc. Such energy sources are depleting rapidly with growing use and these will not be able to satisfy the future needs of the growing population. Moreover, these traditional non-renewable resources require efforts for their extraction, purification as well as burning to convert them into the required useful forms of energy. Burning of fossil fuels leads to production of carbon dioxide, a major air pollutant and greenhouse gas. In the world, fossil fuels are the biggest greenhouse gas emitters and contribute methane, 3/4 of all carbon, and other greenhouse gas emissions.<sup>3</sup> Burning of various kinds of fuels leads to production of other hazardous gases such as CO<sub>2</sub>, CO, SO<sub>2</sub>, NO<sub>x</sub>, along with particulate matter, volatile organic compounds (VOCs), etc., which are the primary cause of several health hazards<sup>4</sup> as shown in **Figure 1.4**.

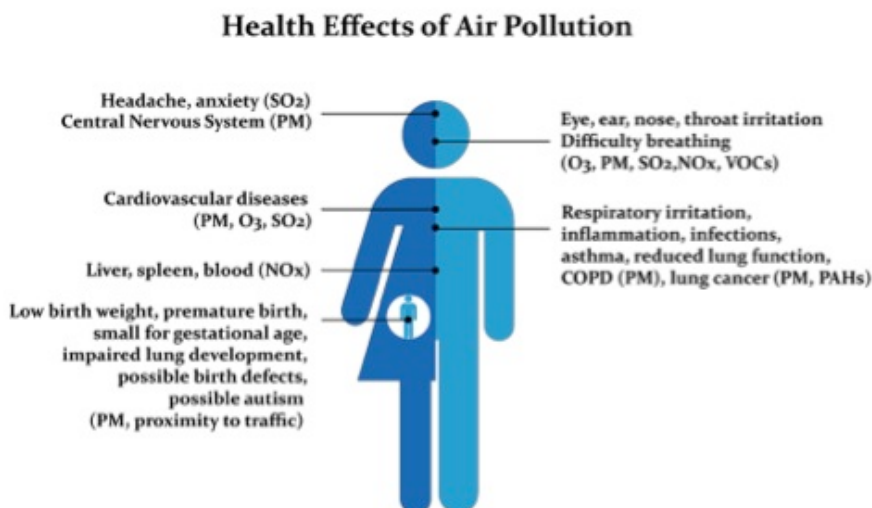


**Figure 1.4:** Health effects of air pollution.

[http://environment-pollution.weebly.com/uploads/2/9/5/6/29566681/613097\\_orig.jpg](http://environment-pollution.weebly.com/uploads/2/9/5/6/29566681/613097_orig.jpg).

Air pollution and greenhouse effects are concurrently affecting the UV protecting ozone layer. As a consequence, diseases like cancer, UV-rays induced skin problems are placing lives of the humans in danger.

As the worldwide demand for the energy is increasing day by day and the planet's resources are exhausting rapidly, there is clearly an urgent need to manage the existing resources and to find new innovative solutions to the problems of energy.

### 1.2.2 Renewable Energy

As indicated in **Figure 1.3**, the use of different renewable energy sources has reached only up to 19% of the total energy consumption by the sector. These are clean, green (environmentally friendly), and low cost alternative energy sources, which will be the key to our sustainable future. In the forthcoming section the renewable sources of energy are described in brief.

#### 1.2.2.1 Biomass

One of the most consumed forms of the renewable energy sources is the biomass -the energy derived from the organic matter. There are broadly three classes of the biomass viz. woody biomass, non-woody biomass and animal/human-

derived biomass.<sup>5</sup> Plant residues, waste wood, industrial wood residues etc. form the class of woody biomass. Oil, sugar, starch, waste and residues from food industries comprise the non-woody biomass. The animal/human derived biomass class contains the household and industrial organic waste, slaughter waste etc. Energy derived from biomass is called as bioenergy. **Figure 1.5** depicts sources of biomass and conversion of it to bioenergy.

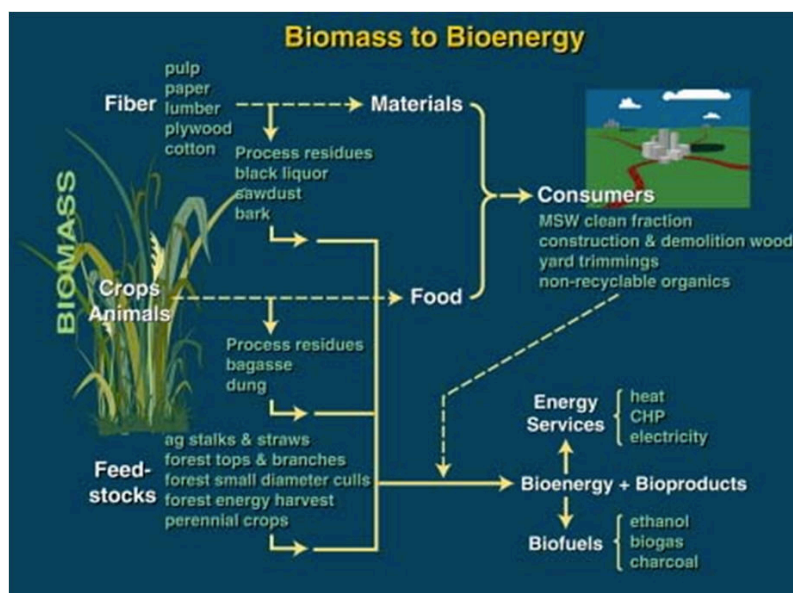


**Figure 1.5:** Biomass to bioenergy

([greenenergy.reviewforcash.com](http://greenenergy.reviewforcash.com))

Biomass can be converted into heat, electricity, biofuels, etc. **Figure 1.6** indicates the various methods of processing the biomass to generate energy forms from the biomass feedstock. Primary processes include gasification, pyrolysis and combustion. After the intermediate processing, the final energy forms like electricity, fuel gases, methane, etc. are formed in the energy plants. Compared to other forms, energy from biomass requires big power plants and processing units, which in turn leads to enormous economic investment. The foremost disadvantage of the biomass energy production is that the combustion causes emission of toxic gases in the air.<sup>6</sup>

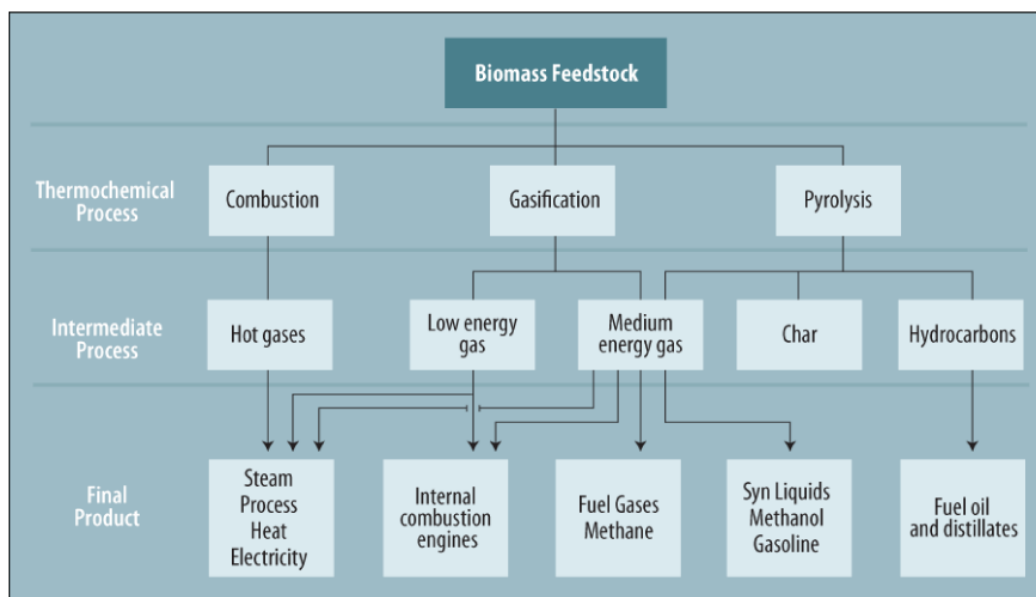


**Figure 1.6:** Methods to convert biomass into various products.

([http://static.trunity.net/files/171801\\_171900/171890/biomass-crs-figure-1.png](http://static.trunity.net/files/171801_171900/171890/biomass-crs-figure-1.png))

### 1.2.2.2 Wind energy

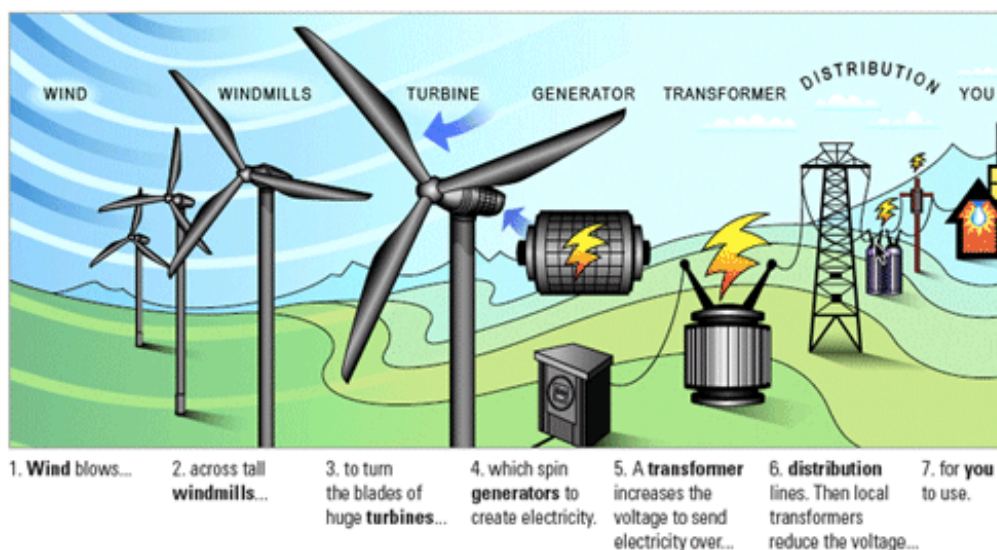


**Figure 1.7:** Wind energy to electricity.

([http://www.xcelenergy.com/staticfiles/xcel/images/ElecGen762\\_wind.gif](http://www.xcelenergy.com/staticfiles/xcel/images/ElecGen762_wind.gif))

The wind energy (**Figure 1.7**) refers to the conversion of mechanical energy carried by the wind into electrical energy with the use of turbines or to other forms of energy as desired. Wind energy is a clean, green source of energy; as it does not produce any byproducts like greenhouse gases or any form of



pollutants.<sup>7</sup> Wind power generation has evolved over the years. As the wind flow and speed varies according to the change in the climate (it is not a constantly available source, it is an intermittent source), it is usually associated with the other electric power sources for steady stream of energy.

Around 40% of electricity in the Denmark is generated by wind power,<sup>8,9</sup> and around 83 other countries in the world are consuming wind power in different proportions depending on the availability of strong wind systems to satisfy their electricity demands.<sup>10</sup> Worldwide, the total wind energy production is rapidly growing and has reached about 4% of the total electricity usage.<sup>11</sup> This form of renewable energy also requires large initial economic investment.

### 1.2.2.3 Hydro Energy

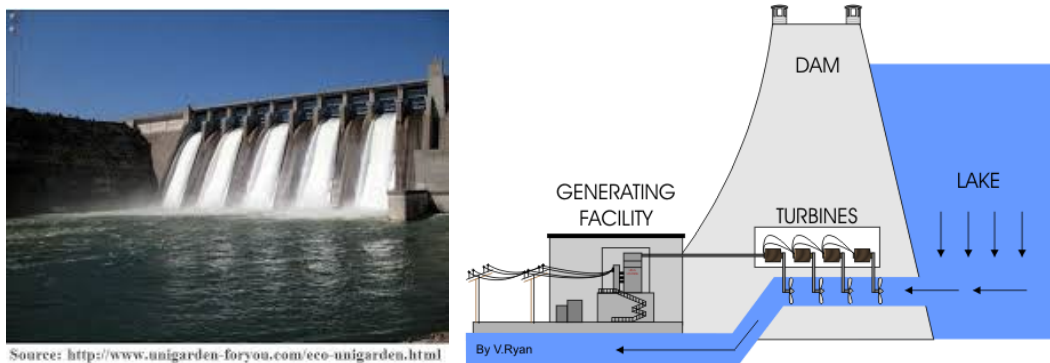


**Figure 1.8:** Hydro power

(<http://www.technologystudent.com/energy1/hydr1.htm>)

This energy is derived from down-stream running water. The reservoirs or tanks are built on the river. Water discharged from the tanks or the reservoir flow through a turbine and causes the turbine blades to rotate or spin by the force of flowing water, which in turn triggers a generator for the production of electricity. The hydroelectric power plant certainly does not need a huge dam. Several hydroelectric power plants make use of a small channel for passage of flowing water that can cause a turbine to spin.<sup>12</sup> Nevertheless, while the maximum amount of energy in the U. S is obtained from fossil fuel and then from nuclear power plants; hydroelectricity is significant, as more than 6% share is of hydro power.<sup>13</sup> Amongst the renewable sources, hydroenergy is a very

important and extensively used source. Essentially, 19% of global electricity production is from hydro concept.<sup>14</sup>

#### 1.2.2.4 Geothermal Energy

Another renewable source of energy is geothermal energy (**Figure 1.9**), which means Earth heat. This is the alternative energy for the future and having a potential to replace fossil fuels. In this case, mostly a stream of hot water vapor is passed across the turbines for the production of electricity.

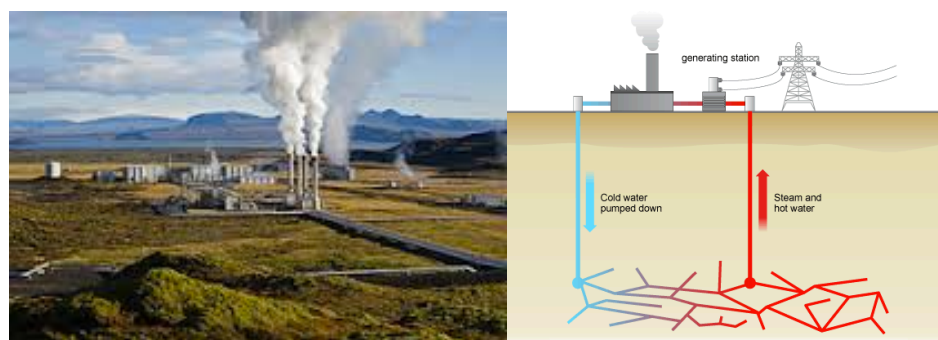


**Figure 1.9:** Geothermal Energy

([https://en.wikipedia.org/wiki/Geothermal\\_energy](https://en.wikipedia.org/wiki/Geothermal_energy)

[http://www.bbc.co.uk/schools/gcsebitesize/science/aqa\\_pre\\_2011/energy/mainselectricityrev5.shtml](http://www.bbc.co.uk/schools/gcsebitesize/science/aqa_pre_2011/energy/mainselectricityrev5.shtml))

Internal heat content of the Earth is about  $10^{31}$  Joules that is many times more than the global requirement. U.S. (2687 MW), Philippines (1967 MW) and Indonesia (992 MW) produce a significant amount of electricity from geothermal energy. From the geothermal power, Iceland acquires approximately 50% of its energy. In this energy source gases like hydrogen,  $\text{CO}_2$ , ammonia are evolved from the Earth's crust containing trace amount of arsenic, which is a toxic element.<sup>15</sup>

#### 1.2.2.5 Solar Energy

Amongst all forms of renewable energy sources, solar energy is the most abundant (**Figure 1.10**) form of energy over the planet. However, this energy is very dilutely distributed across the planet surface. The concentration of the solar energy also varies worldwide. At the upper atmosphere; the Earth accepts

174,000 terra-watts (TW) of incoming solar radiation. Roughly 30% of it is reflected back and the remaining amount is absorbed by clouds, oceans and land masses.

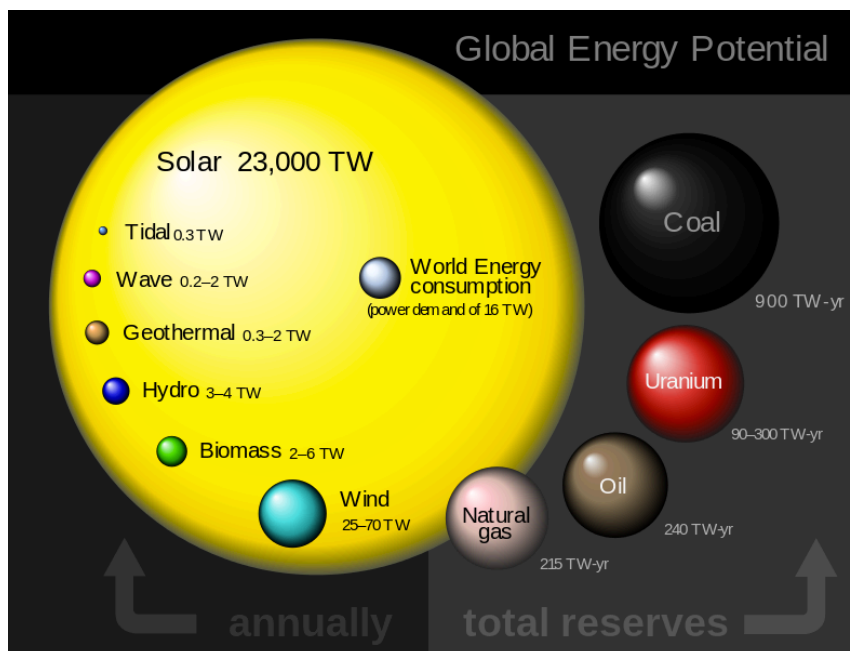


**Figure 1.10:** Comparison of solar energy with other energy forms

The solar power can be converted into usable forms of energy using technologies like photovoltaics, solar thermal etc. Solar energy is perhaps the most clean and totally cost-free source available to mankind.

In order to attain highly efficient harvesting of solar or other forms of renewable energy at low cost, advanced materials research is absolutely essential. Towards this end, the past decade has witnessed a tremendous progress and the emergence and rapid growth of nanotechnology has contributed greatly to this progress. Totally new and highly innovative designs of devices and systems are currently being pursued to solve the energy problem and by implication some of the other big challenges which basically emanate from the same. In addition to energy harvesting, energy storage and conservation are equally important endeavors. Since the usage of the most renewable sources of energy such as solar energy is not concurrent with their availability, the storage of harvested energy is extremely important for latter use. Research on battery systems,

thermal storage, phase change materials, etc. is therefore a major focus of current research. Energy conservation is also a very important goal of energy research for obvious reasons. Low power consuming inexpensive lighting or display systems are therefore attracting great attention lately. In this work, we have dealt with designs of organic and polymeric systems and materials as well as related device architectures for efficient solar energy harvesting, energy storage and electrical energy conservation in display systems. In the following, background information related to the specific problems undertaken in this work is briefly reviewed.

## **Section1: Energy Conversion**

### **1.3 Solar Energy Conversion**

Solar energy, a renewable source of energy, is available in plenty on the earth surface. This energy can be used directly or can be converted into other usable forms of energy. Various technologies have been implemented till today for solar energy harvesting and conversion; and these are still growing. Following are some intensely researched technologies for solar energy conversion:

- Solar Photovoltaics
- Solar Thermal
- Solar to Fuel: water splitting, hydrogen generation

### **1.4 Photovoltaics: Solar Cell**

The area of photovoltaics has always attracted great attention of researchers all over the world as the electricity thus generated can be distributed by using local distribution grid. In the solar cell device, the conversion of solar energy directly into the electricity is achieved by using devices based on semiconducting materials, which exhibit photovoltaic effect. French experimental physicist Edmund Becquerel observed the “Photovoltaic effect” in 1839.<sup>16</sup> Principally most of the early generation photovoltaic devices are based on p-n junction semiconductor systems (**Figure 1.11**).

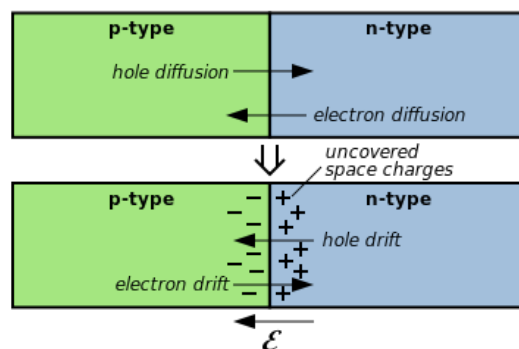


**Figure 1.11:** A p-n junction and depletion region.

([https://en.wikipedia.org/wiki/Depletion\\_region](https://en.wikipedia.org/wiki/Depletion_region))

The p and n-type regions are joined together to get the p-n junction. At the interface, diffusion of electrons occurs from n-type material into p-type region. The process continues to get the positive charges accumulated in the n-type area while negative charges are accumulated in the p-type area. This creates an electric field termed as the “built-in potential”. Eventually the equilibrium state is achieved where no charge carries flow across the junction producing a “potential barrier” at the interface region, called as the depletion region. In a photovoltaic device when sunlight illuminates, it creates free electrons and holes in and around the depletion region. The generated electrons and holes are carried away to the opposite directions by the built-in potential across the depletion layer creating a photo-voltage and the external load connected to p-n region carries the current. Though the concept of solar light to electricity conversion existed before 1900, the actual practical silicon solar cell with efficiency of 6% was demonstrated by Bells Labs in 1954. Thereafter several generations of photovoltaic technologies have been developed and power conversion efficiency values in the range of 20-40% have been realized.<sup>17,18</sup>

#### 1.4.1 Distinctive Generations of Solar Cell

There are various designs of solar cells based on the types of materials and architectures as well as physical mechanisms that have been researched over the years. Based on their efficiency values, stability etc. they have found uses in different application sectors. Some basic classification of solar cell types is shown in **Figure 1.12**.

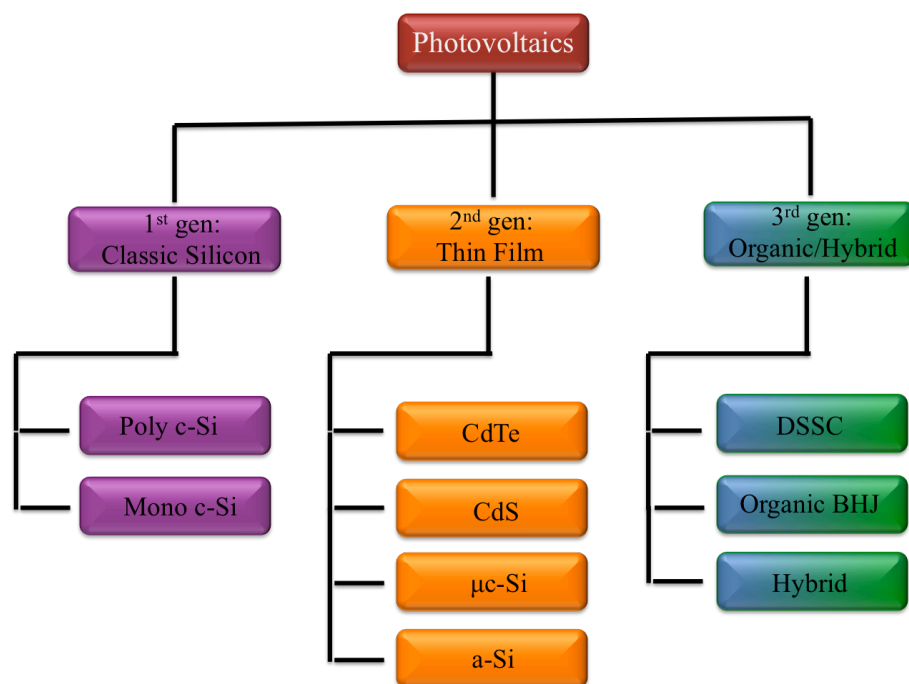


**Figure 1.12:** Different types and generations of solar cell.

#### 1.4.1.1. Classical Silicon Solar Cells:

Classic silicon solar cells (**Figure 1.13**) are the very first generation solar cells. Existing photovoltaic production is using 90% of first generation p-n junction solar cells, which are mainly only one junction solar cells, formed by monocrystalline silicon wafers (c-Si) or polycrystalline silicon (poly c-Si).

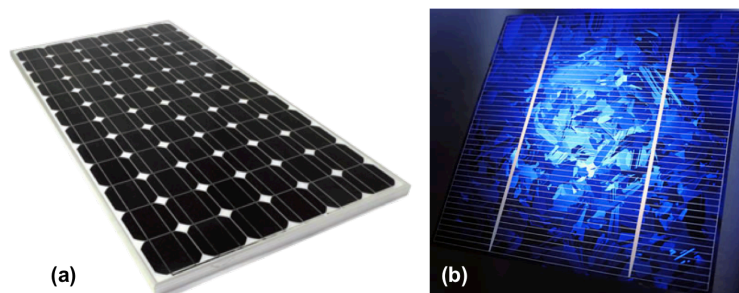


**Figure 1.13:** Classic silicon solar cells- (a) Monocrystalline solar cell (b) polycrystalline solar cell.

(<http://www.verdiatechnologies.com/solar-modules-cells/mono-crystalline/>  
<http://www.wifinotes.com/energy/types-of-solar-cells.html>)

The module level efficiency of single crystal silicon cells is 18-19%. However, 12-14% is delivered by polycrystalline silicon solar cells<sup>19</sup> and these are the

most efficient, robust, reliable and well-established solar cells. However, their processing comprises of high temperature and high vacuum conditions which makes them very expensive, though large scale production has downgraded the costs over the years. Still their cost (single crystalline silicon solar cells) and brittle nature are the limitations in the context of the large scale implementation.

#### 1.4.1.2. Thin Film Solar Cells:

Thin film solar cells have emerged as second-generation solar cells (**Figure 1.14**). They are relatively cheaper than the conventional c-Silicon cells and materials with lesser purity than Si-solar cells are also acceptable and give optimum performance. In this category; on the substrates like glass, plastic or metal, thin films of several nanometers or micrometers of the photovoltaic materials are used.

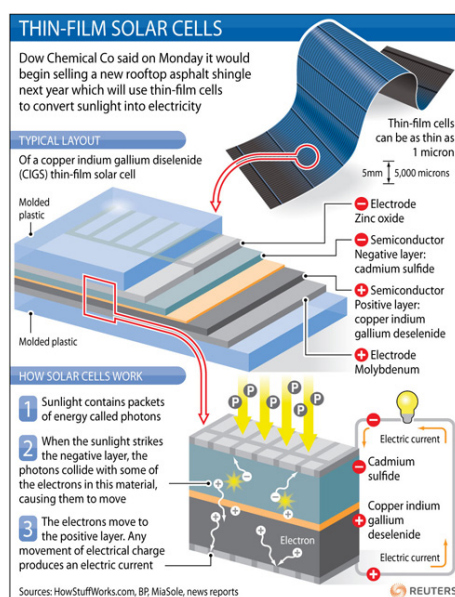


**Figure 1.14:** Thin film solar cells

(<http://blogs.reuters.com/from-reuterscom/2009/10/06/graphic-thin-film-solar-cells/>)

Generally, the materials used include amorphous silicon (a-Si), micro-crystalline silicon ( $\mu\text{c-Si}$ ), CdTe, CIGS, CZTS and thin film silicon. Over the years, the efficiency number has significantly improved for CIGS and CdTe (above 21 %). So far promising conversion efficiencies have been stated for the a-Si (6-9%),<sup>20</sup>  $\mu\text{c-Si}$  (11%),<sup>21</sup> CIGS (20%),<sup>22</sup> and CdTe (20%).<sup>23</sup> Even though thin film



technology is cost effective, material uniformity and reproducibility confines further and large scale scope of applicability. Toxicity of some of the elements used is also a concern.

#### 1.4.1.3. Organic/Hybrid Solar Cells:

The third generation solar cells include organic, polymeric solar cells and hybrid solar cells, which are multi-junction solar cells. Unlike the conventional solar cells, the new generation solar cells make use of photoactive organic (small molecules, polymers, **Figure 1.15**), and certain metal oxide inorganic semiconducting materials. Although the current efficiency values are comparatively low as compared to c-Si cells along with issues about stability, there is a wide scope for further development of the 3rd generation solar cells as the variety of materials and their combinations that are possible are many with different possible device architectures. Furthermore, this emerging technology offers newer benefits that emanate from solution processing character of the protocols involved; the materials are less expensive, flexible, and easily amenable to large-scale production by roll to roll printing technique.

The simplest design of an organic solar cell comprises of opto-electronically active conjugated polymer placed between two conducting electrodes whereby the photo-generated charges are separated. Karg et al. reported 0.1 % efficiency on the basic structure of ITO/PPV/Al.<sup>24</sup> The further developments led to the bilayer type of device architectures. In this case, the active matrix consists of two materials, one electron donor and other electron acceptor. The excitons are generated and separated at donor-acceptor interface because of difference in the ionization potential and electron affinity of these materials. For example, 1% efficiency was presented for the PPV/C60 case.<sup>25</sup> However, in both these devices recombination and short diffusion length (10 nm) limited the further efficiency enhancement.

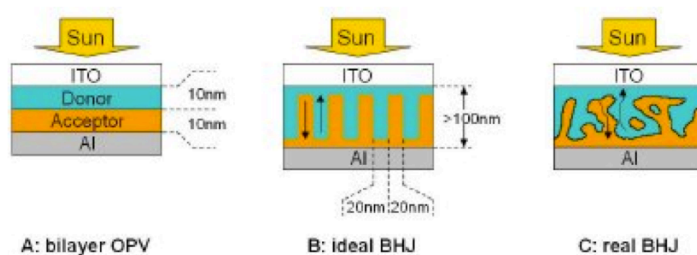


**Figure 1.15:** Organic solar cell



<http://www.azonano.com/article.aspx?ArticleID=2434>

Thereafter, the third type of architecture evolved and this makes use of the nanoscale blend of donor and acceptor materials together, and is named as the Bulk Heterojunction solar cell (BHJ). The advantage of such architecture is that this allows the exciton to diffuse comparatively easily across the interface, which is in the range of the excitonic diffusion length. The methods of processing are being improved and the efficiencies have escalated from 2.5 % to greater than 10 %.<sup>26</sup>

Additional class of third generation solar cells is named as hybrid solar cells wherein organic plus inorganic materials are functionally assembled together. The organic part is comprised of light absorbing, hole transporting conjugated polymer(s) or small molecule(s) and the inorganic part consists of materials that carry electrons or holes.

There are three kinds of hybrid solar cells based on their donor-acceptor material class: Dye Sensitized Solar Cells (DSSC), Quantum Dot Solar Cells (QD-DSSC) and Polymer-nanocomposite hybrid solar cell. In the polymer-nanocomposite cell the blend of nanomaterials and polymers is made, which has the advantages of the high surface area of nanoparticles for better charge transfer processes. Generally the nanomaterials used are metal oxides and sulfides like TiO<sub>2</sub>, ZnO, SiO<sub>2</sub>, CdS, CdSe, etc. and conjugated polymers like P3HT, MEH-PPV etc.<sup>27</sup>

*Dye Sensitized Solar Cell forms the first part (Energy conversion) of this thesis and is amongst the leading third generation solar cell technology. This solar cell architecture is discussed briefly in the next sections.*

### **1.5. Dye Sensitized Solar Cell (DSSC)**

Dye sensitized solar cell (DSSC)- a third generation, advanced solar cell is believed to be the promising substitute to the well-established silicon solar cell technologies because of its fairly good power conversion efficiency, use of relatively low cost materials and the device simplicity. The design of the device mimics Nature's light absorption during photosynthesis and its use in redox processes; hence DSSC can be articulated as artificial photosynthesis to generate electricity.

DSSC, which is often recognized as the Grätzel cell that was developed in 1991 by Micheal Gratzel and Brian O'regan at École Polytechnique Fédérale de Lausanne (EPFL), Switzerland.<sup>28</sup> The first report of the DSSC demonstrated conversion efficiency of 7.1 %, which has by now improved to 13 %. Since its discovery; efforts have been made across the world, on improving various components of DSSC and their combinations so as to push efficiency number higher to really compete with the silicon solar cell technology. Till date, DSSCs are at the frontiers in third generation solar cells, although during the last few years the perovskite cells have gained significant grounds with efficiencies crossing 20%.

### 1.5.1. Various Components of DSSC

The DSSC device architecture is shown in **Figure 1.16**.

**a) Substrate:** Mostly, a glass having the transparent conducting oxide (TCO) coating is used as the bottom electrode. It is usually fluorine doped tin oxide (FTO) or sometimes indium doped tin oxide (ITO). The crucial part for the selection of the substrate is that the conductivity of the electrode must be higher but at the same time transparency should be good too. Hence, generally FTO glass used is with low sheet resistance of 10-15  $\Omega/\square$  and transparency of > 80 %.

**b) Working electrode:** The working electrode comprises of a porous semiconducting metal oxide layer on a transparent conducting substrate. This is one of the most important layers or the component of the device architecture as it governs many factors like dye loading, electron transport and collection, which in turn affect the photo-voltage, photocurrent and the efficiency of the device. The materials used for this are n-type, nano-dimensional, semiconducting metal oxides like  $\text{TiO}_2$ ,  $\text{ZnO}$ ,  $\text{SnO}_2$ , etc. Amongst these,  $\text{TiO}_2$  has been explored more widely. The metal oxide layer should meet several criteria to be able to render the desired high efficiency.

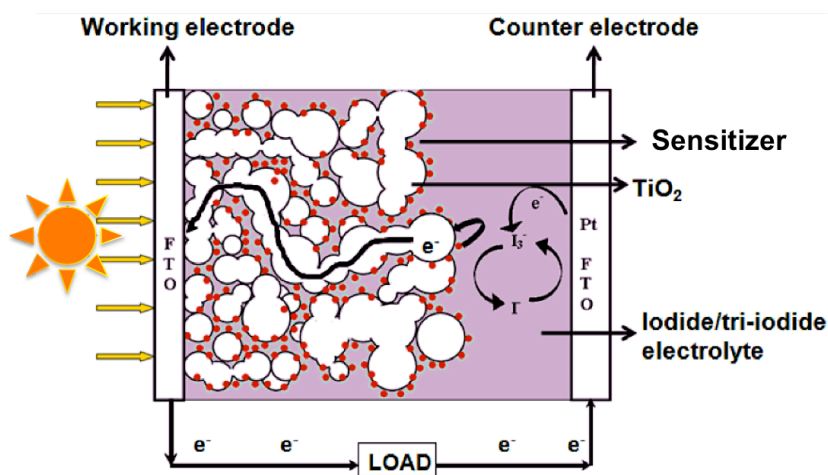


**Figure 1.16:** DSSC device architecture

An appropriate band matching is required to enable excitonic dissociation and charge separation i.e. the metal oxide conduction band must be below the LUMO of a sensitizer. The semiconducting film should be of high surface area metal oxide for more dye loading. Another key factor is the porosity of the film, which helps in the electrolyte diffusion to build electrical connectivity. The conductivity of the metal oxide should be good in order to facilitate better charge transport.

**c) Dye/ Sensitizer:** The important component of the DSSC device is the dye/ sensitizer, as it absorbs sunlight. The sensitizer is required to satisfy some important considerations in order to exhibit a good performance: (1) The sensitizer should absorb a broad range of the solar spectrum extending even up to the IR region with high molar extinction coefficient, (2) It should have appropriate binding functionalities like carboxylic acid, phosphonate group, pyridine, silane, etc. to anchor on the  $\text{TiO}_2$  surface,<sup>29-35</sup> (3) The conduction band of the  $\text{TiO}_2$  must lie below the LUMO of the sensitizer, (4) The sensitizer should have HOMO lower with respect to the electrolyte for better regeneration *via* electrolyte or hole transport layer, (5) It should show enough thermal and photo stability.

*Since the work reported in the thesis deals with the polymeric sensitizer modification for DSSC; this section is described in more details.*

Several materials work as sensitizers as they can fulfill the above requirements and these fall into three major categories: Organic, Inorganic and Organometallic materials. **Figure 1.17** gives the view at glance of the sensitizer evolution over years, which is described in the sections below.

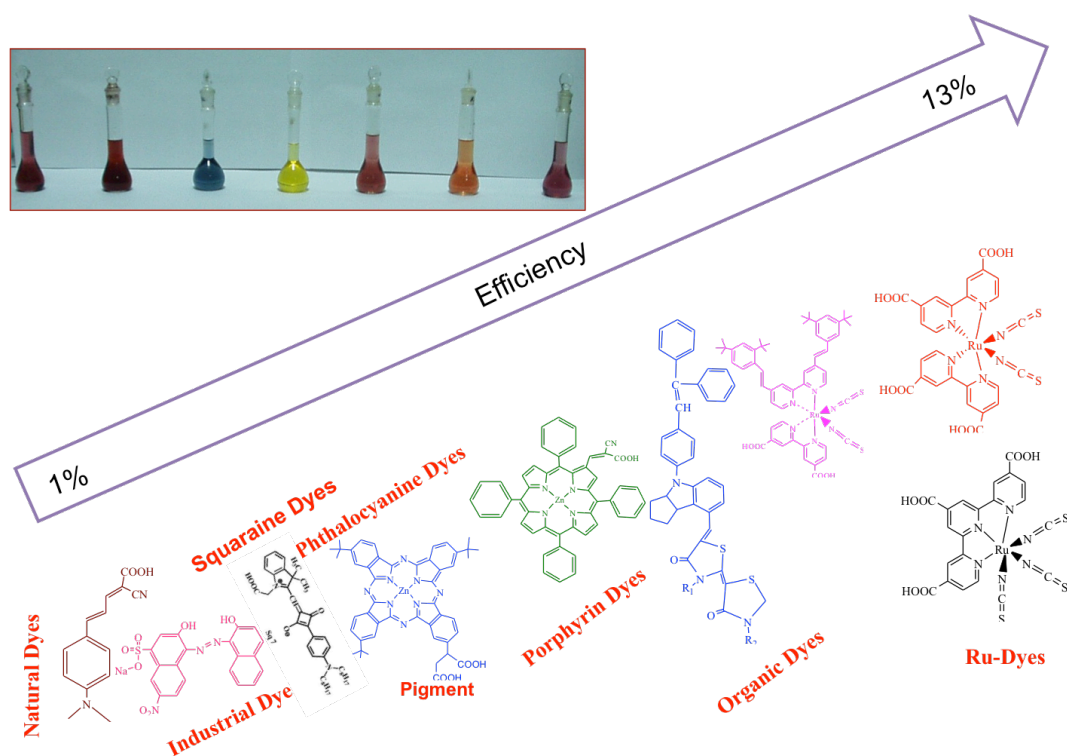


**Figure 1.17:** Evolution of different types of sensitizers.

**(i) Organometallic Materials:** Taking the advantage of metal-ligand charge transport, good absorption in the visible region, and better molar extinction coefficient; organometallic class has been well explored as a sensitizer. The first report was on the ruthenium-based complex, which is the organometallic complex used as a dye in DSSC.<sup>27</sup> Ruthenium being rare earth metal; the numerous organometallic complexes with varying metal core and different ligand structures have been synthesized and explored for their use in DSSC. Organometallic materials such as porphyrines, phthalocyanines, pigments etc. have also been explored. The maximum conversion efficiency reported for DSSC was 12.3 %<sup>36</sup> using Zn-porphyrine based system as a sensitizer. Lower thermal stability of many of these organometallic complexes limits their use as sensitizers. Following dyes have been commercialized for DSSC (**Figure 1.18**).

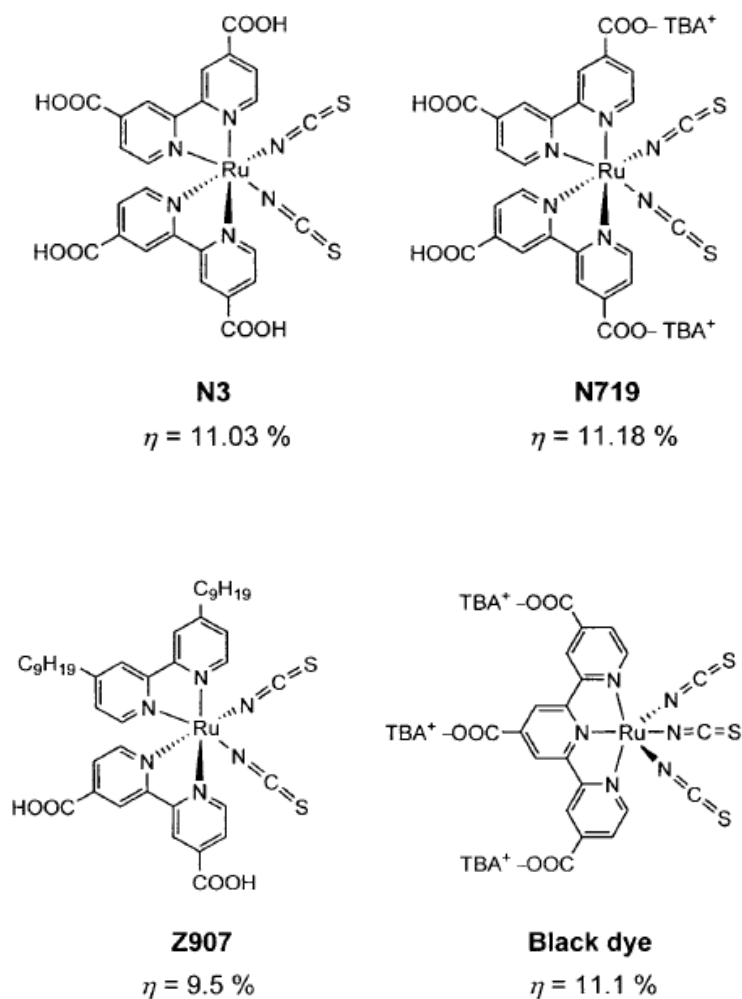


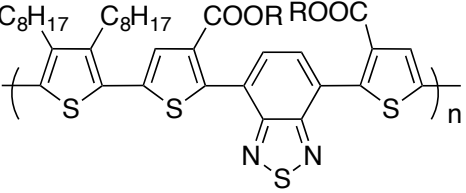
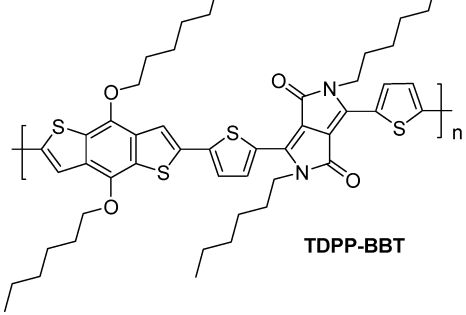
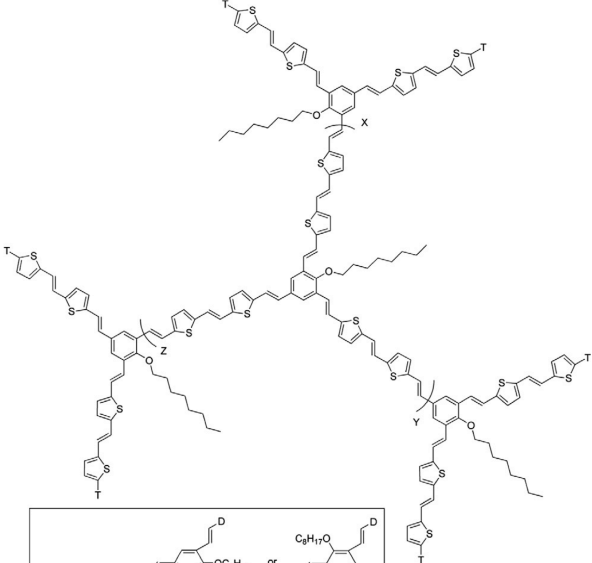
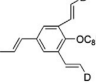
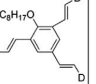
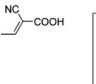

**Figure 1.18:** Commercially available ruthenium dyes

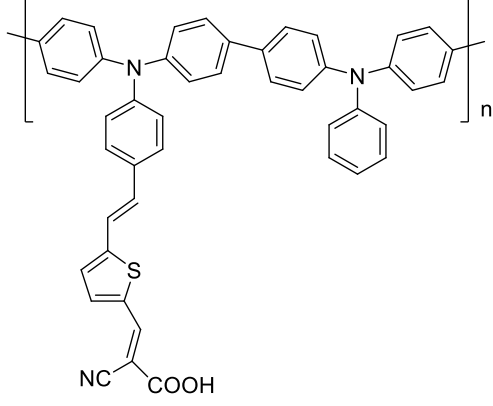
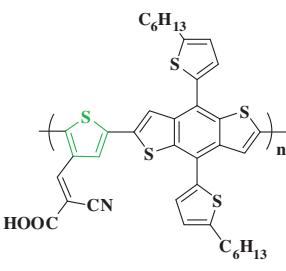
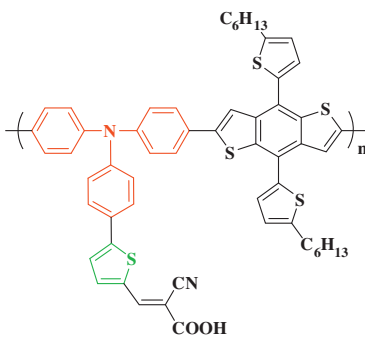
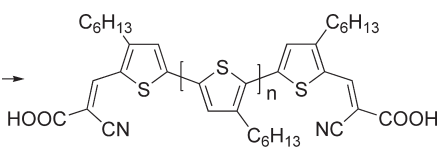
**(ii) Inorganic Materials:** Quantum dots have also been explored for DSSC as sensitizers and have attracted significant interest lately and the so developed area is named as QD-SSC. Quantum dots of several materials like CdS, PbS, CdTe, CdSe etc. with many varying sizes and structures (like core-shell types) have been synthesized and tested for the DSSC devices. The plus points of quantum dots as sensitizers include easy band tunability by varying sizes, high quantum yields, multiple exciton generation, etc. The efficiencies of the QD-SSCs have improved from less than 1% up to more than 6% over the past years.<sup>37</sup> Tedious synthetic steps and toxicity of some of the components are the major issues for these materials, which need to be addressed.

**(iii) Organic/ Polymeric Materials:** To overcome the complications and difficulties of other sensitizer materials, this class of metal free organic materials

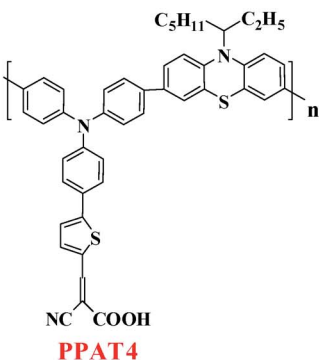
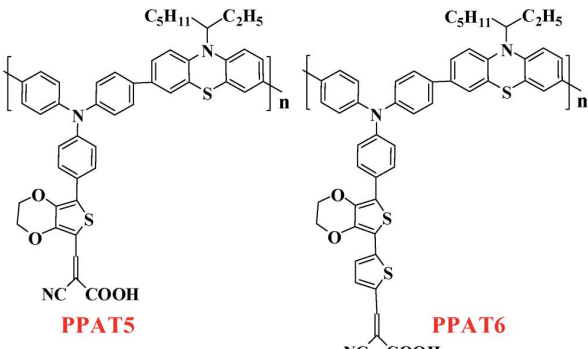
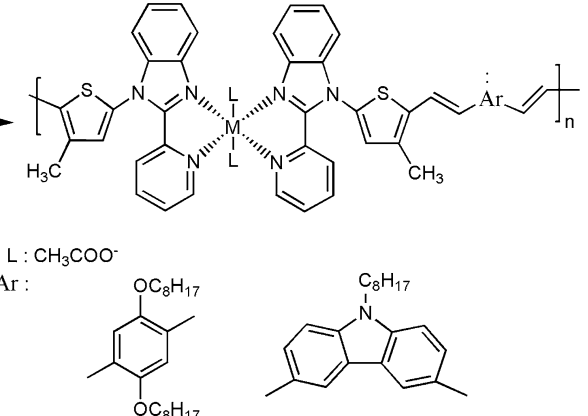
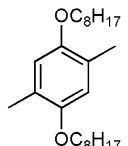
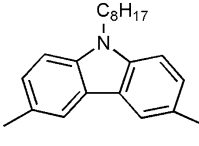
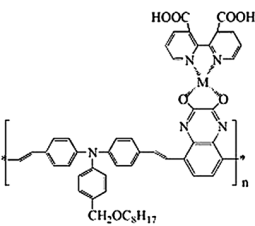


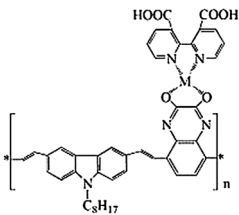
**Table 1.1:** List of polymers used as sensitizers in DSSC

No.	Polymer	Efficiency (%)	Reference
1		2.9	46
2	 <p style="text-align: center;"><b>TDPP-BBT</b></p>	2.4	47
3	 <div style="border: 1px solid black; padding: 5px; margin-top: 10px;"> <p><b>H-tpa</b> T = tpa =  or </p> <p><b>H-cya</b> T = cya = </p> <p><b>H-pca</b> T = 2/3 tpa + 1/3 cya</p> <p style="text-align: center;"><b>D</b> = </p> </div>	3.9	48

4		3.3	49
5	<p data-bbox="552 629 639 663"><math>C_6H_{13}</math></p>  <p data-bbox="552 976 632 999"><b>PPTB-8</b></p>  <p data-bbox="552 1379 632 1402"><b>PPAB-7</b></p>	3.6	50
6	 <p data-bbox="647 1603 679 1626"><b>P3</b></p>	2.18	51



7	 <p style="text-align: center;"><b>PPAT4</b></p>	4.7	52
	 <p style="text-align: center;"><b>PPAT5</b>                      <b>PPAT6</b></p>	3.7, 4.1	
8	 <p>L : CH<sub>3</sub>COO<sup>-</sup> Ar :</p> <p style="text-align: center;">   </p> <p>P1: M=Zn(II)                      P3: M=Zn(II) P2: M=Co(II)                      P4: M=Co(II)</p>	P1-2.1 P2-2.2 P3-2.3 P4-2.4	53
9	 <p style="text-align: center;"><b>PAL1 [M=Cd(II)]</b> <b>PAL2 [M=Cu(II)]</b></p>	1.69 (PAL1) 1.51 (PAL2)	54

	PBL1 [M=Cd(II)]	1.76	
	PBL2 [M=Cu(II)]	1.65	(PBL2)

**d) Electrolyte:** This is the redox mediator prepared using an organic solvent and it plays role to regenerate the oxidized sensitizer molecules. Electrolyte is used for the electron collection at the working electrode and carrying them to the oxidized dye molecules *via* external circuit for regeneration. The redox potential of an electrolyte lying above the LUMO of a dye is thus a prerequisite for its good performance. The diffusion properties of electrolyte also play vital role to counteract mass-transport confinement caused by microporosity. Theoretically,  $V_{oc}$  is the difference of value between quasi-Fermi level of  $TiO_2$  (the oxide used to form the mesoporous layer) and the redox potential of the electrolyte. Most commonly the redox mediator used is composed of iodide/ triiodide ( $I^-/I_3^-$ ) because of the corresponding appropriate energy levels and kinetics<sup>58</sup> and it satisfies the above conditions well. Recently, cobalt-based electrolyte has also been demonstrated to be a better electrolyte.<sup>36</sup> Polysulfide based electrolytes are usually suitable for QD-DSSCs.<sup>59</sup> A range of redox mediator systems are tested for DSSC devices such as  $Br^-/Br_3^-$ ,  $(SCN)^-/(SCN)_2$ ,  $SeCN^-/(SeCN)_3^-$ ,  $Fe(CN)_6^{3-}/Fe(CN)_6^{4-}$ ,<sup>60</sup> and Co(II)/ Co(III) complex. The liquid electrolyte has some disadvantages like leakage and stability. Also iodine based electrolyte corrodes the platinum counter electrode. Hence, to overcome these problems, ionic liquid electrolytes, gel electrolytes,<sup>61-62</sup> polyionic liquid electrolytes, solid state electrolytes<sup>63</sup> have been demonstrated. These gel electrolytes have shown promising results regarding stability as well as efficiency. However, none of the electrolytes have been able to solve all the problems, hence there is plenty of room for research on new electrolyte systems.

**e) Counter Electrode:** The counter electrode is prepared by coating platinum nanoparticles on FTO. The role of platinum is to enhance the charge transfer reaction occurring between iodide and tri-iodide as a catalyst.<sup>64</sup> However, high

cost and less abundance of the platinum has directed researchers' attention towards the replacement of platinum, in order to have inexpensive yet efficient counter electrode. Hence materials like functionalized graphene,<sup>65</sup> CNTs,<sup>66</sup> mesoporous carbon,<sup>67</sup> sulphides, carbides, nitrides and some organic inorganic composites<sup>68</sup> have been and are being tested for this application.

### 1.5.2. Working Principle of DSSC

**Figure 1.20** depicts the working principle of DSSC, which is based on the relative and appropriate band alignments of the components involved in the device fabrication.

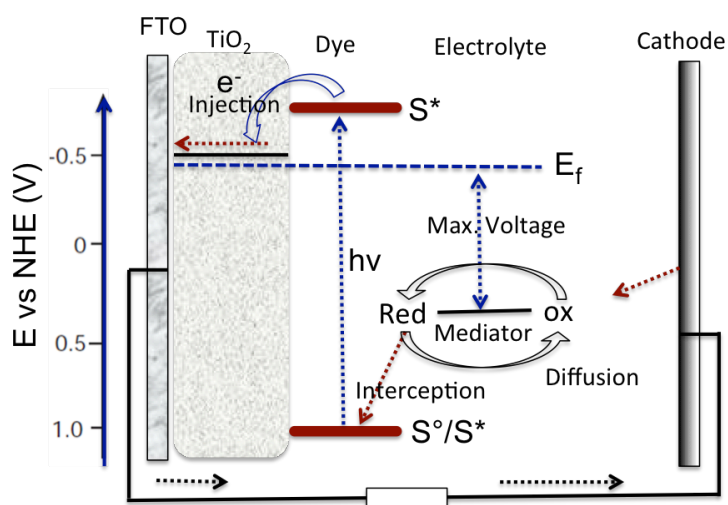
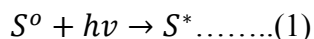
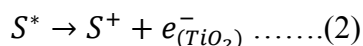


**Figure 1.20:** Working principle of DSSC

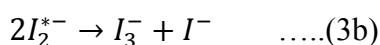
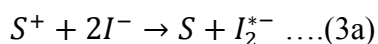
The device is illuminated from the side of the working electrode i.e. FTO-TiO<sub>2</sub> side. This light is absorbed by the dye/sensitizer resulting in molecular excitation. In the excitation process, the incident photon absorption leads to transfer of the electron from HOMO of dye to the LUMO level, which is symbolized by following equation,



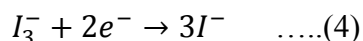
S<sup>0</sup> is ground state and S\* denotes excited state, of the sensitizer molecule. As LUMO of a dye is placed above the TiO<sub>2</sub> conduction band, the photo-excited electron is transferred to TiO<sub>2</sub> conduction band from the LUMO of a dye converting the dye molecule to its oxidized form as,



This electron diffuses through mesoporous conducting TiO<sub>2</sub> network and reaches the counter electrode through external circuit, which causes current flow. The oxidized dye molecule reacts with the redox mediator ( $I^-/I_3^-$  electrolyte) by transferring the electron to the dye (equation 3a) converting iodide to tri-iodide species *via* an intermediate radical  $I_2^{*-}$  (equation 3b), and gets neutralized.



This process is called as the dye-regeneration. The electrolyte should be chosen in such a way that the HOMO of the dye lies energetically below the redox level of the electrolyte. Hence the process is thermodynamically favorable. The tri-iodide species gets reduced by the electron transfer from the counter electrode, which came from the external circuit. This is represented by equation 4.



The electrolyte regeneration and hence dye regeneration can be the rate limiting step, which can affect the overall performance of DSSC. Thus, in order to increase the rate of reaction, a platinum catalyst is used which is coated on the surface of FTO. These reactions (1 to 4) depict the re-generative cyclic paths in DSSC giving rise to photocurrent and voltage. The other reactions such as recombination pathways opposite to above reactions occur simultaneously in the device. Such recombination processes are mainly the efficiency limiting processes.

### 1.5.3 Kinetics

**Figure 1.21** illustrates the kinetics of the processes that occur within DSSC, which governs the performance of photovoltaic device. When light falls on the device, the dye gets excited and the charge carriers are generated (equation 1).

The photo-generated charge carriers have two main pathways to travel based on the energy levels. The first is the electron injection into the TiO<sub>2</sub> conduction band and the second is recombination with the hole in the HOMO level of the dye.

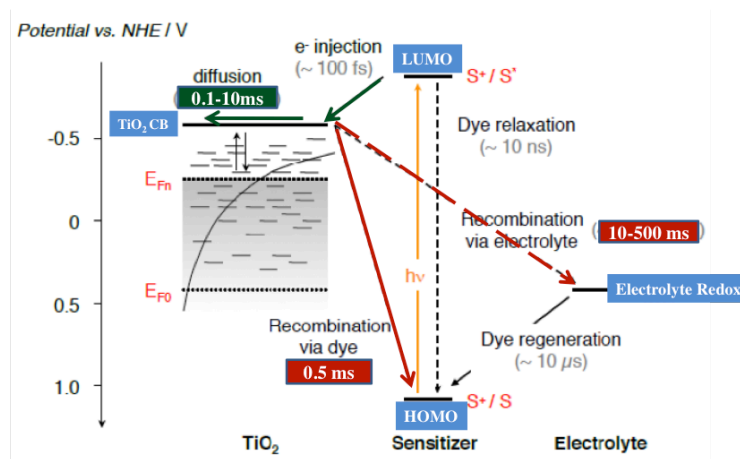


**Figure 1.21:** Kinetics involved in each step of DSSC

The time domains of the kinetics parameters for each process are listed in **Table 1.2**.

**Table 1.2:** Lifetime of each process within DSSC

No.	Process	Life-time
1	Electron injection from dye to TiO <sub>2</sub>	~ 100 fs
2	Electron diffusion through TiO <sub>2</sub> matrix to FTO	0.1 to 10 ms
3	Electron recombination <i>via</i> dye	0.5 ms
4	Recombination <i>via</i> electrolyte	10-500 ms
5	Dye regeneration	~ 10 μs
6	Dye relaxation	~ 10 ns

The process of electron injection has a lifetime of ~ 100 fs which is 10<sup>3</sup>-10<sup>4</sup> times faster than the dye relaxation time (10 ns). Furthermore, from the conduction band of TiO<sub>2</sub> these injected charge carriers can undergo two

recombination processes, *viz.* recombination with the oxidized dye (10-500 ms) and recombination with the electrolyte (0.5 ms). Thus, one of the key points for the better performance of DSSC is this faster charge injection step. The dye regeneration *via* redox mediator is also faster than the recombination of electron with the oxidized dye. This leads to accumulate the charges in TiO<sub>2</sub>, which generates quasi-Fermi level within TiO<sub>2</sub>. The quasi-Fermi level is governed mainly by charge injection, charge carrying and recombination rates. The difference among the TiO<sub>2</sub> quasi-Fermi level and electrolyte redox potential is open circuit voltage of DSSC during illumination at a particular intensity. The photocurrent is regulated by the transport rate of carriers through TiO<sub>2</sub> towards FTO and the rate of recombination of photo-generated charge carriers with the electrolyte. Transport occurs *via* diffusion process, which includes electrons trapping and de-trapping. Hence the lifetime of this process is in milliseconds. This time scale is in the time domains of the recombination processes and hence there is always a competition with the diffusion process on similar timescale. These are therefore the limiting factors in the DSSC performance.

#### 1.5.4 Parameters Governing the DSSC Performance

The section deals with the characterizing parameters and governing factors of the performance of DSSC.

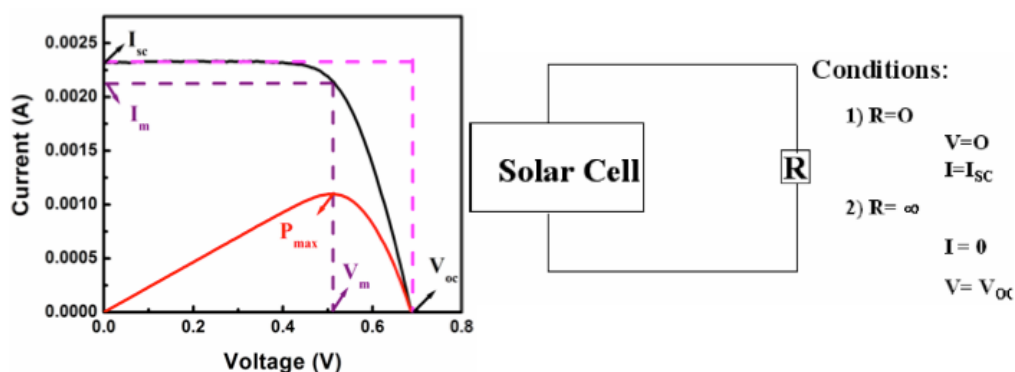


**Figure 1.22:** IV parameters of solar cell.

**(a) Open Circuit Voltage (V<sub>OC</sub>) :** Figure 1.22 represents the typical J-V curve for the solar cell on the basis of which the performance is evaluated. V<sub>OC</sub> is

distance between TiO<sub>2</sub> quasi-Fermi level and electrolyte redox level. It is mathematically expressed as follows,

$$V_{OC} = \frac{E_{CB}}{q} + \frac{kT}{q} \ln\left(\frac{n}{N_{CB}}\right) - \frac{E_{redox}}{q}$$

$E_{CB}$  represents the TiO<sub>2</sub> conduction band edge energy value, 'n' gives the injected electron concentration in TiO<sub>2</sub>,  $N_{CB}$  is the trap states density below the edge of conduction band, and the electrolyte's redox potential is given by  $E_{redox}$ . The  $V_{oc}$  depends on the absorption of a sensitizer, which governs the 'n'. The quality of TiO<sub>2</sub> nanoparticles decides the trap state density  $N_{CB}$  and also the electrolyte's redox potential. In the experiment,  $V_{oc}$  is measured as the difference between the working electrode potential and counter electrode potential of the DSSC when  $R=\infty$  and  $I=0$ , the open circuit condition. The intercept on the x-axis of the J-V curve represents  $V_{OC}$  for the given device.

**(b) Short Circuit Current Density ( $J_{SC}$ ):** In the illuminated device, the shorting of the working and counter electrodes (load  $R=0$ ) produces the current density known as the short circuit current density and the intercept at y-axis of the J-V curve gives its value. In DSSC, the spectral response, the molar extinction coefficient of a dye and the recombination dynamics govern  $J_{SC}$ . Therefore, the dyes with higher extinction coefficients, more visible range absorbance (~400-850 nm) and appropriate HOMO-LUMO alignments are the ongoing quest in the DSSC.

**(c) Fill Factor (FF):** It is defined as the ratio of the maximum power output ( $P_{max}$ ) that can be extracted from a solar cell to the product of  $J_{SC}$  and  $V_{OC}$ . Fill factor is expressed as,

$$FF(\%) = \frac{V_{max} \cdot I_{max}}{V_{OC} \cdot I_{SC}} \times 100$$

$V_{max}$  is the voltage corresponding to the  $P_{max}$  and  $I_{max}$  is the current corresponding to  $P_{max}$ . Geometrically, the fill factor is the representation of the

rectangular character of the J-V curve. FF is reliant on series ( $R_{sc}$ ) and shunt resistance ( $R_{sh}$ ) as well. The  $R_{sc}$  comprises of the electrodes contact resistance, bulk resistance of device, and the sheet resistance of the FTO. The larger values of  $R_{sc}$  can affect  $P_{max}$  of the DSSC resulting into the FF value drop.  $R_{sc}$  is the reciprocal value of a slope of the J-V curve taken at  $V_{OC}$ . The photo-generated electron-hole pairs alternatively recombine in the photoactive layer. As a consequence of this, photo-current as well as  $P_{max}$  lowers down. The resistance to such recombination route inside that photoactive layer is characterized as the shunt resistance ( $R_{sh}$ ).  $R_{sh}$  should possess the higher value for realizing maximum efficiency.  $R_{sh}$  can be acquired by taking the inverse of a slope of the J-V curve measured at  $J_{SC}$ .

**(d) Efficiency ( $\eta$ ):** The power conversion efficiency is the ratio output power to the input power, which is expressed as,

$$Efficiency (\eta)(\%) = \frac{V_{OC} \cdot I_{SC}}{P_{in}} \cdot FF(\%)$$

The efficiency of DSSC is measured under standard condition of ‘AM1.5 Global’ solar irradiance ( $100\text{mW}/\text{cm}^2$ ) at a temperature of  $25\text{ }^\circ\text{C}$ .

**(e) Incident Photon to Current Conversion Efficiency (IPCE):** ‘External Quantum Efficiency’, Quantum efficiency (QE) or Incident Photon to Charge Conversion Efficiency (IPCE) is a measure of the effectiveness of a solar cell device producing photo-generated charges at the specified wavelength. It is the ratio of number of incident photons and photo-generated charges. This is a function of the value of wavelength of excitation:

$$IPCE (\lambda) = \frac{1240 \times I_{SC}}{\lambda \times \phi}$$

Where,  $I_{SC}$  is the short circuit current density ( $\text{mA}/\text{cm}^2$ ),  $\lambda$  is the wavelength (nm) and  $\phi$  is the incident radiation light flux ( $\text{W}/\text{m}^2$ ). For DSSC, the term is defined as:



$$IPCE(\lambda) = LHE(\lambda) \times \phi_{(inj)} \times \eta_{(coll)}$$

At a particular wavelength  $\lambda$ , LHE ( $\lambda$ ) stands for light-harvesting efficiency for the photons,  $\phi$  (inj) represents the quantum yield of injected electrons for the excited dye to the conduction band of semiconducting TiO<sub>2</sub> and  $\eta$  (coll) stands for the fraction of charges capable to reach the contact at the back. By integrating the product of IPCE and incident photon flux (Pin) over the spectral distribution, estimation of J<sub>SC</sub> can be made.

## Section 2: Energy Storage

### 1.6 Storage of Energy

In the previous section, we presented a detailed discussion about the need and requirements for the renewable sources and energy harvested from them. The major renewable sources considered are sun and wind. However, it is difficult to generate energy from renewable sources concurrently with its corresponding demand in the time domain of use; e.g. solar cells will not function at night. Thus, types of technologies like solar, wind, etc. are intermittent and can amend the output very quickly opposite to the demand and can wane for extended periods of time across the domain. Hence the generated energy needs appropriate storage mechanisms and systems in this regard.

The most prominent electrical-energy storage systems are batteries and supercapacitors.<sup>69</sup> The efficiency of the energy storage devices is calculated in terms of power and energy densities of the system. Supercapacitors are efficient in terms of power density though weaker in terms of energy density. Batteries have high energy density but relatively low power density.<sup>70-71</sup> For various applications, traditionally batteries have been the most preferred energy storage devices. However, they suffer drawbacks such as less stability and durability in addition to low power densities. With newer application requirements such as harvesting braking energy for vehicles for green transportation, devices that can be charged and discharged quickly are desired. Supercapacitors fit this bill. They are sought after devices, which have high power density with relatively adequate energy density. Recently, innovative designs of hybrid supercapacitor-battery systems have attracted the attention of researchers. The Ragone plot

shown in the **Figure 1.23** compares the performance parameters of different charge storage systems.

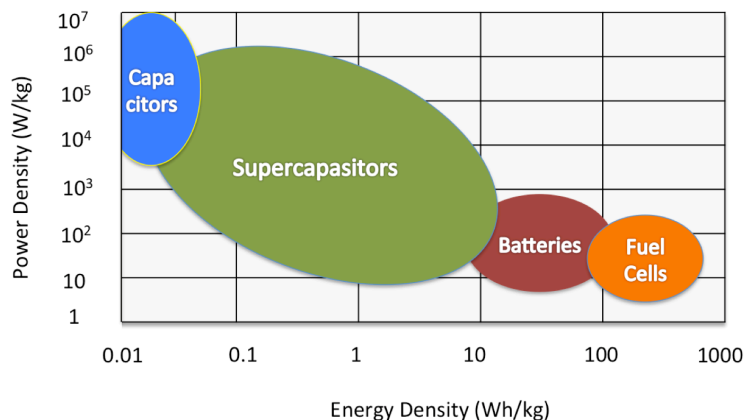


**Figure 1.23:** The Ragone plot

(<http://large.stanford.edu/courses/2012/ph240/aslani1/>)

### 1.6.1 Supercapacitors

Supercapacitors, unlike the conventional solid dielectric capacitors, are based on entirely different charge storage principle and are classified as electrostatic double-layer capacitance storage or electrochemical pseudocapacitance storage or a combination of both. **Figure 1.24** shows different mechanisms for the capacitors.

In the conventional capacitors, the dielectric material or an insulator is inserted between two conducting materials across which the charging voltage is applied. Under the application of an external voltage, the opposite charges get accumulated on the surfaces of respective electrodes due to polarization of the dielectric.

The capacitance ( $C_S$ ) is given by the formula,

$$C_S = \frac{Q}{V}$$

Where,  $Q$  represents the charge stored and  $V$  stands for the applied voltage. Usually, for the conventional capacitor,  $C_S$  is related directly to the each electrode surface area ( $A$ ), and is related inversely to the distance ( $d$ ) between the two electrodes.

$$C_S = \frac{\epsilon_0 \epsilon_r A}{d}$$

Where,  $\epsilon_r$  and  $\epsilon_0$  are constants and signify the dielectric constant (permittivity) of the insulating material in-between the electrodes and free space, respectively. Clearly, the specific capacitance increases with decrease in  $d$ . As discussed in the distinctly different charge storage design concepts of supercapacitors and pseudocapacitors below, this ‘ $d$ ’ can be reduced down to sub-nanometer dimensions, thereby enhancing the value of the capacitor dramatically.

Supercapacitors are classified into electrical double layer capacitors (EDLC), pseudocapacitors and hybrid capacitors depending upon their mechanism of action (**Figures 1.24, 1.25**).

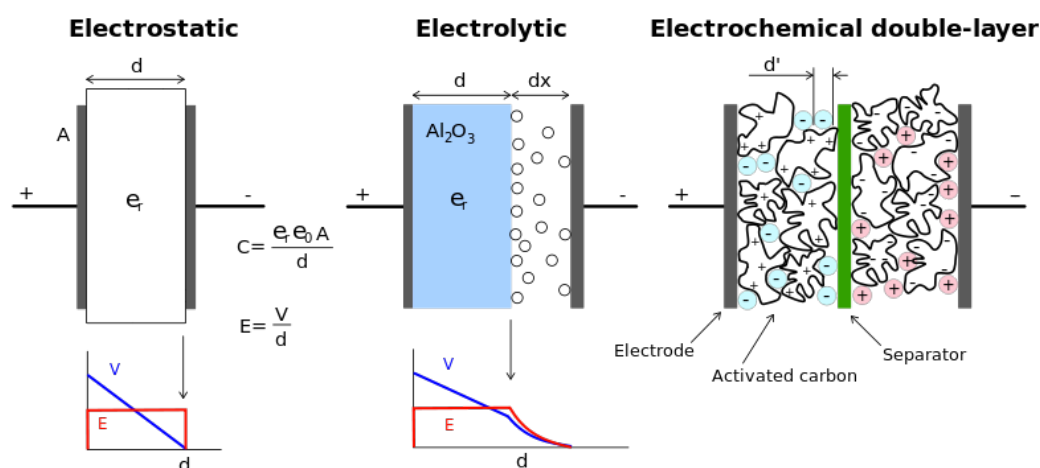


**Figure 1.24:** Double layer capacitors

([https://en.wikipedia.org/wiki/Electric\\_double-layer\\_capacitor](https://en.wikipedia.org/wiki/Electric_double-layer_capacitor))

Electrochemical Double Layer Capacitors (EDLCs) are made of highly porous conducting carbon electrode materials separated by an electrically insulating but ion-conducting membrane and filled with an electrolyte. They store charges by the adsorption of positive and negative charged ions on the respective electrodes, when an external field is applied. Pseudo-capacitors (PCs) store charges by using the mechanism of fast reversible surface redox reactions. Hybrid capacitors, also termed as Li-ion hybrid electrochemical capacitors (Li-HEC), are fabricated by using a battery type insertion electrode, preferably LIB anode,

and a counter electrode which is a supercapacitor component, mostly carbonaceous materials, which forms an electric double layer.<sup>72</sup> This hybrid system has an advantage of higher energy density than supercapacitors and high power density than LIBs.

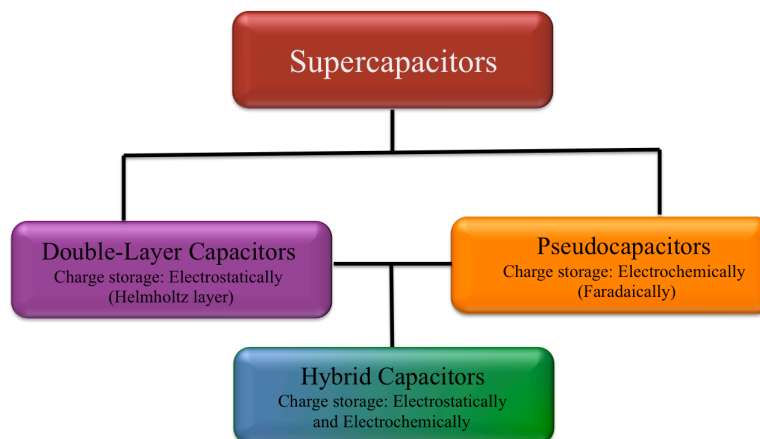


**Figure 1.25:** Classification of supercapacitors

### 1.6.1.1 Parameters for Device Characterization

Energy density (Wh/kg): Energy density is the amount of energy stored in the system with respect to the specific volume or mass. It is represented as follow,

$$E = \frac{1}{2}CV^2$$

Power density (W/kg): The power density is the rate of energy transfer per unit volume and is given by,

$$P = \frac{E}{t}$$

Where t is the time over which the energy E can be harnessed.

### 1.6.2 Electrical Double Layer Capacitance (EDLC)

As stated above, an EDLC supercapacitor is an electrical double layer capacitor, which consists of two high surface area electrodes separated by an electrolyte. (Figure 1.26<sup>73</sup>) High surface area materials (mostly mesoporous conducting carbons) are usually coated on the current collector to make the electrodes. Under the application of an electric field, the ionic charges move across the electrolyte, forming a double layer at the electrodes and thereby rendering very

high capacitance. Depending on the electrolyte used, the EDLCs are divided further into aqueous and organic EDLCs. In the aqueous EDLCs, the electrolytes used are water based e.g. 1M KOH, 1M H<sub>2</sub>SO<sub>4</sub>, etc. In the organic systems the electrolytes are based on organic solvents such as propylene carbonate, dimethyl carbonate, acetonitrile, etc. Generally, high surface area porous carbon materials are used as electrodes for EDLCs because these properties allow storing more charges by providing more area for adsorption. With the same material on both electrodes, such devices are called as symmetric supercapacitors.

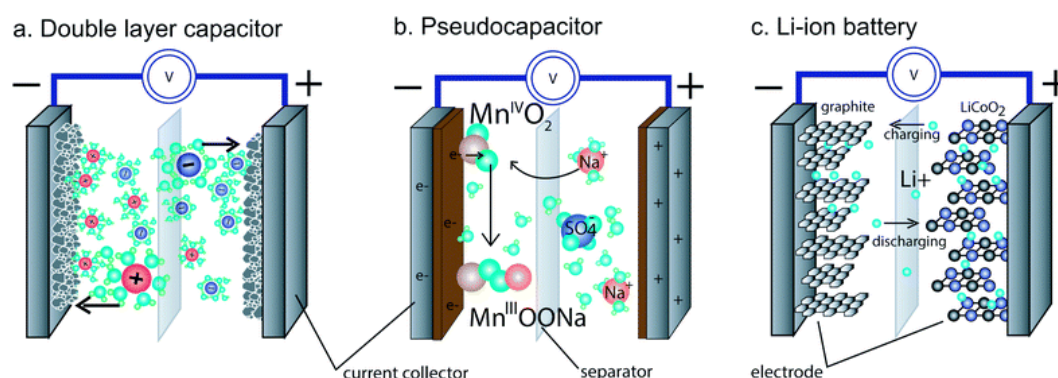


**Figure 1.26:** Mechanisms for (a) double layer, (b) pseudocapacitor and (c) Li-battery

### 1.6.2.1 List of Factors Affecting the Performance of EDLC

- 1. Conductivity of the material:** The material used for the making of electrode must have high electrical conductivity in order to carry the current through the circuit.
- 2. Surface area and Pore size distribution:** The material should be mesoporous with high surface area and hierarchical pore size distribution to facilitate ionic transport during the charging and discharging processes.
- 3. Ionic conductivity of the electrolyte:** The electrolyte ionic conductivity is important for efficient charge transfer and low series resistance.
- 4. Separator:** The ionic transport across the separator should be efficient but the separator must be electrically insulating to avoid shorting of the storage electrodes.

### 1.6.3 Pseudocapacitor

This is a double layer capacitor with a specific difference in the mechanism of action at the electrode surfaces. In this case the electrode material reacts reversibly with the electrolyte, the mechanism being called as Faradaic charge transfer reaction. Highly porous metal oxides, sulfides etc. are commonly used as electrode materials in pseudocapacitors. The reaction happens at the metal center, which reversibly gets oxidized and reduced. The capacitance values are usually much higher than the EDLC, since unlike EDLCs it is not just a surface adsorption phenomenon involving a hydrated ion or an ion with its organic complement. The charge transfer renders it a single naked ion process thereby enhancing the storage density.

### 1.6.4 Hybrid Supercapacitors

This is an asymmetric design of a supercapacitor unlike EDLCs, as it is composed of different electrodes. One electrode is usually an EDLC electrode i.e. carbon electrode, and another is a battery electrode. Typically, lithium based electrode (eg.  $\text{Li}_4\text{Ti}_5\text{O}_{12}$ ) is used hence it is called as lithium ion hybrid electrochemical capacitor (Li-HEC). The mechanism for this includes both the reactions, Faradaic reactions at lithium electrode and non-Faradaic adsorption phenomenon on the carbon electrode.

### 1.6.5 Lithium-ion Battery (LIB)

In 1990, Whittingham *et al.* invented LIB.<sup>74</sup> The device is composed of two electrodes. LIB anode is typically formed by carbon based materials, transition metal oxides and alloying materials like Si while the cathode material is a lithiated metal oxide eg.  $\text{LiCoO}_2$  (Lithium Cobalt Oxide). In this lithium-ion intercalation and de-intercalation is the basic mechanism of charge storage. Hence, mostly graphite sheets have been explored as anode. However the performance of the graphite based electrodes is limited due to restricted surface area; hence other materials like alloys, transition metal oxides etc. are now being researched.

### 1.6.6 Materials/ Components of the Device

The specific capacitance of a device depends on the properties of the electrode materials and the applied voltage. Not only does the specific capacitance value, but other parameters like device stability, cyclic life etc., are also governed by the materials used. Hence the material selection is of fundamental importance to various charge storage device systems.

### 1.6.7 Electrode Materials

High surface area and good electrical conductivity are the prime factors required for materials used for the electrodes. Higher surface area facilitates adsorption of more charges on the given mass of material, which in turn results in a high capacitance value. Apart from the high surface area, the pore size distribution is also important. This factor decides the accessibility of the available pore area. Various carbon based materials like CNT, graphene,<sup>75-77</sup> activated carbon, etc.<sup>78-79</sup> have been studied for EDLC systems. Different forms, morphologies and high surface area porous carbon forms have been synthesized from several sources and have been explored for charge storage systems. The controlled pyrolysis of several materials *viz.* natural waste, biomass, organic and polymeric materials has opened up innovative opportunities for making the desired carbon forms for the respective applications.

### 1.6.8 Electrolyte

This is an important factor that decides the charge-discharge rate of the device and its stability, as this should be tolerant to the applied external voltage. The nature of electrolyte also controls the solid electrolyte interface (SEI) formation and related issues with, defines the device performance. Various types of electrolytes have been used for the supercapacitor applications. For example, an acidic electrolyte can be  $H_2SO_4$  and a basic electrolyte can be KOH.  $Na_2SO_4$ , LiCl,  $Li_2SO_4$ , NaCl etc. are the examples of neutral electrolytes. Usually few molar KOH or  $H_2SO_4$  is used as the electrolyte in the aqueous based systems and for carbon based electrodes. The energy density in the case of aqueous systems can be improved only by material selection and not by high voltage as the water splitting occurs above 1.23 V. Hence organic electrolytes are preferred. Some organic solvents are stable up to 3 V.<sup>80</sup> As the energy density is proportional to

the applied voltage, the higher voltage window is suitable for practical applications. Ethylene carbonate, propylene carbonates, acetonitrile etc. are commonly used solvents and TEABF<sub>4</sub>, LiPF<sub>6</sub>, TEAPF<sub>6</sub> etc. are used for the preparation of electrolyte. Polymeric, ionic conducting electrolytes, gel based electrolytes, ionic-liquid electrolytes have also been studied in the same context.<sup>81-86</sup>

#### **1.6.8.1 Electrolyte Parameters:**

1. Resistance or conductivity of the electrolyte: The viscosity of the electrolyte solution decides the mobility of the ions therein. This is an important parameter to consider for realizing high rate charge-discharge.
2. Voltage Stability: The range of voltage for every electrolyte system is different. This should be considered properly while using the electrolyte in the device. The voltage range for the measurements and device operation is to be selected in such a way that electrolyte should not decompose within the operating voltage.

### **Section 3: Energy Conservation**

#### **1.7 Energy Conservation**

It is the prime necessity of the emergent world to conserve the harvested and stored energy and use it economically and appropriately. The reduction of energy consumption by using low power devices and efficient energy usage without much waste unfolds the actual meaning of energy conservation. This would rather help in future energy crises as the world is growing rapidly and energy is required for every aspect of the modern electrically driven world.

There are several ways to save or conserve energy<sup>87</sup> and some are listed below:

- \* Turning off electronic devices when not in use
- \* Correcting/replacing water-leakage systems to save water
- \* Use of air conditioners only when required
- \* Making more use of natural light
- \* Use of energy efficient lighting and display systems, which require less electrical energy to give the same illumination etc.



In many of the urban usage, the primary energy consumption is by lightening and display systems.

Various display systems depending on different technologies have evolved with time viz. CRT (cathode ray tube), LCD (Liquid crystal display), SED (Surface conduction electron-emitter display), FED (Field emission display), LED (Light emitting diode), OLED (organic light emitting diode), etc. Since this thesis deals with a development of a potential polymeric material for lightweight, flexible field emission display system, we discuss below the related field emission process.

### **1.7.1 Field Emission Display**

It is a flat panel display in which the field electron emission process is employed to generate a source of electrons that hits the phosphor screen producing a color image.<sup>88</sup> Field emission display has the advantages like brighter image, fast response time, high contrast level and most importantly low power consumption (almost half power than CRT display).

#### **1.7.1.1 The Field Emission Phenomenon**

The field emission or cold emission is the emission of electrons into vacuum from the surface of material under the influence of the applied electrostatic field.<sup>89</sup> Unlike the other forms of electron emission (thermionic emission, photoelectric emission, etc.), in field emission the tunneling of electrons occurs across the electrically deformed potential barrier. Field emission is a quantum mechanical tunneling phenomenon. In most other emission processes the potential energy barrier is to be overcome by the external energy leading to their higher energy demand. In the field emission process, the potential barrier deformation at the surface of the material is caused by an applied electric field as high as  $10^7$  V/cm (0.3-0.6 V/Å) through local nano-tip features as a result of which electrons tunnel out from the deformed potential barrier.<sup>90</sup>

The electrons near the Fermi level of the material are responsible for the field emission at the onset potential. With the increasing potential, electrons from the levels below Fermi level start tunneling through the barrier. Hence, this is also named as cold emission.

As stated above, for the realization of a very high local electric field at the surface, the emitter should have a sharp apex radius of few Å. Additional practical concern is the necessity of ultrahigh vacuum conditions. The prerequisite of UHV conditions is also to withstand the emitter geometry by avoiding or reducing under reverse ion bombardment. The intense electric field is expected to cause ionization of residual gas molecules. Thus, the ions accelerated by such high potential difference also bombard the emitter surface and can result in surface erosion by sputtering. The material surface has to be robust to withstand this effect.

In 1897, R. W. Wood observed the field emission phenomenon during some experiments on the discharge tube.<sup>91</sup> Though, Wood was the first to notice field emission, Schottky tried to describe the mechanism of emission as the reduction of the barrier up to Fermi level.<sup>92</sup> Moreover, according to Gosling the electron emission process is independent up to 1500 °K and hence he suggested that there might be quantum mechanical tunneling mechanism responsible for the emission.<sup>93</sup> Later in 1928, Fowler-Nordheim expressed it by using modern quantum mechanical approach.<sup>94</sup> In 1937, E. W. Muller used highly perfect emitter tips of different metallic emitters (tungsten, nickel, molybdenum and copper), which resulted in beautiful field emission patterns.<sup>95</sup> Muller's experiment was in good agreement with the Fowler- Nordheim theory.

#### **1.7.1.2 Fowler- Nordheim Theory (F-N Theory)**

Fowler and Nordheim, by using wave mechanical formulation of quantum mechanics, rationalized the basic process of field electron emission from metals. This theory explained the quantum mechanical tunneling of electrons through potential barrier in the existence of high electrostatic field. The F-N theory is founded on the assumptions such as;

- Metal emitter is at absolute zero.
- Free electron model is applicable for the metal.
- The surface of the emitter surface is plane and smooth.
- The potential barrier at the surface comprises of the image force potential and the potential representing the applied electric field.
- The local work function is uniform across the emitter surface and is independent of the external applied electric field.

The process of field electron emission is shown in **Figure 1.27**. The figure represents the plot of  $V(x)$  (electron's potential energy) in eV against its distance  $x(\text{\AA})$  from the metal surface under the applied electric field, which is superimposed on the energy of electron in the conduction band. Assuming that the potential energy of electron ' $V_p$ ' in a metal is constant, ' $\varphi$ ' gives a work function, ' $e$ ' is electronic charge and the applied electric field strength is given by ' $E$ '.

In the metals, the potential energy  $V_p$  is given by,

$$V(x) = V_p \quad \text{For } x < 0$$

$$\text{and} \quad V(x) = \frac{-e^2}{4x} - eEx \quad \text{For } x > 0$$

Where,  $\frac{-e^2}{4x}$  represents the image force potential and the applied electric field potential is  $-eEx$ .

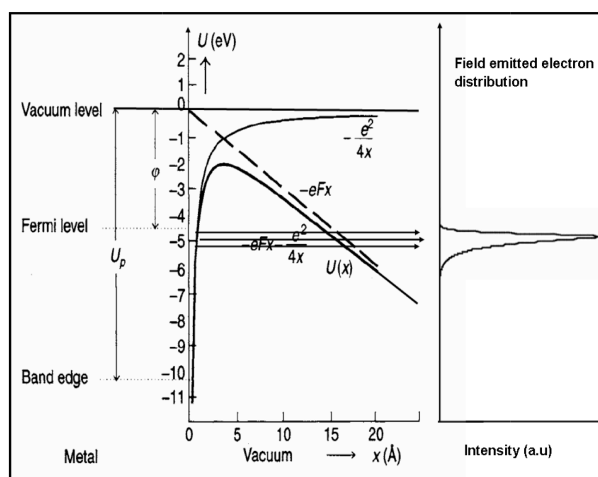


**Figure 1.27:** Potential energy of an electron as a function of distance  $x$ .

The Coulomb attraction between the emitted/ tunneled out electron and its image (its vacancy or hole created after electron emission) inside the metal surface is called as the image potential. It can be expressed by  $-eEx$ , which results in the deformation of the potential barrier.

The distortion / deformation of potential barrier is a result of the work done by the external electric field application. Therefore, the potential energy for  $x > 0$  is given by:

$$V(x) = \frac{-e^2}{4x} - eEx$$

The width of this deformed barrier is,

$$\delta = \frac{\phi}{eE}$$

This width plays an important role in the mechanism of field emission. Although classically the kinetic energy to cross the barrier is insufficient, the electron can tunnel through the deformed potential as this width of potential barrier becomes comparable to the de-Broglie wavelength of electrons, which may result in the penetration of the wave function across the deformed potential barrier. This tunneling of electron is quantum mechanical phenomenon. By solving the Schrodinger equation for a simple triangular barrier, Fowler-Nordheim described the field emission process. Since 1928, the theory was revised several times and is currently stated as ‘‘Fowler-Nordheim equation’’, as derived by Murphy and Good.<sup>96</sup> Fowler-Nordheim (F-N) equation demonstrates a correlation between electron emission current ( $I$ ), applied voltage ( $V$ ) and work function ( $\phi$ ) of the emitter and is represented as follows,

$$I = 1.54 \times \frac{10^{-6}(\beta^2 V^2 A)}{t^2(y)\phi} \cdot \exp \left[ \frac{(-6.8 \times 10^7 \phi^{\frac{3}{2}})}{\beta V} f(y) \right]$$

Where,  $f(y)$  and  $t(y)$  are varying parameters as a function of the applied field. ‘ $y$ ’ is given by,

$$y = \frac{1}{\phi} (e^3 E)^{1/2}$$

The exponential factor ( $\phi^{\frac{3}{2}}/E$ ) in the F-N equation implies that a small change in work function can change the current density substantially.<sup>97-98</sup>

Normally, during the experiment, emission current ( $I$ ) is measured as a function of the applied potential ( $V$ ) between the anode and cathode. The current density  $J$  and local electric field (or surface field)  $E$  are related and given by,

$$I = JA$$

$$E = \beta V = \frac{V}{kr}$$

Where,  $A$  is area of emitter in  $\text{cm}^2$ ,  $\beta$  represents the field enhancement factor, which is determined from the emitter geometry, the tip radius is given by  $r$  and  $k$  is geometrical factor appearing due to conical shrank of the tip. Usually, for metals  $k$  is taken as  $\sim 5$ .

The plot of  $\log(I/V^2)$  versus  $(10^4/V)$ , called as F-N plot or F-N characteristic, investigates the F-N equation further. The linear F-N plot is typically observed for a metallic emitter. The slope of the F-N plot is given by,

$$m = -\frac{2.97 \times 10^3 \phi^{\frac{3}{2}}}{\beta} s(y)$$

Where,

$$s(y) = f(y) - \frac{y}{2} \left[ \frac{df(y)}{dy} \right]$$

$\phi$ ,  $\beta$  and  $A$  are not dependent of  $V$ . If the image force is neglected, the function  $s(y)$  reaches unity and in turn  $m$  will nearly be constant resulting in straight line F-N plots. For a given emitter, the work function can be calculated by using slope equation for known  $\beta$  value (radius of emitter is useful to know  $\beta$ ). Also, from the same slope equation  $\beta$  can be estimated for the known work function value.

### 1.7.2 F-N Theory for Semiconductors

The above F-N theory discussion is valid only for pure metallic emitters. For semiconducting emitters the theory turn out to be complex because of various aspects like effective electron mass, surface states, field penetration, n-type or p-type doping, band structures etc. Stratton *et al.*<sup>99</sup> explained the effect of field penetration and surface states of electron emission for the semiconducting materials and postulated that the surface states affecting field emission characteristics are temperature dependent. Baskin explained field emission from an n-type semiconductor.<sup>100</sup> Modinos proposed briefly the theory of field emission from semiconductors.<sup>98</sup> Recently; Forbes and Deane attempted revision of F-N theory<sup>101</sup> and restructured the F-N theory. Forbes stated a revised arithmetical form for empirical field emission I-V characteristics.<sup>102</sup>

*In the previous sections, the need for energy and its conservation, storage and conservation have been discussed. Along with those sections some examples of classes of materials being used are also discussed. In the forthcoming section we present a brief discussion regarding polymers for diverse energy applications.*

### 1.8 Polymers

Polymers occur since the existence of life. Shellac, horns, latex, amber, etc. are some of the examples of naturally existing polymers. J. J. Berzalius coined the term “polymer” in 1833. In 1920, Hermann Staudinger developed the concept and introduced the term “macromolecules”. After that the field of polymer science evolved greatly and now polymers have occupied almost all branches of applications. Polymers have become the part of day-to-day life in the current era. These are the large molecules made up of the repeating units called as monomers. Unlike other organic molecules polymers shows diverse range of properties.

Polymers can be tuned in various ways. Polymer properties<sup>103</sup> can be altered or tuned by:

- \* Selection of monomer
- \* Monomer functionalization
- \* Arrangement of monomers in copolymers

- \* Polymerization methods
- \* Architecture of polymers (**Figure 1.28**)
- \* Molecular weight or chain length of polymer
- \* Post polymer functionalization

Due to this diversity, polymers have gained special attention and applications in almost all fields. **Figure 1.29** illustrates some of the areas of applications where the polymers are used.

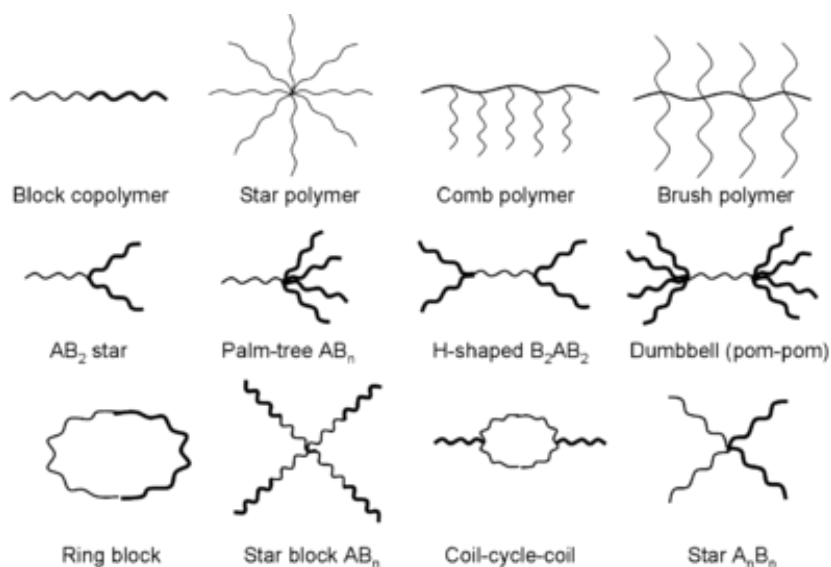


**Figure 1.28:** Variety of architectures of polymers

(<https://en.wikipedia.org/wiki/Polymer>)

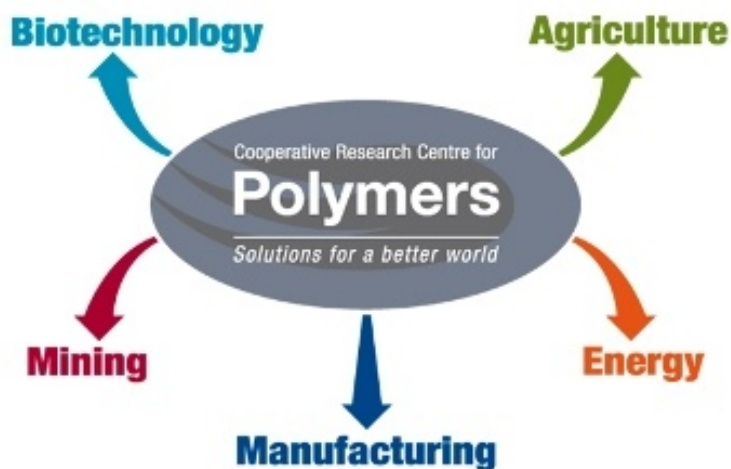


**Figure 1.29:** Applications of polymers

(<http://www.swinburne.edu.au/engineering/cmp/images/research/crcpareas.jpg>)

Polymers show applications in broad range as plastics for day-to-day life, high performance plastics, resins, thermosets, elastomers, coatings, etc. The application zone of the polymers is decided predominantly by their structure, which in turn decides chemical nature, physical properties, etc. Few examples are listed here: 1) polyethylene is used for packaging, bags etc. 2) Nylon 6 is high strength, tough polymer which finds applications in various sectors such as in automotive industry, in toothbrush, for formation of ropes, net etc. 3) Other class of polymer named as conjugated polymers have the advantage in optoelectronic devices. These polymers are semiconducting materials. 4) Another class: ionic liquid polymers are useful in batteries, fuel cell, etc. as they are capable of conducting ions.

### 1.9 Polymers for Energy Applications

Polymers can be considered as leading candidates for various energy applications because of their versatility in chemical and structural features. Polymers offer innumerable new prospects for the energy generation, storage and energy savings.

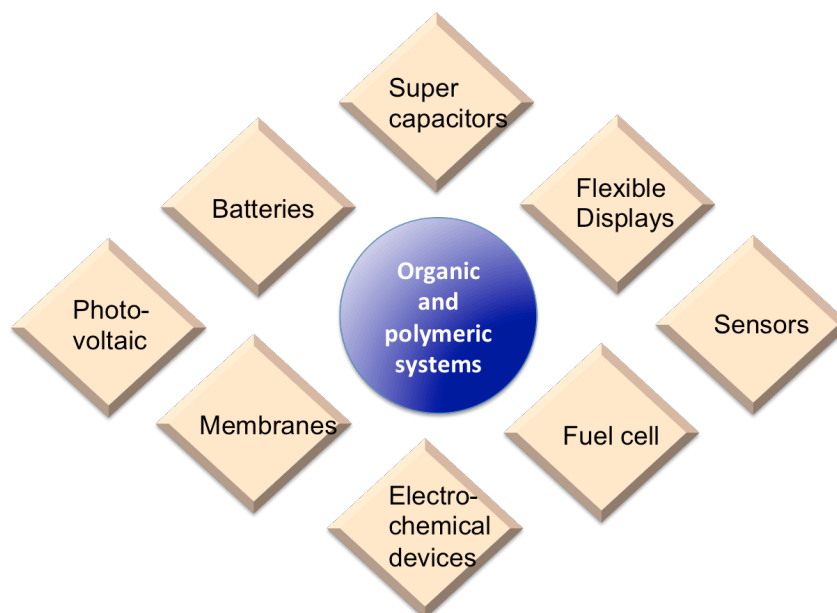


**Figure 1.30:** Polymers for various energy applications

Polymers have proved to be promising materials for such applications because of their intrinsic benefits like light weight, cost effective manufacture/fabrication, easy processing like solution processability, diverse scope for tuning their



properties (e.g., by processing, formulation, selection of monomers, molar mass, compositions, etc.).

Additionally, new advanced and easy solutions for devices like flexible solar cells or batteries are possible because of polymers.<sup>104</sup>

These characteristics of polymers are advantageous for the progress of device systems with qualities like high surface area, charge transport facilitation, and chemical functionalization according to respective device, etc. **Figure 1.30** shows the diversity of energy applications for polymers.

### 1.9.1 Polymers in Solar Cells

For various applications, polymers are being used starting from substrate to active materials. Potential of using various polymers lies in the synthesis methodologies, which opens up the sea of different structures to get desirable properties. As compared to inorganic materials (for e.g. silicon based materials), polymers are flexible, somewhat cost-effective, and easy to manufacture.

- a) Polymers as substrate: polyethylene terephthalate (PET) is used as a flexible substrate. Indium tin oxide (ITO) is coated on the PET as transparent conducting oxide. This ITO-coated PET becomes one of the electrodes for many devices.
- b) Polymers as sealant: light-curing polymers, thermal curing polymers, or photopolymerizable functional materials etc.<sup>105</sup> are used as sealants for devices. eg. surllyn generally used for DSSC device sealing
- c) Polymers as active materials for bulk heterojunction solar cells (BHJ) or organic photovoltaics (OPV): A class of conjugated polymers, which absorbs in visible range, is used for the BHJ device as the photoactive material. The conjugation is responsible for visible absorption and hole transportation.
- d) Polymers as hole transport materials (HTM) in DSSC: generally they are not absorbing in visible range. These kinds of polymers are able to show good redox properties. These include some conjugates polymers, polyamides, polyazomethines, poly(1, 3, 4- oxadiazoles), etc.
- e) Polymers as sensitizer in DSSC: conjugated, photoactive polymers are used. Polymers like polythiophene derivatives, polytriaryl amine derivatives, etc have shown promising results.

### 1.9.2 Polymers in Energy Conservation

- Polymers as substrate: ITO-coated PET plays a role of one of the electrodes for many devices like OLEDs, flexible display systems.
- Polymers as hole transport materials (HTM) in OLEDs: They should have good redox properties. Polymers like poly triarylamine, polyfluorenes etc. are employed as hole transport materials in the OLED devices.
- Polymers as active materials: Solution processed, luminescent conjugated polymers such as PPV, polythiophenes etc. have been studied for the application of OLEDs and FETs. Polymers like polypyrrole, polyaniline, polythiophene and their composites, etc. have been explored for the field emission studies.

*In the present thesis, for energy conversion (polymer as a sensitizer in DSSC) as well as conservation (phenazine based PPV for field emission), PPV derivatives that fall under the class of conjugated polymers have been studied.*

#### 1.9.2.1 Conjugated Polymers

The area of pi-conjugated polymers and their use in electronic devices began with the discovery of the polyacetylene-conducting polymer.<sup>106,107</sup> These are organic macromolecules, which contains single-double bonds in an alternating way.

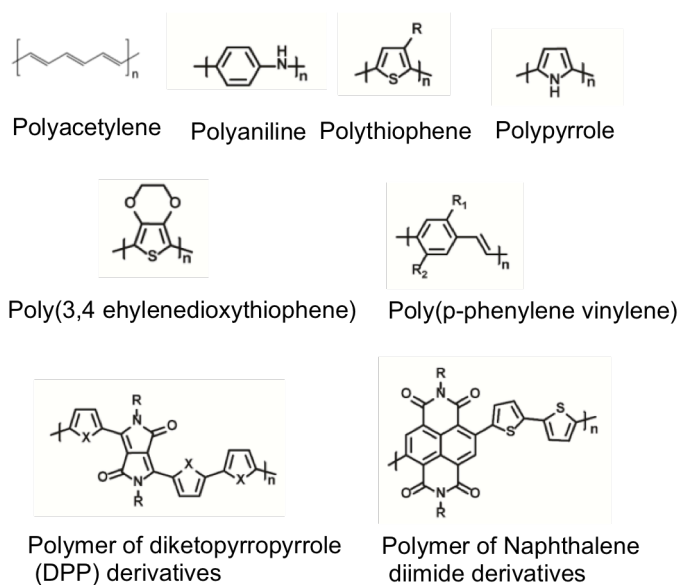


**Figure 1.31:** Few representative examples of conjugated polymers

Due to overlapping of p-orbitals,  $\pi$ -electrons are delocalized. This delocalization is the cause of properties like absorption, electronic conductivity, etc. These polymers are semiconducting or insulating depending on their chemical composition, structure and doping. Conjugated polymeric systems are solution processible and hence find the potential applications in flexible electronics.<sup>108</sup> Conjugated polymers open up the field of flexible organic electronics.<sup>109</sup>

The  $\pi$ -conjugated polymers are intrinsically conducting polymers. **Figure 1.31** illustrates representative structures of the conjugated polymers. The properties of the conjugated polymers are easy to tune by altering of the polymer backbone or the side groups. By tuning the chemical structure of the conjugated polymer, they can be explored for the range of applications such as OLEDs, solar cells, FETs, sensors, etc.<sup>110-117</sup> **Figure 1.32** depicts the application range of conjugated polymers at a glance.

Polymers have the advantages such as film forming nature, mechanical strength and flexibility over the small molecules as well as inorganic materials.<sup>118</sup> Molecular weight, side chains, functional groups and the film formation methods collectively decides the behavior of the polymers in solution state to solid-state. As a result of this, polymers exhibits different morphologies, which in turn affects the device performance.<sup>119</sup>

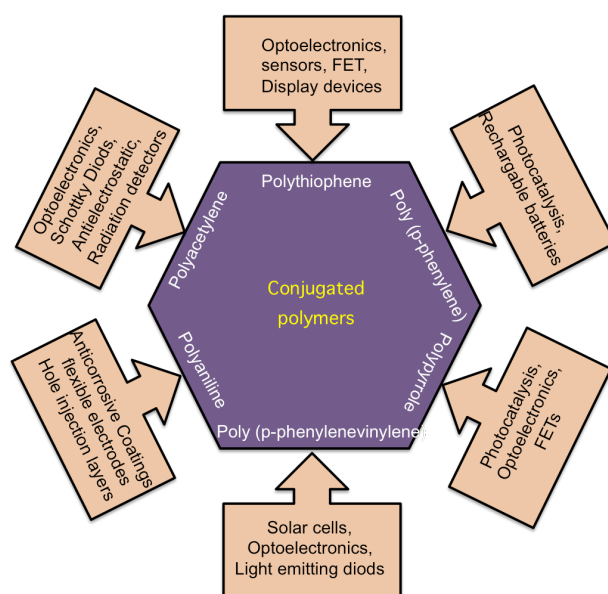


**Figure 1.32:** Conjugated polymers: perspective

### 1.9.2.2 Band Theory for Conjugated Systems:

The alternating single and double bond is the prerequisite for the conjugation.<sup>120</sup> The  $\pi$  electrons are delocalized and participate in the conduction mechanism. The band gap ( $E_g$ ) for the conjugated polymers is the difference between highest occupied molecular orbital (HOMO) (valance band) and lowest unoccupied molecular orbital (LUMO) (conduction band) of the polymer. The difference between HOMO- LUMO depends on the monomer repeat unit number that is illustrated in **Figure 1.33**.

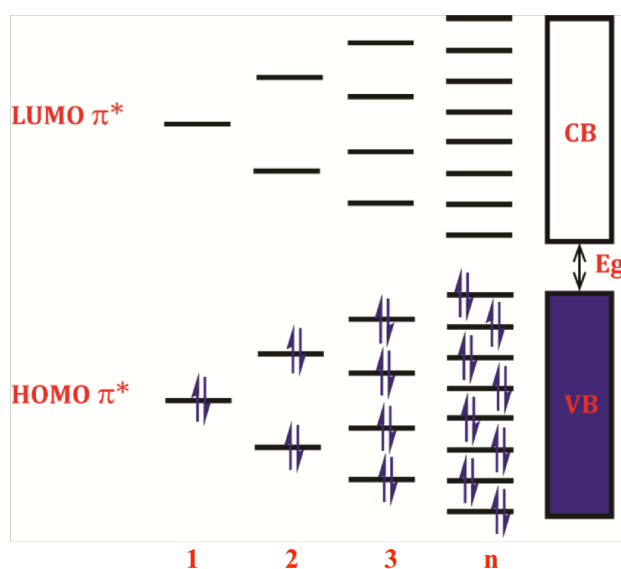


**Figure 1.33:** Representation of the band gap modulation with the increasing number of repeating units.

The hybridization states of the monomers decide the bandwidth of the monomer units, which is responsible for the degree of separation between HOMO and LUMO. The ground state is unstable and thus experiences Peierls distortion, which is the cause of bond length alteration. Furthermore,  $\pi$  bond splits into valance bond (HOMO) and conduction band (LUMO). Thus, the conjugated materials acquire the semiconducting properties.<sup>121</sup>

### 1.9.2.3 Challenges in Conjugated Polymers

Although the conjugated polymers find much superior advantages like flexibility, solution processability, etc. over the inorganic materials; they face some limitations/ disadvantages.

- \* Tricky synthesis
- \* Reproducibility
- \* Attainment of high molecular weight
- \* Problems in high temperature, UV stability

The drawbacks mentioned above are the downsides of conducting polymers with respect to semiconducting inorganic materials. They need to be improved in all aspects.

### 1.9.3 Poly (p-phenylene vinylene) (PPV)

The conducting polymer, poly(phenylene vinylene) is a class of oldest conjugated polymer having phenylene and vinylene alternate units connected together. An ordered crystalline film has been processed from this polymer. This is also called as rigid rod like polymer. PPV is the most studied material for basic photophysics of conjugated polymers due to their extended conjugation, good stability, structural simplicity, and band gap that falls in the visible range.<sup>122</sup>

#### History of PPV:

In the area of polymer electronics, PPV has been the most studied class of conjugated polymer. PPV was reported as the first electroluminescent polymer. In 1990, electroluminescence of yellow-green color was shown using PPV.<sup>123</sup> The first ever demonstration of bulk heterojunction solar cell (BHJ) was displayed in 1995 using blend of poly[2- methoxy-5-(2-ethylhexyloxy)p-phenylene vinylene] (MEH-PPV) and fullerene derivative.<sup>124</sup> Sulfonated PPV was reported as the first conjugated polyelectrolytes and explored for the fluorescent sensors.<sup>125</sup> Optically pumped polymer lasers were demonstrated in 1996 for the first time by using derivatives of PPV.<sup>126</sup>

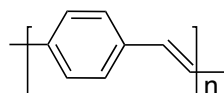


**Figure 1.34:** Basic structure of PPV

### 1.9.3.1 Synthesis Routes for PPV

Unsubstituted PPV is insoluble material, which is hard to process. To overcome this drawback, new derivatives with new synthetic protocols have been proposed. Peregichka et al reviewed the advances and challenges in PPVs.<sup>127</sup>

Various methods of synthesis of PPVs have been explored and are listed below:

❖ P-Quinodimethane Intermediates used for polymerizations:

- The Gilch Route:

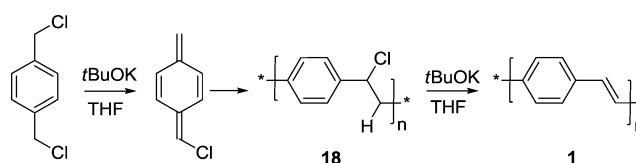


**Figure 1.35:** Gilch polymerization approach. (Reproduced and reprinted by the permission from the reference 127: *Isr. J. Chem.* 2014, 54, 674 – 688)

**Figure 1.35** represents the Gilch polymerization approach. In 1965, Gilch and Wheelwright at Union Carbide developed the method for PPV using a strong base only. Gilch route proved to be economical for industrial scale synthesis of PPV.

- Wessling Precursor Route: In 1996, Wessling and Zimmerman demonstrated use of sulfonium groups for substitution of chlorine on p-xylene precursor. This was followed by addition of base to yield poly-p-xylylene precursor that is sulfonium-substituted and heating this precursor formed PPV.

## ➤ Chemical Vapor Deposition

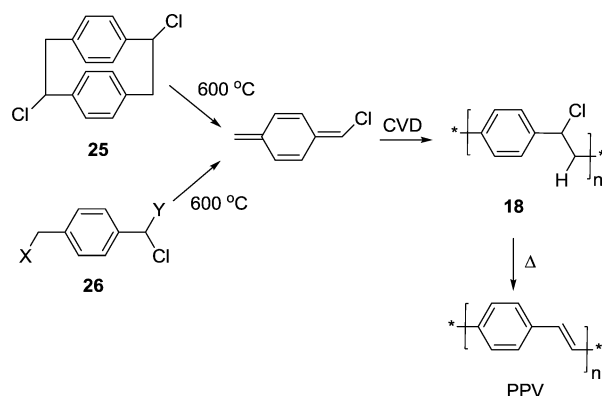


**Figure 1.36:** Chemical vapor deposition for synthesis of PPV. (Reproduces and reprinted by the permission from the reference 127: *Isr. J. Chem.* 2014, 54, 674 – 688)

The chemical vapor deposition mechanism for PPV synthesis is shown in **Figure 1.36**. The precursor film was obtained by CVD method, which is then followed by heating to get PPV.

❖ Olefin Metathesis Polymerizations:

This type of polymerization provides the route for high molecular weight PPVs.

- Ring-Opening Metathesis Polymerization (ROMP): In 1992, direct PPBV synthesis from ROMP was shown using paracyclophanediene.
- Acyclic Diene Metathesis (ADMET) Polycondensation: By using this strategy, *all-trans* PPV has obtained.

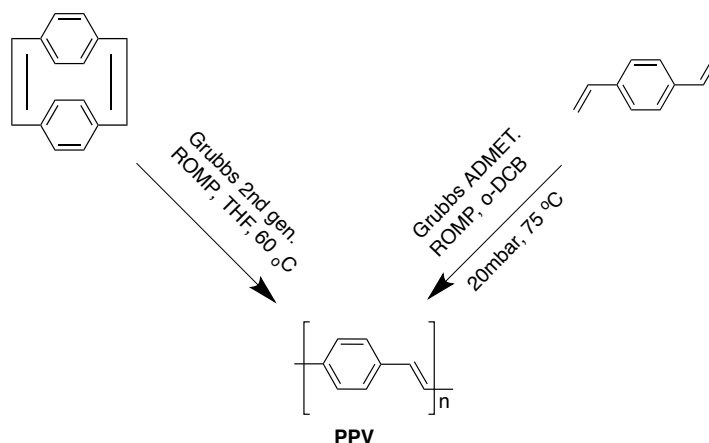


**Figure 1.37:** Olefin metathesis polymerizations for synthesis of PPV.

❖ Nucleophilic poly-condensations reactions

- Wittig-type polycondensations
- Knoevenagel polycondensation
- Siegrist polycondensation

**Figure 1.38** shows Wittig type polymerization methods for synthesis of PPV. These nucleophilic polycondensation reactions are base promoted reactions. In Wittig type reactions and Knoevenagel polymerizations, potassium t-butoxide is preferably used while in Siegrist Polycondensation strong base such as n-butyl lithium is used.

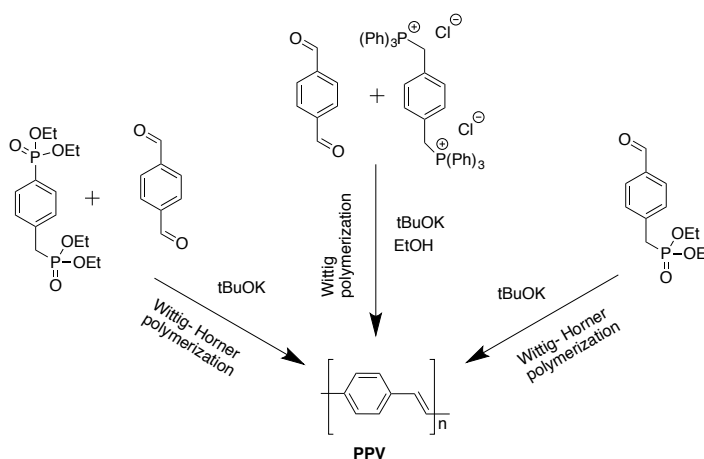


**Figure 1.38:** Wittig type polymerization methods for synthesis of PPV.

❖ Palladium-Catalyzed C-C Coupling Polymerizations

- Mizoroki-Heck polycondensation



- Suzuki polycondensation
- Stille polycondensation

Metal catalyzed carbon-carbon coupling reactions have attracted attention of researchers over the past few decades.<sup>128</sup> Especially, palladium catalyzed C-C bond formation reactions are interesting for the synthesis of PPV and other conjugated polymers. **Figure 1.39** depicts routes for metal catalyzed reactions to synthesize PPV.

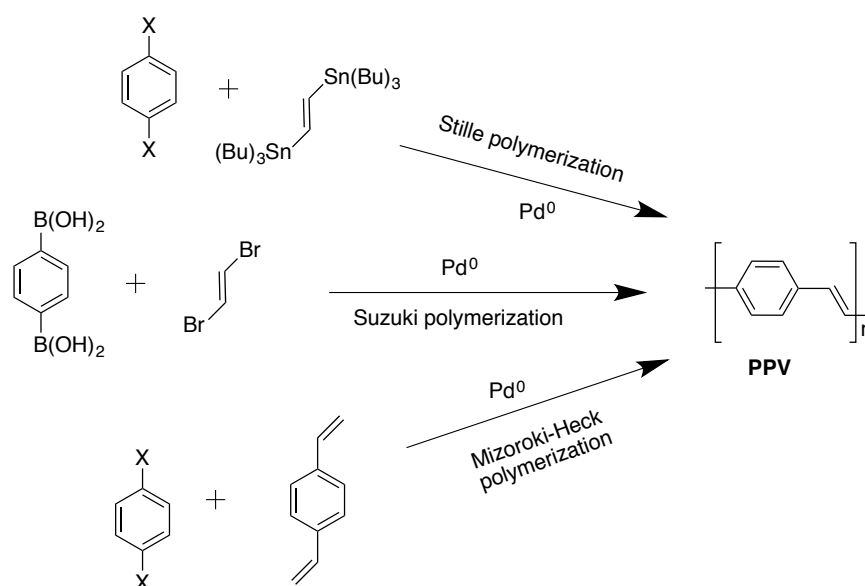


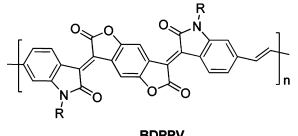
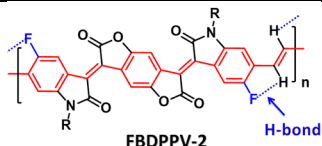
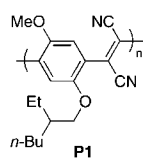
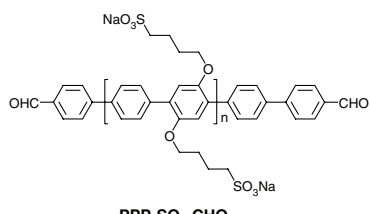
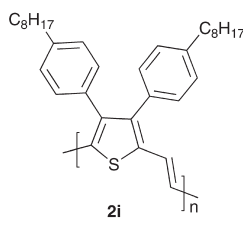
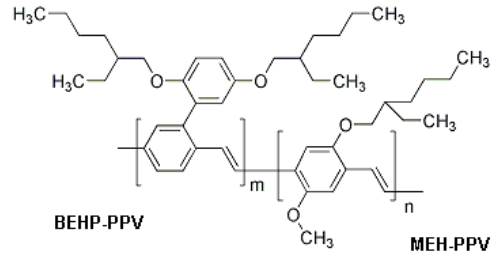
**Figure 1.39:** Palladium catalyzed reactions for synthesis of PPV.

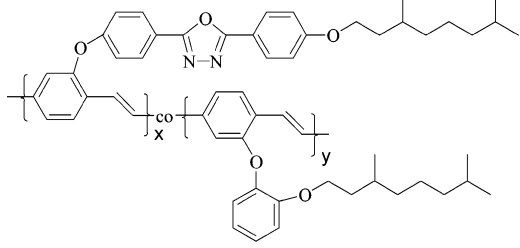
### 1.9.3.2 Properties of PPV

Most of the properties of PPVs are in-between properties of polyacetylenes and polyphenylenes (PPP). They are chemically more stable than polyacetylenes. The band gap of many PPV derivatives lies in the range of 2.4–2.5 eV.<sup>129</sup> PPVs are more flexible structurally than PPPs. The flexible structure is attributed to conformational disorder. Furthermore the optical properties of PPV derivatives are considerably influenced by conformational factors. eg. PPV shows solvatochromism.<sup>130</sup> Good solvents lead to extended chain conformations resulting into red shifted absorbance while poor solvents lead to coiling of chains showing blue shift.<sup>131</sup> They are soluble in many organic solvents and hence are the potential candidates for the solution-processed devices. PPVs are

intrinsically low conducting. They show increased conductivity upon doping. Employing various electron donating and withdrawing groups during synthesis can tune the electrical, physical and optical properties of PPVs. **Table 1.3** shows various derivatives of PPV, which have been synthesized and used for several applications.

**Table 1.3:** Derivatives of PPV used for various applications

No	Polymer (PPV)	Application	Reference
1.	 <p>BDPPV</p>	FET	132
2.	 <p>FBDPPV-2</p> <p>H-bond</p>	OFET	133
3.	 <p>P1</p>	Synthesis methodology	134
4.	 <p>PPP-SO<sub>3</sub>-CHO</p>	FRET	135
5.	 <p>2i</p>	OPV	136
6.	 <p>BEHP-PPV</p> <p>MEH-PPV</p> <p>m:n = 0.6:0.4</p>	OLED	137

7.		OLED	138
----	---	------	-----

### 1.9.4 Polymers in Energy Storage

Figure 1.40 illustrates the scenario of the diverse applications of polymers in charge storage systems. Polymers forms important share in the sector of energy storage.

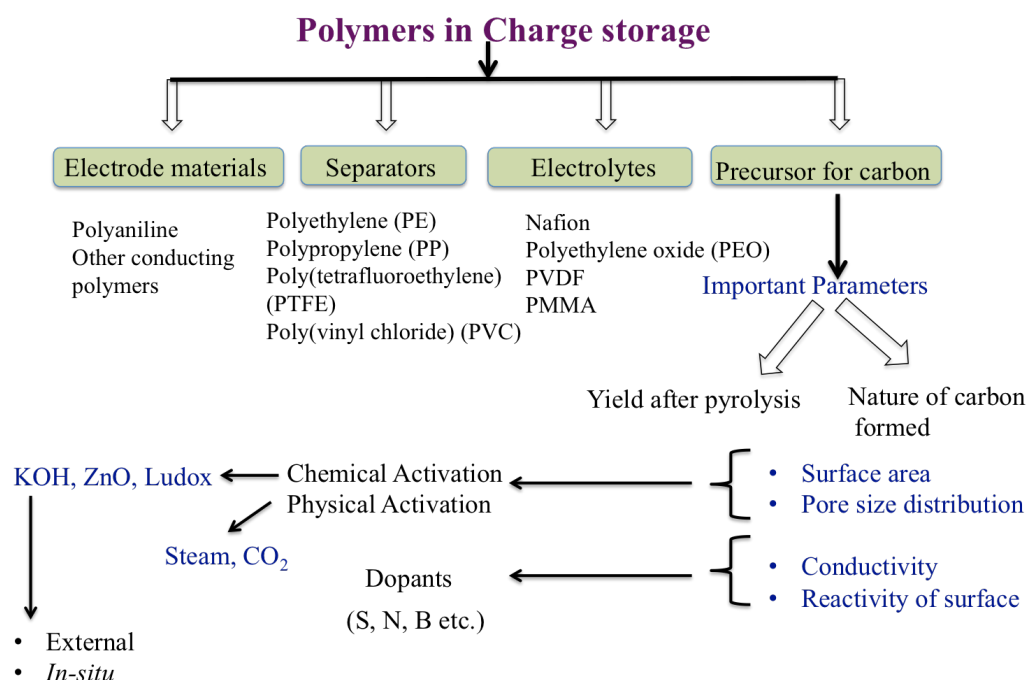


**Figure 1.40:** Overview of the use of polymers in energy storage systems

- Polymers as substrate: ITO-coated PET as flexible substrate.
- Polymers as electrolyte: The electrolyte is the material, which is ion carrier in the system. For the solid-state devices, generally ionic conducting polymers like Naffion (in fuel cells), polyethylene oxide, PMMA etc. have been studied and used.
- Polymers as electrode materials in supercapacitors and pseudocapacitors: Conductiong polymers like polyaniline, polythiophene etc. and their

derivatives, composites can be used as electrode materials on the surface of which the electrochemical reactions happen.

- d) Polymers as separators: Insulating polymers with high strength and flexibility namely polyethylene, polypropylene etc. have been explored as separator materials in charge storage devices like batteries and supercapacitors.
- e) Polymers as precursors for functionalized carbon: Now a days carbon based storage devices are capturing the market due to the scalability, processability, easy processing methods, cost effective synthesis methods etc. The desired carbon can be obtained by selecting the appropriate precursor for corresponding applications like batteries, supercapacitors, gas adsorption etc. Polymers can be considered as rich carbon source. By designing, choosing appropriate polymer one could achieve desired doping, surface area and conductivity of the carbon with different morphologies.

*In the present thesis the pyrolysis of polystyrene derivative for the formation of desired carbon for its use in the charge storage application has been focused.*

Various derivatives of polystyrene have been synthesized or modified and pyrolyzed to use them in different applications like supercapacitor, oxygen reduction, etc. **Table 1.4** illustrates the different uses of the polystyrene derived carbon material. The carbon is formed by the pyrolysis at high temperature and in some cases activation is done.

**Table 1.4:** List of different polymer derived carbon for various applications.

No	Polymer for pyrolysis	Use	Reference
1	Poly (4-sodium styrene sulfonate-co-maleic acid) sodium salt	Supercapacitor	139
2	Sulfonated Poly(styrene-co-methacrylic acid)	supercapacitor	140

	(SPS-COOH) Sphere		
3.	Polystyrene foam-packaging material	Oxygen reduction (ORR)	141
4.	PMMA-block-polystyrene	CO <sub>2</sub> capture, supercapacitor	142
5.	Polyphenylacetylene derivatives	CO <sub>2</sub> capture, supercapacitor, hydrogen storage	143
6.	Crosslinked polystyrene	Supercapacitor	144
7.	Seaweed biopolymer (Sodium alginate)	Supercapacitor	145
8.	Ionic liquid (Ethyl linked bis(N-(2-cyanoethyl)-imidazole)) n=2; Nonyl linked bis(N-(2-cyanoethyl)-imidazole)) n=9; Bis(trifluoromethylsulfonyl)-imide, Bis(pentafluoroethylsulfonyl)-imide.)	ORR	146
9.	Polyethylene glycol	*	147
10.	Cellulose acetate	*	148
11.	Polyethylene glycol	*	149
12.	Aromatic polyamides	*	150
13.	Polyacrylate-metal complexes	supercapacitor	151

\* only the synthesis of a carbon derived from the pyrolysis of polymer reported

Polystyrene showed to be the better precursor for carbon synthesis by pyrolysis. The synthesis and modification of polystyrene has been well established.

#### Outline of The Thesis:

The present thesis deals with use of polymeric systems for energy conversion, storage and conservation applications. Also, the work deals with the synthesis and targeted modifications of poly(phenylene vinylene) system and polystyrene system.

The **second** chapter deals with the brief discussion about the device fabrication and the characterization techniques used.

The **third** chapter presents the solar energy conversion aspect. The chemical modification of **BEHP-co-MEH PPV** was achieved to incorporate the carboxylic acid anchoring group. Modified **BEHP-co-MEH PPV** was used as the sensitizer in DSSC application. The anchoring group modification enhanced the power conversion efficiency of DSSC up to 3 %.

The **fourth** chapter deals with the synthesis of polystyrene derivative *via* click chemistry approach. The pendent carboxylic acid groups were converted into the corresponding potassium salts. This polymer was used as the precursor for the preparation of high surface area, mesoporous carbon for supercapacitor and Li-HEC applications.

The **fifth** chapter focuses on synthesis of conjugated polymer *viz.* phenazine-containing poly(phenylene vinylene) (**PHN-PPV**). The polymer was synthesized using Wittig- Horner polycondensation method. **PHN-PPV** was explored for field emission studies.

The **sixth** chapter is the concluding chapter and also describes the future scope of the current research work.

**References:**

1. <http://zezantam.com/2013/07/02/week-two/>
2. <http://www.eia.gov/cfapps/ipdbproject/iedindex3.cfm?tid=44&pid=44&aid=2&cid=ww,&syid=1980&eyid=2012&unit=QBTU>
3. [http://www.lopedevega.es/wiki/index.php?title=Fossil\\_power\\_2014](http://www.lopedevega.es/wiki/index.php?title=Fossil_power_2014)
4. <http://www.cleanerandgreener.org/resources/air-pollution.html>
5. <https://en.wikipedia.org/wiki/Biomass>
6. Union of Concern scientist, Science for healthy planet and safer world, <http://www.ucsusa.org/>
7. [https://en.wikipedia.org/wiki/Wind\\_power](https://en.wikipedia.org/wiki/Wind_power)
8. Rasmussen, Jesper Nørskov. "Vindmøller slog rekord i 2014 " In English: New record for wind turbines in 2014. *Energinet.dk*, 6 January 2015. Accessed: 6 January 2015. Archived on 6 January 2015
9. <http://online.wsj.com/articles/denmarks-wind-power-output-rises-to-record-in-first-half-1409750563>
10. REN21 (2011). "Renewables 2011: Global Status Report" (PDF). p. 11.
11. The World Wind Energy Association (2014). *2014 Half-year Report*. WWEA. pp. 1–8.
12. <http://www.renewableenergyworld.com/hydropower/tech.html>
13. <http://water.usgs.gov/edu/wuhy.html>
14. (Source: Energy Information Administration)
15. [https://en.wikipedia.org/wiki/Geothermal\\_energy#Economics](https://en.wikipedia.org/wiki/Geothermal_energy#Economics)
16. Becquerel A.E., Acad, C. R.. *Sci.* **1839**, 9, 561- 567.
17. Goetzberger, A.; Luther, J.; Willeke, G. *Solar Energy Materials & Solar Cells* **2002**, 74, 1- 11.
18. Lee, Y. J.; Kim, B. S.; Ifitiquar, S. M.; Park, C.; Yi, J. *Journal of the Korean Physical Society* **2014**, 65, 355-361.
19. Green, M. A.; Emery, K.; Hishikawa, Y.; Warta, W.; Dunlop, E. D.; *Prog. Photovolt: Res. Appl.* **2011**, 19, 565-572.
20. <http://energy.gov/eere/sunshot/sunshot-initiative>
21. Gupta, S. *Understanding of Nano Science And Technology* **2006**, Global Vision Publishing Ho.

22. Compaan, A. D. *Solar Energy Materials & Solar Cells* **2006**, 90, 2170–2180.
23. Gloeckler, M.; Sankin, I.; Zhao, Z. *IEEE Journal of Photovoltaics* **2013**, 3, 1389–1393.
24. Karg, S.; Riess, W.; Dyakonov, V.; Schwoerer, M. *Synthetic Metals* **1993**, 54, 427-433.
25. Halls, J. J. M.; Pichler, K.; Friend, R. H.; Moratti, S. C.; Holmes, A. B. *Appl. Phys. Lett.* **1996**, 68, 3120-3122.
26. [https://en.wikipedia.org/wiki/polymer-fullerene\\_bulk\\_heterojunction\\_solar\\_cells#citenote-6](https://en.wikipedia.org/wiki/polymer-fullerene_bulk_heterojunction_solar_cells#citenote-6)
27. Reeja-Jayan B.; Manthiram, A. *RSC Adv.* **2013**, 3, 5412-5421.
28. Oregan, B.; Gratzel, M. *Nature* **1991**, 353, 737.
29. Bae E.; Choi, W. *J. Phys. Chem. B* **2006**, 110, 14792-14799.
30. Stern, C.; Lemeune, A. B.; Gorbunova, Y.; Tsivadze, A.; Guillard, R. *Turk. J. Chem.* **2014**, 38, 980-993.
31. Park, L. H.; Bae, E.; Lee, J-J.; Park, J.; Choi, W. *J. Phys. Chem. B* **2006**, 110, 8740-8749.
32. Jradi, F. M.; Kang, X.; O’Neil, D.; Pajares, G.; Getmanenko, Y. A.; Szymanski, P.; Parker, T. C.; El-Sayed, M. A.; Marder, S. R. *Chem. Mater.* **2015**, 27, 2480–2487.
33. Cui, J.; Lu, J.; Xu, X.; Cao, K.; Wang, Z.; Alemu, G.; Yuang, H.; Shen, Y.; Xu, J.; Cheng, Y.; Wang, M. *J. Phys. Chem. C.*, **2014**, 118, 16433–16440.
34. Mai, C-L.; Moehl, T.; Hsieh, C-H.; Decoppet, J-D.; Zakeeruddin, S. M.; Grätzel, M.; Yeh, C-Y. *ACS Appl. Mater. Interfaces* **2015**, 7, 14975–14982.
35. Pellegrina, Y.; Le Pleuxa, L.; Blarta, E.; Renauda, A.; Chavillonb, B.; Szuwarskia, N.; Boujtita, M.; Cariob, L.; Jobicb, S.; Jacquemina, D.; Odobela, F. *Journal of Photochemistry and Photobiology A: Chemistry* **2011**, 219, 235–242.
36. Yella, A.; Lee, H-W.; Tsao, H. N.; Yi, C.; Chandiran, A. K.; Nazeeruddin, M. K.; Wei-Guang Diao, E.; Yeh, C-Y.; Zakeeruddin, S. M.; Grätzel, M. *Science* **2011**, 334, 629.
37. Hod I.; Zaban, A. *Langmuir*, **2014**, 30 (25), 7264–7273.



38. Mishra, A.; Fischer, M. K. R.; Buerle, P. *Angew. Chem. Int. Ed.* **2009**, 48, 2474 – 2499.
39. (a) Mishra, A.; Fischer, M. K. R.; Buerle, P. *Angew. Chem. Int. Ed.* **2009**, 48, 2474 – 2499. (b) Ooyama Y.; Harima, Y. *Eur. J. Org. Chem.* **2009**, 2903.
40. (a) Hara, K.; Sayama, K.; Ohga, Y.; Shinpo, A.; Suga S.; Arakawa, H. *Chem. Commun.* **2001**, 569 (b) Hara, K.; Kurashige, M.; Dan-oh, Y.; Kasada, C.; Shinpo, A.; Suga, S.; Sayama K.; Arakawa, H. *New J. Chem.*, **2003**, 27, 783; (c) Wang, Z. S.; Cui, Y.; Hara, K.; Dan-oh, Y.; Kasada C.; Shinpo, A. *Adv. Mater.* **2007**, 19, 1138.
41. Liangwa M.; Chen, J. *Chem. Soc. Rev.* **2013**, 42, 3453.
42. (a) Marszalek, M.; Nagane, S.; Ichake, A.; Humphry-Baker, R.; Paul, V.; Zakeeruddin S. M.; Grätzel, M. *J. Mater. Chem.*, **2012**, 22, 889, (b) Hung, W-I.; Liao, Y-Y.; Hsu, C-Y.; Chou, H-H.; Lee, T-H.; Kao, W-S.; Lin, J. T. *Chem. Asian J.* **2014**, 9, 357 – 366.
43. (a) Burke, A.; Schmidt-Medne, L.; Ito S.; Grätzel, M. *Chem. Commun.* **2007**, 234 (b) Yum, J. H.; Walter, P.; Huber, S.; Rentsch, D.; Geiger, T.; Nuesch, F.; Angelis, F. D.; Grätzel M.; Nazeeruddin, M. K. *J. Am. Chem. Soc.* **2007**, 129, 10320.
44. (a) Tan, S.; Zhai, J.; Fang, H.; Jiu, T.; Ge, J.; Li, Y.; Jiang L.; Zhu, D. *Chem.–Eur. J.* **2005**, 11, 6272. (b) Kosa, T.; Palffy-Muhoray, P. *Mol. Cryst. Liq. Cryst.* **2004**, 421, 107.
45. (a) Ito, S.; Zakeeruddin, S. M.; Humphry-Baker, R.; Liska, P.; Charvet, R.; Comte, P.; Nazeeruddin, M. K.; Péchy, P.; Takata, M.; Miura, H.; Uchida S.; Grätzel, M. *Adv. Mater.* **2006**, 18, 1202. (b) Horiuchi, T.; Miura, H.; Sumioka K.; Uchida, S. *J. Am. Chem. Soc.* **2004**, 126, 12218. (c) Horiuchi, T.; Miuraand, H.; Uchida, S. *J. Photochem. Photobiol., A*, **2004**, 164, 29. (d) Ito, S.; Miura, H.; Uchida, S.; Takata, M.; Sumioka, K.; Liska, P.; Comte, P.; Péchy P.; Grätzel, M. *Chem. Commun.*, **2008**, 5194.
46. Fang, Z.; Eshbaugh, A. A.; Schanze, K. S. *J. Am. Chem. Soc.* **2011**, 133, 3063.
47. Kanimozhi, C.; Balraju, P.; Sharma, G. D.; Patil, S. *J. Phy. Chem. C*, 114, 7, **2010**, 3287.

48. Tang, Y.; Shen, P.; Ding, T.; Huang, H.; Zhao, B.; Tan, S. *European Polymer Journal* **46**, **2010**, 2033–2041.
49. Zhang, W.; Fang, Z.; Su, M.; Saeys, M.; Liu, B. *Macromol. Rapid Commun.* **2009**, *30*, 1533.
50. Wang, G.; Ding, W.; Wang, H.; Zhou, X.; Yu, G.; Pan, C. *Synthetic Metals* **209**, **2015**, 119–127.
51. Krüger, R. A.; Gordon, T. J.; Baumgartner, T.; Sutherland, T. C. *ACS Appl. Mater. Interfaces* **2011**, *3*, 2031–2041.
52. Wang, G.; Wu, Y.; Ding, W.; Yu, G.; Hu, Z.; Wang, H.; Liu, S.; Zou Y.; Pan, C. *J. Mater. Chem. A*, **2015**, *3*, 14217.
53. Peng, D.; Zhang, W.; Tang, G.; Zhou, J.; Hu, J.; Xie, Q.; Zhong, C. *J Iran Chem Soc* **2015**, *12*, 397–404.
54. Peng, D.; Tang, G.; Hu, J.; Xie, Q.; Zhou, J.; Zhang, W.; Zhong, C. *Polym. Bull.* **2015**, *72*, 653–669.
55. Zhang, G.; Bala, H.; Cheng, Y.; Shi, D.; Lv, X.; Yu Q.; Wang, P. *Chem. Commun.* **2009**, 2198.
56. Yao, Z.; Zhang, M.; Wu, H.; Yang, L.; Li, R.; Wang, P. *J. Am. Chem. Soc.*, **2015**, *137*, *11*, 3799–3802.
57. Narayan, M. R. *Renewable and Sustainable Energy Reviews*, **2012**, *16*, 208–215.
58. Huang, S. Y.; Schlichthorl, G.; Nozik, A. J.; Gratzel, M.; Frank, A. J. *Journal of Physical Chemistry B* **1997**, *101*, 2576–82.
59. Li, T. L.; Lee Y. L.; Teng, H. *Energy Environ. Sci.*, **2012**, *5*, 5315–5324.
60. Daeneke, T.; Uemura, Y.; Duffy, N. W.; Mozer, A. J.; Koumura, N.; Bach, U.; Spiccia, L. *Advanced Materials*, **2012**, *24*, 1222-1225.
61. Wang, P.; Zakeeruddin, S. M.; Moser, J. E.; Nazeeruddin, M. K.; Sekiguchi, T.; Gratzel, M. *Nature Materials* **2003**, *2*, 402.
62. Kelkar, S.; Pandey, K.; Agarkar, S.; Saikhedkar, N.; Tathavadekar, M.; Agrawal, I.; Gundloori, R. V. N.; Ogale, S. *ACS Sustainable Chem. Eng.* **2014**, *2*, 2707–2714.
63. Li, Q.; Zhao, J.; Sun, B.; Lin, B.; Qiu, L.; Zhang, Y.; Chen, X.; Lu, J.; Yan, F. *Adv. Mater.* **2012**, *24*, 945–950.
64. Wu, M.; Ma, T. *ChemSusChem* **2012**, *5*, 1343 – 1357.

65. Mayhew, J. D. R.; Bozym, D. J.; Punckt, C.; Aksay, I. A. *ACS Nano*, **2010**, 4, 6203-6211.
66. Lee, W. J.; Ramasamy, E.; Lee, D. Y.; Song, J. S. *ACS Appl. Mater. Interfaces*, **2009**, 1, 1145- 1149.
67. Ramasamy, E.; Lee, J. *Carbon*, **2010**, 48, 3715-3720.
68. Mulmudi, H. K.; Batabyal, S. K.; Rao, M.; Prabhakar, R. R.; Mathews, N.; Lam Y- M.; Mhaisalkar, S. G. *Phys. Chem. Chem. Phys.*, **2011**, 13, 19307–19309.
69. Winter, M.; Brodd, R. J. *Chem. Rev.* **2004**, 104, 4245.
70. Jayalakshmi, M.; Balasubramanian, K. *Int. J. Electrochem. Sci.*, **2008**, 3, 1196.
71. Scrosati, B.; Garche, J. *J. Power Sources*, **2010**, 195, 2419.
72. Amatucci, G. G.; Badway, F.; Du Pasquier A.; Zheng, T. *J. Electrochem. Soc.*, **2001**, 148, A930.
73. Jost, K.; Dion G.; Gogotsi. Y. *J. Mater. Chem. A*, **2014**, 2, 10776-10787.
74. Whittingham, M. S. *Chem. Rev.* **2004**, 104, 4271.
75. Zhai, Y.; Dou, Y.; Zhao, D.; Fulvio, P. F.; Mayes R. T.; Dai, S. *Adv. Mater.* **2011**, 23, 4828–4850.
76. Stoller, M. D.; Park, S.; Zhu, Y.; An, J.; Ruoff, R. S. *Nano Lett.* **2008**, 8, 3498–3502.
77. Jiang, H.; Lee P. S.; Li, C. *Energy Environ. Sci.* **2013**, 6, 41– 53.
78. Karthikeyan, K.; Amaresh, S.; Lee, S. N.; Sun, X.; Aravindan, V.; Lee, Y-G.; Lee, Y. S. *ChemSusChem* **2014**, 7, 1435.
79. Zhu, H.; Wang, X. L.; Liu, X. X.; Yang, X. R. *Adv. Mater.* **2012**, 24, 6524.
80. Lei, C.; Wilson, P.; Lekakou, C. *Journal of Power Sources.* **2011**, 196, 7823–7827.
81. Feng, G.; Qiao, R.; Huang, J.; Dai, S.; Sumpter B. G.; Meunier, V. *Phys. Chem. Chem. Phys.*, **2011**, 13, 1152–1161.
82. Yang, X.; Zhang, L.; Zhang, F.; Zhang, T.; Huang, Y.; Chen, Y. *Carbon* **2014**, 72, 381.
83. Kang, Y. J.; Chun, S. J.; Lee, S. S.; Kim, B. Y.; Kim, J. H.; Chung, H.; Lee, S. Y.; Kim, W. *ACS Nano* **2012**, 6, 6400.

84. Yang, X.; Zhang, F.; Zhang, L.; Zhang, T. F.; Huang, Y.; Chen, Y. S.; *Adv. Funct. Mater.* **2013**, 23, 3353.
85. Zhang, F.; Lu, Y.; Yang, X.; Zhang, L.; Zhang, T.; Leng, K.; Wu, Y.; Huang, Y.; Ma, Y.; Chen, Y. *Small* **2014**.
86. Wang, H.; Xu, Z. W.; Kohandehghan, A.; Li, Z.; Cui, K.; Tan, X. H.; Stephenson, T. J.; King'ondo, C. K.; Holt, C. M. B.; Olsen, B. C.; Tak, J. K.; Harfield, D.; Anyia, A. O.; Mitlin, D. *ACS Nano* **2013**, 7, 5131.
87. <http://humantouchofchemistry.com/importance-of-energy-conservation.htm>
88. [https://en.wikipedia.org/wiki/Field\\_emission\\_display](https://en.wikipedia.org/wiki/Field_emission_display)
89. Good, R. W.; Muller, E.W.; *Handguch der Physik*, vol.21, 176, **1950**.
90. Van Oostrom, A. G. J. *Philips Res. Report Suppl.* No.1, **1966**.
91. Wood, R. W. *Phys. Rev.* **1987**, 5, 1.
92. W. Schottky, *Z. Physik.*, **1923**, 14, 63
93. Gossling, B. S.; *Phil. Mag.* 1, 609, **1926**.
94. Fowler R. H.; Nordheim L.W. : *Proc. Roy. Soc. (London) A*, **1928**, 119, 173 (1928).
95. Muller E. W. *Z. Physik*, 126, 642, **1949**.
96. Murphy, E. L.; Good, R. H. *Phys. Rev.*, 102, **1958**, 1464.
97. Gomer, R. Field Emission and Field Ionization, *Haward university Press, Ny*, **1961**.
98. Modinos, A. Field Emission, Thermionic and Secondary Electron Emission spectroscopy, (*Plenum Press, New York*, **1984**).
99. Stratton, R. *Phys. Rev.*, 125, **1962**, 67.
100. Baskin, L. M.; Lvov, O. L.; Fursey, G. N. *Phys. Stat. Sol. (b)*, 47, **1971**, 69.
101. Forbes R. G.; Deane, J. H. B. *Proc. Royal Soc. A*, **2007**, 463, 2907.
102. Forbes, R. G. *Appl. Phys. Lett.*, **2008**, 92 (2008) 193105.
103. (a) Principles of Polymerization, 4th Edition, George Odian. (b). Introduction to Physical Polymer Science, 4th Edition, L. H. Sperling.
104. [http://www.chemistryviews.org/details/event/5838011/Polymers\\_\\_Energy\\_Synthesis\\_Engineering\\_Characterisation\\_and\\_Applications.html](http://www.chemistryviews.org/details/event/5838011/Polymers__Energy_Synthesis_Engineering_Characterisation_and_Applications.html)
105. <http://www.threebond.co.jp/en/product/productinformation/tb3035b.html>

106. Chiang, C. K.; Fincher, C. R.; Park, Y. W.; Heeger, A. J.; Shirakawa, H.; Louis, E. J.; Gau, S. C.; MacDiarmid, A. G. *Phys. Rev. Lett.* **1977**, *39*, 1098.
107. (a) Facchetti, A.; *Chem. Mater.* **2011**, *23*, 733. (b) Mei, J.; Diao, Y.; Appleton, A. L.; Fang, L.; Bao, Z. *J. Am. Chem. Soc.* **2013**, *135*, 6724. (c) Dou, L.; Liu, Y.; Hong, Z.; Li, G.; Yang, Y. *Chem. Rev.* DOI: 10.1021/acs.chemrev.5b00165.
108. PPV in BHJ ("Solar Cells - New Aspects and Solutions", book edited by Leonid A. Kosyachenko, ISBN 978-953-307-761-1, chapter 19: Organic Bulk Heterojunction Solar Cells Based on Poly(p-Phenylene-Vinylene) Derivatives. By Cigdem Yumusak and Daniel A. M. Egbe. DOI: 10.5772/22306
109. V. Podzorov. *Nature Materials* *12*, 2013, 947–948
110. (a) Jung, B. J.; Tremblay, N. J.; Yeh, M-L.; Katz, H. E. *Chem. Mater.* **2011**, *23*, 568. (b) Klauk, H. *Chem. Soc. Rev.* **2010**, *39*, 2643. (c) Yang, J.; Yan, D.; Jones, T.S.; *Chem. Rev.* **2015**, *115*, 5570. (d) Wang, C.; Dong, H.; Hu, W.; Liu, Y.; Zhu, D. *Chem. Rev.* **2012**, *112*, 2208. (e) Mas-Torrent, M.; Rovira, C. *Chem. Rev.* **2011**, *111*, 4833. (f) Amanda R. Murphy, A. R.; Fréchet, J. M. J. *Chem. Rev.* **2007**, *107*, 1066.
111. (a) Cheng, Y-J.; Yang, S-H.; Hsu, C-S. *Chem. Rev.* **2009**, *109*, 5868. (b) Lu, L.; Zheng, T.; Wu, Q.; Schneider, A. M.; Zhao, D.; Yu, L. *Chem. Rev.* **2015**, DOI: 10.1021/acs.chemrev.5b00098. (c) Song, B.; Rolin, C.; Zimmerman, J. D.; Forrest, S. R. *Adv. Mater.* **2014**, *26*, 2914. (d) Hains, A. W.; Liang, Z.; Woodhouse, M. A.; Gregg, B. A. *Chem. Rev.* **2010**, *110*, 6689.
112. (a) A.C. Grimsdale, K. L.Chan, R. E. Martin, P. G. Jokisz, A. B. Holmes. *Chem. Rev.* 2009, **109**, 897. (b) Grimsdale, A. C.; Chan, L. K.; Martin, R. E.; Jokisz, P. G.; Holmes, A. B. *Chem. Rev.* 2009, **109**, 897. (c) Friend, R. H.; Gymer, R. W.; Holmes, A. B.; Burroughes, J. H.; Marks, R. N.; Taliani, C.; Bradley, D. D. C.; Santos, D. A. D.; Bredas, J. L.; Logdlund, M.; Salaneck, W. R. *Nature* **1999**, *397*, 121.
113. (a) Vilela, F.; Zhanga, K.; Antonietti, M. *Energy Environ. Sci.* **2012**, *5*, 7819. (b) Mike, J. F.; Lutkenhaus, J. L. *J. Polym. Sci., Part B: Polym. Phys.* **2013**, *51*, 4. (c) Nov k, P. Iler, K.; Santhanam, K. S. V.; Haas, O.

- Chem. Rev.* **1997**, 97, 207. (d) Wang, G.; Zhang, L.; Zhang, J. *Chem. Soc. Rev.* **2012**, 41, 797. (e) Snook, G. A.; Kao, P.; Best, A. S. *J. Power Sources* **2011**, 196, 1. (f) Simon, P.; Gogotsi, Y. *Nat. Mater.* **2008**, 7, 845.
114. (a) Beaujuge, P. M.; Reynolds, J. R. *Chem. Rev.* **2010**, 110, 268. (b) Skotheim, T. A.; Reynolds, J. *Conjugated Polymers: Theory, Synthesis, Properties, and Characterization* **2006**, ISBN 9781420043587 - CAT# 43587. (c) Mortimer, R. j.; Dyer, A. L.; Reynolds, J. R. *Displays* **2006**, 27, 2.
115. (a) Ouyang, J.; Chu, C-W.; Szmanda, C. R.; Ma, L.; Yang, Y. *Nat. Mater.* **2004**, 3, 918. (b) Heremans, P.; Gelinck, G. H.; Müller, R.; Baeg, K.-J.; Kim, D.-Y.; Noh, Y.-Y. *Chem. Mater.* **2011**, 23, 341.
116. (a) McQuade, D. T.; Pullen, A. E.; Swager, T. M. *Chem. Rev.* **2000**, 100, 2537. (b) Kim, H. N.; Guo, Z.; Zhu, W.; Yoon, J.; Tian, H.; *Chem. Soc. Rev.* **2011**, 40, 79. (c) Rahman, M. A.; Kumar, P.; Park, D-S.; Shim, Y-B. *Sensors* **2008**, 8,118.
117. (a) Deshpande, P. P.; Jadhav, N. G.; Gelling, V. J.; Sazou, D. J. *Coat. Technol. Res.* **2014**, 11, 473. (b) Frau, A. F.; Pernites, R. B.; Advincula, R. C. *Ind. Eng. Chem. Res.* **2010**, 49, 9789. (c) Zarras, P.; Stenger-Smith, J. D.; Wei, Y. *Electroactive Polymers for Corrosion Control* **2003**, 978-0-8412-3790-2. (d) Rohwerder, M. *Intelligent Corrosion Protection by Conducting Polymers* **2009**, DOI: 10.1021/bk-2009-1002.ch014.
118. (a) Kim, D. H.; Han, J. T.; Park, Y. D.; Jang, Y.; Cho, J. H.; Hwang, M.; Cho, K. *Adv. Mater.* **2006**, 18, 719. (b) Sirringhaus, H.; Brown, P. J.; Friend, R. H.; Nielsen, M. M.; Bechgaard, K.; Langeveld-Voss, B. M. W.; Spiering, A. J. H.; Janssen, R. A. J.; Meijer, E. W.; Herwig, P.; de Leeuw, D. M. *Nature* **1999**, 401, 685.
119. (a) Lim, J. A.; Lee, H. S.; Lee, W. H.; Cho, K. *Adv. Funct. Mater.* **2009**, 19, 1515. (b) Tsao, H. N.; Mullen, K. *Chem. Soc. Rev.* **2010**, 39, 2372.
120. (a) Wood, P. *Conformational Disorder and the Degree of Conjugation in Conjugated Polymers*, PhD thesis, University of St. Andrews, **2002**. (b). Atkins, P.W *Molecular Quantum Mechanics*, chapter 10, p. 275, Oxford University Press, **1983**. (c) Heeger, A.J.; Kivelson, S.; Schrieffer, J. R.; Su, W.P. *Rev. Mod. Phys.* **1988**, 60, 781.

121. (a) Liu, D. Y. PhD Thesis University of Florida, **2011**. (b) Mike, J. F. PhD thesis Iowa State University, **2011**. (c) Bolin, M. H. PhD thesis Linköping University, **2011**.
122. (a) Hu, D.; Yu, J.; Wong, K.; Bagchi, B.; Rossky, P. J.; Barbara, P. F. *Nature* **2000**, 405, 1030 – 1033; (b) Collini, E.; Scholes, G. D. *Science* **2009**, 323, 369 – 373.
123. Burroughes, J. H.; Bradley, D. D. C.; Brown, A. R.; Marks, R. N.; Mackay, K.; Friend, R. H.; Burns, P. L.; Holmes, A. B. *Nature* **1990**, 347, 539 – 541.
124. Yu, G.; Gao, J.; Hummelen, J. C.; Wudl, F.; Heeger, A. J. *Science* **1995**, 270, 1789 – 1791.
125. Shi, S.; Wudl, F. *Macromolecules* **1990**, 23, 2119 – 2124.
126. Tessler, N.; Denton, G. J.; Friend, R. H. *Nature* **1996**, 382, 695 – 697.
127. I. F.; Wudl, F.; Perepichka D. F. *Isr. J. Chem.* **2014**, 54, 674 – 688.
128. Johansson Seechurn, C. C. C.; Kitching, M. O.; Colacot, T. J.; Snieckus, V. *Angew. Chem. Int. Ed.* **2012**, 51, 5062 – 5085.
129. Perepichka, D. F.; Perepichka, I. F.; Meng, H.; Wudl F. in *Organic Light-Emitting Materials and Devices* (Eds.: Z. Li, H. Meng), CRC Press, Boca Raton, FL, **2006**, pp. 45 – 294
130. Traiphol, R.; Sanguansat, P.; Srihirin, T.; Kerdcharoen, T.; Osotchan, T. *Macromolecules* **2006**, 39, 1165 – 1172.
131. Kçhler, A.; Hoffmann, S. T.; Bessler, H. *J. Am. Chem. Soc.* **2012**, 134, 11594 – 11601.
132. Lei, T.; Dou, J-H.; Cao, X-Y.; Wang, J-Y.; Pei. J. *J. Am. Chem. Soc.*, **2013**, 135 (33), 12168–12171.
133. Lei, T.; Xia, X.; Wang, J-Y.; Liu, C-J.; Pei. J. *J. Am. Chem. Soc.*, **2014**, 136 (5), 2135–2141.
134. Moslin, R. M.; Andrew, T. L.; Kooi, S. E.; Swager. T. M. *J. Am. Chem. Soc.*, **2009**, 131 (1), 20–21
135. Kwak, C. K.; Kim, D. M.; Lee, C-S.; Lee, M.; Lee, T. S. *J. Nanosci. Nanotechnol.* 10, 6920–6924, **2010**.
136. Diliën, H.; Palmaerts, A.; Lenes, M.; de Boer, B.; Blom, P.; Cleij, T. J.; Lutsen, L.; Vanderzande, D. *Macromolecules* **2010**, 43, 10231–10240.

137. Characterization of Thin Films of Conjugated Polymer (BEHP-PPV) – co– (MEH-PPV) for OLEDs Application. J.C. Sánchez, A. Escobosa, M. Estrada
138. Jin, S-H.; Kim, M-Y.; Kim, J. Y.; Lee, K.; Gal, Y-S. *J. Am. Chem. Soc.*, **2004**, *126* (8), 2474–2480
139. Yadav, P.; Banerjee, A.; Unni, S.; Jog, J.; Kurungot, S.; Ogale, S. *ChemSusChem* **2012**, *5*, 2159 – 2164.
140. Lee, J-S.; Kim, S-I.; Yoon, J-C.; Jang, J-H. *ACS Nano*, **2013**, *7* (7), 6047–6055.
141. You, C.; Liao, S.; Qiao, X.; Zeng, X.; Liu, F.; Zheng, R.; Song, H.; Zeng, J.; Li, Y. *J. Mater. Chem A* **2014**, *2*, 12240.
142. Li, Z.; Wu, D.; Huang, X.; Ma, J.; Liu, H.; Liang, Y.; Fu, R.; Matyjaszewski, K. *Energy Environ. Sci.* **2014**, *7*, 3006.
143. Grundy, M.; Ye, Z. *J. Mater. Chem. A* **2014**, *2*, 20316.
144. Xu, F.; Cai, R.; Zeng, Q.; Zou, C.; Wu, D.; Li, F.; Lu, X.; Liang, Y.; Fu, R. *J. Mater. Chem.* **2011**, *21*, 1970.
145. Raymundo-Piñero, E.; Leroux, F.; Béguin, F. *Adv. Mater.* **2006**, *18*, 1877–1882.
146. Zhang, Z.; Veith, G.M.; Brown, G. M.; Fulvio, P. F.; Hillesheim, P. C.; Daiac, S. and Overbury, S. H. *Chem. Commun.*, **2014**, *50*, 1469.
147. Tang, J.; Fan, G.; Li, Z.; Li, X.; Xu, R.; Li, Y.; Zhang, D.; Moon, W-J.; Kaloshkin, S. D.; Churyukanova, M. *Carbon* **55**, **2013**, 202–208.
148. Dubrovina, L.; Naboka, O.; Ogenko, V.; Gatenholm, P.; Enoksson, P. *J Mater Sci* **2014**, *49*, 1144–1149.
149. Takahashi, Y.; Fujita, H.; Lin, W-H.; Li, Y-Y.; Fujii, T.; Sakoda, A. *Adsorption* **2010**, *16*, 57–68.
150. Sánchez-Sánchez, A.; Suárez-García, F.; Martínez-Alonso, A.; Tascón, J. M. D. *Carbon*, **70**, **2014**, 119 – 129.
151. Chen, X. Y.; Chen, C.; Zhang, Z. J.; Xie, D. H.; Liu, J. W. *J. Mater. Chem. A*, **2013**, *1*, 4017.



## Chapter 2

### Experimental Methods and Characterization Techniques

This chapter discusses about the device fabrication methods and the techniques used for the characterization of the materials under study.

## Section – I

### 2.1 Synthesis/Deposition Techniques

#### 2.1.1 DSSC Device Fabrication:

The fabrication of a device is a crucial task to get a stable and high efficiency device. Device fabrication includes following steps (**Figure 2.1**):

- FTO substrate cleaning
- Making blocking layer of  $\text{TiO}_2$  on FTO
- $\text{TiO}_2$  paste making and application of  $\text{TiO}_2$  on to the blocking layer. Annealing at  $450\text{ }^\circ\text{C}$  for 60 min. This layer acts as a working electrode or photo-anode
- $\text{TiCl}_4$  treatment
- Sensitization with the dye by immersing  $\text{TiO}_2$  films in the dye solution for 24 h.
- Preparation of electrolyte solution using 0.6 M 1-propyl-2,3-dimethyl-imidazolium iodide, 0.1 M LiI, 0.05 M  $\text{I}_2$ , and 0.5 M 4-tert-butylpyridine in acetonitrile
- Preparation of Pt-counter electrode by drop casting platinum solution on FTO and heating it at  $450\text{ }^\circ\text{C}$  for 60 min.
- Sealing of device.

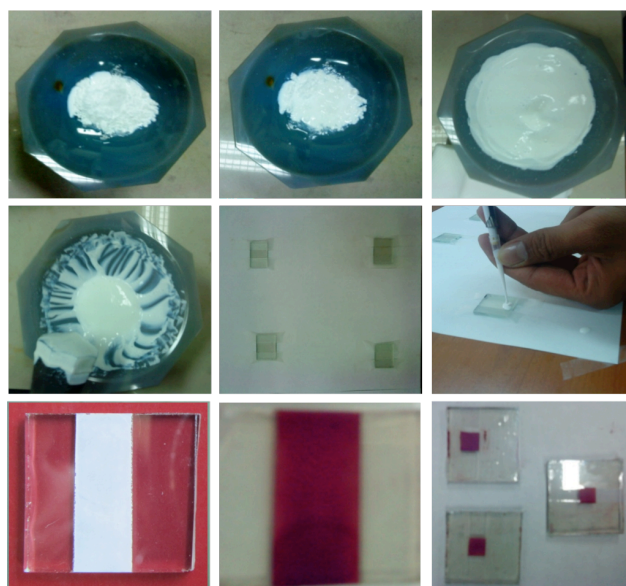


**Figure 2.1:** DSSC device fabrication.

### 2.1.2 High Temperature Pyrolysis

In the pyrolysis method, the carbon material is synthesized by heating the precursor material at a high temperature. The temperature range may vary according to the application of final product. Usually, the range of temperature is 800-1000 °C for the functionalized carbon preparation. The heating is usually performed using split tube furnace under the inert atmosphere. This process achieves production of charcoal, activated carbons, etc. Pyrolysis is also used for synthesis of various forms of carbon like graphene, carbon nanotubes, etc. from biomass and polymeric precursors.

## 2.2 Techniques for Characterization of the Materials

For the material to be considered as suitable candidate for any kind of device application, it is very important to have detailed characterization of the properties of materials with respect to structural, electrical, morphological, optical, etc. The properties of a material have dynamic relationship with the processing and fabrication methods and hence the characterization becomes very important prior to any device fabrication and application to extract the accurate information from the material made. Here, this section describes in brief the principles and importance of the different characterization techniques used for the analysis.

### 2.2.1 Nuclear Magnetic Resonance Spectroscopy (NMR)

NMR is rather low energy technique, which operates in the region of  $10^{-3} - 10^{-1}$  Joules/mol. This energy affects the nuclear spins under magnetic field in the material under analysis. This is very important spectroscopic technique in the field of synthetic organic chemistry as it gives valuable structural information. The properties of nuclear spin are obtained by calculating the spin energy levels using,

$$\text{No. of spin states} = 2I + 1 \quad (I = \text{spin quantum number})$$

NMR gives the information about the spin response to the applied radio frequency. All atomic nuclei are not NMR active. Nuclei with spin quantum

number of half-integer are generally NMR active. The signal intensity in NMR for the corresponding nuclei depends upon their abundance in nature.

NMR active nuclei (generally used)<sup>1</sup>:

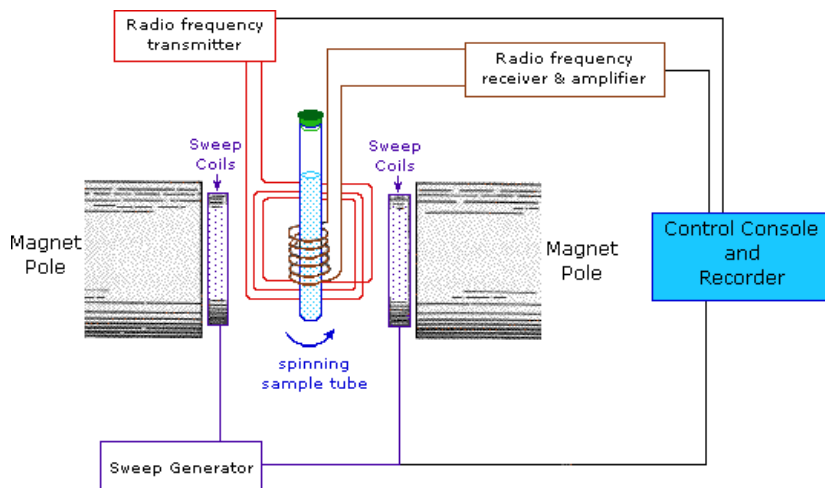


**Figure 2.2:** Schematic representation of NMR spectroscopy system.

(<http://www2.chemistry.msu.edu/faculty/reusch/VirtTxtJml/Spectrpy/nmr/nmr1.htm>)

- $^1\text{H}$  = 99.9 % abundance, very sensitive, sharp and high intensity signals, shows all types of coupling like homo as well as hetero-nuclear
- $^{13}\text{C}$  = 1.1 % abundance, less sensitive, difficult to detect homo-nuclear signals
- $^{15}\text{N}$  = low abundance
- $^{19}\text{F}$  = > 99% abundance
- $^{31}\text{P}$  = > 99 % abundance
- $^{29}\text{Si}$  = low abundance

*Instrumentation:* The system consisting of,

- Strong magnets
- Transmitter of radio frequency
- Sample holder
- Amplifier
- Detector

- Display system
- Cooling system

Under the application of external magnetic field, randomly oriented sample nuclei get aligned with respect to the external magnetic field. The nuclear spin excitation is caused by passing radio frequency through the sample. The excited spin relaxes and emits the radiation, which is detected by the detector. Detector detects this energy and Fourier transformed signals are generated by the system. The mode of spin relaxation (spin-spin relaxation and/or spin lattice relaxation) and the spin environment affect the position and pattern of signal.

### 2.2.2 UV-Vis Spectroscopy

One of the most important non-destructive tools to understand the optical properties of the material in solution as well as film state is ultraviolet-visible (UV-Vis) spectroscopy.<sup>2</sup> This spectroscopic technique provides the information regarding absorbance/ transmittance/ reflectance of a sample with respect to the incident wavelength range from UV-NIR of the electromagnetic spectrum. When the incident light of UV-NIR region is having higher energy than the band gap of the material, material absorbs light and generates the UV-Vis spectrum.

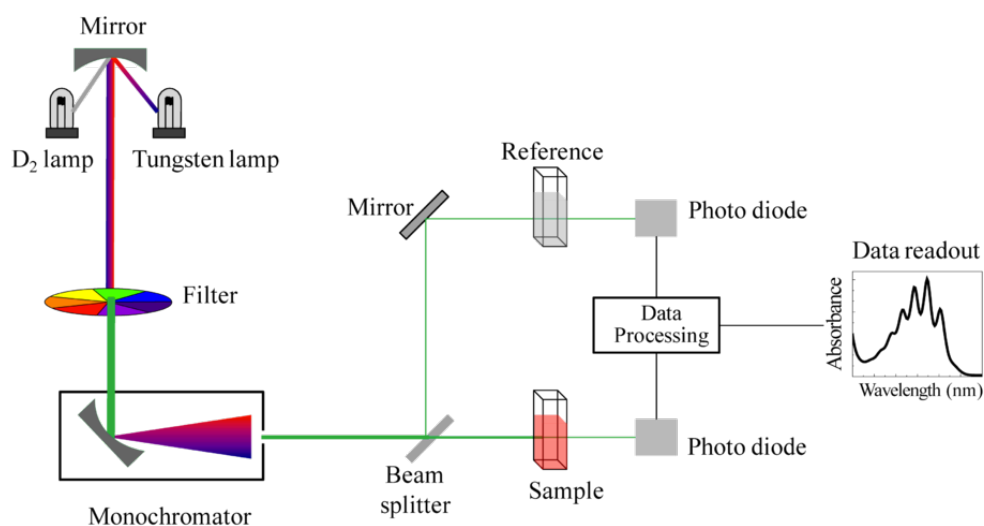


**Figure 2.3:** Schematic description of UV-Vis setup

[https://en.wikipedia.org/wiki/Ultraviolet%E2%80%93visible\\_spectroscopy](https://en.wikipedia.org/wiki/Ultraviolet%E2%80%93visible_spectroscopy)

*Instrumentation:* The UV-Vis spectrometer consists of the following:

- Light source (Deuterium lamp for UV region of 190 to 350 nm and Halogen or tungsten lamp for visible region of 330 to 900 nm)
- Monochromator to select specific wavelength.
- Photomultiplier tube for detection of output signals.

*Principle and Applications:* Absorbance, transmittance and the reflectance are the three modes to use UV-Vis spectrometer. For the samples dissolved in solvents, absorbance mode is used which is governed by Beer-Lambert's Law:

$$\frac{I}{I_0} = e^{-kcl} \quad \text{or} \quad \frac{I}{I_0} = 10^{\epsilon cl} = T$$

Where,

$\kappa$  = constant, for particular spectroscopic transition under consideration.

$\epsilon$  = molar absorption coefficient,  $c$  = concentration

$T$  = transmittance =  $I / I_0$ , ratio of intensity of incident radiation ( $I_0$ ) to transmitted radiation ( $I$ )

Taking logarithms of the above equation,

$$\ln(I_0 / I) = \epsilon cl = A, \quad (A = \text{absorbance})$$

Hence, absorbance is directly proportional to the concentration of sample when  $\epsilon$  and  $l$  are kept constant.

For the solid samples or the film samples, diffused reflectance (DRS) mode is used.

$$[F(R)hv]^{1/n} \propto (hv - E_g) \quad \text{Where,} \quad F(R) = \frac{(1-R)^2}{2R}$$

$F(R)$  is a modified Kubelka – Munk function.  $R$  = reflectance,  $n=1/2$  for direct band gap materials and  $n=2$  for indirect band gap materials. From the plot of  $[F(R)hv]^{1/n}$  vs  $hv$ , band gap ( $E_g$ ) can be determined by extrapolating the straight line tangent to the plot.<sup>3</sup>

Above equation is used to obtain Tauc's plot from DRS spectrum to calculate the band gap of a semiconducting material.

### 2.2.3 Photoluminescence (PL) Spectroscopy

The extent of instinctive light emission is the luminescence and the measurement is called as PL spectroscopy.<sup>4,5</sup> PL gives information about the states of the energy in the given material. For chemistry applications, it helps to find out the

macromolecular interactions, aggregates etc. while in material prospects it helps surface properties, system disorder, etc. The intensity of a spectrum relates to the surface-interfaces quality. Depending upon the type of decay (radiative, non-radiative etc.) the intensity varies. Advanced tool like transient PL provides information about excited state lifetime and dynamics. This helps to understand the actual mechanism of the device in detail.

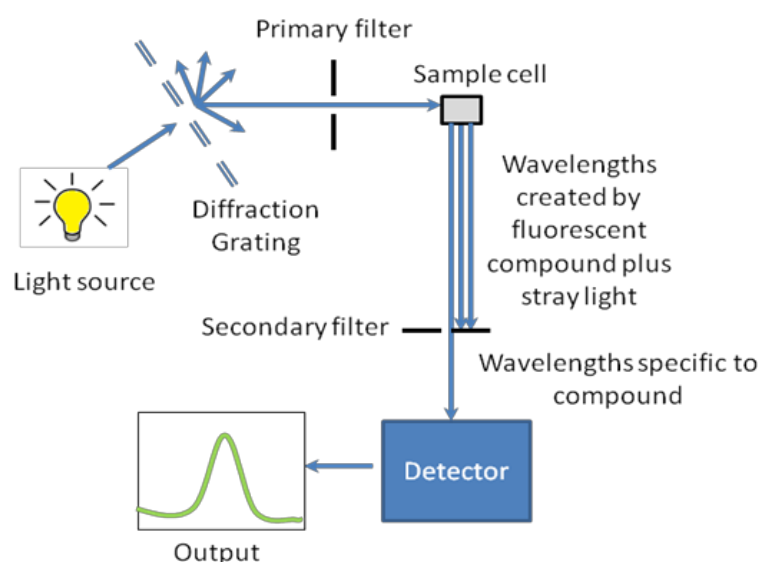


**Figure 2.4:** Photoluminescence Spectroscopy- schematic representation

([http://cnx.org/contents/7b4dfcf8-b28e-4148f2f1ff39052669f@13.7:30/Nanomaterials\\_and\\_Nanotechnolo](http://cnx.org/contents/7b4dfcf8-b28e-4148f2f1ff39052669f@13.7:30/Nanomaterials_and_Nanotechnolo))

*Instrumentation:*

- Light source (Mercury vapor lamp or xenon arc for UV and visible light source)
- Diffraction gratings
- Filters (for reduction of transmitted and diffracted light)
- Detector

PL can be performed in the solution state as well as for the films.

#### 2.2.4 Fourier Transform Infrared Spectroscopy (FT-IR)

In this technique, material is exposed to the radiation of the energy of the order of  $10^3$ - $10^5$  Joules/mol. IR radiations are absorbed by the material and excited to the higher energy state. When the natural vibrational frequencies of molecule

matches with the incident IR frequencies there is an increase in the amplitude of the vibrational frequencies of molecules due to resonance. However, all bonds are not able to absorb these frequencies. Symmetric molecules do not absorb IR frequency. On the other hand, the bonds, which absorb IR frequency, possessing a dipole moment change with respect to time. Since, every bond has different frequency of vibrations, IR is used to find the type of bond as well as match the molecules.

*Instrumentation:* The instrument consists of the IR source, the monochromator and the detector.<sup>6,7</sup> Generally, source is in the filament-form controlled by electric current. The IR radiations coming from source pass through the monochromator and fall on the material. Material absorbs IR, and the pyroelectric or photoconductive detectors detect transmitted energy.

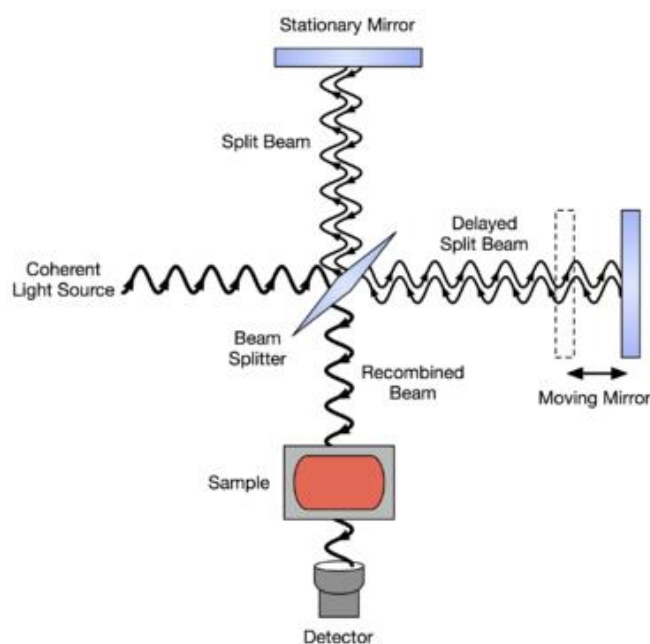


**Figure 2.5:** Representation diagram of FTIR system

([https://en.wikipedia.org/wiki/Fourier\\_transform\\_infrared\\_spectroscopy](https://en.wikipedia.org/wiki/Fourier_transform_infrared_spectroscopy))

*Principle:* For the harmonic oscillator, total energy is proportional to vibrational frequencies.

$$E_{osc} \propto h\nu_{osc}$$

The bond's natural frequency is represented by,



$$\bar{\nu} = \frac{1}{2\pi c} \sqrt{\frac{K}{\mu}}$$

Where,  $K$  is constant in dynes/cm that varies from bond to bond and  $\mu$  is the reduced mass of atoms in the molecule in amu,  $\bar{\nu}$  represents frequency in  $\text{cm}^{-1}$  and  $c$  is the velocity of light.

Fundamentally, the information is obtained as a function of time. However, it is not easy to interpret. Hence, a mathematical operation called as Fourier Transformation is performed to get the frequency domain spectrum and it is called as FT-IR.

### 2.2.5 Raman Spectroscopy

Raman spectroscopy is based on the scattering phenomenon.<sup>8,9</sup>

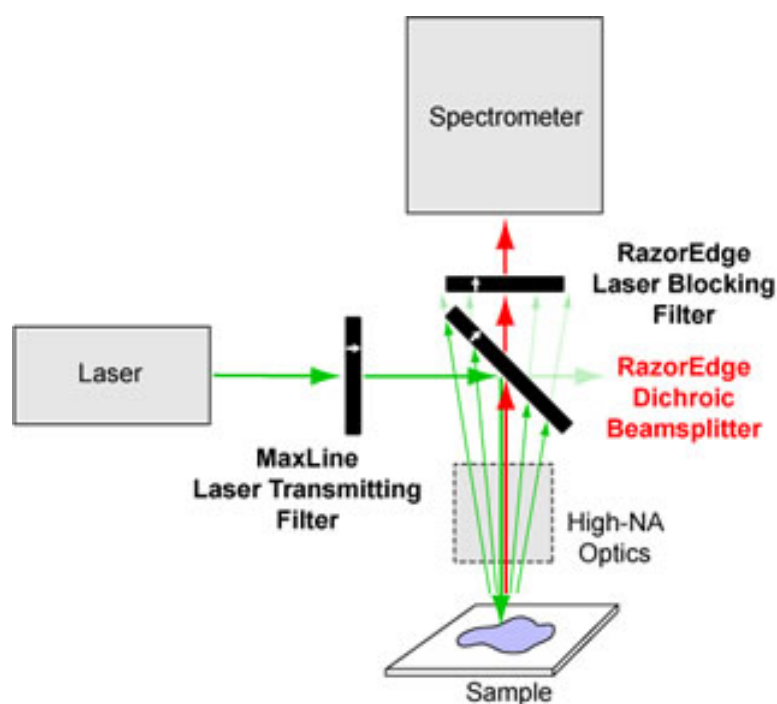


**Figure 2.6:** Raman spectroscopy diagram

<http://www.semrock.com/high-performance-raman-spectroscopy.aspx>

When the monochromatic light falls on the sample, and if the scattered light is same as incident one then it is called as Rayleigh scattering while certain other light around that also gets scattered, which is called as Raman scattering. This technique gives information about rotational, vibrational, and other lower

frequency modes in the system. For chemistry applications, Raman spectroscopy provides information about of chemical bond vibrations and molecular symmetry while for applications in solid-state physics it is useful for the characterization of a crystalline solid such as symmetry, size, orientation, and defects in the system.

*Instrumentation:* High intense beam of light of narrow wavelength is used. The source is typically lasers like HeNe laser or Ar laser having wavelengths of 514 and 632 nm, respectively. The incident laser light passes through the sample and the detector detects scattered light. The change in scattered light is called as Raman shift. The shifts may be of the higher wavelength or lower wavelength respective to the response from material, which are represented by anti-Stokes' or Stokes' lines in the spectrum.

### 2.2.6 X-Ray Diffraction (XRD)

This is a non-destructive technique used to characterize crystalline materials.<sup>10,11</sup> This gives the typical characteristic spectrum for the amorphous materials and crystalline materials. For the field of supercapacitors, battery, etc. this gives information of typical amorphous or crystalline materials. For the polymer field this provides information about the film compactness, chain packing of the polymers. For the material science, the phase, size, cell parameters, growth properties of the nano-materials are determined by XRD technique.

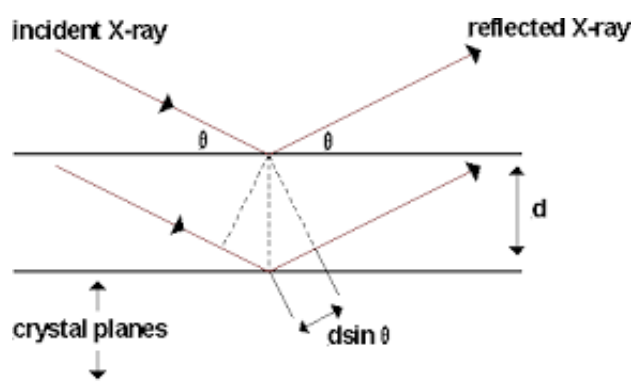


**Figure 2.7:** Mechanism of X-ray diffraction.

It is the measure of the diffracted angle from the lattice planes when the monochromatic light falls on the given material.

The Bragg's equation ( $n\lambda=2d\sin\theta$ ) gives the relation between angle of scattering and the distance between the lattice planes ( $d$ ), from which one can obtain lattice parameters of the material.

The width of the XRD peak relates to the size and strain in the nanomaterial and described by Scherrer's Formula,

$$D = \frac{0.9 \lambda}{\beta \cos \theta}$$

The full width half maxima (FWHM) for the corresponding angle  $\theta$  is given by  $\beta$ .

### 2.2.7 X-Ray Photoelectron Spectroscopy (XPS)

It is also termed as electron spectroscopy for chemical analysis (ESCA).<sup>12</sup> This is the surface technique by which the information about composition of elements, their chemical state and empirical formula are collected for the given material.

*Instrumentation:* The XPS instrument is composed of:

- X-Ray photoelectron source (Al or Mg source)
- Vacuum chamber (ultrahigh vacuum)
- Sample placing chamber, sample stage
- Electron collection lense (at sample platform)
- Electron energy analyser
- Electron detector system

Monochromatic radiations of X-ray or UV are allowed to strike the sample. The electrons with varying kinetic energy are ejected from the sample that passes through the energy filter. The filter allows certain kinetic energy (KE) possessing electrons to reach the detector. This is known as  $E_{pass}$  – The pass energy. The detector detects number of ejected electrons with that KE. The different electrons possess different binding energies. The binding energy of ejected electrons is plotted against the intensity for the analysis. According to the element and the electronic state, the binding energy varies. From this the information about the elements and their oxidation states can be extracted.

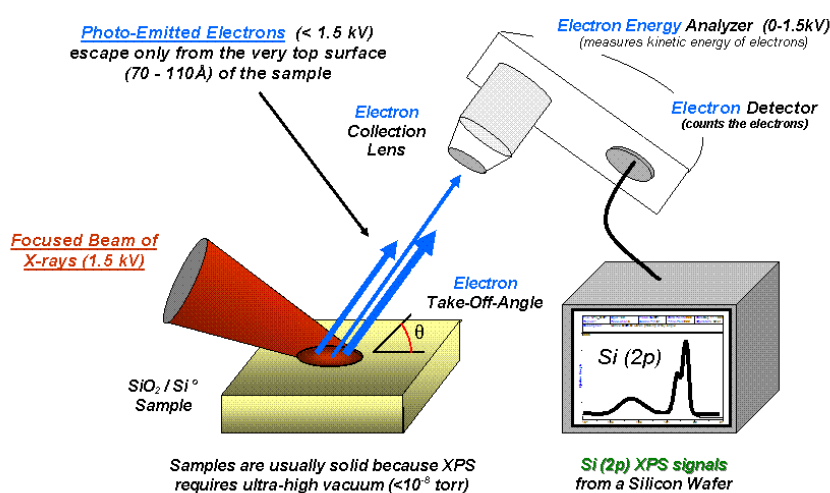


**Figure 2.8:** Schematic illustration of XPS

([https://en.wikipedia.org/wiki/X-ray\\_photoelectron\\_spectroscopy](https://en.wikipedia.org/wiki/X-ray_photoelectron_spectroscopy))

*Principle:* Working principle is based on photoelectric effect (ejection of electrons upon incident light).

XPS spectra are acquired by determining the kinetic energy and number of the emitted electrons. Generally, electrons are emitted from 0-10 nm distance.

The KE of the emitted electron is given by,

$$KE = h\nu - \phi - E_b$$

where,  $h\nu$  is incident photon energy, ( $h$  = Planck's constant,  $\nu$  = incident photon frequency) and  $E_b$  gives the electron binding energy. As the energy of the incident X-ray beam and  $\phi$  (work function) are known factors, the binding energy of the electron can be obtained from measurement of the kinetic energy of the ejected electron.

### 2.2.8 Field Emission Scanning Electron Microscope (FESEM)

This surface technique is important to explore the morphology of the material. In this, sample imaging is performed using an electron beam.

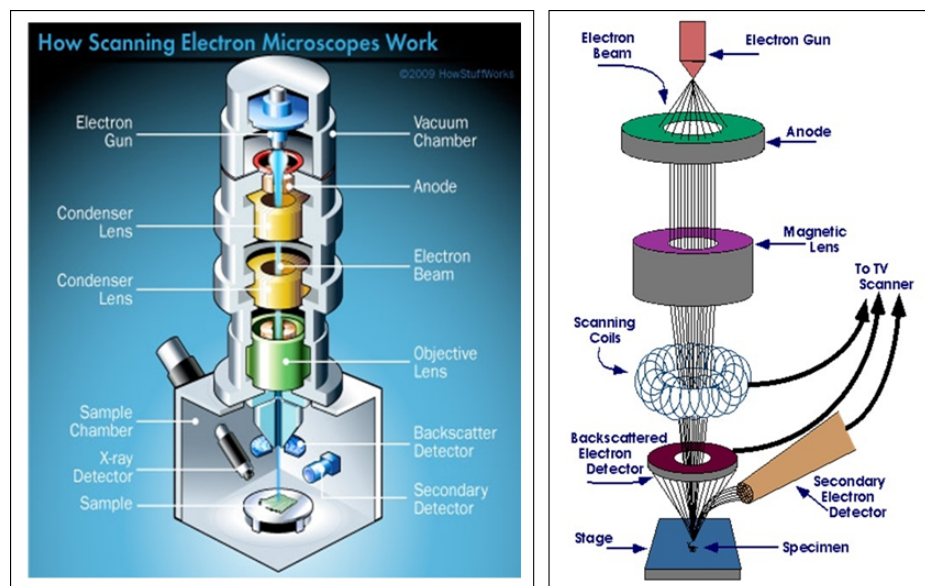


**Figure 2.9:** SEM instrument and mechanism

(<http://emicroscope.blogspot.in/2011/03/scanning-electron-microscope-sem-how-it.html>)

*Instrumentation:* FESEM comprises of:

- FE electron gun
- Condenser lenses
- Objective lens
- Sample stage
- Detectors (X-Ray detector, back scatter detector, secondary detector)

Field emission electron gun is used as a source of electrons. Incident electron beam is a cause of generation of several types of signals from the sample surface. For the imaging, the secondary electrons discharged from the atom are used. The ejected electrons are collected and accelerated in the presence of high positive potential. The electrical signal is produced with the help of photomultiplier tube. This signal is represented as 2D distribution of intensity of electrons, which is viewed as an image.<sup>13,14</sup>

### 2.2.9 Energy Dispersive X-ray Analysis (EDAX)

Energy dispersive X-ray analysis is the system used to understand the sample's chemical composition under study. The basis lies in the fact that each element has its own unique atomic structure which gives the corresponding particular emission of X-ray. When an electron is detached from the inner shell the hole is created at that place. So, the atom reshuffles itself by transferring the outer shell electron to the inner shell hole. This process of electron transfer occurs with the emission of an X-ray radiation having the energy equivalent to the difference between the two levels. These X-rays are detected by energy dispersive meter.

### 2.2.10 Transmission Electron Microscope (TEM)

TEM is used to get the information about morphology, size, lattice parameters, defects, crystal structure of the nanomaterials. The advantage of TEM over SEM is its unique capability to resolve the crystal lattice as it uses very high electron energy (~ 300 kV).

*Instrumentation:* In the TEM setup, the column arrangement is present, which is composed of:

- An electron source (eg. LaB<sub>6</sub>)
- Electron accelerating electrodes
- Electromagnets (used for focussing and deflecting electron)
- Electron detection sensor system (CCD)

Using a high-energy electron (300 kV), atomic scale resolution is possible in TEM due to reduction of the de Broglie wavelength associated with an electron to a smaller fraction (~nm).

The beam of electrons is allowed to fall onto the sample, as a consequence of this secondary emission, back scattering, transmission of electrons and X-ray emission takes place. The analyser analyzes transmitted electrons. To get selected area diffraction pattern (SAED), measurement of angular distribution of scattering can be performed in the form of diffraction patterns.<sup>15</sup>

This SEAD pattern is useful to calculate lattice plane's d spacing by the following formula,

$$d = \lambda L$$

where,  $r$  gives radius of the rings obtained from diffraction pattern,  $L$  stands for specimen and the photographic plate distance.

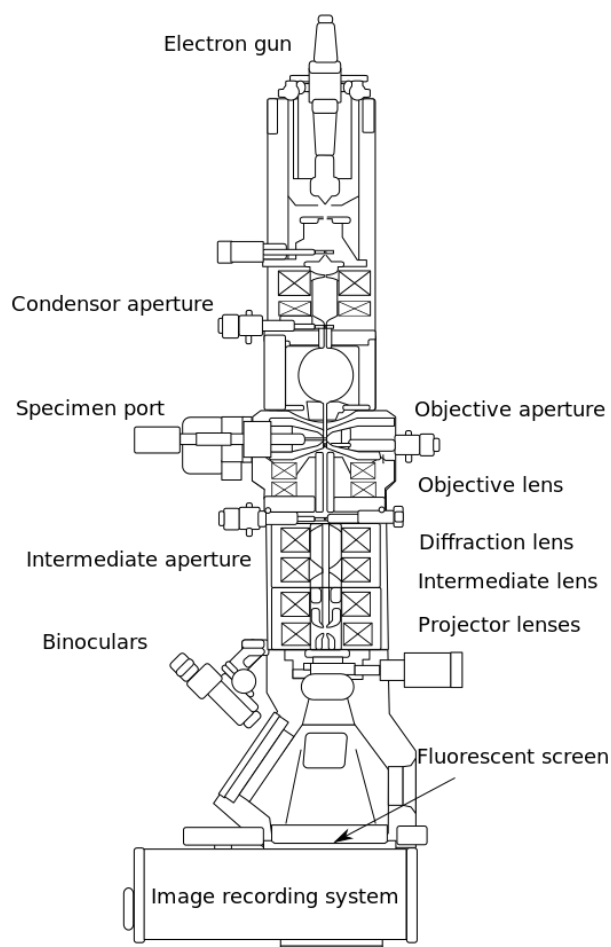


**Figure 2.10:** TEM setup

[https://en.wikipedia.org/wiki/Transmission\\_electron\\_microscopy](https://en.wikipedia.org/wiki/Transmission_electron_microscopy)

### 2.2.11 Atomic Force Microscopy (AFM)

The technique is also termed as scanning force microscopy. It is a very high resolution (up to nanometers level) microscopy used for the determination of surface roughness, softness, surface atomic structures and their interactions, etc.

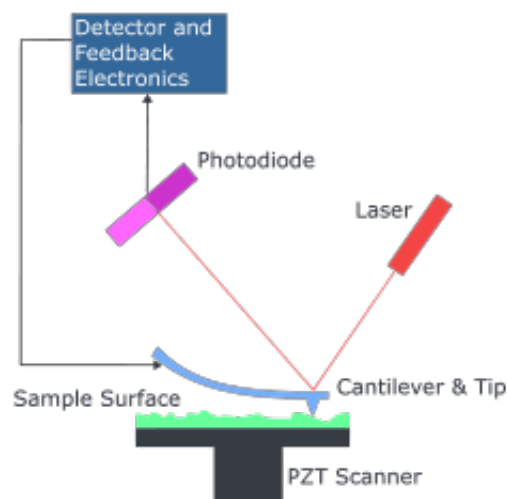


**Figure 2.11:** Schematic representation of AFM<sup>16</sup>

<http://hank.uoregon.edu/experiments/AFM/afm.html>

*Instrumentation:* This contains following parts,

- Cantilever (mounted on support using pizo-element.)
- Sharp tip (very cricial and important part hving nanometer scale)
- Detector (photodiode, interferrometer, etc.)
- Sample stage (can move in all three directions)

There are several modes of AFM imaging operation:

- Contact approach (static mode in which dragging of tip across the sample surface produces image)
- Tapping approach (dynamic mode that touches the sample at regular intervals by using cantilever oscillations)
- Non-contact approach

When the tip comes into vicinity of the surface of material under consideration, the cantilever deflection takes place due to presence of forces between the tip of cantilever and sample. This is governed by Hooke's law ( $F = -kX$ ).



### 2.2.12 Thermogravimetric Analysis (TGA)

This method is used to examine the temperature dependant features of the materials like polymers, carbon materials, ceramics, etc.<sup>17</sup>

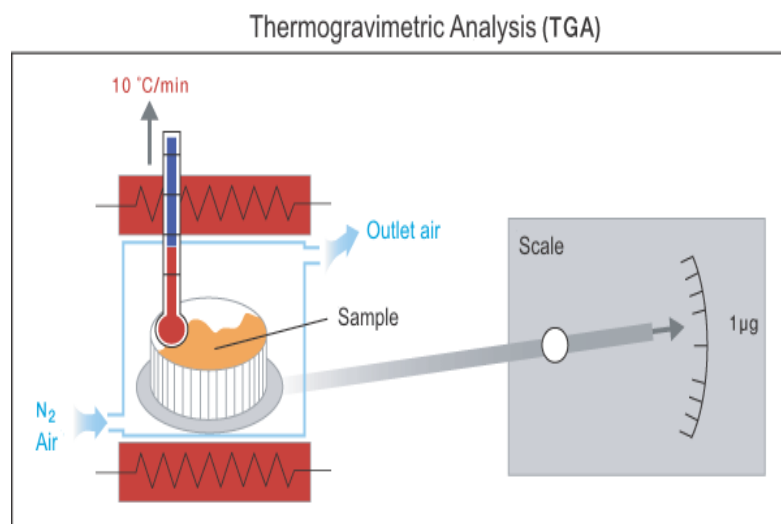


**Figure 2.12:** TGA diagrammatic representation

(<http://www.itc.tu-bs.de/Abteilungen/Makro/Methods/dsc.htm>)

**Figure 2.12** shows typical TGA setup. The sample under study is placed in the pan associated with temperature and weight analyzer. Under inert or oxidative atmosphere (air), using particular heat rate the sample is subjected to heating and the change in weight as a function of temperature is measured. Generally increase in temperature causes decomposition of sample that causes weight loss under inert atmosphere while sometimes reaction with oxygen causes weight gain.

### 2.2.13 Gel Permiation Chromatography (GPC)

The technique is used for the determination of the molecular weight and molecular weight distribution of the polymer sample.<sup>18</sup>

*Instrumentation:* GPC contains,

- Pump system (for pumping the sample solution into the system)
- Injector (injection of solution into mobile phase)
- Set of columns

- Detector (RI, UV and light scattering detector)

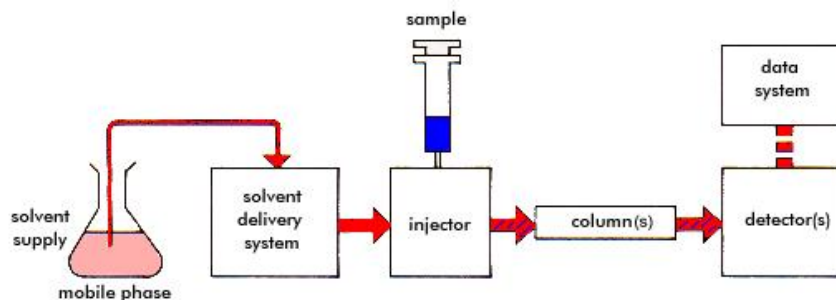


**Figure 2.13:** GPC setup

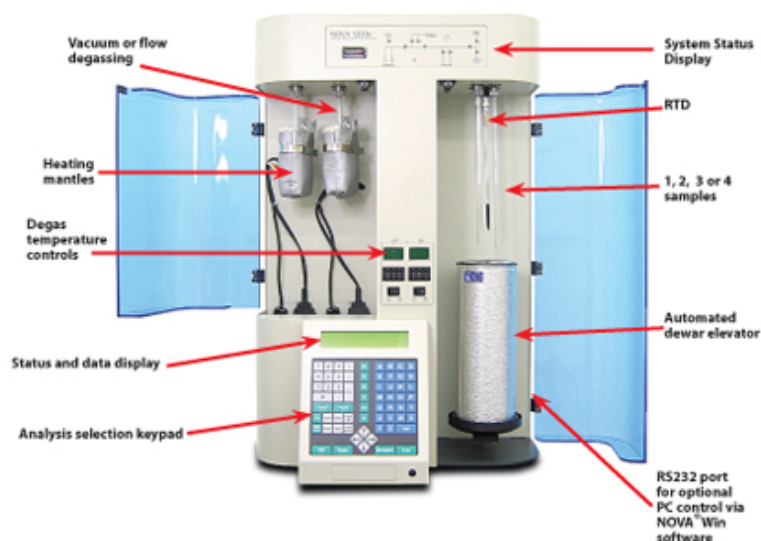
[http://www.waters.com/waters/en\\_IN/GPC---Gel-Permeation-Chromatography-Beginner%27s-Guide/nav.htm?cid=10167568&locale=en\\_IN](http://www.waters.com/waters/en_IN/GPC---Gel-Permeation-Chromatography-Beginner%27s-Guide/nav.htm?cid=10167568&locale=en_IN)

The sample is injected and flows through the porous material packed columns. The separation of the sample takes place depending upon the hydrodynamic radius of the components. The detectors detect the sample coming out from the column in terms of the retention time. According to the retention times the estimation of molecular weights is performed.

#### 2.2.14 Surface Area: BET Analysis

In 1938, Stephen Brunauer, Paul Hugh Emmett and Edward Teller published for the first time analysis of surface area. It is employed to characterize the porous materials in terms of surface area and distribution of pore size.

It is based on the phenomena of adsorption-desorption of non reactive gases like  $N_2$ ,  $CO_2$ , Ar, etc.



Rear of Instrument: RS 232 Port for PC Control via NOVAVin 2.0  
Printer Port

**Figure 2.14:** BET analysis instrument<sup>19</sup>

([http://www.quantachrome.com/gassorption/nova\\_series.html](http://www.quantachrome.com/gassorption/nova_series.html))

BET equation is represented as,

$$\frac{1}{v\left[\left(\frac{P_0}{P}\right) - 1\right]} = \frac{c - 1}{v_m c} \left(\frac{P}{P_0}\right) + \frac{1}{v_m c}$$

The adsorbed volume is given by  $v$ . At the temperature of adsorption,  $P$  and  $P_0$  are the equilibrium and saturation pressure of adsorbate.  $v_m$  represents the monolayer adsorbed quantity of gas molecules and  $c$  is the BET constant and is given as,

$$c = e^{\frac{E_1 - E_L}{RT}}$$

$E_1$  and  $E_L$  are the respective heats of adsorption of the first and next layers.

The graph of  $\frac{1}{v\left[\left(\frac{P_0}{P}\right) - 1\right]}$  against  $\frac{P_0}{P}$  is plotted, which is termed as adsorption isotherm.

The monolayer adsorbed gas quantity  $v_m$  is obtained from the intercept and constant  $c$  is obtained from the slope. The total surface area and BET specific surface area are calculated by,

$$S_{total} = \frac{v_m N s}{V} \text{ and } S_{BET} = \frac{S_{total}}{a}$$

Where, N is Avogadro number, s and V are the gas molecule's adsorption cross-section and molar volume respectively, and a stands for the mass of a sample. The type of isotherm gives information about type of porosity.

### 2.2.15 Electrochemical Measurements

The electrochemical analysis performed using Autolab, Bologic potentiostats and Arbin battery analyzer. The supercapacitor measurements were done in a two electrode symmetric cell with active material on both the electrodes. For Li-HEC, materials were tested in the half cell configuration with the active material as the working electrode and LTO ( $\text{Li}_4\text{Ti}_5\text{O}_{12}$ ) as counter electrodes.

#### 2.2.15.1 Cyclic voltammetry (CV)

This is very important technique in electrochemistry to obtain qualitative analysis about feasible electrochemical reactions. The information like oxidation/reduction potential, reaction kinetics and reversibility of redox reactions can be extracted. It is also useful in measurements of various energy applications like electrochemical energy storage and conversion systems such as batteries, supercapacitors, solar cells, fuel cells, water splitting, etc.

For finding the oxidation/reduction potentials of the materials like polymers, organic molecules, etc., CV measurements are performed using three electrode system.

This include:

- Reference electrode (eg. Ag/AgCl, Ag/AgNO<sub>3</sub>, calomel, etc.) Depending on the solvent used for the electrochemical analysis, the choice of reference electrode is made. For the same material there could be different values of oxidation/reduction peak position corresponding to the reference electrode.
- Counter electrode (platinum foil or graphite)
- Working electrode (material under study is coated on a conducting substrate that acts as working electrode, eg. coating on Pt wire.)

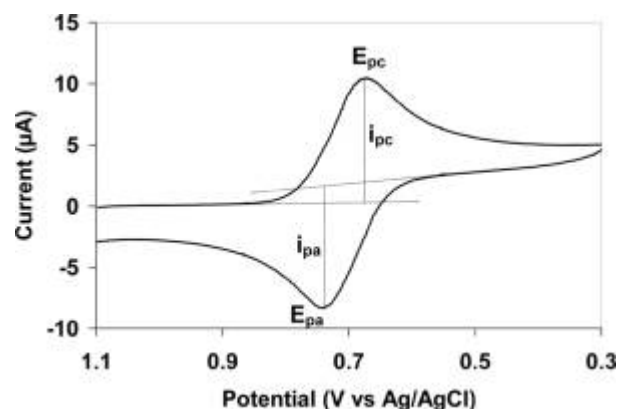


**Figure 2.15:** A typical cyclic voltammogram

[https://en.wikipedia.org/wiki/Cyclic\\_voltammetry](https://en.wikipedia.org/wiki/Cyclic_voltammetry)

For the measurement, the current is analysed as a function of potential sweep between  $V_1$ - $V_2$  amongst working and counter electrodes at some constant time intervals/ rate called as scan rate (V/s).

### 2.2.15.2 Galvanostatic Charging-discharging Measurements

For energy storage devices like supercapacitors and batteries, this measurement is very important to gain the information regarding charge storage capacity, cyclic reversibility and stability. During the experimental process, a constant current is applied between counter and working electrodes with subsequent measurement of potential with time is done. Depending on the material of electrode and type of electrolyte (aqueous, organic, ionic liquids, etc.), the potential window measurement is chosen.

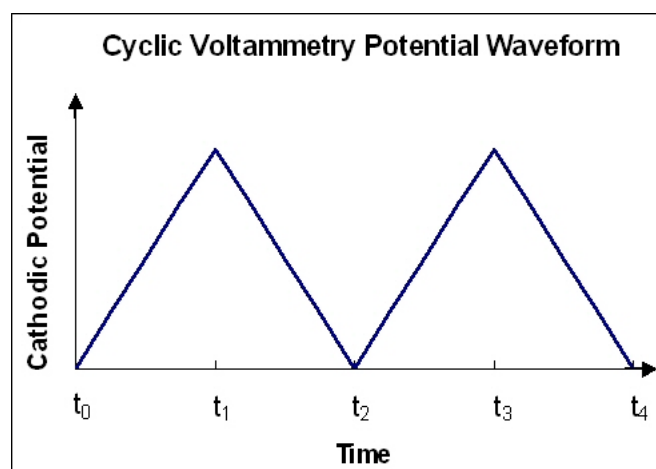


**Figure 2.16:** CV potential waveform

[https://en.wikipedia.org/wiki/Cyclic\\_voltammetry](https://en.wikipedia.org/wiki/Cyclic_voltammetry)

From charge-discharge measurements, the specific capacitance ( $C$  in F/g) is calculated by using the following formula when current  $I$  is applied to the electrode having active material loading of  $m$ .

$$C = \frac{2I}{m \frac{dv}{dt}}$$

Where,  $\frac{dv}{dt}$  is the slope of the discharge curve.

### 2.2.15.3 Electrochemical Impedance Spectroscopy (EIS)

To study the interface of electrode-electrolyte, EIS is the most sensitive and powerful tool. It is used to get the double layer capacitance and series resistance for the case of supercapacitor. For solar cell devices, it helps to get an idea regarding the interfaces and the resistances (Ohmic loss/impedance) in the system.

The AC frequency of different range (from 100 nHz to 1MHz) is applied and the real and imaginary types of impedance is evaluated by plotting real part ( $Z'$ ) against imaginary part ( $Z''$ ), which is called as Nyquist plot. The Nyquist plot provides series resistance (obtained from X-intercept), charge transfer resistance (from the value diameter of each semicircle) and the electrolyte-electrode interface in the system.

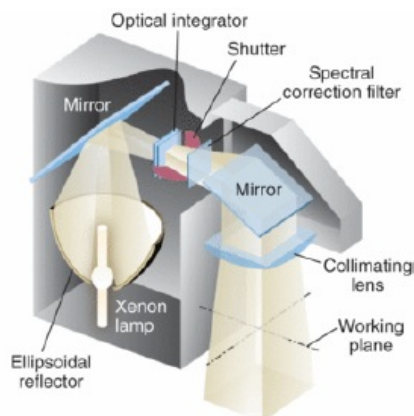
### 2.16 Solar Simulator

The instrument is used for the characterization of the optoelectronic devices predominantly solar cells. This works as artificial sun and provides the intensity of the natural sunlight for indoor measurements.

*Instrumentation:* It is typically composed of.

- Light source (xenon lamp of different powers like 250 Watts or 450 Watts)
- Mirrors
- Optical filters

- Reflectors
- Shutter



(a)



(b)

**Figure 2.17:** (a) Schematic representation of solar simulator, (b) Instrument photograph of solar simulator at CSIR-National Chemical Laboratory

(J. Jeong, <http://www.laserfocusworld.com/articles/print/volume-43/issue-3/features/photovoltaics-enhancements-enable-solar-simulators-to-shed-light-on-new-photovoltaic-designs.html>, 2007.)

Apart from this basic setup, solar simulator is attached to the Keithley unit, which acts as voltage source current measurement setup. The plot of current against voltage gives characteristic properties of solar cells.

### 2.17 Field Emission Study

In the field emission, the emission of condensed phase electrons occurs into the vacuum phase with the application of electrostatic field at room temperature.

*Instrumentation:* The setup is composed of,

- UHV (ultra high vacuum) system
- Working chamber with planer diode system (sample frame, phosphor screen)
- Voltage source
- Current detector

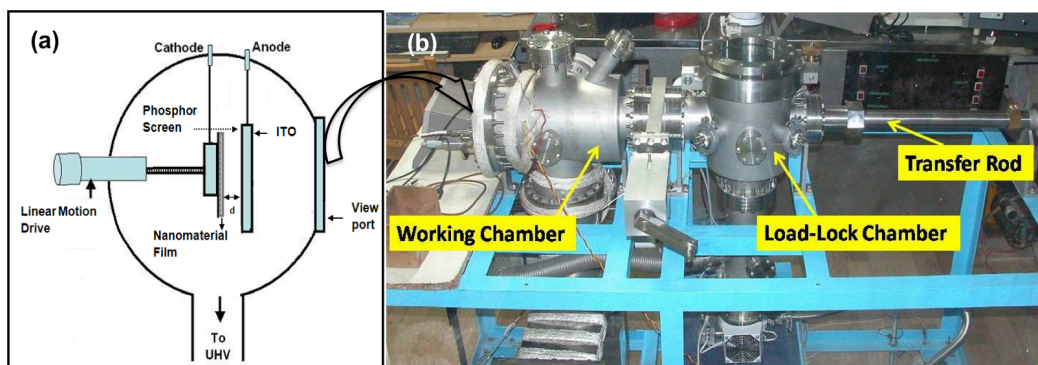


**Figure 2.18:** (a) Configuration of planer diode system, (b) Field emission setup

The sample is coated on the conducting substrate and it is placed in the planer diode configuration setup. This is the cathode in the experiment. The anode is phosphor coated conducting screen on which emission is seen. The distance between the anode and cathode is maintained to the optimal value in order to get proper emission current. For the current work, the distance kept was 1.5 mm between anode and cathode. Under the vacuum, with increasing voltage the emission as well as current increases up to certain saturation point that depends on the material. The important parameters are turn on voltage, threshold voltage and current density at the threshold voltage for field emission



## References

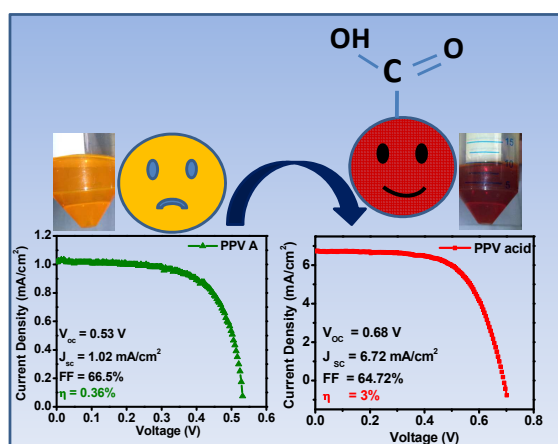
1. <http://www.chem.wisc.edu/areas/reich/nmr/07-multi-01-nuclear.htm>
2. T. Owen, *Fundamentals of UV-visible spectroscopy*, Hewlett-Packard publication, Germany, **1996**.
3. Game, O.; Singh, U.; Gupta, A. A.; Suryawanshi, A.; Banpurkar, A.; Ogale, S. *J. Mater. Chem.* **2012**, 22, 17302-17310.
4. [http://cnx.org/contents/7b4dfcf8b28e4148f2f1ff39052669f@13.7:30/Nanomaterials\\_and\\_Nanotechnology](http://cnx.org/contents/7b4dfcf8b28e4148f2f1ff39052669f@13.7:30/Nanomaterials_and_Nanotechnology)
5. T. H. Gfroerer, *Encyclopedia of Analytical Chemistry*, R.A. Meyers (Ed.), John Wiley & Sons Ltd, Chichester, 2000, 9209–9231.
6. *Fundamentals of Molecular Spectroscopy*, 4th Ed., Tata McGraw Hill Publishing Co. Ltd., 2002.
7. *Interpretation of Infrared Spectra: A Practical Approach*, *Encyclopedia of Analytical Chemistry* C. N. Banwell, E. M. McCash, A Book: J. Coates, R.A. Meyers (Ed.), 10815, John Wiley & Sons Ltd, 2000.
8. D. A. Long, *Raman Scattering*, McGraw Hill Book Company, New York, **1977**.
9. A. R. Barron, *Surface-Enhanced Raman Spectroscopy for the Study of Surface Chemistry*, <http://www.cnx.org/contents/f8a19258-739c-43d6-9b26-cc6b9cf70821@1>, **2010**.
10. R. W. G. Wyckoff, *Crystal Structures*, 2nd ed., Wiley, New York, **1964**;
11. B. D. Cullity, *Elements of X-Ray Diffraction*, Addison-Wesley Publishing Company, Inc., Massachusetts, **1956**.
12. <http://www2.cemr.wvu.edu/~wu/mae649/xps.pdf>
13. G. Lawes, *Scanning electron microscopy and X-ray microanalysis: Analytical chemistry by open learning*, John Wiley & sons, **1987**;
14. J. Atteberry, *How Scanning Electron Microscopes Work*, <http://science.howstuffworks.com/scanning-electron-microscope.htm>, **2009**.
15. a) Ding, Y.; Wang, Z. L. *Journal of Physical Chemistry B* **2004**, 108, 12280; b) Duan, J. H.; Yang, S. G.; Liu, H. W.; Gong, J. F.; Huang, H. B.; Zhao, X. N.; Zhang, R.; Du, Y. W. *Journal of the American Chemical Society* **2005**, 127, 6180.

16. <http://hank.uoregon.edu/experiments/AFM/afm.html>
17. <http://www.itc.tu-bs.de/Abteilungen/Makro/Methods/dsc.htm>
18. [http://www.waters.com/waters/en\\_IN/GPC---Gel-Permeation-Chromatography-Beginner%27s-Guide/nav.htm?cid=10167568&locale=en\\_IN](http://www.waters.com/waters/en_IN/GPC---Gel-Permeation-Chromatography-Beginner%27s-Guide/nav.htm?cid=10167568&locale=en_IN)
19. [http://www.quantachrome.com/gassorption/nova\\_series.html](http://www.quantachrome.com/gassorption/nova_series.html)

## Chapter 3

### Carboxyl-Modified Conjugated Polymer Sensitizer for Dye Sensitized Solar Cells: Significant Efficiency Enhancement

A simple two-step strategy was developed to introduce carboxyl groups *via* Vilsmeier–Haack formylation on the commercially available conjugated polymer *viz.* (poly{[2-[2',5'-bis(2''-ethylhexyloxy)phenyl]-1,4-phenylenevin-ylene]-co-[2-methoxy-5-(2'-ethylhexyloxy)-1,4-phenylenevin-ylene]}) (**BEHP-co-MEH PPV**) followed by Knoevenagel condensation with cyanoacetic acid. Adsorption of the carboxyl-modified polymer onto TiO<sub>2</sub> film and *J-V* curves were studied for the dye sensitized solar cell and compared with the base polymer **BEHP-co-MEH PPV**. Carboxyl-modification of **BEHP-co-MEH PPV** resulted in significant enhancement in the efficiency (3%), compared to the base polymer, which showed an efficiency of only 0.36%. The details of the synthetic procedure, characterization and the photovoltaic property measurements are presented and discussed.



The contents of this chapter have been published in *J. Mater. Chem.*, 2012, 22, 23267–23271

### 3.1 Introduction

Dye sensitized solar cells (DSSCs) are considered to be potential alternatives to the conventional silicon solar cells due to use of relatively low cost materials and possibility of large scale production on hard and flexible substrates. Based on organic-inorganic hybrid architectures, DSSCs have already shown fairly high power conversion efficiencies (PCE) primarily with ruthenium based dyes as sensitizers.<sup>1-4</sup> The use of such metal containing dyes, however, represents a major disadvantage in terms of the cost as rare earth metals are expensive. Another disadvantage is the instability of these dyes at high temperature, which limits certain otherwise potentially accessible cell processing protocols and explorations of cell performance at higher temperatures. Moreover, the efficiency of these dyes is dependent on many factors such as the structure of dyes, electrolytes, photo-anodes, etc.<sup>5,6</sup> In view of these considerations; explorations of metal-free dyes have attracted considerable scientific attention. Metal-free dyes which include small organic molecules<sup>7-9</sup> and conjugated polymers (CPs) with a broad-band absorption in the visible region are promising candidates for DSSCs. Ability of such dyes to load on the semiconducting metal oxide structure facilitates the photo-excited electron-hole pair transfer *via* proper matching of their HOMO-LUMO levels with the respective electrodes<sup>10</sup> and the electrolyte<sup>11</sup> which is the key to their effective use in DSSC architecture.

Conjugated polymers (CPs) have broadband absorption in the visible region due to their extended conjugation and exhibit interesting charge carrier transport properties. They are potential candidates for DSSCs because of high molar extinction coefficient, tunable optical properties, and solution processability. In addition to being useful as possible sensitizers, CPs can be employed as electrolytes in solid state DSSCs.<sup>12-15</sup> Recently, various CPs have been used as sensitizers in DSSCs.<sup>16-19</sup> However, considerable work is needed to obtain more insight into their utilization and functioning in DSSCs. Amongst the various reports, comparatively high numbers for PCE in polymer sensitized solar cells have been reported for triphenyl based polymer by Zang et al. (3.3%)<sup>20</sup> and terthiophene benzothiadiazole polymer by Fang et al. (3%).<sup>21</sup>

Our work is focused on using a conjugated polymer as a sensitizer in the DSSC with the iodide/triiodide redox couple. We have modified a commercially available conjugated polymer viz. (poly{{2-[2',5'-bis(2''-ethylhexyloxy)phenyl]-1,4-phenylenevin-ylene]-co-[2-methoxy-5-(2'-ethylhexyloxy)-1,4-phenylene vinylene]}) **BEHP-co-MEH PPV (PPV A)** so as to introduce carboxylic acid as the anchoring groups on the polymer chain. The anchoring group effect is a crucial factor in the device performance. Carboxylic acid groups are known to have a good adsorption on TiO<sub>2</sub> through Ti–O–C covalent bond, which also helps in the efficient charge injection. There are evidences from analysis and computer simulation about the role of such anchoring groups.<sup>22–26</sup> In the present work, our main emphasis was to design a strategy to introduce carboxyl groups on the **BEHP-co-MEH PPV (PPV A)** and study the effect of carboxyl anchoring group on the overall performance of the dye sensitized solar cell. The performance of the base polymer **PPV A** which is devoid of the carboxyl functionality was very low as compared to the carboxyl-modified one which showed ca. 10 fold increase in the device performance with IPCE ~50% and PCE 3%.

## 3.2 Experimental Section

### Materials:

**BEHP-co-MEH-PPV (PPV A)** (M<sub>w</sub>-18900, 60: 40) and POCl<sub>3</sub> were purchased from Sigma-Aldrich and were used as received. N,N-Dimethyl formamide (DMF) and toluene were dried over calcium hydride followed by distillation under reduced pressure.

### 3.2.1 Synthesis

#### 3.2.1.1 Vilsmeier–Haack formylation of **BEHP-co-MEH-PPV (PPV A)**:

Into a 500 mL two-necked round bottom flask equipped with a rubber septum, a magnetic stirring bar and a reflux condenser, was added **PPV A** (0.3 g, 1.3 mmol) under argon atmosphere. Dry 1,2-dichlorobenzene (250 mL) was added to the reaction mixture and **PPV A** was dissolved by ultra-sonication for 50 min and purged with argon for 10 min. DMF (0.13 mL, 1.66 mmol) was added using a syringe and the reaction mixture was cooled to 0 °C using an ice bath. POCl<sub>3</sub>

(0.15 mL, 1.66 mmol) was added drop wise using a syringe with continuous stirring, under argon atmosphere. After completion of addition, the reaction mixture was allowed to attain room temperature and stirred for 10 min. The reaction mixture was then heated at 70 °C for a period of 12 h. The reaction mixture was allowed to cool at room temperature. It was then diluted with 30 mL of chloroform and poured into ice-cold water and stirred for 1 h. The organic layer was separated, dried over anhydrous sodium sulfate and filtered. The solvent was removed under reduced pressure. Further purification was done by washing with methanol. Methanol was decanted and the product was dried in a vacuum oven at 60 °C for 6 h. Yield- 0.2 g

### ***3.2.1.2 Knoevenagel Condensation of BEHP-co-MEH-PPV-aldehyde (PPV CHO) with Cyanoacetic Acid:***

Into a 100 mL single necked round bottom flask, **PPV CHO** (0.19 g, 0.87 mmol) was taken and degassed by three simultaneous freeze–pump–thaw cycles. Dry toluene (45 mL) was added by using a syringe into the reaction vessel and **PPV CHO** was dissolved by ultrasonication for 15 min. The solution was transferred into a 250 mL two-necked round bottom flask and piperidine (0.06 mL, 1.13 mmol) was added under argon atmosphere. Cyanoacetic acid was then added to the reaction mixture (0.096 g, 1.13 mmol), and refluxed for 17 h. The reaction mixture was cooled and toluene was removed under reduced pressure. Methanol (30 mL) was added to the reaction mixture and stirred for 30 min to remove excess piperidine and cyanoacetic acid. After stirring for 30 min, methanol was decanted and the orange product **PPV acid** was dried in a vacuum oven at 60 °C for 6 h. Yield- 0.16 g.

### **3.2.2 Characterization of Physical Properties**

The absorption spectra of solutions of **PPV A** and **PPV acid** (0.05 mM) were recorded in chloroform on a CARY 5 UV-Vis-NIR spectrophotometer (Varian, Inc.). Diffused reflectance spectra (DRS) were recorded on Jasco instruments and FTIR spectra were recorded using Perkin Elmer instruments. NMR spectra were recorded on a Bruker 500 MHz spectrometer at resonance frequency of 500 MHz for <sup>1</sup>H using chloroform-d (Sigma-Aldrich) and methanol-d<sub>4</sub> (Sigma-Aldrich) as a solvent. TGA was recorded using TGA-7 Perkin Elmer instrument.

The  $J-V$  characteristics were measured under exposure with  $100 \text{ mW cm}^{-2}$  (450 W xenon lamp, Newport), 1 sun AM, and simulated sunlight as a solar simulator. The current was measured using a Keithley 2400 source. Measurements of the incident-photon-to-current conversion efficiency (IPCE) were performed by changing the excitation wavelength (Newport).

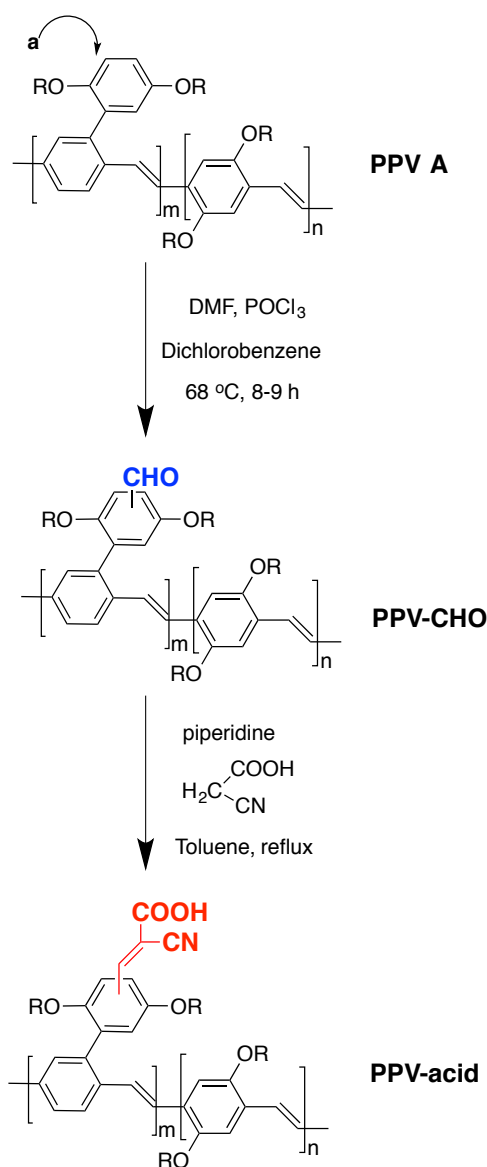
### 3.2.3 Fabrication and Testing of DSSCs

To make and to study the DSSC, doctor blading method for the  $\text{TiO}_2$  film preparation was employed. After making the films, they were annealed at  $450 \text{ }^\circ\text{C}$  for 60 min. For sensitization, the films were dipped in samples viz. solutions of modified or unmodified polymer in chloroform for 24 h at room temperature. The films were then rinsed with chloroform to remove excess polymeric dye on the surface and air-dried at room temperature. This was followed by redox electrolyte addition and top contact of Pt coated FTO. The electrolyte used was 0.6 M 1-propyl-2,3-dimethyl-imidazolium iodide, 0.1 M LiI, 0.05 M  $\text{I}_2$ , and 0.5 M 4-tert-butylpyridine in acetonitrile. The  $J-V$  characteristics and incident photon to current conversion efficiency (IPCE) were then measured.

## 3.3 Results and Discussion:

### 3.3.1 Synthesis of Acid Derivative of BEHP-co-MEH-PPV Starting from BEHP-co-MEH-PPV:

The synthesis of **PPV acid** involves two steps consisting of well-known organic transformations (**Scheme 3.1**). Vilsmeier–Haack formylation is a useful method for introduction of formyl groups on the electron rich aromatic rings. Polymer **PPV A** contains electron rich aromatic rings and thus is a good candidate to perform the formylation reaction. Also **PPV A** contains vinylene bonds, which are compatible towards the formylation conditions. The first step involves Vilsmeier–Haack formylation of the base polymer **PPV A** using  $\text{N,N}$ -dimethyl formamide (DMF) and phosphoryl chloride ( $\text{POCl}_3$ ) affording its aldehyde derivative. Knoevenagel condensation of **PPV CHO** with cyanoacetic acid in the presence of piperidine yielded **PPV acid**. The reactions were followed by  $^1\text{H}$  NMR spectra of the polymers (**Figure 3.1**).



**Scheme 3.1:** Synthesis of **PPV acid**

The appearance of the characteristic peaks of the aldehyde functional group at 9.83 ppm and 10.13 ppm in the <sup>1</sup>H NMR spectra after the Vilsmeier–Haack formylation confirmed the formation of the **PPV CHO**. We observed two peaks for aldehyde in the NMR spectrum which could be attributed to the formylation at two different positions, as the **PPV A** contains two types of electron-rich aromatic rings having different chemical environments. The disappearance of the aldehyde peaks in the <sup>1</sup>H NMR spectrum of **PPV acid** confirmed the condensation of the aldehyde with the cyanoacetic acid group affording the target product, acid derivative of the polymer (**PPV acid**) (Scheme 3.1).



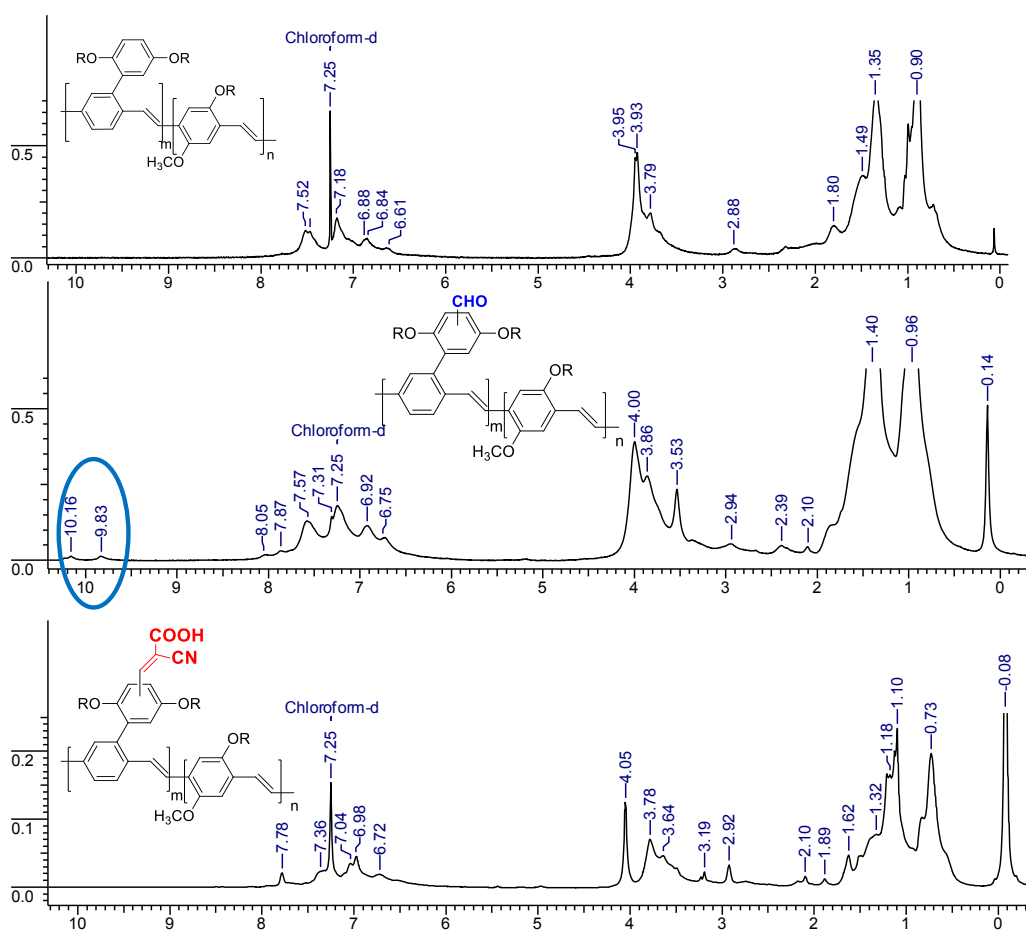


**Figure 3.1:**  $^1\text{H}$  NMR spectra of **PPV A**, **PPV CHO** and **PPV acid**.

### 3.3.2 UV-Visible Spectroscopy:

The absorption spectrum of the modified polymer **PPV acid** is compared with the **PPV A** in chloroform solution (0.05 mmol) in **Figure 3.2**. The base polymer **PPV A** showed broadband absorption in the visible region from 350 nm to 550 nm with the absorption maximum at about 460 nm. Polymer **PPV acid** showed a broadband absorption from 350 nm to 600 nm and absorption maximum at 450 nm with a blue shift. After modification of polymer, a red shift was expected in the UV-visible absorption spectrum because of the extension in conjugation due to incorporation of cyanoacrylic acid moiety. However, surprisingly the modified polymer showed a blue shift in absorption spectrum.

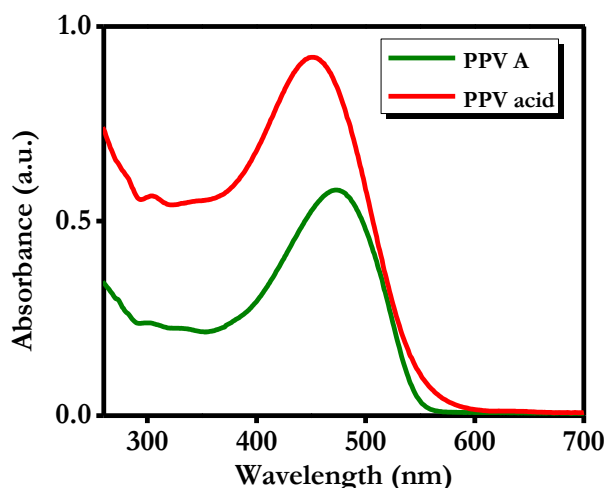


**Figure 3.2:** UV-Vis spectra of **PPV A** and **PPV acid** derivative.

The observed blue shift for **PPV acid** absorption spectrum may be due to break in conjugation in case of probable meta-substitution as indicated in **Scheme 3.1**.<sup>27,28</sup>

The molar extinction coefficients were calculated from the corresponding absorption spectra of **PPV A** and **PPV acid** and values were found to be  $4.2 \times 10^5 \text{ cm}^{-1} \text{ mol}^{-1}$  and  $7.9 \times 10^5 \text{ cm}^{-1} \text{ mol}^{-1}$ , respectively.

### 3.3.3 Diffuse Reflectance Spectra (DRS):

DRS were recorded for the **PPV A** as well as the **PPV acid** in their powder form and data is shown in **Figure 3.3**. These spectra exhibited broad absorption of the polymer with a small tail above 600 nm in the case of **PPV acid** as well as small blue shift in the absorption maxima of **PPV acid** from 460 nm (**PPV A**) to 450 nm in accordance with UV-Vis spectra discussed in the text.

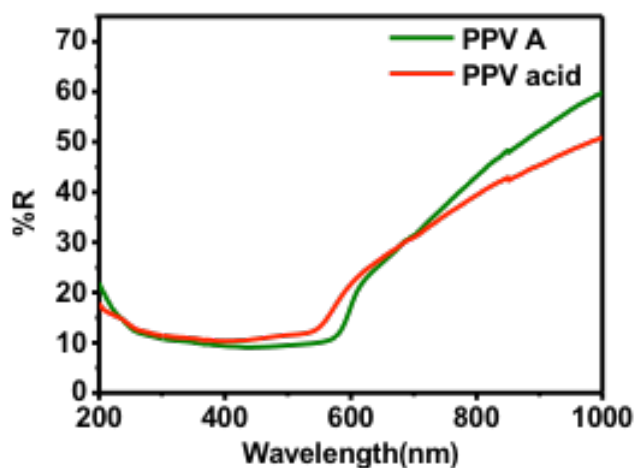


**Figure 3.3:** DRS spectra of **PPV A** and **PPV acid**.

### 3.3.4 Photoluminescence Spectroscopy (PL):

**Figure 3.4 (a)** and **(b)** depicts the PL spectra of the **PPV A** and the **PPV acid**, respectively. Both **PPV A** and **PPV acid** showed emission at around 550 nm (2.254 eV) for the excitation maxima at 480 nm (~ 2.583 eV) for **PPV A** and 460 nm (~ 2.695 eV) for **PPV acid**, respectively. In the case of **PPV acid** the e-h binding energy is ~0.441 eV while for the **PPV A** it is ~0.329 eV.

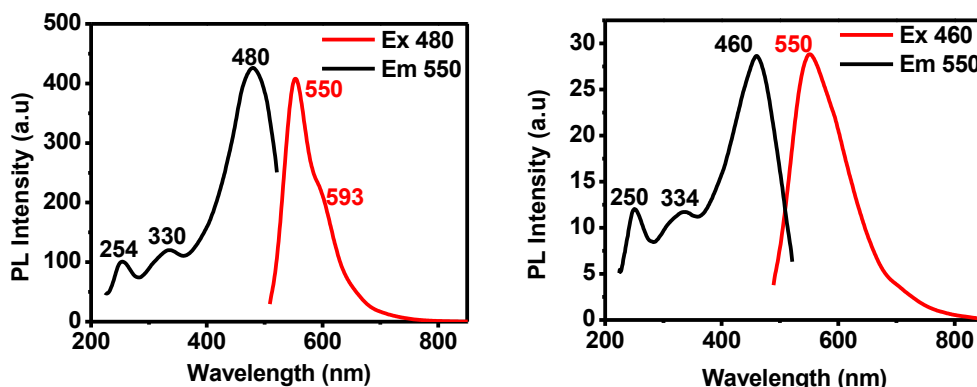


**Figure 3.4:** Photoluminescence spectra of **(a) PPV A** and **(b) PPV acid**.

Thus, there is a small increase in the band gap energy after the modification because of the electron withdrawing effect of  $-\text{COOH}$  and  $-\text{CN}$  groups, which corroborates with the UV-Vis spectra (**Figure 3.3**), and the band diagram (**Figure 3.7**)

### 3.3.5 Infrared Spectroscopy (FTIR study):

**Figure 3.5** represents the FTIR spectra of polymers taken in the solid state using a KBr pellet.

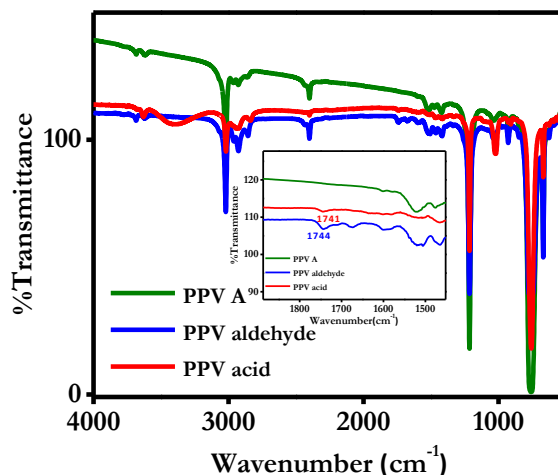


**Figure 3.5:** FTIR spectra of **PPV A**, **PPV CHO** and **PPV acid** (inset showing expanded portion of carbonyl region, clearly shows the carbonyl stretching frequency).

The peaks at  $1741\text{ cm}^{-1}$  and  $1744\text{ cm}^{-1}$  represent the characteristic carbonyl frequencies in **PPV CHO** and **PPV acid**, respectively. Also the presence of a broad absorption near  $3400\text{--}2400\text{ cm}^{-1}$  (at  $3390\text{ cm}^{-1}$ ) in the **PPV acid** indicates the  $\text{-OH}$  frequency.

### 3.3.6 Band Alignment of Polymer with $\text{TiO}_2$ :

The band alignment of the **PPV A** and **PPV acid** with the  $\text{TiO}_2$  was obtained using cyclic voltammetry (**Figure 3.6**). Electrochemical properties (cyclic voltammetry) of the **PPV A** and modified polymer **PPV acid** were studied in the dichloromethane solution. HOMO of the modified polymer **PPV acid** is  $-4.9\text{ eV}$  and that of the base **PPV A** is  $-4.8\text{ eV}$  with reference to the vacuum level. The band gap increased from  $2.58\text{ eV}$  to  $2.69\text{ eV}$  in **PPV acid**, supporting the blue shift observed in the UV-Vis spectra.

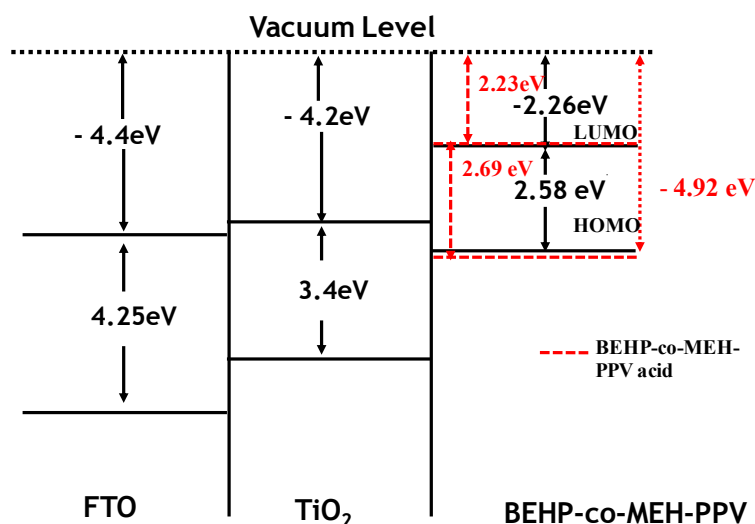


**Figure 3.6:** Band alignment of PPV A and PPV acid with TiO<sub>2</sub>.

### 3.3.7 J–V Characterization and IPCE Measurements:

The TiO<sub>2</sub> type was optimized for the better efficiency. Selection of TiO<sub>2</sub> is an important parameter. The size of the TiO<sub>2</sub> and the polymeric dye should be compatible. **Table 3.1** shows the details about the TiO<sub>2</sub> type optimization. Sol-gel TiO<sub>2</sub>, which forms a very compact film, was not suitable for the polymeric dye. The better performance was obtained by using P25 powder of TiO<sub>2</sub>.

**Table 3.1:** Optimization of TiO<sub>2</sub> type and polymeric dye concentration.

No.	Film material	Time (h)	PPV-A dye concentration (mmol)	Efficiency (%)
1	P25	24	0.05	0.46
2	P25	24	0.05	0.55
3	P25	24	0.1	0.8
4	P25	24	0.3	0.32
5	Sol-gel TiO <sub>2</sub>	24	0.1	0.16
6	Sol-gel TiO <sub>2</sub>	48	0.1	0.14
7	Mesoporous TU10	24	0.1	0.3
8	Electrospun TiO <sub>2</sub>	24	0.1	0.12
9	ZnO	24	0.05	0.08

Another important parameter is the thickness of the TiO<sub>2</sub> film. For the optimization of the thickness; 4, 8, and 12 μm thick films were made and the performance was checked (**Table 3.2**). It was observed that 12-μm thick P25 TiO<sub>2</sub> film gave better efficiency. Thus this condition was set for the further measurements.

**Table 3.2:** Thickness optimization of TiO<sub>2</sub> film.

No.	Film type	Thickness (μm)	Efficiency (%)
1	P25	4	0.68
2	P25	8	0.71
3	P25	12	0.70
4	Sol-gel TiO <sub>2</sub>	12	0.26

Thus, with the optimized conditions of TiO<sub>2</sub> thickness and the dye concentration, DSSC device using **PPV acid** as sensitizer was made and I-V characteristics were recorded.

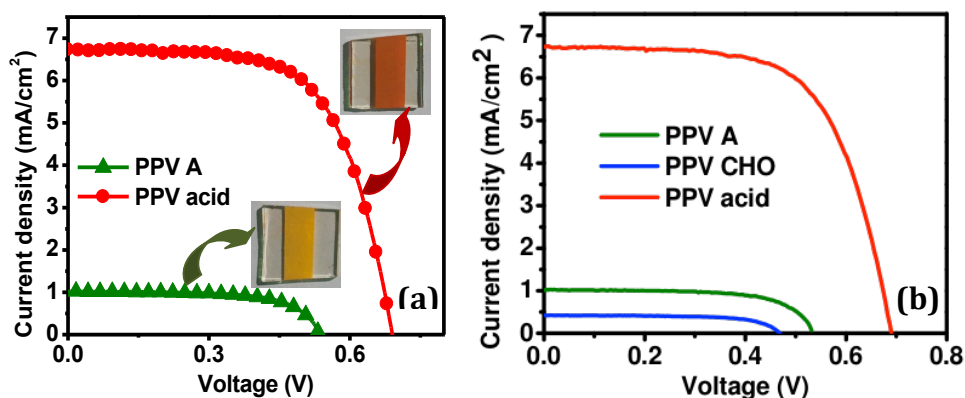


**Figure 3.7:** J-V characterization for the (a) **PPV A** and **PPV acid**, (b) comparison of J-V curves for **PPV A**, **PPV CHO** and **PPV acid**

J-V characteristics for the DSSCs are shown in **Figure 3.7 (a)** for the case of commercial Degussa P25 TiO<sub>2</sub> nanoparticle films using base polymer **PPV A** and **PPV acid** polymer dye. The thickness of the TiO<sub>2</sub> films used was 8–10 micrometers. **Figure 3.7 (b)** represents the comparison of I-V characteristics of **PPV A**, **PPV CHO** and **PPV acid**.

**Table 3.3** represents comparison of the **PPV A**, **PPV-CHO** and **PPV acid** dyes on the optimized films of TiO<sub>2</sub> (P25 films, 12 μm thick)

**Table 3.3:** Comparison of **PPV A**, **PPV-CHO** and **PPV acid** dyes on the optimized films.

No.	Dye	Efficiency (%)
1	PPV A	0.36
2	PPV-CHO	0.13
3	PPV-acid	3.0

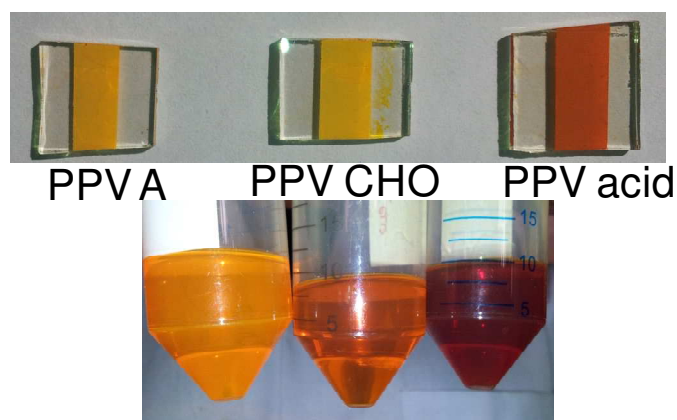


**Figure 3.8:** (Top) TiO<sub>2</sub> films sensitized with **PPV A**, **PPV CHO** and **PPV acid** by dipping in their chloroform solutions (Below)

**Table 3.4:** Solar cell parameters for **PPV A** and **PPV acid**.

No.	Polymer	V <sub>OC</sub> (V)	J <sub>SC</sub> (mA/cm <sup>2</sup> )	FF (%)	Efficiency (%)
1	PPV A	0.53	1.02	66.55	0.36
2	PPV acid	0.69	6.71	64.71	3.0

The current density is seen to have increased dramatically from 1 mA cm<sup>-2</sup> to 6.7 mA cm<sup>-2</sup> in the case of **PPV acid**, resulting in a power conversion efficiency of 3

%. The  $V_{OC}$  is also seen to have increased significantly from 0.53 V to 0.69 V.

**Figure 3.9** shows the IPCE measurement data for  $TiO_2$  sensitized with the polymer dye as a function of wavelength. IPCE was calculated using the equation:

$$IPCE (\%) = \frac{1240J_{SC}}{\lambda P_{in}}$$

Where,  $J_{SC}$  is the short-circuit current density,  $\lambda$  is the wavelength of the incident light, and  $P_{in}$  is the power of the incident light. The **PPV acid** exhibited 47% broad peak of IPCE as against the base polymer **PPV A** which showed only 7% IPCE. This indicates that there is effective charge transfer because of the good adsorption and electronic anchoring of the  $-COOH$  functional groups on the surface of  $TiO_2$  in the modified polymer **PPV acid**.

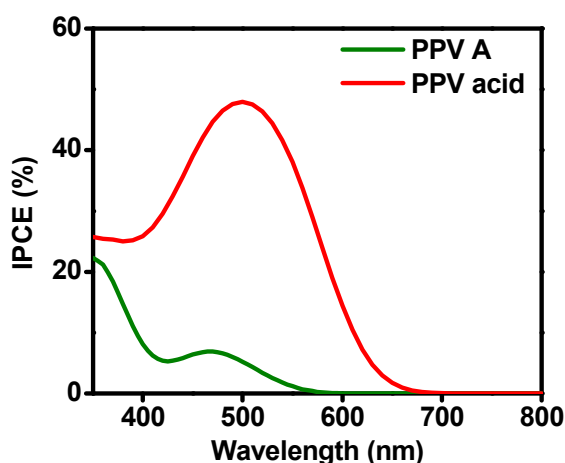


**Figure 3.9:** IPCE measurements of **PPV A** and **PPV acid** dye loaded  $TiO_2$  films.

The  $-COOH$  functional group thus plays a very important role in the charge transfer in case of **PPV acid**.

The IPCE peak in the case of **PPV acid** is seen to be broad and centered at around 500 nm, which is red shifted from the optical absorption peak at around 450 nm (**Figure 3.2**). Such red shift has been reported and attributed to aggregation of dye on  $TiO_2$  or influence of double layer at the interface between  $TiO_2$  and the electrolyte.<sup>29,30</sup> Interestingly, for the non-adsorbing **PPV A** dye the



IPCE and optical absorption maxima remained close. This explains the change from a blue shift for **PPV acid** in UV-vis absorption (as in **Figure 3.2** to a red shift in the IPCE as in **Figure 3.9**).

### 3.3.8 Atomic Force Microscopy (AFM) and Scanning Tunneling Microscopy (STM) Studies on Bare TiO<sub>2</sub> and PPV-acid dye Loaded TiO<sub>2</sub> Thin Film:

We also employed atomic force microscopy (AFM) and scanning tunneling microscopy (STM) techniques to further establish and elucidate the nature of binding of the **PPV acid** on the anatase TiO<sub>2</sub> surface. The results presented clearly bring out that inclusion of -COOH functional group does enable the desired anchoring of the dye on the TiO<sub>2</sub> surface.

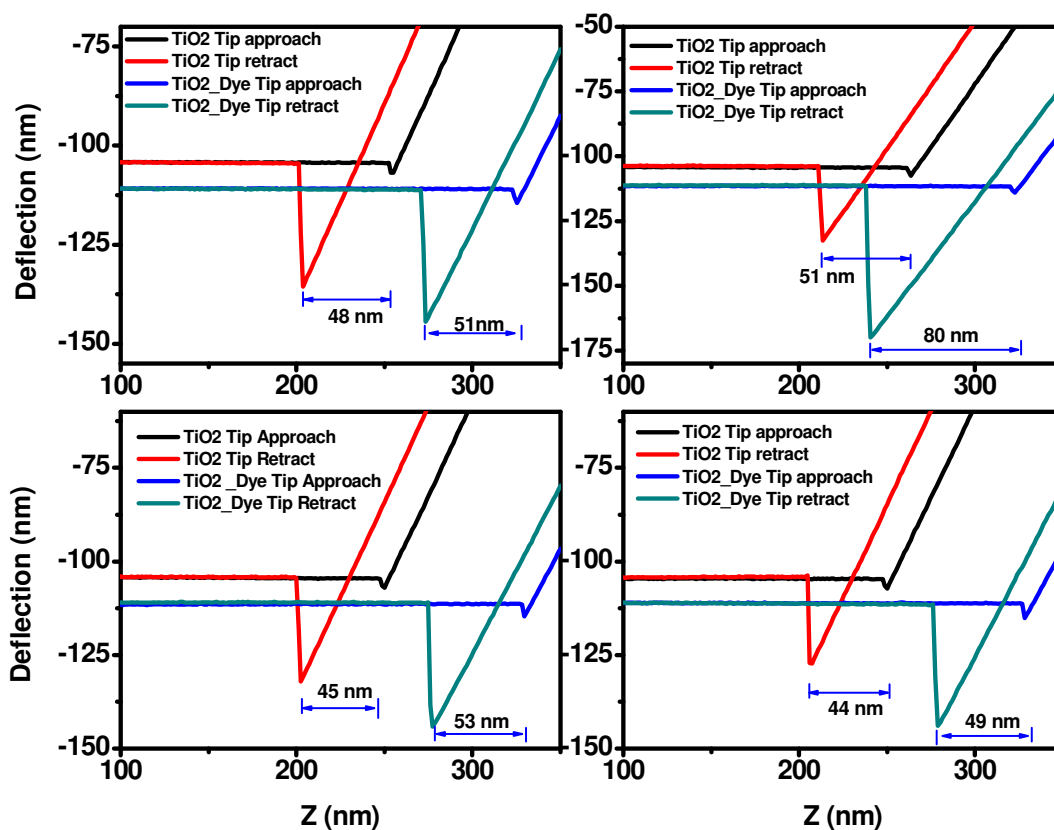


**Figure 3.10:** Force-distance curves taken at four different locations on bare and **PPV acid** dye-loaded TiO<sub>2</sub> surface.

In order to understand and elucidate the nature of adsorption of **PPV-acid** on the TiO<sub>2</sub> surface, 200 nm films of anatase TiO<sub>2</sub> were grown by pulsed laser deposition (PLD) on FTO/glass substrates, and these were studied by Atomic Force Microscopy (AFM) and Scanning Tunneling Microscopy (STM)

techniques without and with adsorbed **PPV-acid** dye molecules. The reason for using PLD films was to ensure reasonable level of surface smoothness to enable proper implementation of the said characterization methods.

In AFM study, the force-distance measurements were performed using a tip with a force constant of about 1 N/m (**Figure 3.10**). In all the force-distance curves recorded at four different points, it is clearly observed that the difference between the sharp dip in the tip approach curve and tip retract curve is not the same for the bare TiO<sub>2</sub> and polymeric dye-loaded TiO<sub>2</sub>. In case of polymeric dye-loaded TiO<sub>2</sub> the required force to detach the tip is higher as compared to bare TiO<sub>2</sub>. This increase in force can be attributed to the elastic stretching of polymeric dye chains adsorbed on to the TiO<sub>2</sub> Surface.<sup>31</sup>

**Figure 3.11** represents the comparison of the STM based I-V (current voltage) curves taken on bare TiO<sub>2</sub> and dye-loaded TiO<sub>2</sub>. These I-V data clearly reveal that the electronic barrier in the case of dye-loaded TiO<sub>2</sub> is higher as compared to bare TiO<sub>2</sub>. The STM topographic images (**Figure 3.12**) also indicate a uniform distribution of dye molecules on the TiO<sub>2</sub> surface, and more importantly, their contribution to electronic transport exhibits more noise, as expected.

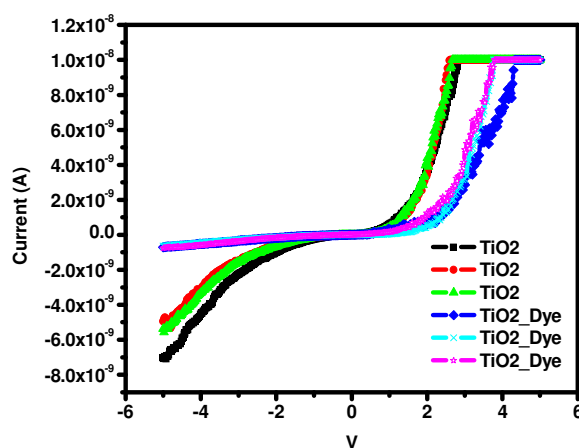


**Figure 3. 11:** STM Spectra taken on bare TiO<sub>2</sub> and **PPV acid** dye loaded TiO<sub>2</sub>.

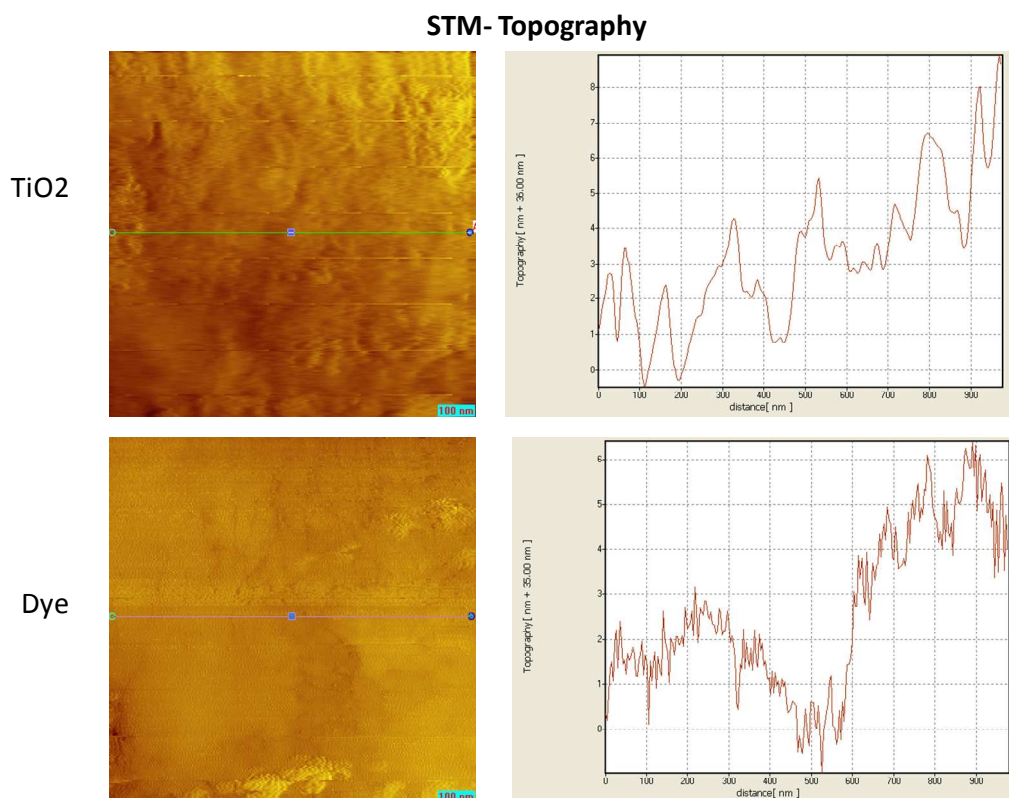


**Figure 3.12:** STM Topography and line scan on bare TiO<sub>2</sub> and **PPV acid** dye loaded TiO<sub>2</sub>

### 3.3.9 Thermogravimetric Analysis of PPV-A and PPV- acid:

Thermogravimetric analysis (TGA) was performed in air for the **PPV A** and the **PPV acid** and thermograms are shown in **Figure 3.13**. Both **PPV A** and **PPV acid** are stable up to ~250 °C.

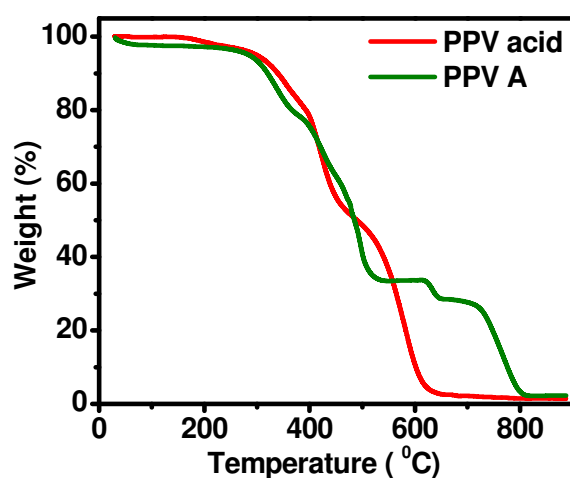


**Figure 3.13:** TG curves of **PPV A** and **PPV acid**.

### 3.3.10 Thermal Stability of the PPV acid Polymeric Dye:

A thermal stability test was conducted on the **PPV acid** based DSSC and the results were compared with the stability of a standard **N719** dye based DSSC. It was found that the solar cell efficiency was stable up to 100 °C for the **PPV acid** dye while that in the case of **N719** it began to degrade above 50 °C (**Figure 3.14**). For the **PPV acid** dye, the efficiency did not drop completely even above 100 °C, but started degrading gradually above 200 °C which is in accordance with the TGA results of the **PPV acid** (**Figure 3.13**).

To investigate thermal stability of DSSC made with the **PPV acid** and traditionally used **N719** dye, heat treatment studies were performed on the sensitized TiO<sub>2</sub> based cells. The solar cells were subjected to heating at different temperatures for 30 min, allowed to cool and then efficiency was measured at room temperature. For Ru-based **N719** dye the power conversion efficiency started decreasing when annealed above 50 °C while in case of **PPV acid** it is stable for heat treatment up to 90 °C. The Ru-based dye showed drop in the efficiency from 5% to less than 0.3% at 200 °C after interval of 30 min at every annealing step from room temperature to 200 °C.

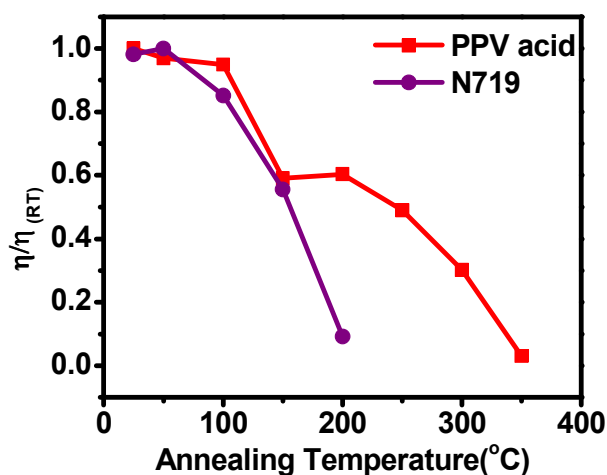


**Figure 3.14:** Solar conversion efficiency with respect to cell processing temperature.

**Table 3.5:** Efficiency of **PPV-acid** and **N719** dye with increasing temperature

No.	Temperature ( °C)	Efficiency (%)	
		PPV-acid	N719
1	RT	3.00	4.9
2	50	2.89	5.0

3	100	2.83	4.3
4	150	1.76	2.8
5	200	1.80	0.5
6	250	1.46	*
7	300	0.90	*
8	350	0.09	*

\* No measurements were performed as the dye underwent degradation.

In the case of **PPV acid**, the conversion efficiency remained stable up to 100 °C and gradually started decreasing from 2.8 % at 100 °C, 1.8% at 200 °C to 0.9% at 300 °C. This showed that, the **PPV acid** is thermally more stable as compared to Ru-based dyes at higher temperature, which was in agreement with the TGA data of the polymer.

### 3.4 Conclusion

In conclusion, we have demonstrated a simple two-step strategy to introduce carboxylic acid groups on a conjugated polymer **BEHP- co-MEH-PPV (PPV A)**. The introduction of carboxyl groups clearly proves to be beneficial for charge injection through proper anchoring to TiO<sub>2</sub> film for its use in DSSCs. Modified polymer **PPV acid** gives considerably high efficiency (3%) as compared with the unmodified counterpart. Such a simple two-step modification may open up new avenues towards potential use of commercially available and thermally stable conjugated polymers for possible use in DSSCs. The DSSC device of polymeric dye was found to be stable up to 90 °C.

## References

1. O'Regan, B.; Grätzel, M. *Nature*, **1991**, 353, 737.
2. Bach, U.; Lupo, D.; Comte, P.; Moser, J. E.; Weissörtel, F.; Salbeck, J.; Spreitzer, H.; Grätzel, M. *Nature*, **1998**, 395, 583.
3. Nazeeruddin, M.; Kay, A.; Rodicio, I.; Humphry-Baker, R.; Muller, E.; Vlachopoulos N.; Grätzel, M. *J. Am. Chem. Soc.*, **1993**, 115, 6382– 6390.
4. Nazeeruddin, M.; Péchy, P.; Renouard, T.; Zakeeruddin, S.; Humphry-Baker, R.; Comte, P.; Liska, P.; Cevey, L.; Costa, E.; Shklover, V.; Spiccia, L.; Deacon, G.; Bignozzi C.; Grätzel, M. *J. Am. Chem. Soc.*, **2001**, 123, 1613.
5. Kyaw, A.; Sun, X.; Zhao, J.; Wang, J.; Zhao, D.; Wei, X.; Liu, X.; Demir H.; Wu, T. *J. Phys. D: Appl. Phys.*, **2011**, 44, 045102.
6. Robertson, N. *Angew. Chem., Int. Ed.*, **2006**, 45, 2338–2345.
7. Marszalek, M.; Nagane, S.; Ichake, A.; Humphry-Baker, R.; Paul, V.; Zakeeruddin, S. M.; Grätzel, M.; *J. Mater. Chem.*, **2012**, 22, 889.
8. Zeng, W.; Cao, Y.; Bai, Y.; Wang, Y.; Shi, Y.; Zhang, M.; Wang, F.; Pan C.; Wang, P. *Chem. Mater.*, **2010**, 22, 1915.
9. Bessho, T.; Zakeeruddin, M.; Yeh, C.; Diau E.; Grätzel, M. *Angew. Chem., Int. Ed.*, **2010**, 49, 6646.
10. Muduli, S.; Game, O.; Dhas, V.; Yengantiwar A.; Ogale, S. *Energy Environ. Sci.*, **2011**, 4, 2835.
11. Yella, A.; Lee, H.; Tsao, H. N.; Yi, C.; Chandiran, A.; Nazeeruddin, M.; Diau, E.; Yeh, C.; Zakeeruddin S.; Grätzel, M. *Science*, **2011**, 334, 629.
12. Zhao, X.; Pinto, M.; Hardison, L.; Mwaura, J.; Muller, J.; Jiang, H.; Witker, D.; Kleiman, V.; Reynolds J.; Schanze, K. *Macromolecules*, **2006**, 39, 6355.
13. Jiang, H.; Zhao, X.; Shelton, A.; Lee, S.; Reynolds J.; Schanze, K. *ACS Appl. Mater. Interfaces*, **2009**, 1, 381.
14. Houarner-Rassin, C.; Blart, E.; Buvatc P.; Odobel, F. *Photochem. Photobiol. Sci.*, **2008**, 7, 789–793.
15. Zang, W.; Cheng, Y.; Yin X.; Liu, B. *Macromol. Chem. Phys.*, **2011**, 212, 15.
16. Kima, M.; Shina, W.; Kimb, W.; Leeb, H.; Parkb, S.; Leeb J.; Jin S. *Mol.*

- Cryst. Liq. Cryst.*, **2007** Vol. 462, pp. 91–99
17. Jiang, H.; Zhao, X.; Shelton, A. H.; Lee, S.; Reynolds J. R.; Schanze, K. S. *ACS Appl. Mater. Interfaces*, **2009**, 1, 381–387.
  18. Kanimozhi, C.; Balraju, P.; Sharma G. D.; Patil, S. *J. Phys. Chem. C*, **2010**, 114, 3287–3291.
  19. Liu, X.; Zhu, R.; Zhang, Y.; Liu B.; Ramakrishna, S. *Chem. Commun.*, **2008**, 3789.
  20. Zhang, W.; Fang, Z.; Su, M.; Saeys M.; Liu, B. *Macromol. Rapid Commun.*, **2009**, 30, 1533–1537.
  21. Fang, Z.; Eshbaugh A. A.; Schanze, K. S. *J. Am. Chem. Soc.*, **2011**, 133, 3063–3069.
  22. Nazeeruddin, M.; Kay, A.; Rodicio, I.; Humphry-Baker, R.; Muller, E.; Liska, P.; Vlachopoulos N.; Grätzel, M. *J. Am. Chem. Soc.*, **1993**, 115, 6382.
  23. Hagfeldt A.; Grätzel, M. *Acc. Chem. Res.*, **2000**, 33, 269.
  24. Zakeeruddin, S.; Nazeeruddin, M.; Humphry-Baker R.; Grätzel, M. *Inorg. Chem.*, **1998**, 37, 5251.
  25. Nazeeruddin, M.; Zakeeruddin, S.; Humphry-Baker, R.; Jirousek, M.; Liska, P.; Vlachopoulos, N.; Shklover, V.; Fischer C.; Grätzel, M. *Inorg. Chem.*, **1999**, 38, 6298.
  26. Kim, Y.; Walker, J.; Samuelson L. A.; Kumar, J. *Nano Lett.*, **2003**, 3, 523.
  27. Thomas, K. R. J.; Kapoor, N.; Lee C. P.; Ho, K. C. *Chem. Asian J.*, **2012**, 7, 738–750.
  28. Mishra, A.; Ma C. Q.; Bäuerle, P. *Chem. Rev.*, **2009**, 109, 1141–1276.
  29. Katono, M.; Bessho, T.; Meng, S.; Humphry-Baker, R.; Rothenberger, G.; Zakeeruddin, S.; Kaxiras E.; Grätzel, M. *Langmuir*, **2011**, 27, 14248–14252.
  30. Hwang, S. Lee, J. H.; Park, C.; Lee, H.; Kim, C.; Park, C.; Lee, M. H.; Lee, W.; Park, J.; Kim, K.; Park N. G.; Kim, C. *Chem. Commun.*, **2007**, 4887–4889.
  31. Kale, S.; Kale, A.; Gholap, H.; Rana, A.; Desai, R.; Banpurkar, A.; Ogale, S.; Shastry, P. *J Nanopart Res*, **2012**, 14, 732.

## Chapter 4

### **High Surface Area Porous Carbon For Ultracapacitor Application by Pyrolysis of Polystyrene Containing Pendent Carboxylic Acid Groups Prepared *via* Click Chemistry**

Strategic designing and synthesis of polystyrene derivative containing pendent carboxylic acid groups was performed *via* click chemistry to achieve micro/meso-porous conducting carbon with high surface area ( $1860 \text{ m}^2 \text{ g}^{-1}$ ) by controlled pyrolysis. The design is done with the objective to get graphene-like framework (by polystyrene backbone), nitrogen doping (by triazole ring) and high porosity (salt of carboxylic acid). Potassium hydroxide was reacted with the carboxylic acid groups of the polymer to achieve uniform *in-situ* molecular activation. The obtained hierarchically porous carbon was characterized and studied for the electric double layer capacitor in organic electrolyte as well as lithium ion hybrid electrochemical capacitor (Li-HEC) performance. A specific capacitance of  $137.8 \text{ F g}^{-1}$  was obtained for the applied current density of  $0.5 \text{ A g}^{-1}$  using tetraethyl ammonium tetrafluoroborate in propylene carbonate as an electrolyte, in the potential range of 0-2.7V. The Li-HEC cell was found to deliver the maximum energy and power densities of  $61 \text{ Wh k g}^{-1}$  and  $10015 \text{ W k g}^{-1}$ , respectively, with  $\sim 70\%$  capacitance retention after 2000 charge-discharge cycles at the current density of  $2 \text{ A g}^{-1}$ .

The contents of this chapter have been published in Materials Today Communications 4 (2015) 166–175.



## 4.1 Introduction

The global energy demands are rising exponentially due to the thrust on rapid development and industrialization, causing fast depletion of non-renewable sources and an alarming increase in the levels of pollution worldwide. This situation has recently led to intensification of efforts on the explorations of clean and green renewable energy resources. There are three key facets of the modern energy technologies namely energy harvesting, storage and conservation. Amongst these perhaps the most challenging and yet uneconomical is the technology for energy storage. This is especially true in so far as the highly desirable large-scale implementation of the new and renewable energy technologies are concerned, and these relate to both the grid based and the distributed power solutions. We need inexpensive, environmental-friendly and non-toxic energy conversion and storage materials to build systems for sustainable growth.<sup>1,2</sup>

Functional carbon materials and their composites with suitably tailored property features form a very important class of materials for the energy storage devices such as supercapacitors and batteries.<sup>3</sup> In fact these materials also find immense applications in other sectors as well, such as water purification, desalination, gas adsorption, CO<sub>2</sub> capture, hydrogen storage, catalysis, oxygen reduction, etc.<sup>4-16</sup> Supercapacitors and batteries offer different domains of strengths in terms of charge/energy storage devices, systems, and applications. Batteries have high energy density but relatively low power density, while supercapacitors can render very high power density but at the cost of relatively low energy density as compared to the battery systems. The two differ quite significantly also in terms of cycling performance and device life. Attempts are currently being made to develop device concepts and designs to address the power and energy density regime in the zone, which falls between the standard domains, afforded by the battery and supercapacitor capabilities. In this entire research effort the key is the design of materials<sup>17</sup>, which form the electrodes of the charge storage devices, where much of the storage action occurs along with carrier transport. Since in this work we are mainly concerned with supercapacitor device, we briefly discuss some recent efforts on making the right kind of carbon material for the corresponding electrodes.

High surface area carbon forms with hierarchical porosity and high electrical conductivity are desired for the supercapacitor application for obvious reasons.<sup>3,4</sup> Such supercapacitor grade carbons have been and are still being synthesized by controlled pyrolysis of different carbon sources such as biomass,<sup>18</sup> natural waste,<sup>19</sup> polymers,<sup>20-21</sup> ionic liquids,<sup>22</sup> metal organic frameworks (MOFs),<sup>23</sup> metal carbides,<sup>24</sup> etc. The porosity is introduced either by activation of the precursor or by using a suitable template. The process of activation (for porosity formation) can be performed either by passing gases like CO<sub>2</sub> and steam during the carbonization process (physical activation) or by adding external activating agents such as KOH or NaOH during carbonization (chemical activation).<sup>25-28</sup> The latter forms compound with carbon at high temperatures, which can later be dissolved, forming the pores. The conductivity depends on the highest processing temperature.

Polymers form an important class of precursors to obtain carbons with several morphologies, conductivity, and surface area/porosity features. Polymers such as polyaniline, polypyrrole, and polyacrylates have been used for the synthesis of porous carbons with high surface area using activation or templates.<sup>26,29</sup> There are only a few reports however on the synthesis of porous carbons by direct pyrolysis of polymer salts<sup>30</sup> without using any external activation. Puthusseri *et al.*<sup>31</sup> and Yadav *et al.*<sup>32</sup> reported the formation of highly porous and good supercapacitor grade carbon by direct pyrolysis of potassium and sodium salts of a polymer, respectively. Gokhale *et al.*<sup>33</sup> have employed pyrolysis of an oligomer for obtaining nitrogen doped 3D porous carbon for the lithium-ion hybrid electrochemical capacitor (Li-HEC) application. Similarly, Puthusseri *et al.* also used hierarchically porous carbon derived from polymer pyrolysis for the Li-HEC application with impressive results.<sup>34</sup>

In most of the works (**Table 4.1**) on the synthesis of high surface area porous functional carbon for charge storage or other applications, the basic choices which control the final product are the precursors, the method and degree of activation, and the thermal processing protocol for pyrolysis. **Table 4.1** summarizes the literature examples of carbon preparation from pyrolysis of polymeric precursors.

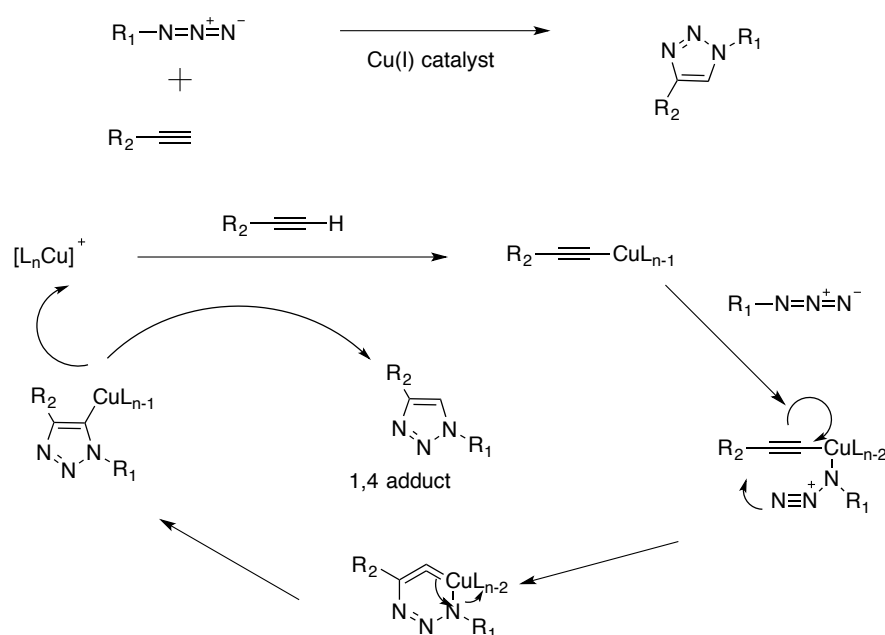
**Table 4.1:** Literature review table for carbon obtained by polymer pyrolysis

Polymer	Surface area (m <sup>2</sup> /g)		Amount of KOH used per gm of precursor	Activating agent	Reference
	without activation	With activation			
Poly (acrylonitrile co-n-butyl acrylate )	500	2570	1	KOH	47
Poly (4-sodium styrene sulfonate-co-maleic acid) sodium salt	1720	-	-	-	32
Poly(acrylic acid-co-maleic acid) sodium salt	188	-	-	-	48
Poly( o - phenylenediamine)	-	591	-	FeCl <sub>3</sub> .6H <sub>2</sub> O	20
Sulfonated Poly(styrene-co-methacrylic acid) (SPS-COOH) Sphere	508	-	-	-	49
Polypyrrole	-	2870	5	KOH	25
Poly(acrylamide-co-acrylic acid) potassium salt	1327	2366	1	KOH	31

It is clear that designing a precursor with a set of property goals in mind may be a more effective approach than choosing the available biomass precursors or polymers and controlling the pyrolysis protocols. Indeed through proper precursor design one could aim at achieving a certain pore size distribution, doping and conductivity in the final carbon product.

The present work is a modest attempt along this line. Herein, we used carboxyl-modified polystyrene derivative synthesized using alkyne-azide click reaction for obtaining functional carbon by controlled pyrolysis. Click chemistry has great importance and wide scope in the field of organic chemistry and for the chemical modification of polymers. "Click Chemistry" is a term that was introduced by K. B. Sharpless<sup>35</sup> in 2001 to illustrate the reactions, which

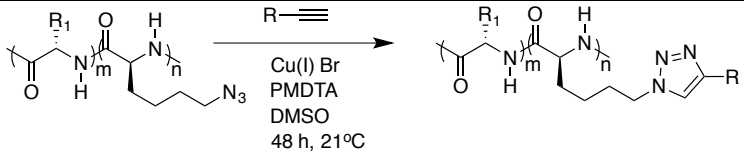
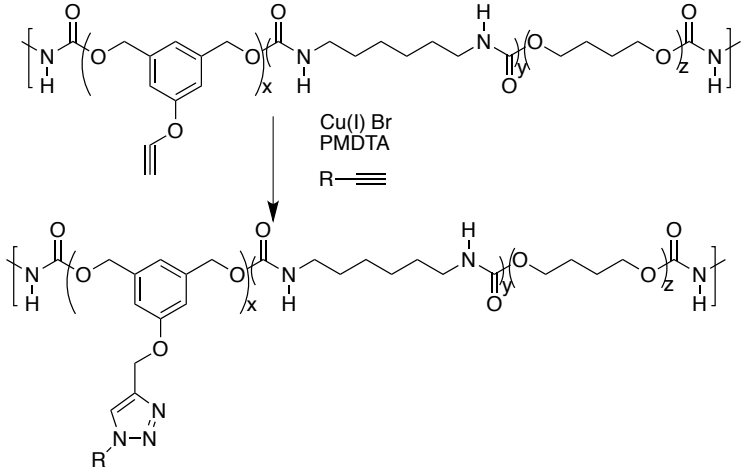
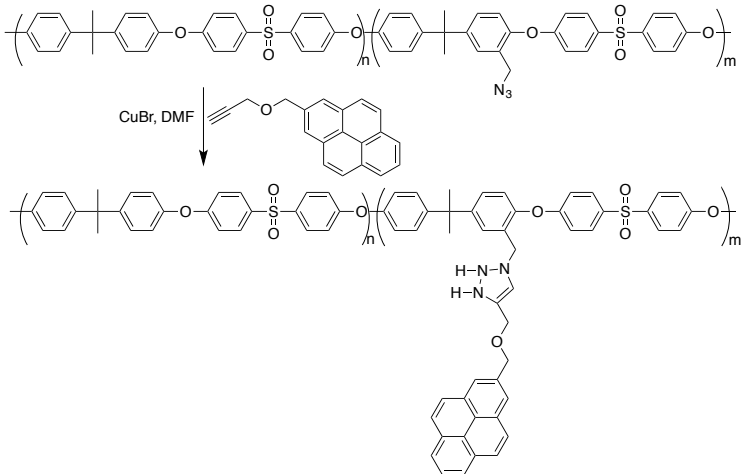
generate materials rapidly and reliably by joining two or more small units together. The click reactions are high yielding without creating byproducts or generating byproducts that can be easily removed without using column chromatography. The click reactions are stereospecific, easy to perform using easily available starting materials under simple reaction conditions, can be implemented in easily removable solvents or even without solvents, and are known for high atom economy<sup>39,40</sup> **Figure 4.1** represents general mechanism of Cu (I) catalyzed azide-alkyne click reaction.



**Figure 4.1:** Representation and mechanism of click reaction.

Click Chemistry has also been employed for post-polymerization modification of the polymers. This provides immense scope to modify polymers in various ways, which is otherwise difficult. The introduction of various functional groups is feasible due to click chemistry. The post polymerization modification approach has advantages like 1) desired molecular weight has already achieved, 2) the functionality, which affects polymerization phenomenon; that can also be, introduced using post-polymerization click reaction. **Table 4.2** shows representative examples for the post-polymerization modification by click chemistry.

**Table 4.2:** Representative examples for post polymerization modification by click chemistry.

No	Polymer Structure	Reference
1.		36
2.		37
3.		38

The click product containing pendant carboxylic acid group formed in our case was then reacted with equimolar amount of KOH to serve as an *in situ* molecular activating agent. The polymer formed was then subjected to pyrolysis in the continuous flow of argon at elevated temperature to get porous conducting carbon with high surface area after appropriate washing. The polymer-derived carbon (**P3KC**) was tested for the electric double layer capacitor (EDLC) type

supercapacitor as well as for the next generation electrochemical Li-HEC. For both these cases, polymer-derived carbon exhibited promising results.

## 4.2 Experimental Section

### Materials:

4-Chloromethyl styrene was procured from M/s Sigma Aldrich and distilled before use to get rid of radical stabilizers present in it. N,N-Dimethylformamide (DMF) and toluene were dried over calcium hydride followed by distillation under reduced pressure. 2, 2'-Azobis (isobutyronitrile) (AIBN) was purchased from M/s Sigma Aldrich and recrystallized from methanol before use.

### 4.2.1 Synthesis of Polymer Precursor

#### 4.2.1.1 Synthesis of Polymer P1: Polymerization of 4-chloromethyl styrene

A typical radical polymerization was performed in the inert atmosphere. In a clean, dry Schlenk tube were added 4-chloromethyl styrene (10 g 0.065 mol) and dry toluene (6 mL) under argon atmosphere. The system was degassed and purged with argon thrice before the addition of AIBN (3.2 mg). After the addition of initiator the reaction mixture was allowed to stir at 90 °C for 3 days. The reaction mixture gradually became viscous. The viscous solution was then precipitated into ice-cold methanol to get poly (4-chloromethylstyrene) (**P1**). The polymer was washed several times with methanol and dried under vacuum. The yield was 9 g (90%). The polymer was characterized by using NMR spectroscopy.

#### 4.2.1.2 Synthesis of polymer P2: Conversion of chloro (-Cl) to azido (-N<sub>3</sub>)

Into a 100 ml two-necked round bottom flask equipped with a rubber septum, was added polymer **P1** (6 g, 0.039 mol) under argon atmosphere. Dry DMF (50 mL) was added to the reaction mixture under argon and **P1** was dissolved by stirring at room temperature for 15 min. Sodium azide (5.11 g, 0.078 mol) was then added to the reaction mixture after clear solution was formed. The reaction mixture was kept stirring at room temperature for 12 h under argon. The pendant azido group containing polystyrene (**P2**) was precipitated into a mixture of cold methanol and water (1:1) (v/v). The precipitate was washed several times with

methanol and dried. The corresponding yield was 5 g (80%). NMR spectrum of polymer **P2** was recorded.

#### ***4.2.1.3 Synthesis of Polymer P3: Azide-alkyne Click Reaction***

Into a 100 mL three-necked round bottom flask equipped with a rubber septum, a magnetic stirring bar, a two-way stopcock and a reflux condenser was added **P2** (2 g, 0.012 mol). Dry DMF (20 mL), N-N di-isopropylethylamine (0.605 g, 0.005 mol) and propiolic acid (1.32 g, 0.0188 mol) were added by syringe into the reaction flask. The reaction mixture was then degassed using 3 successive cycles of freeze-pump-thaw. Copper [I] iodide (0.095 g, 0.5 mmol) was then added to it under argon atmosphere. The reaction mixture was stirred at 70 °C for 24 h. The carboxylic acid functionalized triazole ring-containing polymer (**P3**) was precipitated in cold methanol, washed with methanol and dried under vacuum. The corresponding yield was 2.5 g (89%). The polymer **P3** was characterized by NMR spectroscopy.

#### ***4.2.1.4 Synthesis of P3K: Preparation of Potassium Salt of Carboxylic Acid***

Into a 50 mL single-necked round bottom flask equipped with a magnetic stirring bar and a reflux condenser were added together **P3** (2.7 g, 0.0117 mol), KOH (0.66 g, 0.0117 mol) and distilled water (20 mL). The mixture was stirred at 90 °C for 10 h. The reaction mixture was subjected to drying at 100 °C. The dried polymer salt **P3K** was then used as the precursor for the carbon synthesis. The corresponding yield was 2.6 g (82%).

#### **4.2.2 Synthesis of Porous Carbon (P3KC): Carbon Obtained by Pyrolysis of P3K**

Polymer precursor **P3K** was subjected to pyrolysis at 800 °C for 3 h under continuous flow of argon with the temperature ramp of 10 °C per minute during heating. During cooling the temperature ramp was set at 10 °C per minute till 600 °C and thereafter cooling was done naturally. The obtained carbon was washed with dilute hydrochloric acid by sonication to remove the inorganic impurities from the obtained carbon. The product was washed several times with DI water and filtered through PTFE membrane filter (0.22 µm) under vacuum

followed by DI water washing. The carbon obtained was dried in an oven at 100 °C for 12 h and used for further characterization and measurements.

For comparison purpose, **P1** (poly(4-chloromethyl styrene)) and **P3** (carboxylic acid containing polymer without KOH) were also carbonized to obtain **P1C** and **P3C** samples, respectively, and these were analyzed for different properties.

#### 4.2.3 Structural Characterization

Nuclear magnetic resonance (NMR) spectra were recorded on a Bruker 500 MHz spectrometer at a resonance frequency of 500 MHz for  $^1\text{H}$  using chloroform-*d* (Sigma Aldrich) or methanol-*d*<sub>4</sub> (Sigma Aldrich) as a solvent. A Nicolet Magna IR 750 spectrophotometer was used to perform FTIR in the transmission mode. Gel permeation chromatography (GPC) was performed using Thermo Separation Products equipped with UV 100 and RI 150 detectors (Spectral Series) and chloroform as an eluent at a flow rate of 1 mL min<sup>-1</sup> at 25 °C for the determination of molecular weights and the molecular weight distribution. The concentration of sample used was 2 mg mL<sup>-1</sup> and calibration standards used were polystyrenes with a narrow molecular weight distribution. Thermogravimetric analysis (TGA) was recorded using TGA-7 Perkin Elmer instrument. Powder X-ray diffraction (XRD) of **P3KC** was performed using PAN Analytical powder X-ray diffractometer with nickel-filtered CuK<sub>α</sub> radiation. The bonding structure of the product was further discerned by Raman spectroscopy (LabRAM HR800 from JY Horiba). The structural and morphological characterizations were performed by field emission scanning electron microscope (FESEM) with FEI Nova nanoSEM 450 and transmission electron microscope (HRTEM) using FEI, Tecnai F30, FEG with 300kV. The surface elemental composition was determined by X-ray photoelectron spectroscopy (XPS). XPS was performed using a PHI 5000 Versa Probe II equipped with a monochromatic Al Ka (1486.6 eV) X-ray source and a hemispherical analyzer. The porous structure of the sample was confirmed by N<sub>2</sub> adsorption-desorption isotherm at 77K (Quadrasorb automatic volumetric instrument).



#### 4.2.4 Electrochemical Testing

##### 4.2.4.1 Electrode Preparation for EDLC

(a) For the measurements in aqueous system: 1M H<sub>2</sub>SO<sub>4</sub> was used as the electrolyte and symmetric cell was prepared using two electrodes. A slurry was made of 80 wt.% of polymer derived carbon material (**P3KC**), 15 wt.% of carbon black, and 5 wt.% of binder (Kynar: PVDF) in N-methyl-2-pyrrolidone (NMP). The electrodes were prepared on the torey paper by coating the slurry on it with active mass loading of 1 mg and the specific capacitance was calculated as follows:

$$C_{sp} = \frac{2I}{m \frac{dV}{dt}}$$

Where, ' $C_{sp}$ ' is the specific capacitance in the three electrode system based on active material loading, ' $I$ ' is the constant discharging current, ' $dV/dt$ ' is the discharge slope and ' $m$ ' is the total loading of active material on a single electrode.

(b) For the measurements in organic system: A slurry was made of 80 wt.% of polymer derived carbon material (**P3KC**), 15 wt.% of carbon black, and 5 wt.% of binder (Kynar: PVDF) in N-methyl-2-pyrrolidone (NMP) and was coated on a carbon coated Al foil (15 micron). The carbon coated Al foil coated with **P3KC** was dried in an oven at 100 °C overnight. The loading of carbon material was 0.25 mg cm<sup>-2</sup>. A coin cell was fabricated using the symmetric electrodes of carbon and 1 M tetraethyl ammonium tetrafluoroborate in propylene carbonate (TEABF<sub>4</sub> in PC) as organic electrolyte in the potential range of 0-2.7 V. Cyclic voltammetry (CV) and galvanostatic charging-discharging measurements were done using Autolab Potentiostat with Nova 1.7.

##### 4.2.4.2 Electrode Preparation for Li-HEC

The electrochemical studies of the test electrodes were formulated by keeping 77% active materials (**P3KC** or Li<sub>4</sub>Ti<sub>5</sub>O<sub>12</sub>), 11.5% conductive additive (Super P (Hohsen, Japan) and 11.5% binder (teflonized acetylene black, TAB-2 (Hohsen, Japan)) ratio for both single electrode (half-cell) studies and Li-HEC assembly as well. Ethanol was used as the solvent for the preparation of electrode in agate

mortar. The mixture was pressed over stainless steel mesh (area: 200 mm<sup>2</sup> and thickness: 0.25 mm) using hydraulic press (Specac, UK) and dried overnight at 65 °C before being employed in cell assembly. Both half-cell and Li-HEC were fabricated with CR 2016 coin-cell configuration. In the half-cell studies, metallic Li was used as the reference and counter electrode separated by microporous separator (Whatman, Cat. No. 1825 047, UK). 1 M LiPF<sub>6</sub> in ethylene carbonate (EC)/di-methyl carbonate (DMC) mixture (Selectipure LP30, Merck KGaA, Germany) was used as an electrolyte. For the case of Li-HEC assembly, **P3KC** and Li<sub>4</sub>Ti<sub>5</sub>O<sub>12</sub> were used as positive and negative electrodes under the optimized loading conditions. Galvanostatic charge-discharge studies were performed using an Arbin 2000 battery tester. For comparison purpose, commercial activated carbon (BET surface area 817(±20) m<sup>2</sup>g<sup>-1</sup>, From Norit, Netherlands) was also measured under the same conditions.

### 4.3 Results and Discussion

The structural design and the 3D representation of the synthesized polymer precursor are shown in **Figure 4.2**. The design of this polymer has a specific strategy, as indicated. The choice of polystyrene backbone is made because of the intention of ending with graphitic kind of carbon. The triazole ring was aimed for realizing nitrogen doping.

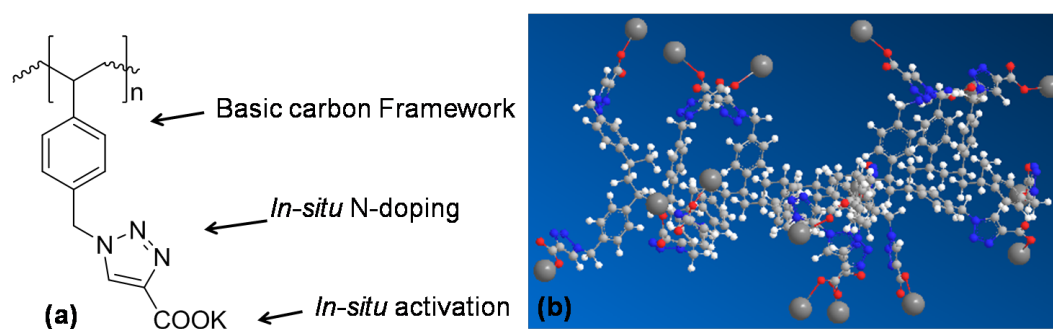
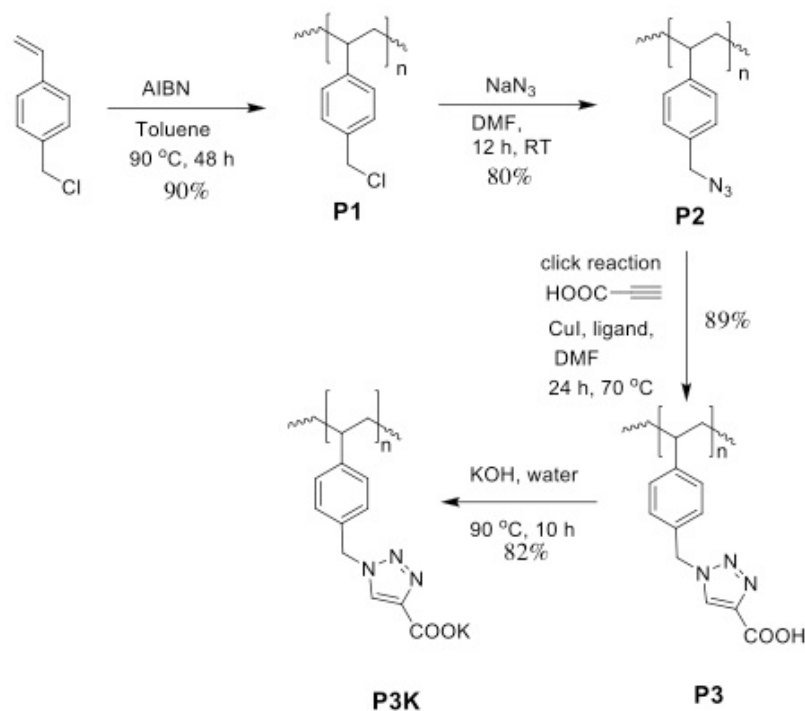


**Figure 4.2:** (a) Illustration of the strategic design of the precursor structure, (b) molecular representation of **P3K** in 3D (Element ID: grey small ball C, grey big ball K, white ball H, blue ball N and red ball O.)



**Scheme 4.1:** Synthesis of polystyrene derivative-a polymeric precursor (**P3K**) for porous carbon.

The carboxylic acid pendant groups are introduced for their conversion to corresponding potassium salt to achieve high degree of pore formation after carbonization and washing.

#### 4.3.1 Synthesis of Polymer Precursor **P3K**

**Scheme 4.1** depicts the synthesis of polymer precursor **P3K**. The polymer **P1** was synthesized by free radical polymerization of 4-chloromethyl styrene using AIBN as the initiator. The number average molecular weight ( $M_n$ ) of  $1.7 \times 10^4$  was obtained. The post polymer functionalization was accomplished to get pendant azido-group containing polymer **P2** using sodium azide. **P2** was then imperiled to click reaction with propiolic acid in order to get the pendant carboxyl functional groups through the formation of triazole ring. The azide-alkyne click reaction is a straightforward and efficient methodology for chemical modification of polymers.<sup>39,40</sup> The carboxyl-functionalized polymer **P3** was then converted to its potassium salt (**P3K**) by using  $\text{KOH}$  in equimolar ratio to the polymer precursor. In this process the carboxylic acid-salt groups are placed as pendant groups to polystyrene chain and these moieties are responsible for pore

formation by forming the salt of carboxylic acid groups. The KOH distribution over the carbon precursor is thus uniform, leading to a narrow pore size distribution and increasing the surface area of the carbon matrix as brought out later. The sample **P3K** was subjected to carbonization at 800 °C under continuous flow of argon. The potassium salt of carboxylic acid in the polymer acts as *in situ* porogen. At higher temperature, potassium reacts with carbon and oxygen from the material and gets converted into  $K_2CO_3$  during the carbonization process, which creates pores after acid washing.<sup>31,32,41</sup> Thus, the porous carbon (**P3KC**) was obtained after acid and water washing.

#### 4.3.2 FTIR Spectra of Polymers P1, P2, and P3

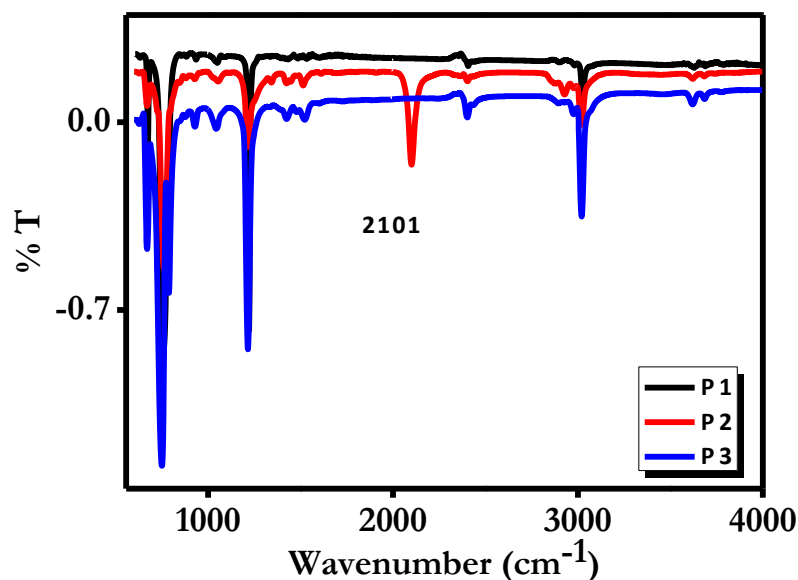


**Figure 4.3:** FTIR spectra of polymers **P1**, **P2** and **P3**

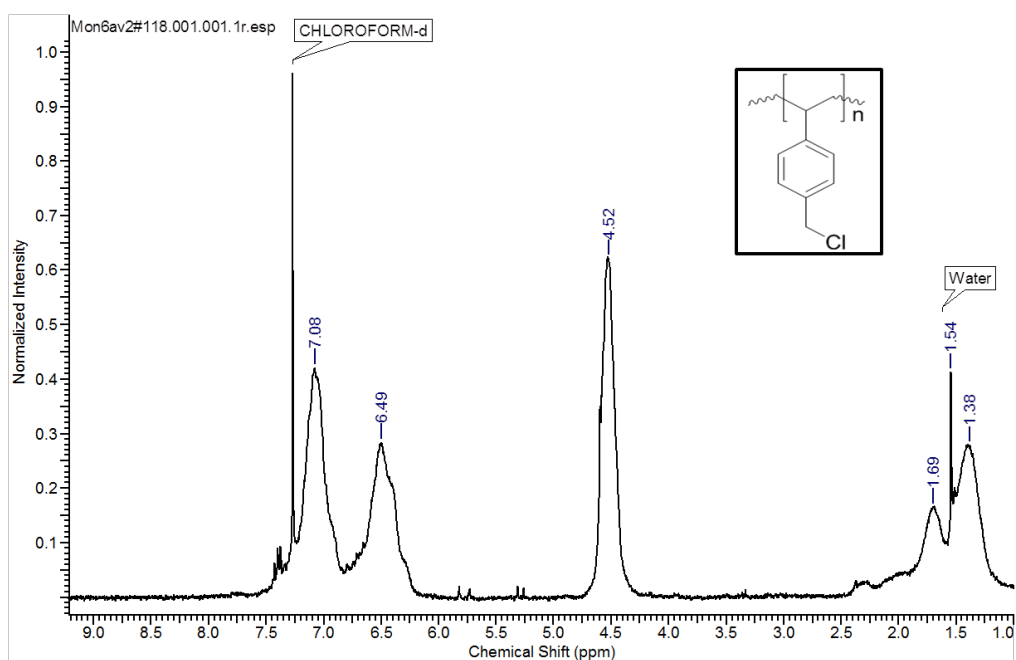
The FTIR spectra for **P1**, **P2** and **P3** are shown in **Figure 4.3**. The characteristic peak of azido for **P2** appeared at  $2101\text{ cm}^{-1}$ . After the click reaction, the peak of azido disappeared indicating completion of reaction.

#### 4.3.3 NMR Spectra of Polymers P1, P2 and P3

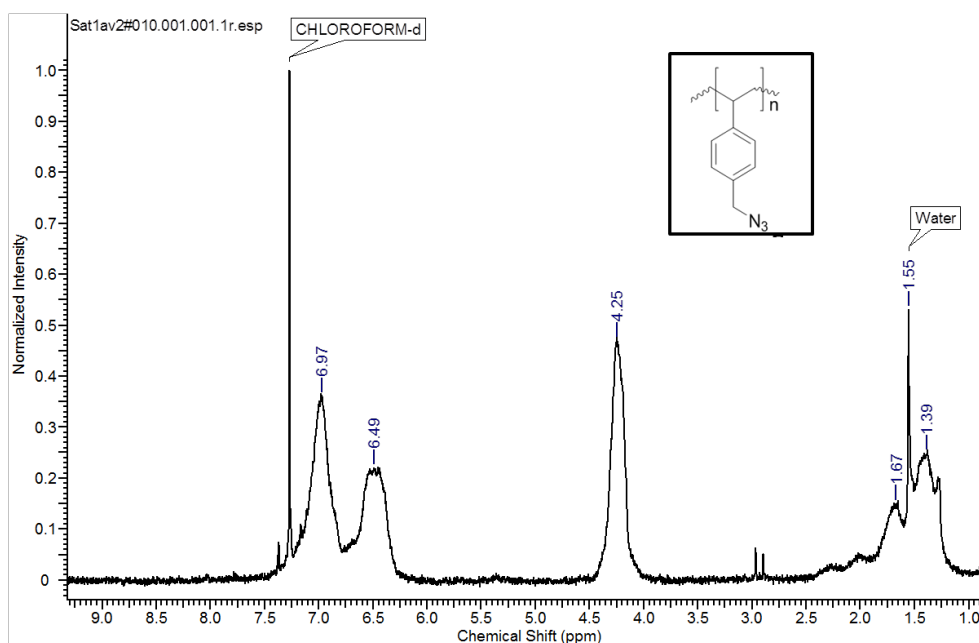
**Figure 4.4 (a)** shows  $^1\text{H}$  spectrum of **P1** [poly(4-chloromethylstyrene)]. Two different types of aromatic protons appeared at 7.08 and 7.49  $\delta$  ppm as a singlet. The benzylic  $-\text{CH}_2$  appeared at 4.52  $\delta$  ppm as a singlet. The peaks 1.38-1.69  $\delta$

ppm corresponds to aliphatic region of the polymer. NMR spectrum of **P2** [Poly(4-azidomethylstyrene)] is shown in **Figure 4.4 (b)**. The peak at 4.25  $\delta$  ppm represents benzylic  $-\text{CH}_2$ . This peak is shifted from 4.52  $\delta$  ppm, when conversion of  $-\text{Cl}$  to  $-\text{N}_3$  was performed.

(a)  $^1\text{H}$  NMR spectrum of **P1** [Poly(4-chloromethylstyrene)]



(b)  $^1\text{H}$  NMR spectrum of **P2** [Poly(4-azidomethylstyrene)]



(c)  $^1\text{H}$  NMR spectrum of **P3** [carboxylic acid functionalized triazole ring-containing polystyrene]

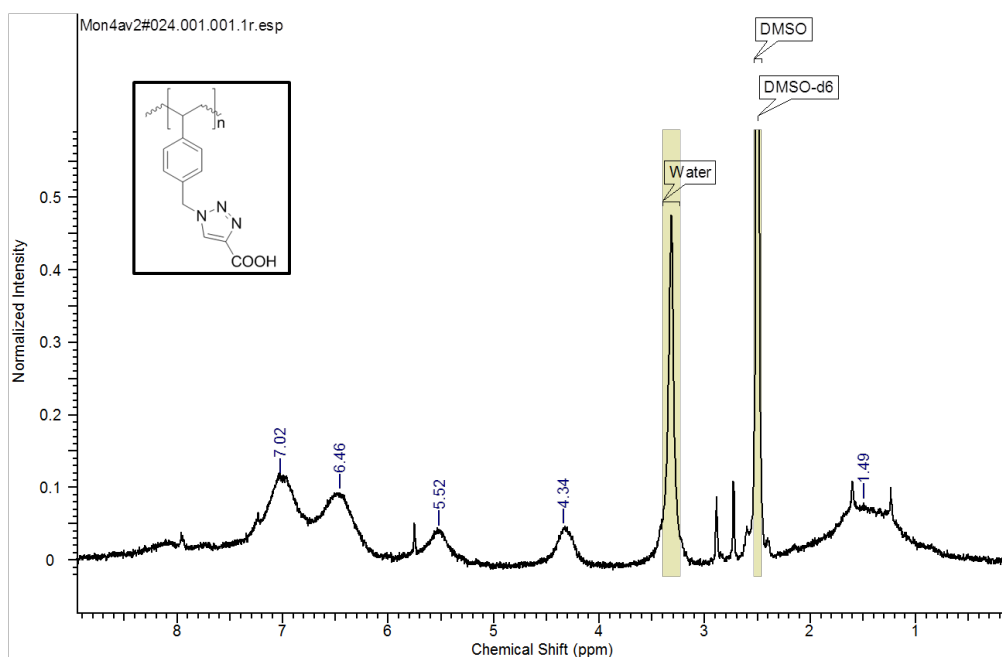


**Figure 4.4:** (a)  $^1\text{H}$  NMR of **P1** [poly(4-chloromethylstyrene)] , (b) NMR of **P2** [poly(4-azidomethylstyrene)] and (c) NMR of **P3** [carboxylic acid functionalized triazole ring-containing polystyrene]

#### 4.3.4 XRD and Raman

**Figure 4.5** shows XRD pattern of **P3KC**. The  $2\theta$  values at  $23.3^\circ$  (the characteristic peak of graphite is at  $26^\circ$ )<sup>42</sup> and  $43.3^\circ$  obtained from XRD confirm the expected incomplete graphitization (turbostratic carbon<sup>42</sup>) of the carbon formed. This is due to the pyrolysis at a relatively low temperature of  $800^\circ\text{C}$ . The broadening and lower intensity indicates formation of thin carbon sheet like structures.<sup>43</sup> The large intensity peak at the low diffraction angle of  $23.3^\circ$  is due to high pore density in the carbon structure.<sup>43</sup>

The Raman spectrum of **P3KC** is shown in **Figure 4.5**. It is clear that the carbon formed by pyrolysis of polymer is disordered. The peaks at around  $1315\text{ cm}^{-1}$  and  $1587\text{ cm}^{-1}$  signify D and G bands, respectively. The G band is attributed to the  $E_{2g}$  phonon vibrations of  $\text{sp}^2$  carbon atoms and the D band (which is absent in the Raman spectrum of pure graphite) indicates the presence of defects in the

carbon formed. The nature of impurities, functionalization and different types/states of disorder in the system are collectively reflected in the Raman spectrum, as the position, intensity and the broadening of D band with respect to G band changes accordingly.

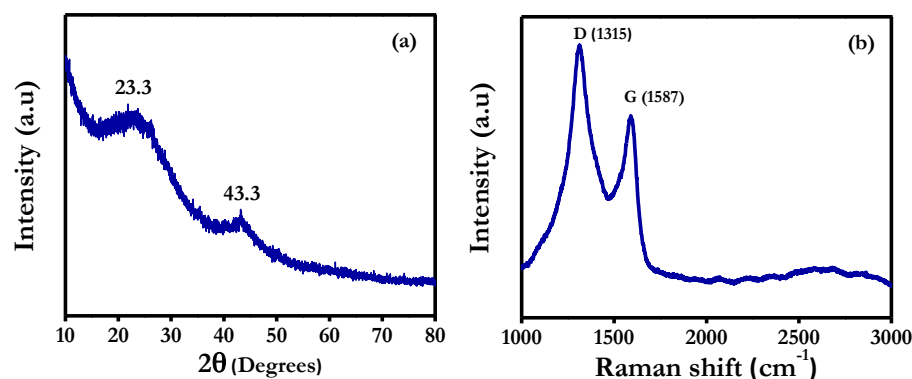


Figure 4.5: (a) Powder XRD pattern of P3KC, (b) Raman spectrum of P3KC

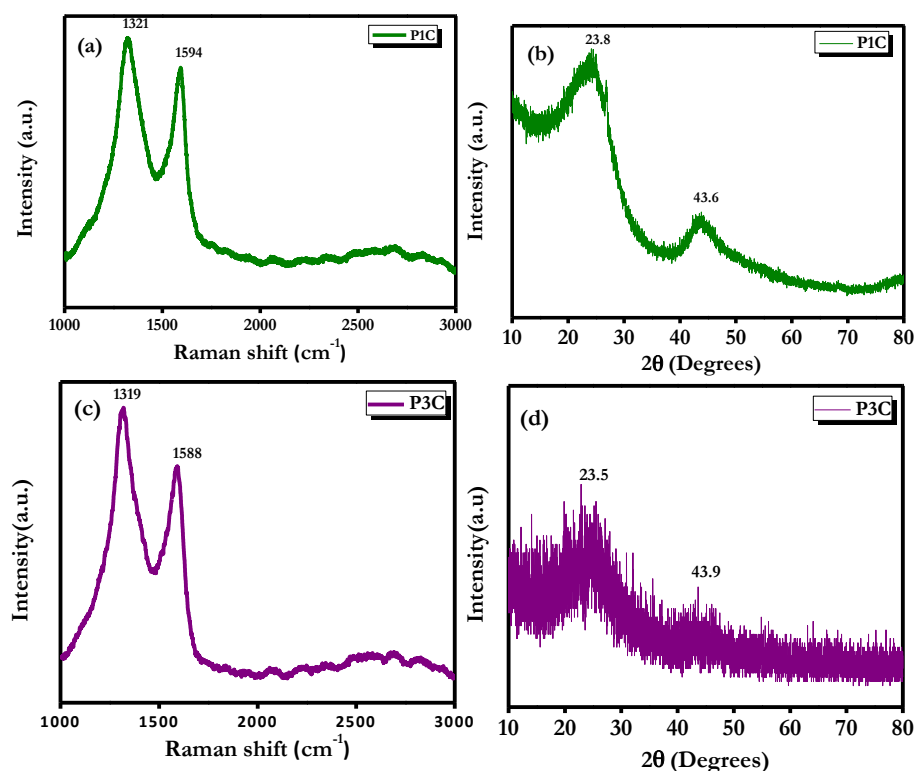


Figure 4.6: Raman Spectra of (a) P1C and (c) P3C, Powder X-ray diffraction pattern of (b) P1C and (d) P3C

For **P1C** and **P3C** as well, the XRD and Raman was performed and shown in the **Figure 4.6**. **P1C** and **P3C** both show the characteristic peaks of amorphous carbon and incomplete graphitization in XRD and Raman spectra.

**Table 4.3:**  $I_D/I_G$  ratio in case of **P1C** and **P3C**

Sample	$I_D$	$I_G$	$I_D/I_G$
<b>P1C</b>	2069	1871	1.10
<b>P3C</b>	986	816	1.20

The ratio of intensities of D band to G band ( $I_D/I_G$ ) gives the expanse of disorder in the system. The  $I_D/I_G$  values in all the different cases of carbon under study were found to be 1.10, 1.20 and 1.33 for **P1C** (carbon obtained from poly (4-chloromethyl styrene)), **P3C** (carbon obtained from carboxylic acid containing polymer without KOH) and **P3KC**, respectively, which are all greater than 1; indicating that the carbon formed is structurally disordered due to the low carbonization temperature of 800 °C. The **P1C** is less disordered and relatively more graphitic than **P3KC**, as there was no carboxyl group functionalization as well as no activating agent present in **P1**.

#### 4.3.5 FESEM and TEM

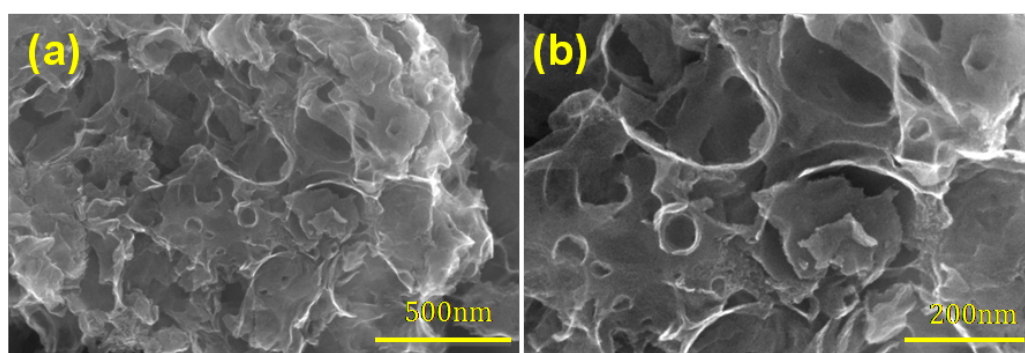


**Figure 4.7:** (a) and (b) FESEM images of **P3KCat** at different scales

The FESEM images (**Figure 4.7 (a) and (b)**) also confirm the nature of porous structures of **P3KC**. The surface undulations with macropores are clearly seen.



The SEM data are in accordance with the HRTEM data and the BET pore size distribution discussed next.

The HRTEM images are shown in **Figure 4.8**. Porous carbon thin sheet-like structures are clearly seen in **Figure 4.8 (a)**. The carbon sheets are seen with folds at the edges (**Figure 4.8 (a), (b)**). The porosity appears to be cellular as reflected in **Figure 4.8 (b)**.

The lattice fringes (**Figure 4.8 (c) and (d)**) are seen with some degree of disorder due to incomplete graphitization in **Figure 4.8 (c)**. The lattice parameter obtained from HRTEM is 3.6 Å, which is typically a characteristic value for graphitic carbon.

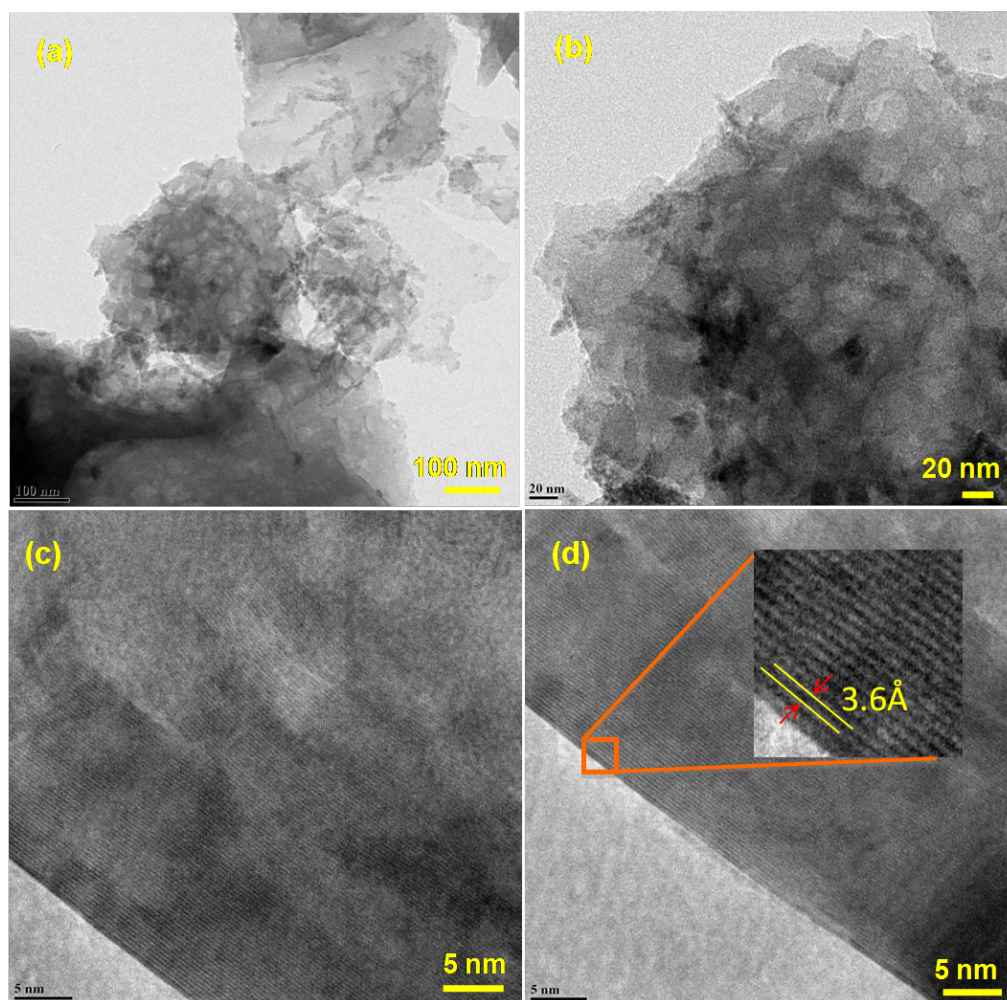


**Figure 4.8:** (a), (b) and (c): HRTEM images of P3KC at different scales, (d) lattice fringes pattern obtained for P3KC

### 4.3.6 XPS of P3KC

XPS of **P3KC** (**Figure 4.9**) confirmed the presence of carbon, nitrogen and oxygen. The spectrum corresponding to each element was deconvoluted to obtain the percentages of carbon (91.8%), oxygen (6%) and nitrogen (2.2%) in the sample (**P3KC**). **Figure 4.9 (a)** corresponds to the C1s spectrum fitted to 3 peaks. The higher intensity peak (284.7 eV) corresponds to the  $sp^2$  graphitic carbon (C=C). The peaks at 285.9 eV and 287.7 eV indicate presence of C-O and C=O, respectively. The O1s spectrum (**Figure 4.9 (b)**) shows a peak at 532.51 eV, which can be attributed to C-O. Adequate amount of oxygen (6%) in the material improves wettability of the electrode, which helps in the formation of the double layer.

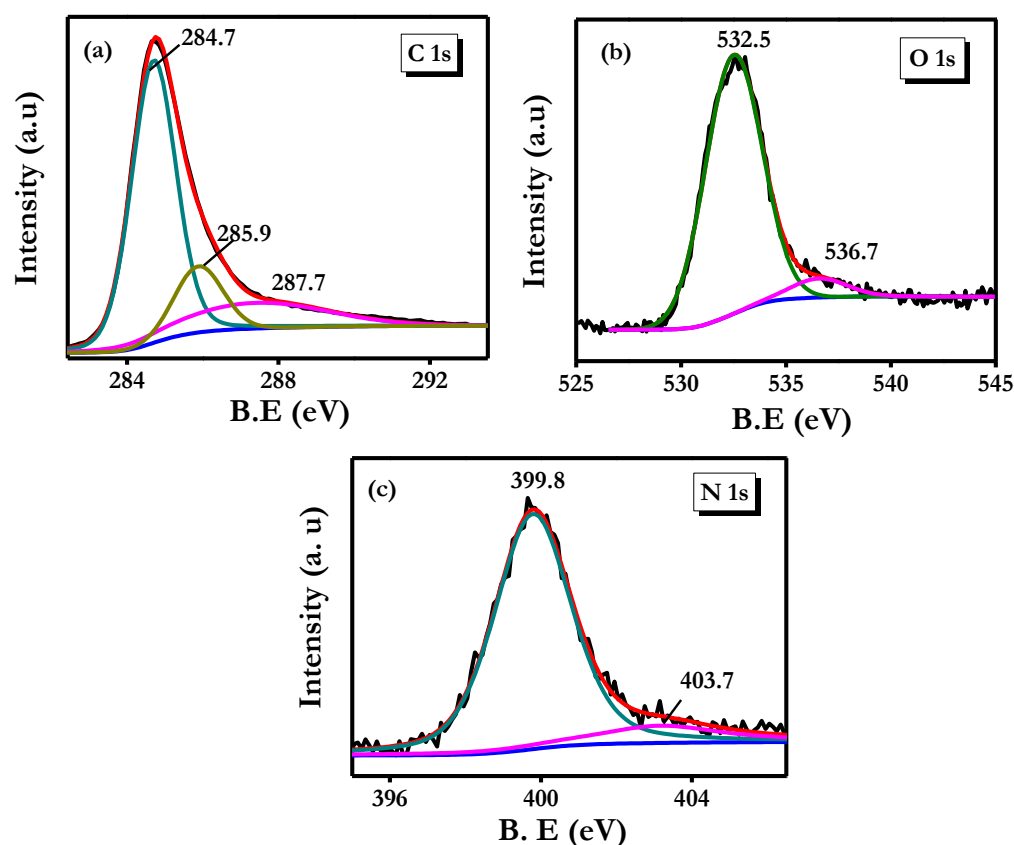


**Figure 4.9:** XPS of **P3KC**: (a) C1s, (b) O 1s, (c) N1s.

The nitrogen incorporation is also confirmed by N1s spectrum (**Figure 4.9 (c)**). The peak at 399.8 eV is attributed to pyrrolic type of nitrogen and the one at 403.3 eV is attributed to oxidized nitrogen. The pyrrolic and pyridinic nitrogen species facilitate the enhancement in electrochemical performance because the

electron lone pair of nitrogen is in conjugation with the graphitic network and enhances conductivity.<sup>44,45</sup>

Measuring resistivity of a porous material is not an easy task. Therefore, we adopted a simple way to obtain a comparison between two forms of carbon by making an arrangement for 2-probe measurement of the powder under static pressed condition as reported earlier.<sup>19</sup> The resistance of the **P3KC** pellet of diameter 4 mm and thickness of 0.5 mm formed under static pressure of 50 kg/cm<sup>2</sup> was 0.685  $\Omega$ , which was almost half the value of 1.33  $\Omega$  obtained for commercial activated Kuraray carbon.

#### 4.3.7 Surface Area Analysis

The BET surface area measurements were performed to get the nature and types of pores formed. The isotherm obtained by N<sub>2</sub> gas adsorption-desorption is shown in **Figure 4.10 (b)**. N<sub>2</sub> adsorption experiments revealed the surface area of 1860 m<sup>2</sup> g<sup>-1</sup> for the case of **P3KC**, which signifies that **P3KC** is a good material for the electrodes in electrical double layer capacitors. For comparison, these data were also recorded for **P1C** and **P3C** samples (**Table 4.4**). As may be noted, these samples have lesser surface area as compared to **P3KC**.

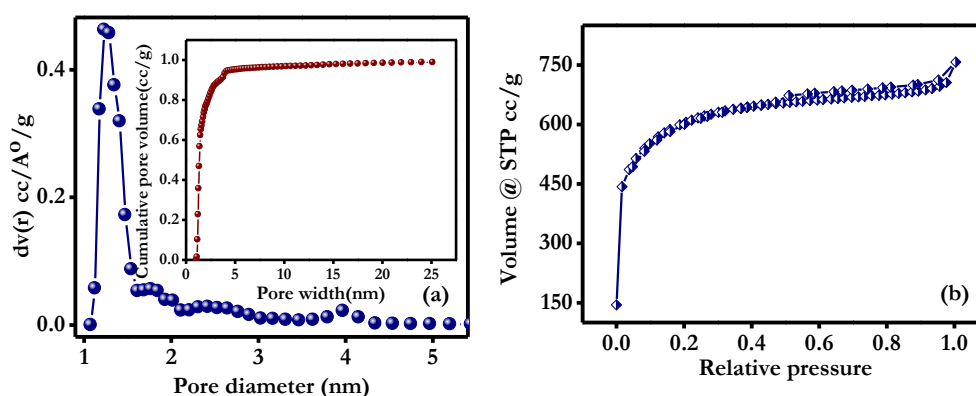


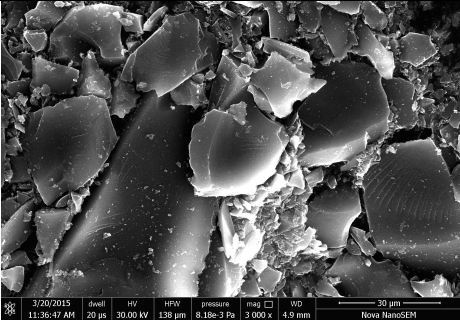
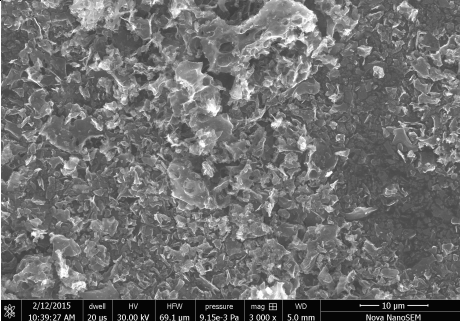
**Figure 4.10:** (a): Pore size distribution of **P3KC** acquired from DFT calculations, (inset- cumulative pore volume) (b) N<sub>2</sub> adsorption-desorption isotherm for **P3KC**.

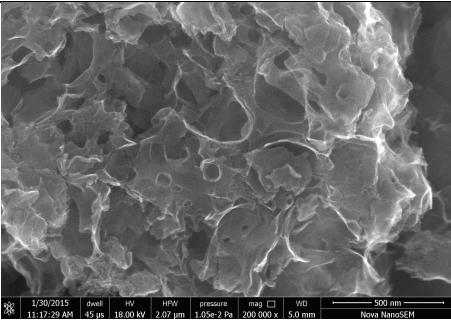
Pore size distribution for **P3KC** is shown in **Figure 4.10 (a)**, which was obtained from the N<sub>2</sub> adsorption-desorption measurements by DFT method.<sup>46</sup> It reveals a narrow distribution of pore sizes in the region of 1.0-1.4 nm, which

shows that large number of micropores are present in **P3KC**. Additionally, pores in the size range of 1.5-4.5 nm (mesopores) are also seen. The advantage of the narrow pore size distribution over the broad distribution is that it gives uniform accessible pores for the electrolyte. Also it is important to note that the supercapacitors perform well when the size of the pores is in the range of the size of solvated ions of the electrolyte or more precisely twice the size of solvated electrolyte ions.<sup>32</sup>

The results of surface area for **P1C** and **P3C** along with **P3KC** are summarized in **Table 4.4**.

**Table 4.4:** Comparison of **P1C**, **P3C** and **P3KC** morphology and surface area

No.	Sample	SEM image	BET surface area (m <sup>2</sup> /g)
1	<b>P1C</b>		10.97
2	<b>P3C</b>		39.67

3	<b>P3KC</b>		1867
---	-------------	--	------

To study the effect of addition of molecular activating agent KOH, gravimetric analysis experiment was performed for the **P3C** and **P3KC** cases. The overall yield calculated after washing both the samples using dilute HCl was 31% and 13% for **P3C** and **P3KC**, respectively. This extra ~18% loss in **P3KC** was the contribution of K to pore formation giving rise to high surface area carbon.

#### 4.3.8 Electrochemical Testing

##### Electrochemical Measurements

The polymer derived porous carbon was subjected to electrochemical performance study. The electrochemical measurements were done for both the aqueous as well as organic supercapacitor. Advantage of using the organic electrolyte over the aqueous electrolyte is that the organic systems can operate at higher potential window and hence higher energy density, as the energy density is linearly proportional to the square of the potential window ( $E = \frac{1}{2}CV^2$ ).

##### 4.3.8.1 Electrochemical Measurements of P3KC in an Aqueous System: 1M $H_2SO_4$

The cyclic voltammogram was acquired in a potential window of 0-1V (**Figure 4.11**) for the scan rate of  $100 \text{ mV s}^{-1}$ . The rectangular kind of nature of the CV signifies that there is a formation of double layer at the interface of electrode and electrolyte without having any side reaction. The galvanostatic charge discharge measurement was done at the current density of  $1 \text{ Ag}^{-1}$ . The specific capacitance of  $175 \text{ Fg}^{-1}$  was obtained at the current density of  $1 \text{ Ag}^{-1}$ .

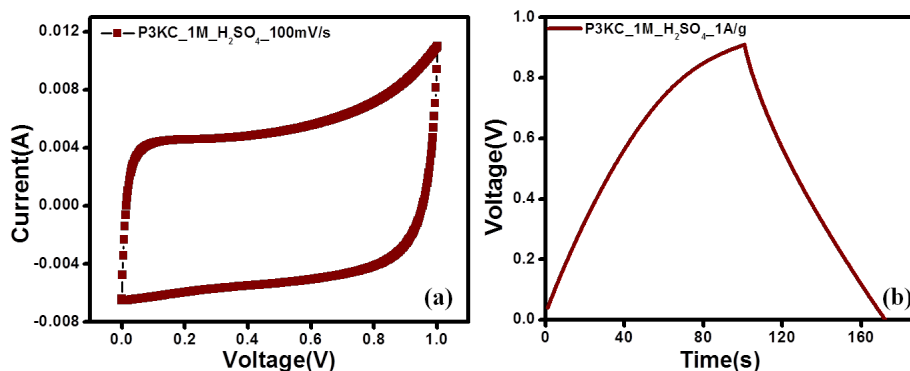


**Figure 4.11:** (a) Cyclic voltammogram (CV) of **P3KC** in 1M  $\text{H}_2\text{SO}_4$  as electrolyte at the scan rate of  $100 \text{ mV s}^{-1}$ , (b) Galvanostatic charging-discharging data for **P3KC** at the current density of  $1 \text{ A g}^{-1}$

#### 4.3.8.2 Electrochemical Measurements in 1M $\text{TEABF}_4$ in Propylene Carbonate (PC) Electrolyte

**Figure 4.12 (a)** shows CV for **P3KC** case for the range of scan rates from  $10 \text{ mV s}^{-1}$  to  $100 \text{ mV s}^{-1}$ . The nature of the CV curve is quite rectangular at low scan rates and it is maintained even at high scan rate of  $100 \text{ mV s}^{-1}$ , which represents the high rate performance. The observed good high rate performance is attributed to high ionic conductivity (because of very high surface area and high pore volume) as well as high electrical conductivity because of the pyrrolic nature of N-doping.

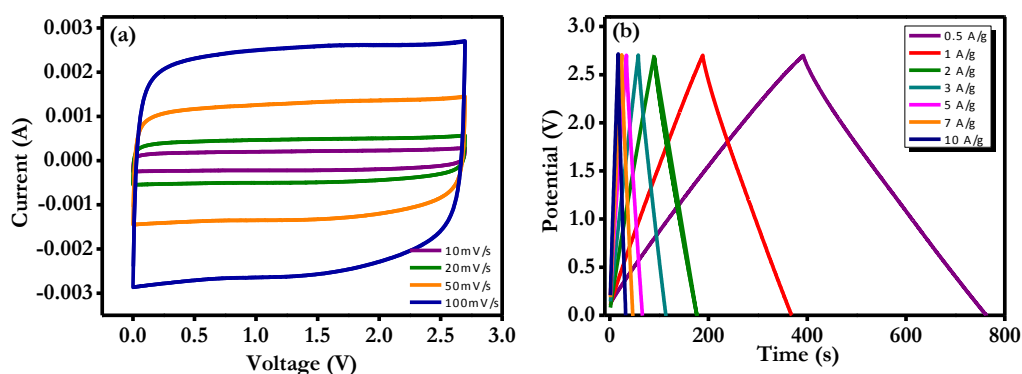


**Figure 4.12:** (a) CV of **P3KC** in  $\text{TEABF}_4$  as electrolyte at different scan rates in the potential range of 0-2.7 V, (b) Galvanostatic charging-discharging data for **P3KC** at the various current densities.

The capacitance values were calculated from the charge discharge plots by the following equation,

$$C_{sp} = \frac{2I}{m\left(\frac{dV}{dt}\right)}$$

Where,  $C_{sp}$  is specific capacitance,  $I$  is the discharging current at constant rate,  $m$  is the total loading of the active material and  $dV/dt$  is the discharge slope.

**Figure 4.12 (b)** represents the galvanic charge discharge measurements performed from  $0.5 \text{ A g}^{-1}$  to  $10 \text{ A g}^{-1}$  of applied current densities. The maximum capacitance measured is  $137.8 \text{ F g}^{-1}$  for the applied current density of  $0.5 \text{ A g}^{-1}$ . When the current density was increased by a factor of 20 ( $10 \text{ A g}^{-1}$ ) the capacitance value became  $111.8 \text{ F g}^{-1}$ .

The plot of specific capacitance values as a function of increasing current density is shown in **Figure 4.13 (a)**, which shows that the  $\sim 77\%$  retention of the capacitance value even at the higher current density of  $10 \text{ A g}^{-1}$ .

**Figure 4.13 (b)** shows the Ragone plot of energy density against power density for the **P3KC** for the organic electrolyte system. All the calculations for Ragone plot were based on active materials only. It is clear that the power density can be increased significantly without much loss in energy density.

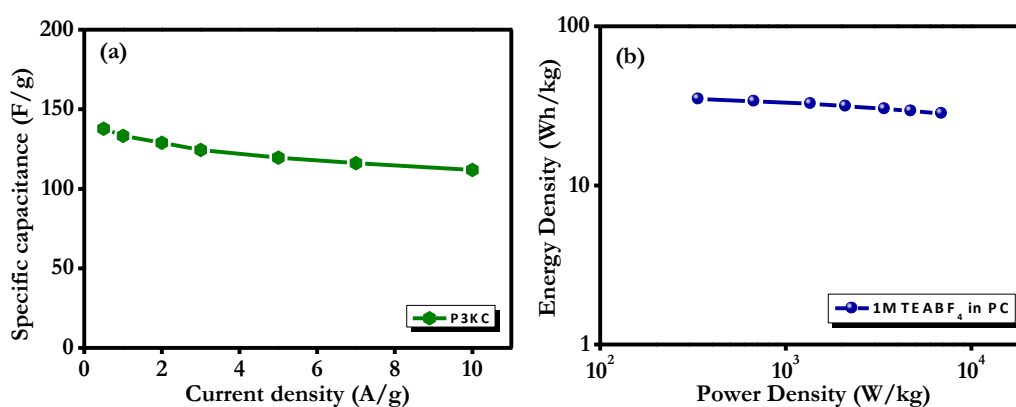


**Figure 4.13:** (a) Specific capacitance measured from charging-discharging at different current densities, (b) Ragone plot



We have furthermore checked the stability of the EDLC cell at  $2 \text{ A g}^{-1}$  for more than 1000 cycles, which indicated that approximately 86% of capacitance retention (**Figure 4.14**).

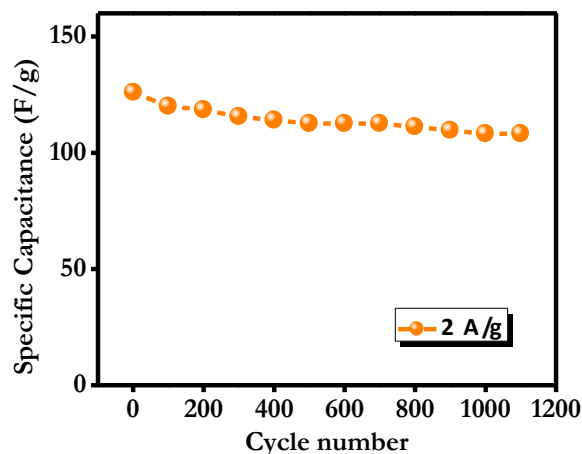


**Figure 4.14:** Cyclic stability data of organic EDLC measurements for **P3KC** case in the coin-cell assembly

#### 4.3.8.3 Impedance Measurements

**Figure 4.15** represents the impedance measurements (Nyquist plots). For the comparison purpose, two assemblies were made. The figure compares the impedance of the coin cell assembly and the Swagelok cell assembly for **P3KC** case. For both the assembly, the electrolyte system used was non-aqueous. Thus, the impedance measurements were carried out in the frequency range of 1 MHz–100 kHz. The plot initially shows a semicircle and then vertically expands. This vertical nature realizes the capacitive performance of the material. The semicircle/s give the information about the resistances involved in the circuit. Generally, the total resistance is the combination of the several resistances such as electrolyte's resistance, resistance within the material, contact resistances, etc.<sup>50</sup> For the case of **P3KC**, this is  $\sim 3 \Omega$  for coin cell assembly and  $\sim 11 \Omega$  for Swagelok cell assembly. The lower value of total resistance was observed for the coin cell assembly. This is because, in the coin cell, the distance between the two electrodes is smaller than in Swagelok cell and due to which the electrolyte resistance is lower. Hence the specific capacitance value for coin cell ( $137 \text{ F g}^{-1}$  at the applied current density of  $0.5 \text{ A g}^{-1}$ ) is higher than the Swagelok cell assembly ( $100 \text{ F g}^{-1}$  at the applied current density of  $0.5 \text{ A g}^{-1}$ ).



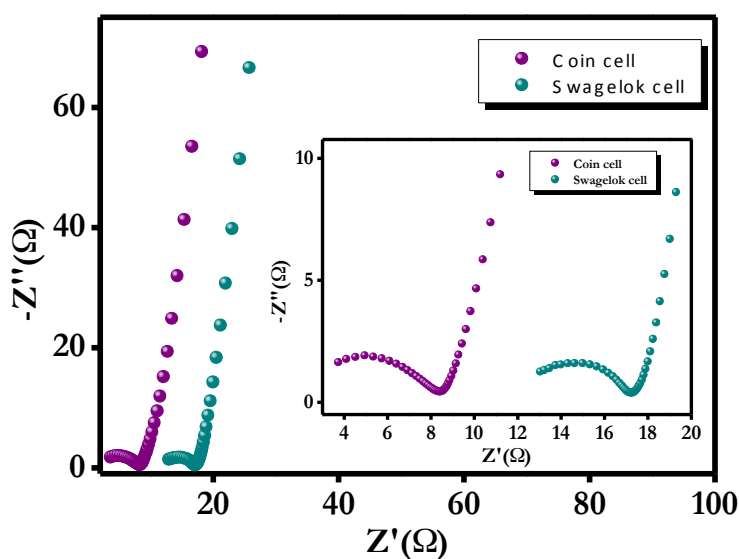


**Figure 4.15:** Comparison of impedance measurements (Nyquist plot) between coin cell and Swagelok cell assembly for **P3KC**

We also examined the same high quality porous carbon for Li-HEC application. This device configuration has the advantage that it enhances the energy density of supercapacitor without compromising the power delivery.

#### 4.3.8.4 Electrochemical Capacitance (Li-HEC) Measurements

In Li-HEC assembly the carbon **P3KC** was used as a cathode and  $\text{Li}_4\text{Ti}_5\text{O}_{12}$  (LTO) was used as the anode material. LTO has a specific advantage for use as anode in Li-HEC assembly, as it is cheap, has low volume change during charging/discharging and can deliver high lithium diffusion coefficient inside the crystal lattice. More importantly, it is chemically resistive in nature. During charging  $[\text{PF}_6]^-$  ions are adsorbed on the carbon surface to form the electrical double layer and lithium ions get intercalated into the LTO lattice.

Before making the full cell assembly of Li-HEC, the individual single electrode performance of **P3KC** and LTO are very important to examine. From the individual cell performance we must determine the mass loading of both the materials required for full cell in order to maintain the charge balance. The single electrode performance of **P3KC** was evaluated with respect to metallic lithium (Li/**P3KC**) and the data is shown in **Figure 4.16 (a)**, which represents a

typical charge-discharge plot of **P3KC** cycled between the potential 3 V to 4.5 V vs lithium at room temperature. A linear charging and discharging nature again confirms formation of electrical double layer at the electrode-electrolyte interface without any discernible Faradic contribution.

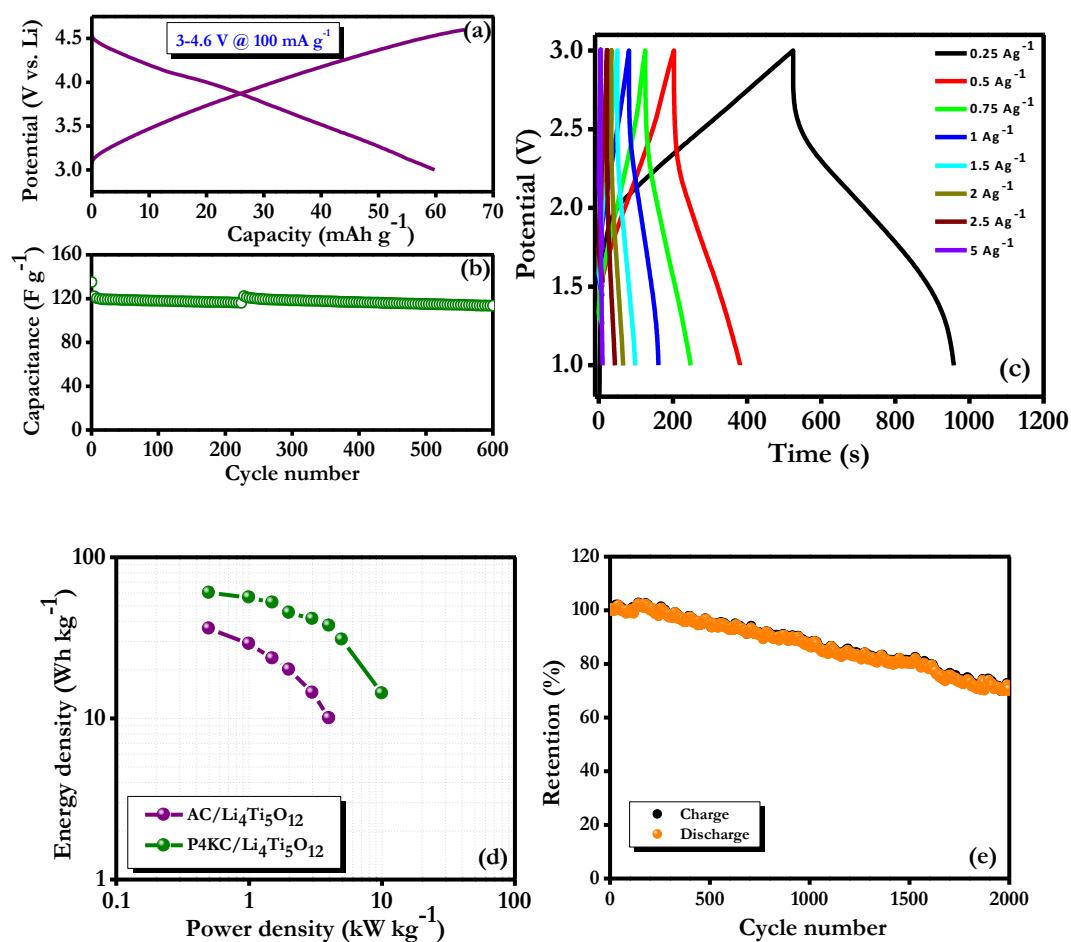


**Figure 4.16:** (a) Typical charging-discharging curves for Li/**P3KC** half-cell, (b) half cell cyclic stability from 3 V to 4.6 V at the current density of  $100 \text{ mA g}^{-1}$ , (c) Galvanostatic charging-discharging curves for **P3KC**/  $\text{Li}_4\text{Ti}_5\text{O}_{12}$  Li-HEC at different current densities between 1V to 3V, (d) Ragone plot of **P3KC**/  $\text{Li}_4\text{Ti}_5\text{O}_{12}$  and commercial AC/  $\text{Li}_4\text{Ti}_5\text{O}_{12}$ , (e) Cyclic stability of **P3KC**/  $\text{Li}_4\text{Ti}_5\text{O}_{12}$  at the current density of  $2 \text{ A g}^{-1}$

The observed capacity of the cell is converted into specific capacitance using the following equation:

$$C (F g^{-1}) = \frac{i(A) \times t(s)}{3600 \times m(g)} = X (mAh g^{-1}) \times \frac{3600}{dV(mV)}$$

Where, C is specific capacitance in  $F g^{-1}$ , I is current applied, t is discharge time, m is active material weight, X is the capacity observed in  $mA h g^{-1}$  and dV is the potential window of the single electrode cell testing. The maximum capacitance observed for **P3KC** in a single electrode configuration is  $134 F g^{-1}$  for the applied current density of  $100 mA g^{-1}$ . Furthermore **P3KC** carbon showed 85 % of capacitance retention after 600 cycles (**Figure 4.16 (b)**). It can be concluded from the single electrode performance that **P3KC** is a suitable candidate as cathode for Li-HEC application.

The single electrode performance of LTO was also examined at the same current densities and it was found to be stable upto 2000 cycles. Based on the single electrode performance of the two electrodes, the ratio of mass loading of cathode and anode was fixed to 2.5 mg LTO and 7.1 mg of **P3KC** for making a full cell Li-HEC configuration. The full cell electrochemical profile of **P3KC/LTO** was cycled between 1 V to 3 V for various applied current densities (**Figure 4.16 (c)**). It is worth mentioning that the current densities were applied for the full cell configuration using the mass loading for both the cathode and the anode such that if the total loading is 10 mg, then 10 mA current is equivalent to  $1 A g^{-1}$ . The discharging time decreased as the current density increased mainly because of more or less surface participation of the ions rather than the bulk of the materials. The specific energy density ( $E_{sp}$ ) and power density ( $P_{sp}$ ) were calculated by the following equation:

$$E = P_{sp} \times t$$

$$P_{sp} = \frac{\Delta E \times i}{m}$$

Where,  $\Delta E = \frac{(E_{max} + E_{min})}{2}$ , m is the active mass loading used for Li-HEC testing,  $E_{max}$  and  $E_{min}$  are the maximum and the minimum potentials of the galvanostatic charge- discharge cycle. The maximum energy density was calculated as  $61 Wh k g^{-1}$  with respect to the power density of  $496.6 W k g^{-1}$  and the maximum power density was calculated  $10015 W k g^{-1}$  with respect to the energy density of  $14.55$

Wh  $\text{k g}^{-1}$ . The observed energy density is better than the commercially available activated carbon as shown in **Figure 4.16 (d)** and **P3KC** in symmetric configuration for the same electrode configuration as well as the same testing conditions. Along with the high performance, **P3KC** also exhibits high cyclic stability (**Figure 4.16 (e)**) (70% of retention after 2000 cycles). The fading in performance with cycles is mainly attributed to the basic intrinsic properties of LTO anode, which can be modified by making suitable nanostructures.

#### 4.4. Conclusion

Strategic designed was proposed and the synthesis of polystyrene derivative was achieved successfully. The polymer was characterized using FTIR and NMR spectroscopy. Highly porous carbon was synthesized by the pyrolysis of a suitably designed and click-chemistry synthesized polymer precursor with *in situ* porogen presence for molecular activation. The BET specific surface area of  $1860 \text{ m}^2 \text{ g}^{-1}$  was realized with a good density of micro/meso-porous and high electrical conductivity, which are appropriate parameters for the supercapacitor application. Supercapacitor measurements performed in the organic electrolyte TEABF<sub>4</sub> in PC yielded the specific capacitance of  $137.8 \text{ F g}^{-1}$  at the applied current density of  $0.5 \text{ A g}^{-1}$ . The Li-HEC measurements performed using the 1M LiPF<sub>6</sub> as the electrolyte showed that the maximum energy density and maximum power density values of  $61 \text{ Wh k g}^{-1}$  and  $10015 \text{ W k g}^{-1}$ , respectively, were obtained. A ~70 % capacitance retention was noted after 2000 cycles.

## References

1. Chen X, Li.; C, Grätzel, M.; Kostecki, R.; Mao, S. S.; *Chem. Soc. Rev.* **2012**, 41, 7909-7937.
2. Aricò, A. S.; Bruce, P.; Scrosati, B.; Tarascon, J. M.; Schalkwijk, W. *Nat. Mater.* **2005**, 4, 366-377.
3. Yan, J.; Wang, Q.; Wei, T.; Fan, Z. *Adv. Energy Mater.* **2014**, 4, 1300816.
4. Titirici, M-M.; White, R. J.; Brun, N.; Budarin, V. L.; Su, D. S.; del-Monte, F.; Clark, J. H.; MacLachlan, M. J. *Chem. Soc. Rev.* **2015**, 44, 250-290.
5. Zhang, P.; Sun, F.; Xiang, Z.; Shen, Z.; Yun, J.; Cao, D. *Energy Environ. Sci.* **2014**, 7, 442–450.
6. Zhong, X.; Yu, H.; Zhuang, G.; Li, Q.; Wang, X.; Zhu, Y.; Liu, L.; Li, X.; Dong, M.; Wang, J-g. *J. Mater. Chem. A* **2014**, 2, 897–901.
7. Palaniselvam, T.; Valappil, M. O.; Illathvalappil, R.; Kurungot, S. *Energy Environ. Sci.* **2014**, 7, 1059–1067.
8. Wu, G.; More, K. L.; Johnston, C. M.; Zelenay, P. *Science* **2011**, 332, 443–447.
9. You, C.; Liao, S.; Li, H.; Hou, S.; Peng, H.; Zeng, X.; Liu, F.; Zheng, R.; Fu, Z.; Li, Y. *Carbon* **2014**, 69, 294–301.
10. Peng, H. L.; Mo, Z. Y.; Liao, S. J.; Liang, H. G.; Yang, L. J.; Luo, F.; Song, H. Y.; Zhong, Y. L.; Zhang, B. Q. *Sci. Rep.* **2013**, 3, 1765.
11. Mo, Z.; Liao, S.; Zheng, Y.; Fu, Z. *Carbon* **2012**, 50, 2620–2627.
12. Zheng, Y.; Jiao, Y.; Ge, L.; Jaroniec, M.; Qiao, S. Z. *Angew. Chem. Int. Ed.* **2013**, 52, 3110–3116.
13. Liang, J.; Zheng, Y.; Chen, J.; Liu, J.; Hulicova-Jurcakova, D.; Jaroniec, M.; Qiao, S. Z. *Angew. Chem. Int. Ed.* **2012**, 51, 3892–3896.
14. Shi, Q.; Peng, F.; Liao, S.; Wang, H.; Yu, H.; Liu, Z.; Zhang, B.; Su, D. *J. Mater. Chem. A* **2013**, 1, 14853–14857.
15. Kicinski, W.; Szala, M.; Bystrzejewski, M. *Carbon* **2014**, 68, 1–32.
16. Liu, Z.; Nie, H. G.; Yang, Z.; Zhang, J.; Jin, Z. P.; Lu, Y.; Xiao, Z. B.; Huang, S. M. *Nanoscale* **2013**, 5, 3283–3288.
17. Simon, P.; Gogotsi, Y. *Nat. Mater.* **2008**, 7, 845.

18. Wahid, M.; Puthusseri, D.; Phase, D.; Ogale, S. *Energy Fuels* **2014**, 28, 4233–4240.
19. Biswal, M.; Banerjee, A.; Deo, M.; Ogale, S. *Energy Environ. Sci.* **2013**, 6, 1249-1259.
20. Zhu, H.; Wang, X.; Liu, X.; Yang, X. *Adv. Mater.* **2012**, 24, 6524–6529.
21. Li, Z.; Wu, D.; Huang, X.; Ma, J.; Liu, H.; Liang, Y.; Ruowen, Fu R.; Matyjaszewski, K. *Energy Environ. Sci.* **2014**, 7, 3006-3012.
22. Yuan, J.; Giordano, C.; Antonietti, M. *Chem. Mater.* **2010**, 22, 5003–5012.
23. Banerjee, A.; Upadhyay, K. K.; Puthusseri, D.; Aravindan, V.; Madhavi, S.; Ogale, S. *Nanoscale* **2014**, 6, 4387–4394.
24. Rose, M.; Korenblit, Y.; Kockrick, E.; Borchardt, L.; Oschatz, M.; Kaskel, S.; Yushin, G. *Small* **2011**, 7(8), 1108–1117.
25. Qie, L.; Chen, W.; Xu, H.; Xiong, X.; Jiang, Y.; Zou, F.; et al. *Energy Environ. Sci.* **2013**, 6(8), 2497–504.
26. Wei, L.; Sevilla, M.; Fuertes, A. B.; Mokaya, R.; Yushin, G. *Adv. Funct. Mater.* **2012**, 22(4), 827–34.
27. Liang, Y.; Liu, H.; Li, Z.; Fu, R.; Wu, D. *J. Mater. Chem. A* **2013**, 1(48), 15207–11.
28. Wang, X.; Liu, C-G.; Neff, D.; Fulvio, P. F.; Mayes, R. T.; Zhamu, A.; et al. *J. Mater. Chem. A* **2013**, 1(27), 7920–6.
29. Grundy, M.; Ye, Z. *J. Mater. Chem. A* **2014**, 2, 20316.
30. Hines, D.; Bagreev, A.; Bandosz, T. J. *Langmuir* **2004**, 20, 3388-3397.
31. Puthusseri, D.; Aravindan, V.; Madhavi, S.; Ogale, S. *Energy Environ. Sci.* **2014**, 7(2), 728–35.
32. Yadav, P.; Banerjee, A.; Unni, S.; Jog, J.; Kurungot, S.; Ogale, S. *ChemSusChem* **2012**, 5(11), 2159–64.
33. Gokhale, R.; Aravindan, V.; Yadav, P.; Jain, S.; Phase, D.; Madhavi, S.; Ogale, S. *Carbon* **2014**, 80, 462–47.
34. Puthusseri, D.; Aravindan, V.; Madhavi, S.; Ogale S. *Electrochim. Acta* **2014**, 130, 766–70.
35. Kolb, H. C.; Finn, M. G.; Sharpless, K. B. *Angew. Chem.* **2001**, 113, 2056 – 2075; *Angew. Chem. Int. Ed.* **2001**, 40, 2004 – 2021.
36. Rhodes, A. J.; Deming, T. J. *ACS Macro Lett.* **2013**, 2, 351–354

37. Fournier, D.; Du Prez, F. *Macromolecules*, **2008**, 41, 13, 4622-30
38. Toiserkani, H.; Yilmaz, G.; Yagci, Y.; Torun, L. *Macromol. Chem. Phys.* **2010**, 211, 2389–2395
39. Binder, W. H.; Sachsenhofer, R. *Macromol. Rapid Commun.* **2008**, 29, 952–981.
40. Espeel, P.; Du Prez, F. E. *Macromolecules* **2015**, 48, 2–14.
41. Putyera, K.; Bandosz, T. J.; Jagieo, J.; Schwarz, J. A. *Carbon* **1996**, 34, 1559-1567.
42. Wang, Y.; Su, F.; Wood, C. D.; Lee, J. Y.; Zhao, X. S. *Ind. Eng. Chem. Res.* **2008**, 47, 2294–2300.
43. Zhu, Y.; Murali, S.; Stoller, M. D.; Ganesh, K. J.; Cai, W.; Ferreira, P. J.; Pirkle, A.; Wallace, R. M.; Cychosz, K. A.; Thommes, M.; Su, D.; Stach, E. A.; Ruoff, R. S. *Science* **2011**, 332, 1537.
44. Shi, Q.; Zhang, R.; Lv, Y.; Deng, Y.; Elzatahrya, A. A.; Zhao, D. *Carbon* **2015**, 84, 335–346.
45. Pandolfo, A. G.; Hollenkamp, A. F. *J Power Sources.* **2006**, 157, 11-27.
46. Pachfule, P.; Kandmabeth, S.; Mallick, A.; Banerjee, R. *Chem. Commun.* **2015**, Advance Article DOI:10.1039/C5CC04130A.
47. Zhong, M.; Kim, E. K.; McGann, J. P.; Chun, S. E.; Whitacre, J. F.; Jaroniec, M.; Matyjaszewski, K.; Kowalewski, T. *J. Am. Chem. Soc.* **2012**, 134(36), 14846–14857.
48. Yadav, P.; Warule, S.; Jog, J.; Ogale, S. *Solid State Communications* **2012**, 152(23), 2092-2095.
49. Lee, J. S.; Kim, S. I.; Yoon, J. C.; Jang, J. H. *ACS Nano* **2013**, 7(7), 6047.
50. Zhang, J.; Zhao, X. S. *ChemSusChem*, **2012**, 5, 818–841.

## Chapter 5

### Phenazine Containing Poly(phenylene vinylene): Synthesis, Characterization and Application to Field Emission

Phenazine-containing poly(phenylene vinylene) (**PHN-PPV**) was synthesized using Wittig-Horner polycondensation of the appropriately designed monomers. This conjugated polymer has been explored for the application of field emission study. The design embraces the specific motivation of incorporating the nitrogen-containing heterocycle *viz.* phenazine in the polymeric backbone. **PHN-PPV** showed reversible redox properties. For **PHN-PPV** turn-on field for  $1 \mu\text{A}/\text{cm}^2$  was observed at  $1.68 \text{ V}/\mu\text{m}$  in the field emission measurements. The maximum current density of  $\sim 4.9 \text{ mA}/\text{cm}^2$  was achieved at the applied field of  $3.6 \text{ V}/\mu\text{m}$ . The emission current showed very good stability for 6 h at constant current of  $1 \mu\text{A}$ .



## 5.1 Introduction

In recent years there has been a tremendous surge of research activity in the field of next generation device systems in view of the exacting demands of the emerging application sectors. In this field particular emphasis is being laid on light weight, flexible, multifunctional and low cost device platforms based on earth abundant materials.<sup>1</sup> Thus, the choice of material systems is as important as the novelty of the device concept or the corresponding architecture. Towards this end, several classes of materials such as elemental and compound semiconductors, metal oxides/sulfides/selenides, low dimensional carbon forms and other 2D inorganic and hybrid materials, as well as small molecules and polymers are being intensely researched.<sup>2-6</sup> In this context, polymers stand out for their intrinsically light weight character, flexibility, low temperature processability, easy scalability, but perhaps most importantly, the ability afforded by the well established polymer synthesis methods to design them to meet a specific performance objective. In this work, we address the issue of field emission, which is central to many applications, especially the modern display systems capable of rendering good luminosity with lower electrical energy inputs; and explore whether a polymer system could be suitably designed to yield a good performance in this respect.

Field emission (FE) is also called as cold cathode emission, in which electrons are emitted in the presence of an applied electric field at the ambient temperature. The applied electric field causes band-bending leading to the formation of a triangular barrier near a tip feature of a material with locally highly intensified electric field causing electron tunneling (emission). Field emission display devices have the ability to provide flat-panel visual displays with upright picture quality at much lower power consumption and low cost than the conventional display systems; hence are regarded as energy saving devices. Since the realization of the significance of field emission displays, the materials used as cathodes in such architectures have evolved from metals to semiconductors to oxides/sulfides. Unfortunately, the volume of work on the use of polymers is rather limited thus far although some excellent papers have shown the promise of this class of materials in the field emission context.<sup>7-15</sup>

Use of specific micro-tipped array-like morphologies hold the key to high intensity emission at low applied potential between the electrodes because the electric field is highly enhanced at the tip. FE studies of carbon nanotubes, silicon nanowires, metal oxide nanowires and other forms of tapering morphologies like nanorods, nanotubes, nanoneedles etc. have been widely reported.<sup>16,17</sup> Wide band gap, good electrical properties, low work function, low electron affinity etc. are the essential quality factors for the material to be applicable as a cathode for field emission. Conducting polymers satisfy several of these requirements and can thus be considered as potentially promising candidates for field emission. However, the consideration of long-term stability, which is based on the electrical, thermal and morphological property domains, is a more serious concern in so far as realistic application goals are concerned.

Pi-conjugated polymers have attracted tremendous attention of researchers in the wide range of areas like solar cell, organic light emitting diodes (OLED), organic field effect transistors (OFET), electromagnetic (EMI) interface shielding, etc. The attributes for this recognition lie in their properties like lightweight, film forming ability, flexibility, stability, relatively high conductivity, etc. Amongst the reported conjugated polymers till date, some conjugated polymers like polyaniline, polypyrrole, PEDOT, polythiophene and their composites with carbon nanostructures and other metal oxides have been synthesized in various ways with interesting morphologies and explored for the field emission application.<sup>18-31</sup> The advantage of such polymers is that they can be synthesized to get specific morphologies like rods, arrays, fibers etc. Unfortunately, some of these materials are not solution processable and are therefore difficult to scale-up for flexible large area display panels. Conjugated polymers, which are solution processable are therefore regarded as technologically more desirable materials for the field emission application.<sup>17</sup> Also, there have been reports on thin film cathodes consisting of nitrogen doped, chemical-vapour-deposited diamond films,<sup>32</sup> and amorphous carbon films.<sup>33</sup>

Poly(pheylene vinylene) (PPV) is a particular class of conjugated polymers, which shows high luminescence, good conductivity, film forming nature, and most importantly, good solubility in common organic solvents, rendering it to be solution processable. A range of PPV series of polymers has

been synthesized and modified till date for diverse end applications such as solar cells,<sup>34,35</sup> OLEDs,<sup>36-37</sup> OFETs,<sup>38-40</sup> etc.

Herein, we have synthesized the PPV system with alkylated phenazine moiety. Phenazine is an important class of nitrogen containing hetero-cycle, which is known for decades for applications in chemical and biological sectors<sup>41-43</sup> and such systems are widely used for various applications such as pharmaceuticals,<sup>44,45</sup> agro-chemicals, pigments, dyes etc. It is a completely conjugated tricyclic molecule with pyrazine as a central ring. It is dibenzo annulated pyrazine. The fascinating structure of nitrogen containing stable ring makes researchers unfold its properties for other applications platforms. Furthermore, it has also been explored for OLEDs,<sup>46-48</sup> solar cells (conjugated polymers and small molecules for DSSC),<sup>49-53</sup> and sensing applications.<sup>54</sup>

Herein, we report for the first time the insertion of reduced phenazine (dihydrophenazine) in the poly(phenylenevinylene) system. Phenazine containing poly(phenylenevinylene) shows film forming ability, good reversible oxidation-reduction properties, ambient condition stability, as well as adequate conductivity. These characteristic features are the key to the field emission properties.

## 5.2 Experimental

### Materials:

Hydroquinone (Sigma Aldrich), potassium carbonate (Merck), 2-ethyl hexyl bromide (Sigma Aldrich), paraformaldehyde (Sigma Aldrich), HBr in acetic acid (Sigma), triethylphosphite (Spectrochem), phenazine (Sigma), sodium dithionite (Merck), 1-bromooctane (Spectrochem), tetrabutyl ammonium bromide (TBAB) (Merck), phosphoryl chloride (Spectrochem), and potassium tertiary-butoxide solution (Sigma) were purchased from commercial sources and were used as received. Solvents were purchased from local sources and used after distillation. Reactions were carried out in oven-dried glassware under a positive pressure of argon atmosphere unless otherwise mentioned. Silica gel (Thomas Baker, 100–200 and 230–400 mesh) was used for column chromatography. Aluminium oxide (neutral) was procured from Spectrochem for column chromatography.

## 5.2.1 Synthesis

### 5.2.1.1 Synthesis of 5,10-dihydrophenazine (1)

Into a 250 mL two-necked round-bottom flask, was dissolved phenazine (5.68 g, 31.5 mmol) in ethanol (120 mL) under argon atmosphere. The solution was refluxed for 30 min and then to this solution was added sodium dithionite (54.88 g, 31.5 mmol) dissolved in water at the same temperature. The color of the reaction mixture turned dark blue, and then precipitate formed in the reaction mixture. The reaction mixture was refluxed for additional 1 h and then cooled to room temperature. The precipitate was filtered, washed with water (300 mL), and dried in vacuum for 30 min. A light green solid was obtained (7.2 g) and was directly used for the next step because of its instability in air.

### 5.2.1.2 Synthesis of [5,10-dioctyl-5,10-dihydrophenazine] (2)

Into a 250 mL round-bottom flask, was dissolved 5,10-dihydrophenazine (**1**) (7.2 g, 39.5 mmol) in dimethyl sulphoxide (~100 mL). To this solution, sodium hydroxide (4.74 g, 0.119 mol), tetra n-butyl ammonium bromide (0.76 g, 2.4 mmol), and 3 mL of water were added under argon atmosphere. The reaction mixture was stirred for 15 min., and then 1-bromooctane (13.65 mL, 79.0 mmol) was added drop-wise. The mixture was then heated at 40 °C for 4 h. After cooling to room temperature, the reaction mixture was poured into ice water (400 mL) and it was extracted with ethyl acetate (2 x 200 mL). The organic layer was washed with water (200 mL), saturated brine solution (100 mL), dried over anhydrous sodium sulfate, filtered, and concentrated *in vacuo*. The crude product was purified by neutral aluminium oxide chromatography using pet ether as an eluent to afford pure compound (**2**) (yield 11.0 g, 69 %). <sup>1</sup>H NMR (CDCl<sub>3</sub>): δ 0.91 (t, 6H), 1.15-1.50 (m, 24H), 3.16 (broad s, 4H), 6.24 (s, 4H), 6.64 (s, 4H). <sup>13</sup>C NMR (Benzene d<sub>6</sub>): 137.93, 121.63, 111.45, 45.84, 32.53, 30.05, 27.54, 25.15, 23.41, 14.73.

### 5.2.1.3 Synthesis of [5,10-dioctyl-5,10-dihydrophenazine-2,7-dicarbaldehyde] (3)

Into a 100 mL round-bottom flask, 5,10-dioctyl-5,10-dihydrophenazine (**2**) (0.5 g, 1.22 mmol) was dissolved in freshly distilled N,N-dimethyl formamide (7 mL) under argon atmosphere at 0 °C. POCl<sub>3</sub> (0.25 mL, 2.7 mmol) was added

drop-wise to the solution at the same temperature. The reaction mixture was stirred at 90 °C for 12 h, then cooled to room temperature and poured into ice water. The pH of reaction mixture was adjusted to 7 by adding dilute NaOH solution drop-wise. The color of the reaction mixture became red orange. The precipitate was filtered and dried *in vacuo*. The crude product was purified by column chromatography using pet ether: dichloromethane (50:50, v/v) to afford an orange solid (**3**) (yield 0.35 g, 61 %). <sup>1</sup>H NMR (CDCl<sub>3</sub>): δ 0.91 (t, 6H), 1.32-1.68 (m, 24H), 3.43 (t, 4H), 6.27 (d, 2H), 6.71 (d, 2H), 7.12 (d, 2H), 9.60 (s, 2H). <sup>13</sup>C NMR (Benzene d<sub>6</sub>): 189.25, 142.68, 135.95, 131.45, 130.10, 110.35, 108.80, 45.92, 32.49, 29.96, 29.80, 27.19, 25.01, 23.42, 14.73.

#### 5.2.1.4 Synthesis of [1,4-bis((2-ethylhexyl)oxy)benzene] (**4**)

Into a three-necked 500 mL round bottom flask equipped with an addition funnel and a reflux condenser, were added activated K<sub>2</sub>CO<sub>3</sub> (43.9 g, 0.317 mol) and hydroquinone (10 g, 0.09 mol). The mixture was evacuated and then purged with argon. Dry DMF (150 mL) was added to it and the mixture was stirred at 60 °C for 2 h. 2-Ethylhexyl bromide (48.45 mL, 0.27 mol) was added drop-wise through the addition funnel. After the completion of addition, the reaction mixture was refluxed for 12 h at 150 °C. After cooling, the reaction mixture was poured into ice water and the product was extracted with ethyl acetate (500 mL). The ethyl acetate solution was further washed with water (800 mL), separated and dried over anhydrous sodium sulfate. The organic phase was concentrated and the product was purified by column chromatography using pet ether: ethyl acetate 95:5 (v/v) to get colorless viscous liquid (**4**) (yield 25 g, 82 %). <sup>1</sup>H NMR (CDCl<sub>3</sub>): δ 0.94 (m, 12H), 1.31-1.56 (m, 16H), 1.76 (m, 2H), 3.80 (d, 4H), 6.84 (s, 4H).

#### 5.2.1.5 Synthesis of [1,4-bis(bromomethyl)-2,5-bis((2-ethylhexyl)oxy)benzene] (**5**)

Into a two necked 250 mL round bottom flask equipped with a reflux condenser, a liquid addition funnel and a magnetic stirrer were added bis-1,4-(ethylhexyloxy) benzene (**4**) (5 g, 0.014 mol), paraformaldehyde (0.92 g, 0.03 mol) and glacial acetic acid (50 mL). The reaction mixture was stirred at room temperature for 30 min. HBr (33 wt % in acetic acid) (5.63 mL, 0.031 mol) was

added drop-wise to the reaction mixture. The reaction mixture was stirred at 70 °C for 8 h in the argon atmosphere. After cooling it to room temperature, the reaction mixture was poured into ice water to obtain a white precipitate. The precipitate was then filtered, washed several times using cold water and dried in vacuum. The crude product was purified by column chromatography (pet ether: ethyl acetate (1%)) (Yield 6.9 g, 88 %) <sup>1</sup>H NMR (CDCl<sub>3</sub>): δ 0.96 (m, 12H), 1.32-1.56 (m, 16H), 1.76 (m, 2H), 3.88 (d, 4H), 4.53 (s, 4H), 6.86 (s, 2H).

#### ***5.2.1.6 Synthesis of [tetraethyl ((2,5-bis((2-ethylhexyl) oxy)-1,4 phenylene) bis(methylene))bis(phosphonate)] (6)***

Into a 100 mL single neck round bottom flask were added 1,4 bis(ethylhexyloxy)-2,5 dibromomethyle benzene (**5**) (1 g, 1.9 mmol) and triethylphosphite (1.6 mL, 0.0046 mol) at once. The reaction mixture was then stirred at 90 °C for 12 h under argon atmosphere. The excess triethylphosphite was removed by vacuum distillation to obtain oily viscous liquid. The product was purified by column chromatography using dichloromethane: methanol, 99:1 (v/v). (Yield 0.85 g, 85 %). <sup>1</sup>H NMR (CDCl<sub>3</sub>): δ 0.92 (m, 12H), 1.23-1.52 (m, 28H), 1.71 (m, 2H), 3.19 (d, 4H), 3.81 (d, 4H), 4.01 (q, 8H), 6.94 (s, 2H). <sup>13</sup>C NMR (CDCl<sub>3</sub>): 150.17, 114.42, 70.93, 61.55, 39.41, 30.33, 28.85, 27.05, 25.33, 23.64, 22.77, 16.07, 13.78, 10.88.

#### ***5.2.1.7 Synthesis of phenazine containing poly(phenylene vinylene) (PHN-PPV)***

The Wittig-Horner polycondensation was carried out according to the reported protocol<sup>55</sup> using potassium tertiary butoxide as a base. A dry two necked 50 mL round bottom flask was fitted with a rubber septum and an argon balloon. The mixture was purged with argon after addition of both the monomers *viz.* (**3**) (0.3 g, 0.64 mmol) and (**6**) (0.41 g, 0.64 mmol) followed by the addition of dry THF (25 mL) under argon atmosphere. Potassium tertiary butoxide solution (1.29 mL, 1M in THF, Sigma Aldrich) was added to the reaction mixture drop-wise with constant stirring. After completion of the addition, the reaction mixture was allowed to stir at room temperature for 4 h. The polymer was precipitated into the cold methanol (200 mL). The red colored precipitate was filtered and was subjected to successive washings of methanol (200 mL). The polymer was

purified by Soxhlet extraction method using the solvents methanol, acetone and chloroform. Yield = 0.4 g.  $^1\text{H}$  NMR ( $\text{CDCl}_3$ ):  $\delta$  0.90-1.0 ( $\text{CH}_3$ ), 1.26-1.81 (aliphatic  $\text{CH}_2$ ), 3.41-3.95 (O- $\text{CH}_2$ , N- $\text{CH}_2$ ), 6.24-7.06 (ArH). Molecular weight obtained by GPC (with respect to polystyrene standard):  $M_n = 6.12 \times 10^3$ ,  $M_w = 1.2 \times 10^4$  and PDI = 1.7.

**PHN-PPV** is soluble in various organic solvents like chloroform, dichloromethane (DCM), toluene, benzene, dichlorobenzene.

### 5.2.2 Characterization

$^1\text{H}$  NMR spectra were recorded on a Bruker-AV 500 MHz spectrometer in solvents as indicated with TMS as an internal standard. The chemical shift values are reported and the coupling constants ( $J$ ) measured in Hz. The molecular weight and the molecular weight distribution was determined by Gel Permeation Chromatography (GPC) which was performed using Thermo Separation Products equipped with UV 100 and RI 150 detectors (Spectral Series) and chloroform as an eluent at a flow rate of  $1 \text{ mL min}^{-1}$  at  $25 \text{ }^\circ\text{C}$ . The concentration of the polymer sample used was  $2 \text{ mg mL}^{-1}$  and polystyrenes with a narrow molecular weight distribution were used as the calibration standards. Thermogravimetric analysis (TGA) was accomplished using TGA-7 Perkin Elmer instrument. **PHN-PPV** sample weight taken was  $\sim 6 \text{ mg}$  for TGA measurements. The film of polymer was characterized by using Field emission scanning electron microscope (FESEM) with FEI Nova nanoSEM 450 for structural and morphological analysis.

### 5.2.3 Preparation of the polymer film for field emission study using spray coating

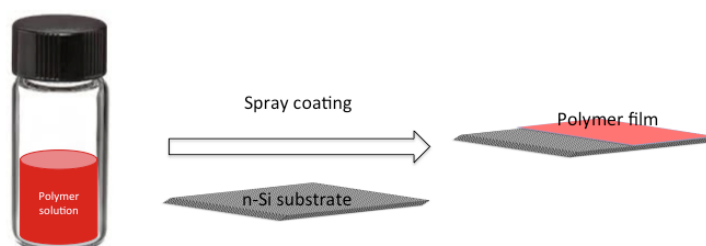


**Figure 5.1:** Polymer film preparation

The polymer film, which was used as cathode for field emission study, was made on a clean single crystal n-Si substrate (Sigma Aldrich N-Silicon wafer (111)) by spray coating method. The polymer solution of 10 mg/ mL in chloroform was used for the film formation. The spray gun (Airbrush set, single action, Paasche, USA) was used for the spray coating. The spray coated film was then subjected to vacuum annealing at 40 °C.

#### 5.2.4 Field Emission Studies

The field emission (FE) measurements of **PHN-PPV** thin film on Si substrate prepared by spray pyrolysis were carried out in an all-metal field emission microscope (FEM) system equipped with load lock facility. The metal FEM system was evacuated to ultra high vacuum (UHV) employing a set of vacuum pumps: a turbo molecular pump backed by a rotary pump, a sputter ion pump, and titanium sublimation pump with liquid nitrogen cooled jacket. The FE studies were performed at the base pressure of  $\sim 1 \times 10^{-8}$  mbar. The FE measurements were carried out in 'planar diode' (also termed as 'close proximity') configuration. In a typical experiment, the cathode (**PHN-PPV** film on Si substrate) was pasted onto a stainless steel stub (diameter  $\sim 30$  mm) using UHV compatible silver paste. A semitransparent cathodoluminescent phosphor screen (an anode) connected to a high precision linear motion drive was held parallel to the cathode. The cathode anode separation was maintained at 2500  $\mu\text{m}$  for all the experiments. For measurements of the emission current as a function of the applied voltage, a Keithley 485 Picoammeter and a Spellman high voltage DC power supply were used. Special care was taken to avoid any leakage current using shielded cables with proper grounding.

### 5.3 Results and Discussion

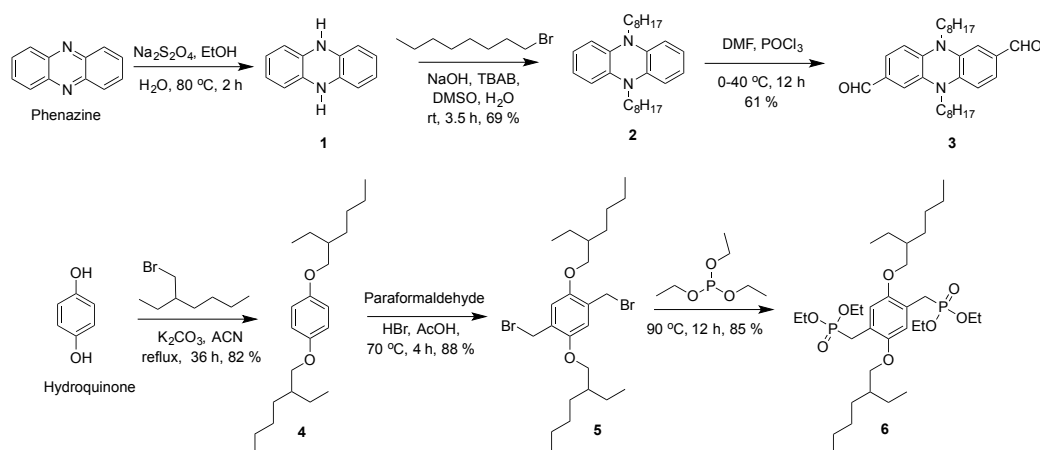
#### 5.3.1 Polymer Design and Synthesis

As stated above, in this work we have synthesized phenazine containing poly(phenylenevinylene) with the incorporation of 5,10-dialkyl-substituted dihydrophenazine *viz.* poly(5,10-octyl- dihydrophenazine)-phenylenevinylene (**PHN-PPV**). The long alkyl chains were introduced in order to achieve the solubility in organic solvents. The alkyl chain substituted 5,10-dihydrophenazine

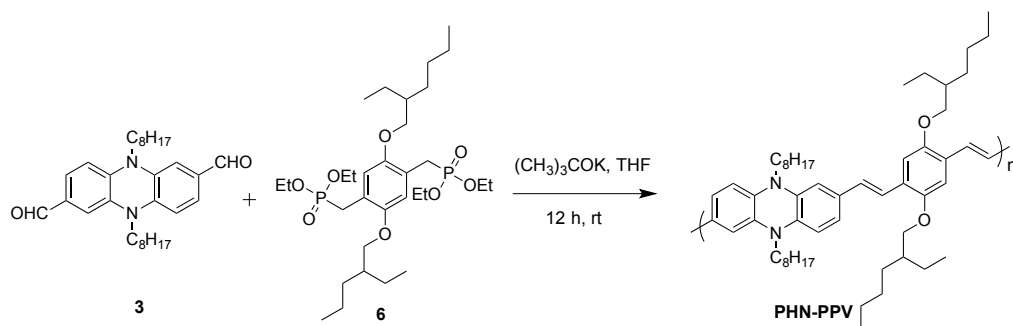


has the strong electron donating ability and hence it has been used as an electron donor in many organic charge transfer crystals.<sup>56</sup> This electron donor property motivated us to select phenazine. Highly electron-rich and redox-active compounds are valuable building blocks in material science.<sup>57</sup> 5,10-Dihydrophenazine systems are attractive as they satisfy such conditions. Due to presence of two tertiary nitrogens, this system is a good redox active system. As 5,10-dialkyl-substituted dihydrophenazine system opens up many possibilities to tune the design, we decided to introduce this moiety into the polymer.

**Scheme 5.1** represents the synthesis of monomers and **Scheme 5.2** depicts the synthesis of phenazine containing poly(phenylenevinylene). Phenazine was reduced using sodium dithionite followed by N-alkylation.<sup>54</sup> The N-alkylated phenazine was then treated with DMF and POCl<sub>3</sub> to get 5,10-dioctyl-5,10-dihydrophenazine-2,7-dicarbaldehyde (**3**).



**Scheme 5.1:** Synthesis of monomers (**3**) and (**6**)



**Scheme 5.2:** Synthesis of PHN-PPV

On the other hand; hydroquinone was subjected to O-alkylation reaction followed by bromomethylation to yield 1,4-bis(bromomethyl)-2,5-bis((2-ethylhexyl)oxy)benzene (**5**). Compound (**5**) was then reacted to triethylphosphite to get tetraethyl ((2,5-bis ((2-ethylhexyl) oxy)-1,4 phenylene) bis(methylene)) bis (phosphonate) (**6**)<sup>58,59</sup>.

**PHN-PPV** is a polymer formed by the condensation of 5,10-dioctyl-5,10-dihydrophenazine-2,7-dicarbaldehyde moiety (**3**) and the tetraethyl ((2,5-bis ((2-ethylhexyl) oxy)-1,4 phenylene) bis(methylene)) bis (phosphonate) (**6**), synthesized by Wittig-Horner polycondensation reaction. Using potassium tert-butoxide as the base for Wittig-Horner polycondensation of (**3**) and (**6**), yielded red colored **PHN-PPV**, which was purified by re-precipitation followed by Soxhlet extraction method.

### 5.3.2 <sup>1</sup>H NMR Spectra of Monomers

<sup>1</sup>H spectrum of 5,10-dioctyl-5,10-dihydrophenazine is shown in the **Figure 5.2**. In the <sup>1</sup>H spectrum of 5,10-dioctyl-5,10-dihydrophenazine, the broad singlet is appeared at 3.16  $\delta$  ppm due to the four protons next to nitrogen confirming the N-alkylation. The remaining alkyl chain protons are appeared at 0.9 - 1.5  $\delta$  ppm. The aromatic protons are of two types as the molecule is symmetric and they appeared as two separate broad peaks at 6.64  $\delta$  ppm and 6.24  $\delta$  ppm.

**Figure 5.3** represents the <sup>1</sup>H spectrum of 5,10-dioctyl-5,10-dihydrophenazine-2,7-dicarbaldehyde. In the <sup>1</sup>H spectrum of 5,10-dioctyl-5,10-dihydrophenazine-2,7-dicarbaldehyde, the appearance of the singlet at 9.60  $\delta$  ppm due to two aldehyde protons. Due to the presence of aldehyde group, the aromatic protons appeared at 6.26  $\delta$  ppm, 6.72  $\delta$  ppm, 7.10  $\delta$  ppm.

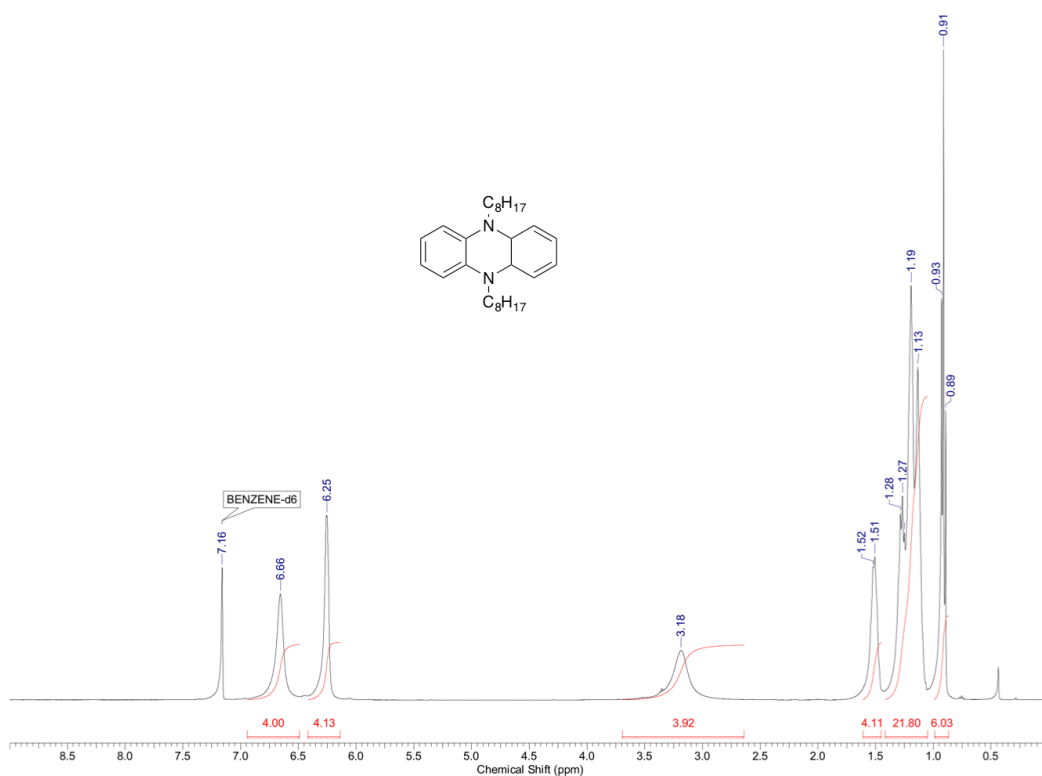


**Figure 5.2:**  $^1\text{H}$  spectrum of 5,10-dioctyl-5,10-dihydrophenazine (in benzene  $d_6$ )

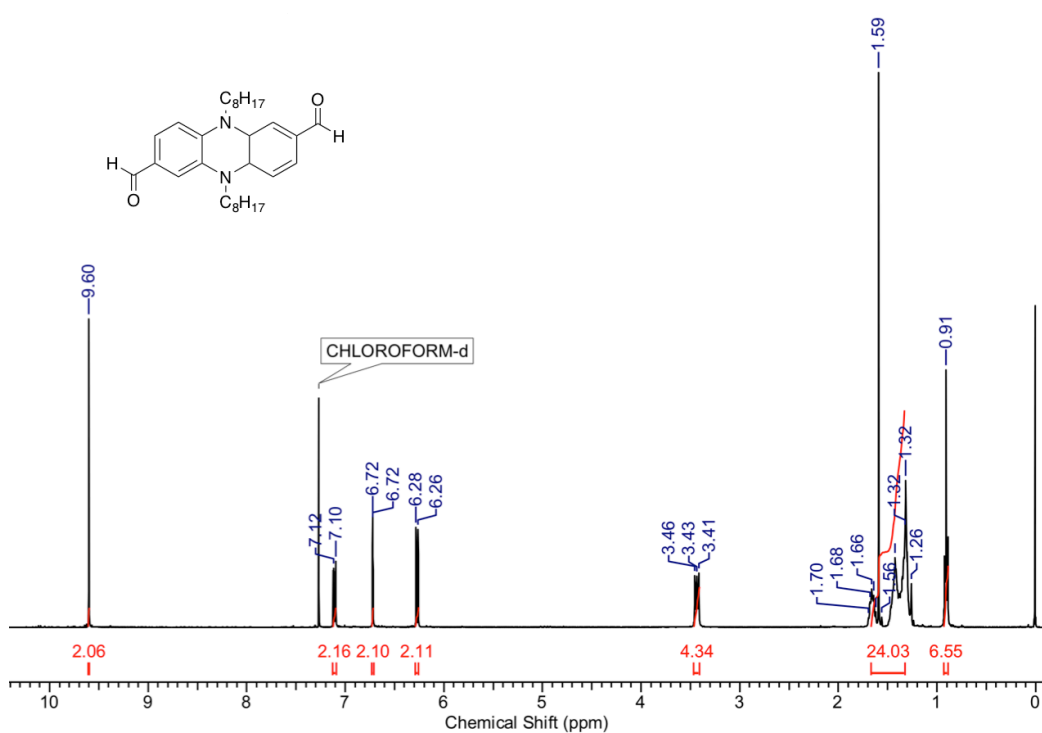


**Figure 5.3:**  $^1\text{H}$  NMR spectrum of 5,10-dioctyl-5,10-dihydrophenazine-2,7-dicarbaldehyde recorded in  $\text{CDCl}_3$

**Figure 5.4** depicts the  $^1\text{H}$  NMR spectrum of tetraethyl ((2,5-bis((2-ethylhexyl)oxy)-1,4 phenylene) bis(methylene))bis(phosphonate). In the spectrum, singlet was appeared at 6.94  $\delta$  ppm due to two aromatic protons. Quintet appeared at 4.01  $\delta$  ppm due to  $-\text{CH}_2$  of phosphonate group. Also, peak at 1.23  $\delta$  ppm appeared due to  $-\text{CH}_3$  of phosphonate.

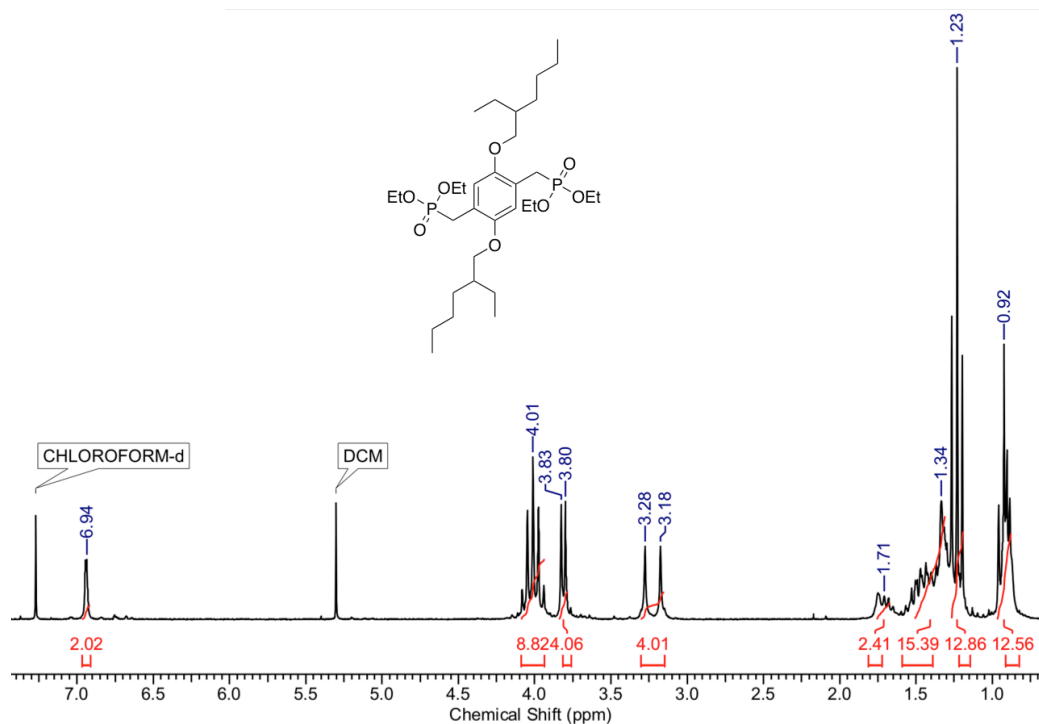


**Figure 5.4:**  $^1\text{H}$  NMR spectrum of tetraethyl ((2,5-bis((2-ethylhexyl)oxy)-1,4 phenylene) bis(methylene))bis(phosphonate) recorded in  $\text{CDCl}_3$

### 5.3.3 $^{13}\text{C}$ NMR Spectra of Monomer (3)

**Figures 5.5** and **5.6** represent  $^{13}\text{C}$  NMR spectra of 5,10-dioctyl-5,10-dihydrophenazine and 5,10-dioctyl-5,10-dihydrophenazine-2,7-dicarbaldehyde recorded in benzene  $\text{d}_6$ . The peaks are in good agreement with the respective structures.

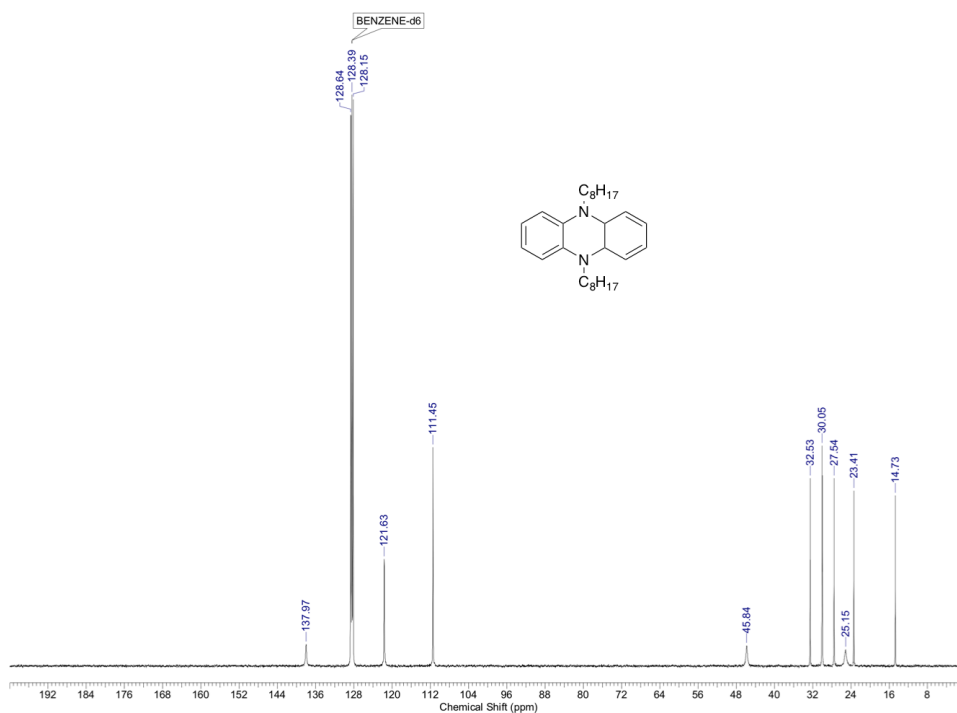


**Figure 5.5:**  $^{13}\text{C}$  spectrum of 5,10-dioctyl-5,10-dihydrophenazine recorded in Benzene  $\text{d}_6$

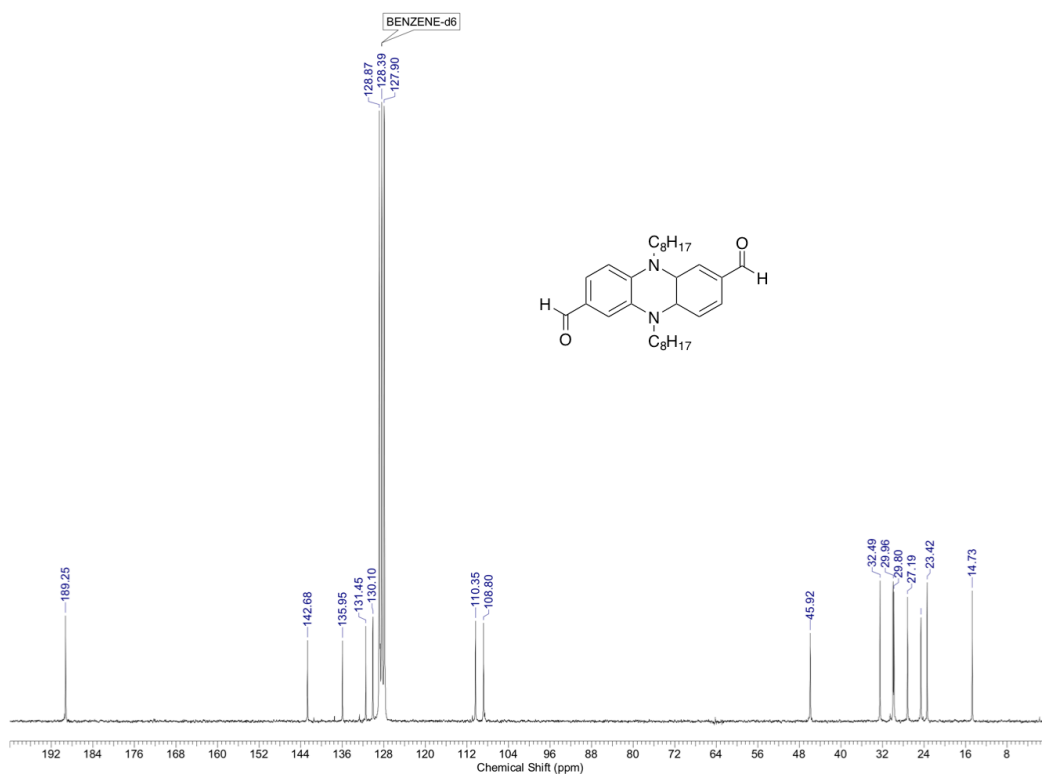


**Figure 5.6:**  $^{13}\text{C}$  NMR spectrum of 5,10-dioctyl-5,10-dihydrophenazine-2,7-dicarbaldehyde recorded in Benzene  $\text{d}_6$

### 5.3.4 MALDI Characterization of Monomers (3) and (6)

**Figure 5.7** shows the MALDI spectrum of monomer (3) - 5,10-dioctyl-5,10-dihydrophenazine-2,7-dicarbaldehyde. The peak at  $m/z$  of 463 characterizes the monomer (3) mass value.

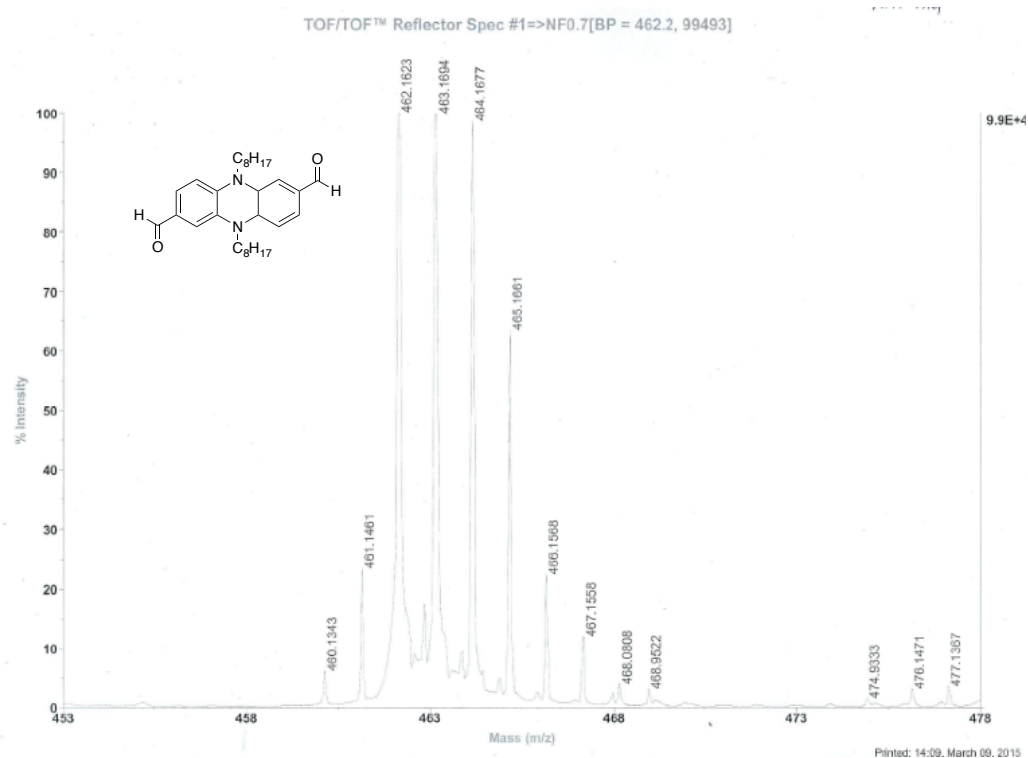


**Figure 5.7:** MALDI spectrum of monomer (3) 5,10-dioctyl-5,10-dihydrophenazine-2,7-dicarbaldehyde.

**Figure 5.8** represents MALDI spectrum of monomer (6)- tetraethyl ((2,5-bis((2-ethylhexyl) oxy)-1,4 phenylene) bis(methylene))bis(phosphonate). The peak at 635  $m/z$  value signifies mass value of monomer (6).

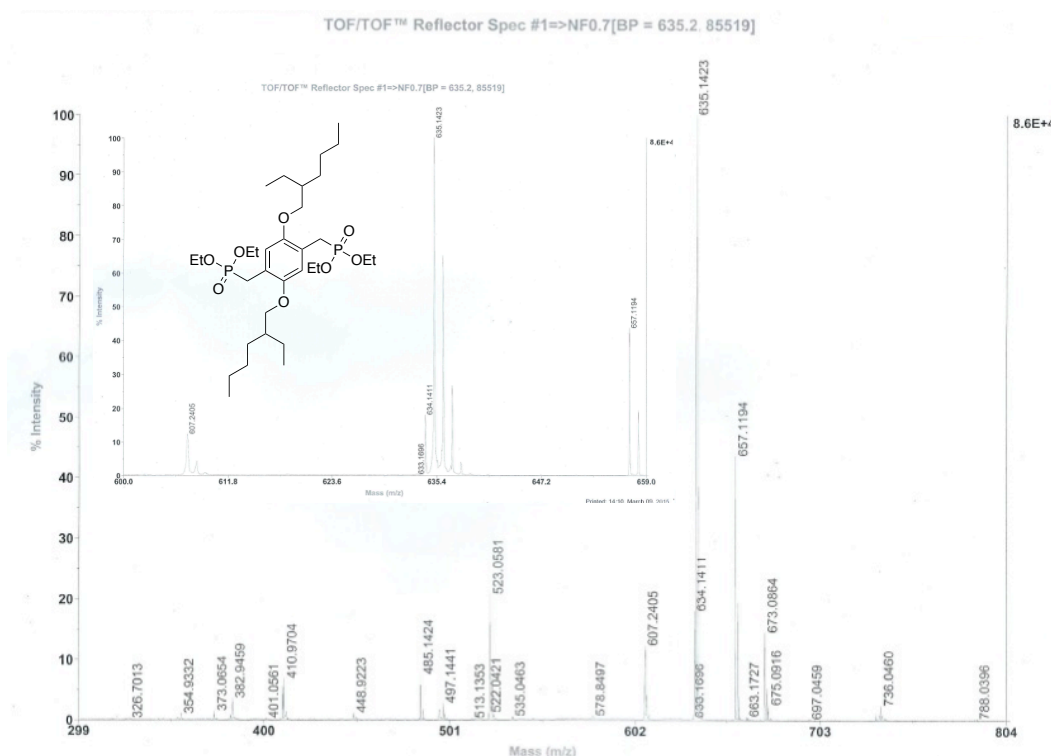


**Figure 5.8:** MALDI spectrum of monomer (**6**) - tetraethyl ((2,5-bis((2-ethylhexyl)oxy)-1,4 phenylene) bis(methylene))bis(phosphonate)

### 5.3.5 NMR Spectrum of PHN-PPV

**Figure 5.9** shows  $^1\text{H}$  NMR spectrum polymer **PHN-PPV**. For the polymer the spectral lines appeared broader. A small peak at 9.69  $\delta$  ppm appeared due to presence of aldehyde end group of the polymer. The peaks at 3.86  $\delta$  ppm and 3.14  $\delta$  ppm are due to  $-\text{OCH}_2$  and  $-\text{NCH}_2$ , respectively. The doublet at 7.89  $\delta$  ppm was attributed to vinylic protons of **PHN-PPV** ( $-\text{CH}=\text{CH}-$ ) and coupling constant of 16 Hz confirmed the trans configuration of **PHN-PPV**.

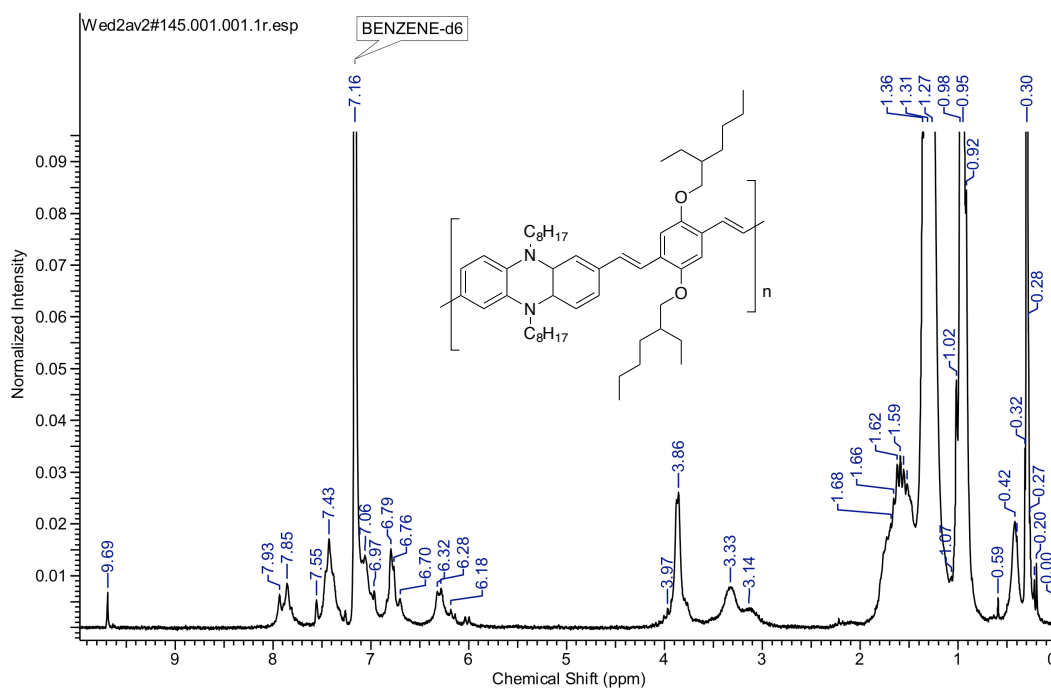


**Figure 5.9:**  $^1\text{H}$  NMR spectrum polymer PHN-PPV

### 5.3.6 UV-Vis and Photoluminescence Spectroscopy

**Figure 5.10 (a)** represents UV visible spectrum of PHN-PPV solution in chloroform. The spectrum clearly reveals that the polymer absorbs in the visible range. The absorption maximum peak at 490 nm is broad in nature with the absorption band edge at 600 nm. The peak appearing at lower wavelength (330 nm) is due to  $\pi$ - $\pi^*$  transitions in the conjugated polymer.

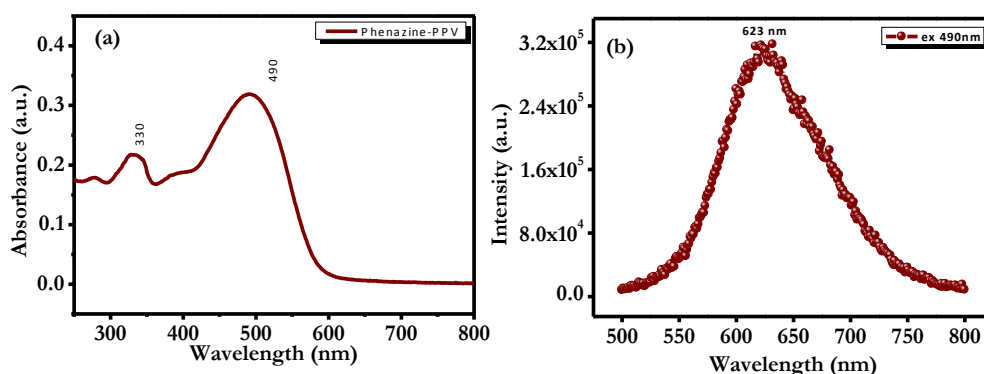


**Figure 5.10:** (a) UV visible spectrum of the PHN-PPV polymer in chloroform solution, (b) Photoluminescence spectrum of PHN-PPV polymer in chloroform solution.



The photoluminescence of the polymer solution in chloroform was recorded which is shown in **Figure 5.10 (b)**. The broad PL was observed with the emission peak at 623 nm when the polymer solution was excited at its maximum absorption value i.e. 490 nm.

### 5.3.7 Electrochemical Properties

To understand the energy levels of the polymer, cyclic voltammetry (CV) study was performed, the result of which is indicated in **Figure 5.8**.

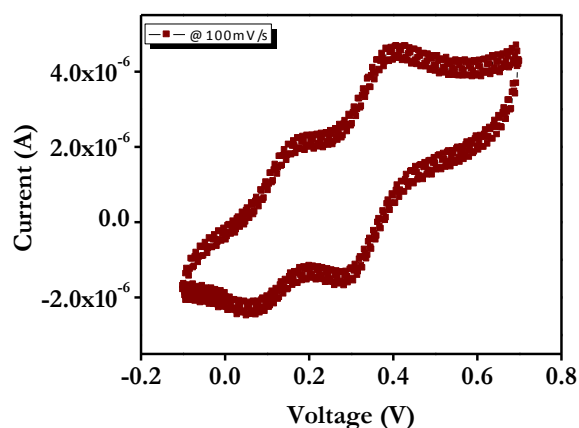


**Figure 5.11:** Cyclic voltammetry for **PHN-PPV** at the scan rate of 100 mV/s

The CV was recorded at the scan rate of 100 mV/s using ferrocene as the internal standard. From the CV it is clear that polymer shows reversible oxidation-reduction nature. The oxidation onset potential value, which is 0.15 V, was used for the calculation of HOMO. The HOMO level value was turned out to be -4.19 eV. The band gap was calculated from the UV-Vis spectrum and it turned out to be 2.5 eV. The oxidation potential in the polymer may correlate with the concept of work function in the case of metals or semiconductors. The lower work function is one of the prerequisite for the field emission application, as it is directly relevant to the value of the turn-on voltage of the field emission device. As stated in the introduction, wide band gap, good electrical properties, low work function, low electron affinity etc. are important parameters to take into consideration. The data indicate that **PHN-PPV** fulfills these requirements at satisfactory level. The lower oxidation onsets and reversible redox properties with wide band gap of 2.5 eV, indicated that **PHN-PPV** could be a potentially useful candidate for field emission device.

### 5.3.8 Thermogravimetric analysis (TGA)

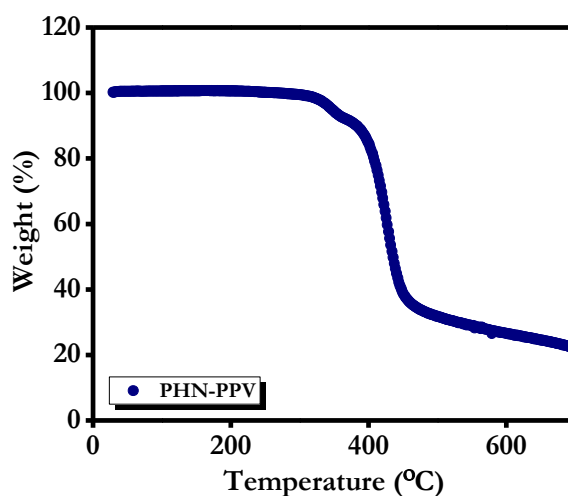


**Figure 5.12:** TG curve of PHN-PPV in the nitrogen atmosphere

Thermogravimetric analysis was performed on the sample at a heating rate of 10 °C/min under nitrogen atmosphere. Thermogravimetric analysis (TG) curve of PHN-PPV is shown in **Figure 5.12**. The  $T_{10}$  value is found to be 373 °C indicating its good thermal stability.

### 5.3.9 Theoretical Studies

To acquire extra insight into the electronic structure, theoretical calculations of repeating unit of PHN-PPV were implemented by density functional theory (DFT) with the Gaussian 09 program at B3LYP/6-311 G\* level.

DFT calculations clearly revealed that the electron density of HOMO is distinctly distributed over 5,10-dioctyl-5,10-dihydrophenazine moiety in the polymer backbone.

This implies that the 5,10-dioctyl-5,10-dihydrophenazine moiety is acting as a strong donor. The HOMO value obtained from this theoretical calculation was -4.3 eV, which is close to the experimental value (-4.2 eV). The LUMO was shown to spread over the phenylenevinylene part of the polymer caused by the absence of any strong acceptor group into the polymer. Moreover, the band gap of 2.8 eV was obtained by the DFT calculations while the experimental optical band gap observed was 2.5 eV.

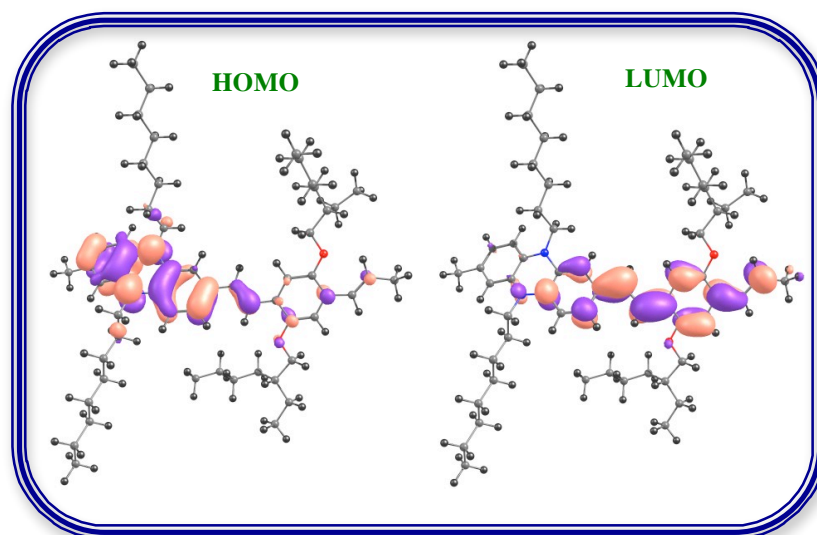


**Figure 5.13:** HOMO and LUMO levels of the monomer of **PHN-PPV**

### 5.3.10 Mott-Schottky and Conductivity Measurements

To interpret whether the polymer exhibit p-type or n-type nature, the Mott-Schottky experiment was performed (**Figure 5.14 (a)**) in 1 M  $\text{H}_2\text{SO}_4$  with three-electrode system, in which Ag/AgCl was used as the reference electrode and the carbon as counter electrode.

**PHN-PPV** film coated on n-silicon substrate made the working electrode. Mott-Schottky measurements were performed at the frequency of 10 KHz. The nature of the slope signifies that **PHN-PPV** is p-type. The flat band potential estimated from the intercept on the X-axis of the linear portion of Mott-Schottky plot is 0.058 V.

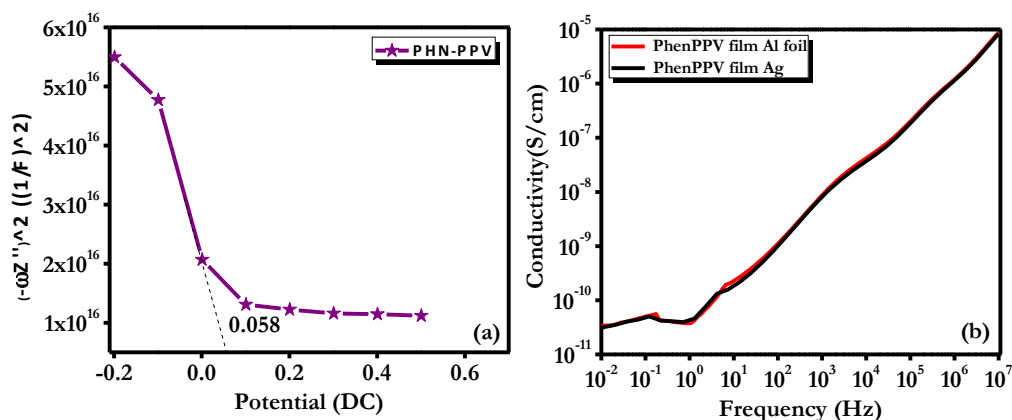


**Figure 5.14:** (a) Mott-Schottky measurements, (b) AC conductivity measurements

The conductivity of **PHN-PPV** was measured using frequency dependent (AC) conductivity measurements; the corresponding data is shown in **Figure 5.14(b)**. The freestanding 0.11 mm thick polymer film was cast and it was directly placed in-between the silver/aluminium electrodes for the electrical conductivity measurements. The conductivity decreases from higher to lower frequency range, which is common for the semiconducting conjugated polymers.

### 5.3.11 Field Emission Studies

For a planar emitter comprised of a thin film of nanostructures deposited on flat substrate, the modified Fowler – Nordheim F-N equation<sup>60</sup> is given as,

$$J = \lambda_M \alpha \phi^{-1} E^2 \beta^2 \exp \left( - \frac{b \phi^{\frac{3}{2}}}{\beta E} v_F \right) \dots\dots (1)$$

Where,  $J$  is the emission current density obtained for the applied electric field  $E$ ,  $\lambda_M$  pre-exponential correction factor,  $\beta$  represents local electric field enhancement factor,  $a$  and  $b$  are constants having values ( $1.54 \times 10^{-6} \text{ A eV V}^{-2}$ ) and ( $6.83 \text{ eV}^{-3/2} \text{ Vnm}^{-1}$ ) respectively,  $v_F$  (correction factor) is a particular value of the principal Schottky-Nordheim barrier function  $v$ , and  $\phi$  is the work function of the emitter material. The value of HOMO is observed to be  $\sim -4.2$  eV.

**Figure 5.15 (a)** depicts the plot of emission current density ( $J$ ) versus applied electric field ( $E$ ). The values of the onset and threshold fields, corresponding to emission current densities of  $10 \mu\text{A/cm}^2$  and  $1 \text{ mA/cm}^2$  are observed to be  $1.93$  and  $2.88 \text{ V}/\mu\text{m}$ , respectively. The  $J$ - $E$  curve exhibits exponential behavior indicating that the emission is due to tunneling of electrons through the deformed potential barrier. Interestingly, a maximum current density of  $\sim 4.9 \text{ mA/cm}^2$  could be drawn from the emitter at an applied field of  $3.6 \text{ V}/\mu\text{m}$ .

The field emission characteristics were further analyzed by plotting a graph of  $\ln(J/E^2)$  versus  $(1/E)$ , known as the Fowler-Nordheim (F-N) plot, shown in **Figure 5.15 (b)**. The F-N plot of **PHN-PPV/Si** emitter exhibited overall linear behavior, over the entire range of applied electric field values. Numerous reports can be found in which field enhancement factor  $\beta$  has been calculated from the

slope of the F-N plot. It has been observed that  $\beta$  value is overestimated for multi-tip emitter. An attempt to estimate local field ( $E_{\text{local}} = \beta E_{\text{av}}$ ) using the  $\beta$  value calculated from F-N plot results in very high magnitude than that required for field emission. Therefore, in this case, we have not estimated the value of  $\beta$  from the F-N plot analysis.

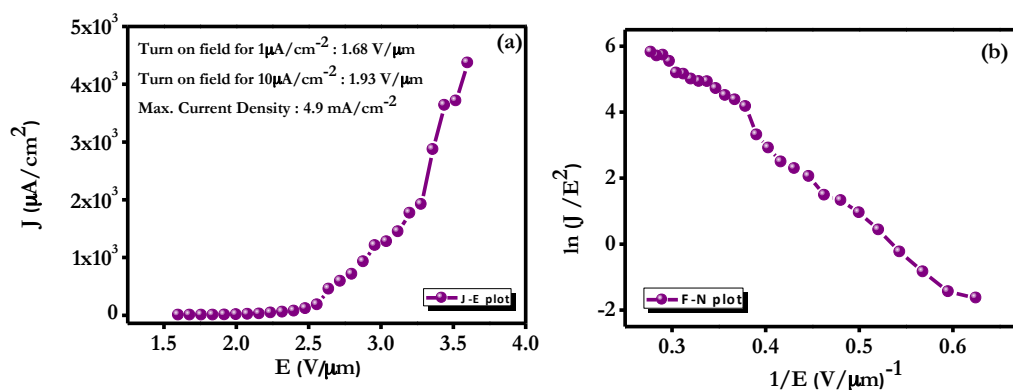


**Figure 5.15:** (a) Emission Current density versus applied electric field (J-E) plot, (b) F-N plot.

From the practical application point of view, emission current stability is very important and a decisive parameter. The emission current-time (I-t) stability recorded at a pre-set value of  $1 \mu\text{A}$  over the duration of 6 h is shown in **Figure 5.16**. The emission current exhibits good stability characterized with some excursions superimposed with 'spike' type fluctuations.

Instantaneous variations in the 'local' work function, or the 'local' electric field that lead to fluctuations in the emission current  $I$ . The variation in the 'local' work function occurs due to field-induced adsorption, migration and desorption of residual gas species. Also the continuous ion bombardment over several hours changes the local radius of curvature (geometrical factor,  $\beta$ ) and hence the strength of the 'local' electric field during the emission current stability tests. In the case of a multi-tip emitter in thin film form the fluctuation in  $I$  arises due to combined effect of both these processes.

In fact due to very high aspect ratio of the nanostructures, the constant ion bombardment of the nanostructure can alter the local radii of curvature significantly, thereby causing even 'extinction' and/or 'generation' of emission

sites. The concurrent ‘appearance’ and ‘disappearance’ of ‘emission spots’ observed in the phosphor screen image supports this argument.

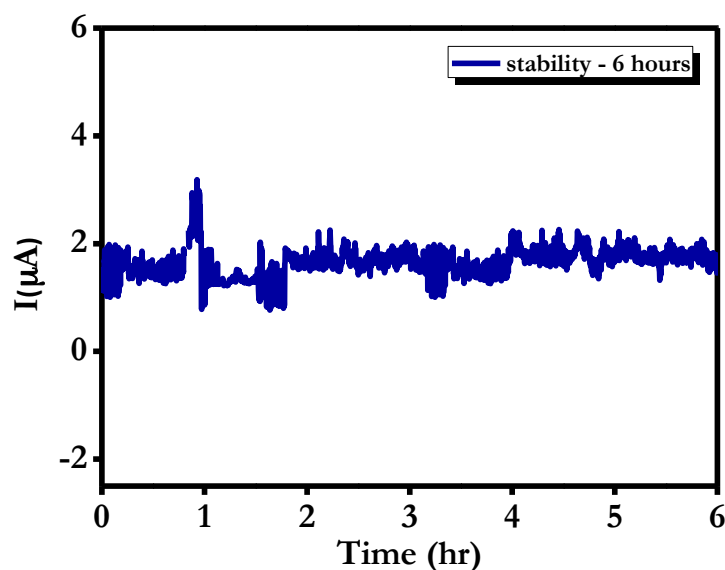


**Figure 5.16:** Stability of the field emitter over the duration of 6 hrs.

### 5.3.12 Field Emission Scanning Electron Microscopy (FESEM)

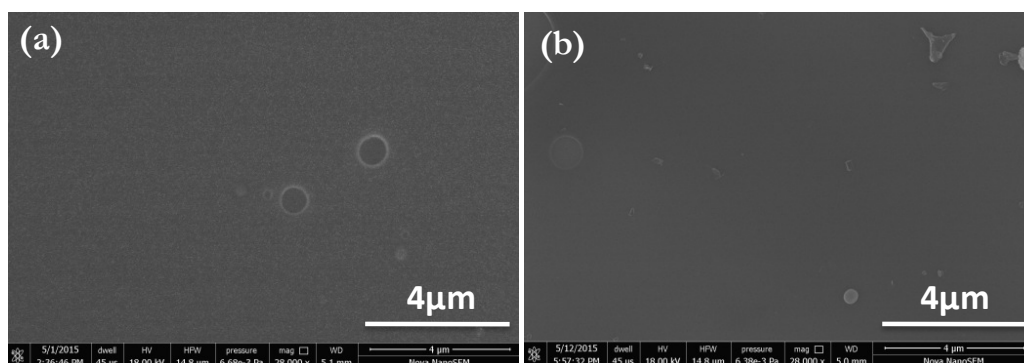


**Figure 5.17:** SEM images of the film before (a) and after (b) the FE measurement.

We have also recorded FESEM images of the films before and after field emission experiment in order to see whether the surface morphology of the emitter sustains the ion bombardment induced effects (**Figure 5.17 (a-b)**). It is observed that the spray-coated film is deposited quite uniformly on the Si-substrate and post field emission experiment the SEM image does not show any

noticeable change in the surface morphology of the emitter. This clearly indicates its mechanical robustness against the ion bombardment.

### 5. 3.13 Field Emission Images

**Figure 5.18** depicts the field emission images recorded at different applied voltages (corresponding to different emission current densities). All the FE images show the presence of very tiny bright spots, indicating a large number of emission sites. The increase in the number of spots along with their respective intensities with increase in the applied voltage is quite obvious. For such a multi-tip emitter, intensity as well as the emission current from the prevailing emitters also increases making them brighter.

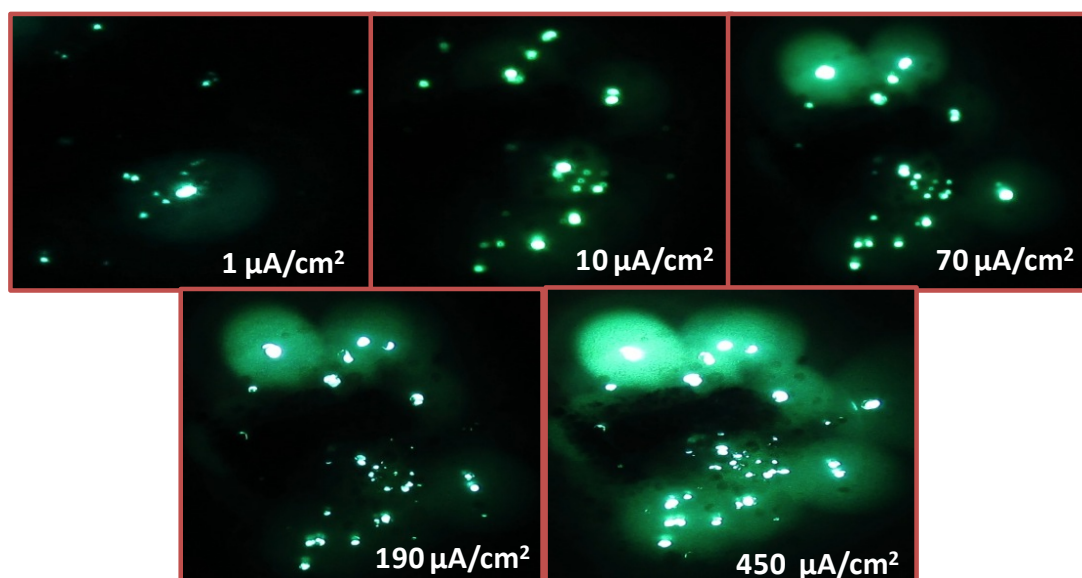


**Figure 5.18:** Field emission images

The promising FE behavior of the **PHN-PPV/Si** emitter can be attributed to its nanometric dimensions and moderate electrical conductivity. The lower oxidation potential ( $\sim 0.2$  V) lowers the field required to eject the electron from the material. In case of inorganic materials (metals/ semiconductors) the FE properties are decided by the work function value. By altering the surface morphology of the polymer emitter, the FE characteristics can be further improved. The synthesis plays important role in the modification of the polymeric systems that could potentially be used as FE material. Incorporation

of electron rich moieties in the material can improve FE properties as it mainly depends on the ejection of electron to the vacuum.

It is further useful to point out that the observed values of applied electric fields corresponding to the onset, threshold and maximum current density in the case of our polymeric system are comparable with those reported for various conducting polymer nanostructures and their nanocomposites. **Table 5.1** depicts the comparative performance of different planar emitters comprising of conducting polymers and their composites

**Table 5.1:** Turn on field and maximum current density values of the different conducting polymer.

Polymer	Turn on field V/ $\mu\text{m}$	Max. Current Density	Reference
PHN-PPV	1.93 (10 $\mu\text{A}/\text{cm}^2$ )	4.9 $\text{mA}/\text{cm}^2$ (3.6 V/ $\mu\text{m}$ )	<i>Present studies</i>
PEDOT-co-T34bT	1.83 (10 $\mu\text{A}/\text{cm}^2$ )	4 $\text{mA}/\text{cm}^2$ (3.6 V/ $\mu\text{m}$ )	20
PEDOT-DBSA	$\sim 3.5 - 4$ (10 $\mu\text{A}/\text{cm}^2$ )	100 $\mu\text{A}/\text{cm}^2$ ( $\sim 4.5$ V/ $\mu\text{m}$ )	18
PANI nanofibrils	$\sim 3 - 5$ (10 $\mu\text{A}/\text{cm}^2$ )	5 $\text{mA}/\text{cm}^2$ (27 V/ $\mu\text{m}$ )	8
PANI/ $\text{HClO}_4$	5.5 ( $\sim 1$ $\mu\text{A}/\text{cm}^2$ )	$\sim 5$ $\mu\text{A}/\text{cm}^2$ ( $\sim 6$ V/ $\mu\text{m}$ )	14
PPy/ $\text{TBAPF}_6$	$\sim 3.5 - 4$ ( $\sim 1$ $\mu\text{A}/\text{cm}^2$ )	50 $\mu\text{A}/\text{cm}^2$ ( $\sim 6$ V/ $\mu\text{m}$ )	14

## 5.4 Conclusions

We have successfully designed and synthesized two monomers *viz.* 5,10-dioctyl-5,10-dihydrophenazine-2,7-dicarbaldehyde and tetraethyl ((2,5-bis((2-ethylhexyl)oxy)-1,4 phenylene) bis(methylene))bis(phosphonate). The monomers were characterized fully and the Wittig - Horner polycondensation was performed in order to achieve a conjugated polymer *viz* phenazine



containing poly(phenylene vinylene) (**PHN-PPV**). **PHN-PPV** exhibited  $M_n$  of  $6 \times 10^3$  and PDI of 1.7. **PHN-PPV** showed lower oxidation potential of  $\sim 0.2$  V and redox properties indicating its suitability as an emitter in the field emission studies. **PHN-PPV** demonstrated acceptable field emission behavior. The lower turn on voltage of  $1.68$  V/ $\mu\text{m}$  was observed for  $1$   $\mu\text{A}/\text{cm}^2$ . The maximum current density measured was of  $\sim 4.9$  mA/ $\text{cm}^2$  for the applied field of  $3.6$  V/ $\mu\text{m}$ . Also, the polymer was found to be stable up to 6 h at constant current of  $1$   $\mu\text{A}$ . Thus, **PHN-PPV** is a welcome addition to the family of polymeric emitter materials available for practical field emission applications.

## References

1. Low-cost Nanomaterials: Toward Greener and More Efficient Energy Applications. edited by Lin Zhiqun, Jun Wang, Springer, 26-Jun-2014 - Technology & Engineering - 488 pages
2. Organic Nanomaterials: Synthesis, Characterization, and Device Applications By Tomas Torres, Giovanni Bottari, John Wiley & Sons, 05-Aug-2013,
3. Carbon materials for advanced technologies T.D. Burchell. Elsevier, 22-Jul-1999
4. Jia, C.; Ma, B.; Xin, N.; Guo, X.. *Acc. Chem. Res.*, Article ASAP, DOI: 10.1021/acs.accounts.5b00133.
5. Pan, J.; Sheng, Y.; Zhang, J.; Huang, P.; Zhang, X.; Feng, B. *ACS Appl. Mater. Interfaces*, **2015**, 7 (15), 7878–7883.
6. Yang, C.; Wei, H.; Guan, L.; Guo, J.; Wang, Y.; Yan, X.; Zhang, X.; Wei, S.; Guo, Z. *J. Mater. Chem. A*, **2015**, 3, 14929.
7. Patil, S. S.; Jha P.; Aswal, D.K.; Guptab, S.K.; Yakhmi, J.V.; Joag D.S.; More, M. A. *Polym. Adv. Technol.* **2012**, 23 215–219.
8. Wang, C.; Wang, Z.; Li, M.; Li, H. *Chem. Phys. Lett.* **2001**, 341, 431-434.
9. Patil, S.S.; Harpale, K. V.; Koiry, S. P.; Patil, K.R.; Aswal, D. K.; More, M. A. *J. Appl. Polym. Sci.* **2015**, 132, 5. DOI: 10.1002/APP.41401
10. Sameera, I.; Bhatia, R.; Ouyang, J.; Prasad, V.; Menon, R. *Appl. Phys. Lett.* **2013**, 102, 033102.
11. Ding, H.; Feng, T.; Chen, Y.; Sun, Z. *Appl. Surf. Sci.* **2012**, 25, 5191–5194.
12. Yan, H.; Zhang, L.; Shen, J.; Chen, Z.; Shi G.; Zhang, B. *Nanotechnology* **2006**, 17, 3446–3450. doi:10.1088/0957-4484/17/14/017
13. Patil, S. S.; Koiry, S. P.; Veerender, P.; Aswal, D. K.; Gupta, S. K.; Joag, D. S.; More, M. A. *RSC Adv.*, **2012**, 2, 5822–5827.
14. Kim, B.H.; Park, D.H.; Joo, J.; Yu, S.G.; Lee, S.H. *Synth. Met.* **2005**, 150, 279–284.

15. Musa, I.; Munindrasdasa, D. A. I.; Amaratunga, G. A. J.; Eccleston, W. *Nature* **1998**, 395 (24), 362.
16. Sridhar, S.; Tiwary, C.; Vinod, S.; Taha-Tijerina, J.J.; Sridhar, S.; Kalaga, K.; Sirota, B.; Hart, A. H. C.; Ozden, S.; Sinha, R. K.; Harsh.; Vajtai, R.; Choi, W.; Kordás, K.; Ajayan, P. M. *ACS nano*. **2014**, 8 (8), 7763-7770.
17. Musa, I.; Munindrasdasa, D. A. I.; Amaratunga, G. A. J.; Eccleston, W. *Nature* **1998**, 395 (24), 362.
18. Kim, B. H.; Kim, M. S.; Park, K. T.; Lee, J. K.; Park, D. H.; Joo, J.; Yu, S. G.; Lee, S. H. *Appl. Phys. Lett.* **2003**, 83 (3), 539.
19. Rujia, Z.; Zhang, Z.; Jiang, L.; Xu, K.; Tian, Q.; Xue, S.; Hu, J.; Bandob, Y.; Golberg, D. *J. Mater. Chem.* **2012**, 22, 19196.
20. Chen, N.; Qian, X.; Lin, H.; Liua H.; Li, Y. *J. Mater. Chem.* **2012**, 22, 11068.
21. Viskadourous, G. M.; Stylianakis, M. M.; Kymakis, E.; Stratakis, E. *ACS Appl. Mater. Interfaces* **2014**, 6, 388–393.
22. Alexandrou, I.; Kymakis, E.; Amaratunga, G. A. J. *Appl. Phys. Lett.* 2002, 80 (8), 1435.
23. Jin, Y. W.; Jung, J. E.; Park, Y. J.; Choi, J. H.; Jung, D. S.; Lee, H. W.; Park, S. H.; Lee, N. S.; Kim, J. M.; Ko, T. Y.; Lee, S. J.; Hwang, S. Y.; You, J. H.; Yoo, J-B.; Park, C-Y. *J. Appl. Phys.* **2002**, 92, 1065.
24. Patil, S. S.; Jha P.; Aswal, D.K.; Guptab, S.K.; Yakhmi, J.V.; Joag D.S.; More, M. A. *Polym. Adv. Technol.* **2012**, 23 215–219.
25. Wang, C.; Wang, Z.; Li, M.; Li, H. *Chem. Phys. Lett.* **2001**, 341, 431-434.
26. Patil, S.S.; Harpale, K. V.; Koiry, S. P.; Patil, K.R.; Aswal, D. K.; More, M. A. *J. Appl. Polym. Sci.* **2015**, 132, 5. DOI: 10.1002/APP.41401
27. Sameera, I.; Bhatia, R.; Ouyang, J.; Prasad, V.; Menon, R. *Appl. Phys. Lett.* **2013**, 102, 033102.
28. Ding, H.; Feng, T.; Chen, Y.; Sun, Z. *Appl. Surf. Sci.* **2012**, 25, 5191–5194.
29. Yan, H.; Zhang, L.; Shen, J.; Chen, Z.; Shi G.; Zhang, B. *Nanotechnology* **2006**, 17, 3446–3450. doi:10.1088/0957-4484/17/14/017

30. Patil, S. S.; Koiry, S. P.; Veerender, P.; Aswal, D. K.; Gupta, S. K.; Joag, D. S.; More, M. A. *RSC Adv.*, **2012**, 2, 5822–5827.
31. Kim, B.H.; Park, D.H.; Joo, J.; Yu, S.G.; Lee, S.H. *Synth. Met.* **2005**, 150, 279–284.
32. Okano, K.; Koizumi, S.; Silva, S. P.; Amaratunga, G. A. J. *Nature* **1996**, 381, 140 – 141.
33. Amaratunga, G. A. J.; Silva, S. R. P. *Appl. Phys. Lett.* **1996**, 68, 2529–2531.
34. Bagher, A. M. *Sustainable Energy*, **2014**, 2(3), 85-90.
35. Mihailetchi, V. D.; Koster, L. J. A.; Blom, P. W. M.; Melzer, C.; de Boer, B.; van Duren, J. K. J.; Janssen, R. A. J. *Adv. Funct. Mater.* **2005**, 15, 795-801.
36. <https://www.cdtltd.co.uk/pdf/p-oled-materials-device-operation.pdf>
37. Suppiah, S.; Mohamad, S. M.; Juhari, N. *Micro and Nanoelectronics (RSM)*, **2011**, IEEE Regional Symposium on 28-30 Sept 2011, DOI:10.1109/RSM.2011.6088367
38. Lei, T.; Xia, X.; Wang, J-Y.; Liu, C-J.; Pei, J. *J. Am. Chem. Soc.* **2014**, 136, 2135–2141.
39. Lei, T.; Dou, J-H.; Cao, X-Y.; Wang, J-Y.; Pei, J. *J. Am. Chem. Soc.*, **2013**, 135 (33), 12168–12171.
40. Todescato, F.; Capelli, R.; Dinelli, F.; Murgia, M.; Camaioni, N.; Yang, M.; Bozio, R.; Muccini, M. *J. Phys. Chem. B*, **2008**, 112 (33), 10130–10136.
41. Hiraoka, S.; Okamoto, T.; Kozaki, M.; Shiomi, D.; Sato, K.; Takui, T.; Okada, K. *J. Am. Chem. Soc.* **2004**, 126, 58–59.
42. Terada, E.; Okamoto, T.; Kozaki, M.; Masaki, M. E.; Shiomi, D.; Sato, K.; Takui, T.; Okada, K. *J. Org. Chem.* **2005**, 70, 10073–10081.
43. Thalladi, V. R.; Smolka, T.; Gehrke, A.; Boese, R.; Sustmann, R. *New J. Chem.* **2000**, 24, 143–147.
44. Price-Whelan, A.; Dietrich, L. E. P.; Newman, D. K. *Nature Chemical Biology* 2006, 2, 71-78.
45. Pierson, L.S.III.; Pierson, E. A. *Appl. Microbiol. Biotechnol.* **2010**, 86(6),1659–1670.

46. Zheng, Z.; Dong, Q.; Gou, L.; Su, J-H.; Huang, J. *J. Mater. Chem. C*, **2014**, 2, 9858–9865
47. Gu, P-Y.; Zhao, Y.; He, J-H.; Zhang, J.; Wang, C.; Xu, Q-F.; Lu, J-M.; Sun, X. W.; Zhang, Q. *J. Org. Chem.*, **2015**, 80 (6), 3030–3035.
48. Lee, J.; Shizu, K.; Tanaka, H.; Nakanotani, H.; Yasuda, T.; Kaji, H.; Adachi, C. *J. Mater. Chem. C* **2015**, 3, 2175–2181.
49. Song, H. J.; Goh, M.; Choi, K. H.; Lee, S.; Moon, D. K.; Shin, G. J. *Journal of Industrial and Engineering Chemistry* 2015, 23 (25), 338–343.
50. Lee, D-C.; Brownell, L. V.; Yan, L.; You, W. *ACS Appl. Mater. Interfaces* **2014**, 6, 15767–15773.
51. Li, G.; Lu, Z.; Li, C.; Bo, Z. *Polym. Chem.* **2015**, 6, 1613-1618.
52. Lu, X.; Lan, T.; Qin, Z.; Wang, Z-S.; Zhou, G. *ACS Appl. Mater. Interfaces* **2014**, 6, 19308–19317.
53. Richard, C. A.; Pan, Z.; Hsu, H-Y.; Cekli, S.; Schanze, K. S.; Reynolds, J. R. *ACS Appl. Mater. Interfaces* **2014**, 6, 5221–5227.
54. Yang, L.; Li, X.; Yang, J.; Qu, Y.; Hua, J. *ACS Appl. Mater. Interfaces* **2013**, 5, 1317–1326.
55. Liu, B.; Yu, W-L.; Pei, J.; Liu, S-Y.; Lai, Y-H.; Huang, W. *Macromolecules* **2001**, 34, 7932-7940.
56. Iwasa, Y.; Koda, T.; Koshihara, S.; Tokura, Y.; Iwasawa, N.; Saito, G. *Phys. Rev. B: Condens. Matter Mater. Phys.* **1989**, 39, 10441–10444.
57. Okamoto, T.; Terada, E.; Kozaki, M.; Uchida, M.; Kikukawa, S.; Okada, K. *Org. Lett.* **2003**, 5 (3), 373-376
58. Koike, R.; Katayose, Y.; Ohta, A.; Motoyoshiya, J.; Nishii, Y.; Aoyam, H. *Tetrahedron* 61, **2005**, 11020–11026
59. Narasimha, K.; Jayakannan, M. *Appl. Mater. Interfaces* **2014**, 6, 19385–19396.
60. Forbes, R. G. *Nanotechnology* **2012**, 23(9), 095706. doi:10.1088/0957-4484/23/9/095706.

## Chapter 6

### Summary and Future Scope

This chapter contains summary of the thesis work and the future scope.

## 6.1 Summary

With the increasing demand for the developing country, the non-renewable energy sources are exhausting with time and there is a further need of the energy. This energy need is indeed increasing very rapidly. Thus we should understand constraints of the non-renewable sources of energy and take a step ahead to look forward to renewable sources as the major source of future energy. Although there are certain challenges involved in the use of all available forms of renewable energy there is a scope to develop new materials and systems for the consumption of such kind of energy.

The overall objective of the present work was to make use of simple chemistry for designing and synthesizing materials for the energy applications. The goal was to synthesize such materials, which could be effectively used for solar cell applications, charge storage applications and energy saving devices. With these objectives in mind and considering the need for future energy, the present attempt of demonstrating polymeric systems for energy applications were undertaken.

### Summary of each area

The outcome of the present work for the energy applications has been described as three chapters in the dissertation. The central theme was to develop polymeric materials for energy applications.

1. Amongst all renewable energy sources, the solar energy is the most abundant form of renewable energy source. Here in the first aspect of work, we have attempted the solar energy harvesting and conversion of it into usable form of energy. The conjugated polymer was modified to possess carboxylic acid groups using simple chemical reactions such as Vilsmeier–Haack formylation and Knoevenagel condensation. The modified polymer was demonstrated as the potential sensitizer in Dye Sensitized Solar Cell (DSSC) device. The modification of the polymer was confirmed using  $^1\text{H}$  NMR and IR spectroscopy. The power conversion efficiency of the device was observed to be 3 %. Carboxyl group anchors well to the surface of the  $\text{TiO}_2$ , enhancing the charge

transport and hence the efficiency of the device. The conjugated polymer used in this work (**BEHP-co-MEH PPV**) exhibits some other advantages such as high thermal stability, solution processability etc. The DSSC device made using **BEHP-co-MEH PPV** as a sensitizer showed the stable power conversion efficiency up to 90 °C.

2. In the second part of work, we used polymer-based material for the charge storage applications. Potassium salt of carboxylic acid containing polystyrene derivative was synthesized and pyrolyzed at high temperature under inert atmosphere to get the porous, functional carbon. The formed polymer derived carbon was explored for the electric double layer capacitor (EDLC) and lithium ion hybrid capacitor (Li-HEC). The surface area of the porous carbon was found to be  $1860 \text{ m}^2 \text{ g}^{-1}$ . The specific capacitance of  $137 \text{ F g}^{-1}$  at the applied current density of  $0.5 \text{ A g}^{-1}$  for the EDLC system. The polymer derived carbon material (**P3KC**) showed the stability for more than 1000 cycles at  $2 \text{ A g}^{-1}$ . Li-HEC measurements were performed using the  $1\text{M LiPF}_6$  as the electrolyte. P3KC was found to possess maximum energy density and maximum power density values of  $61 \text{ Wh k g}^{-1}$  and  $10015 \text{ W k g}^{-1}$ , respectively. A  $\sim 70\%$  capacitance retention is observed after 2000 cycles.
3. The third part of work deals with the energy conservation aspect. Devices like organic field effect transistors (OFET), organic light emitting diodes (OLEDs), field emission display (FED) etc. are considered as devices of energy conservation because they consume less energy and give output similar to traditional devices. Phenazine-containing poly(phenylene vinylene) (**PHN-PPV**) was designed and synthesized using Wittig- Horner polycondensation. The polymer **PHN-PPV** exhibited number average molecular weight of  $6 \times 10^3$ . This conjugated polymer was evaluated for the application of field emission study. The polymer **PHN-PPV** displayed reversible redox properties and lower oxidation onset of  $\sim 0.2 \text{ V}$ . The field emission measurements demonstrated the lower turn on voltage of  $1.68 \text{ V}/\mu\text{m}$  for  $1 \mu\text{A}/\text{cm}^2$ .



## 6.2 Future Scope

The scope and importance of designing and synthesizing appropriate materials for the energy application have been realized and hence there is plenty of room available to achieve the goals of the energy demands. Henceforth, we suggest some future prospects for the design of new materials.

### 1. Conjugated Polymers for Organic Solar Cells

Conjugated polymers for organic photovoltaic applications is the growing branch of organic and polymer chemistry in order to improve the performance and stability of the solar cell devices. There are several reports till date on the different types of conjugated polymers and their use in bulk heterojunction solar cells as an active layer. Nevertheless, there is a wide scope to improve the performance of solar cells by simple modification.

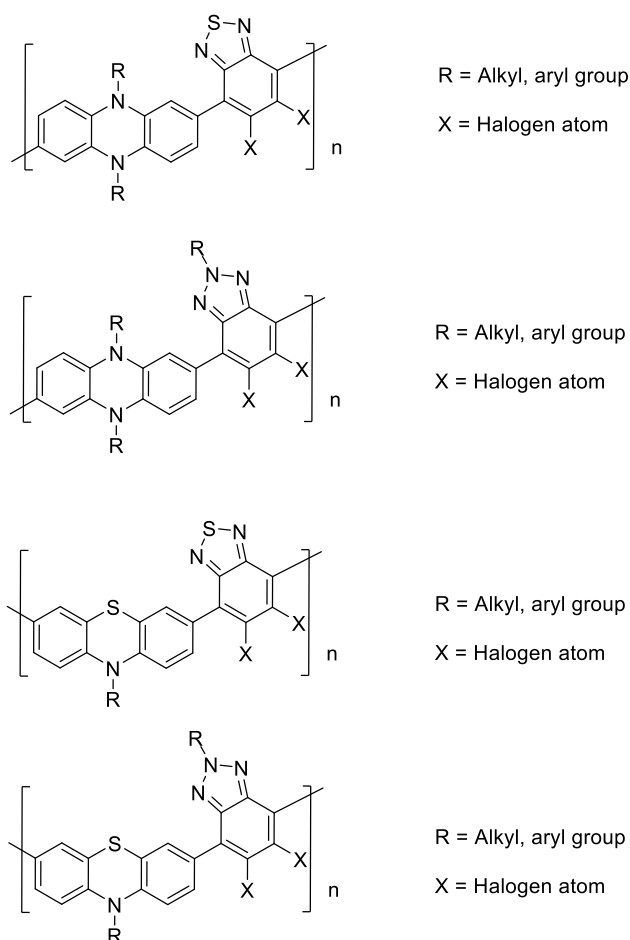


**Figure 6.1:** Donor-acceptor conjugated polymers for organic solar cells

The incorporation of substituted BTDA or benzotriazole as a strong electron withdrawing moiety in to the main core phenazine based polymer will modify its band structure and may improve the absorption spectrum. The solubility of polymer will also be increased due to alkylated benzotriazole unit present in polymer backbone. Therefore, multi-substituted benzotriazole unit can play dual role in active layer. The fluorine substituted benzotriazole will improve its electron withdrawing ability than its bare structure. Also, the incorporation of substituted pyridine in the polymer chain as another electron withdrawing moiety will affect the optical and electrochemical properties of polymer. In most of the sensitizers used in DSSCs, pyridine acts as an electron injector/anchoring group in sensitizers.

## 2. Small Molecules/Polymers for LEDs

Now a days, organic light emitting diodes (OLEDs) became the most popular area of research in the field of electronic devices. The commonly used commercial LEDs are made up of inorganic materials which have limited scope for tuning their properties as well as they are rigid structure that can not be applied for the flexible electronic applications. In case of organic material based LEDs, it is easier to tune the colour, optical properties and other electrochemical properties by simple modification in structure. Almost, all the organic materials are solution processable and easy to handle during device fabrications. We can tune its absorption from UV to visible or even up to IR region by different range of conjugation. There are several reports on blue, green and red light emitting diodes based on organic materials.

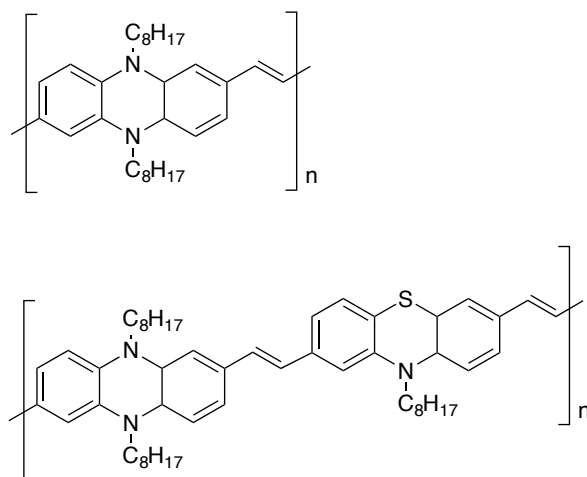


**Figure 6.2:** PPV derivatives for LED applications

### 3. Polymers as Hole Transport Materials (HTM):

The perovskite sensitized solar cells are the predicted future for solar cells. This solar cell is said to be cost effective as compared to silicon solar cells because the synthesis of precursors required for perovskite structure are quite simple and scalable. At the present Spiro-OMeTAD is being used and commercialized as HTM, which gives reasonable performance. Although it is commonly used everywhere, it is very expensive and tedious to synthesize. Hence, there is need and scope to replace Spiro-OMeTAD. The semiconducting polymers would be the better option to reduce the cost and enhance the stability of overall perovskite solar cell device.

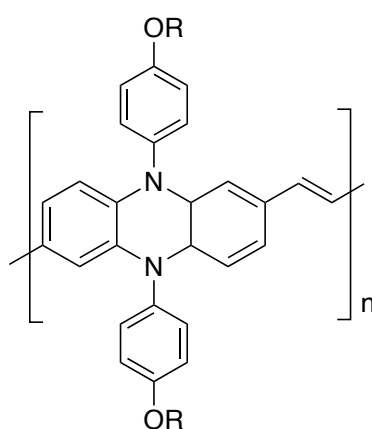


**Figure 6.3:** Representative structure of polymer for hole transport material application

### 4. Polymers in Charge Storage:

Polymers, due to their structural tunability find the advantages almost in every field. Currently, various types of polymers are being explored for the different charge storage mechanisms including electrolytes, electrode materials, etc. Carboxylic acid, ketonic and alcoholic functional groups containing conjugated molecules are demonstrated as a promising anode materials for lithium ion batteries. The design and synthesis of conjugated polymers with pendant oxygen containing groups would be essential. The conjugated backbone takes part in electronic conductivity while oxygen containing groups provides site for lithiation during charging process.

In summary, there are various new opportunities to tune and synthesize the materials, especially polymeric systems for several applications in energy field. We believe that from such kind of research there would be satisfactory outcome in future to overcome the scarcity of the energy.

---

## **Synopsis of the PhD Thesis**

---

<b>Name of the Researcher</b>	<b>: Ms. Shraddha Y. Chhatre</b>
<b>Faculty</b>	<b>: Science</b>
<b>Subject</b>	<b>: Chemistry</b>
<b>Title of the THESIS</b>	<b>: “Synthesis and Chemical Modification of Polyphenylene Vinylene and Polystyrene Systems for Energy Applications.”</b>
<b>Name of the Guide</b>	<b>: Dr. P. P. Wadgaonkar</b> Polymer Science and Engineering Division, CSIR-National Chemical Laboratory, Pune
<b>Name of the Co-guide</b>	<b>: Dr. S. B. Ogale</b> Physical and Materials Chemistry Division, CSIR-National Chemical Laboratory, Pune
<b>Place of Research</b>	<b>: Polymer Science and Engineering Division, Physical and Materials Chemistry Division, CSIR-National Chemical Laboratory, Pune</b>

---

### **Introduction:**

The present era is of innovation and discovery due to globalization and advances in communication and information technology. The expansion of globalization is a consequence of faster and increased ways of communications, networking and transportations all around the world. As a consequence of this, the modern society has identified several grand challenges in the areas such as food, water, energy, environment, security, education, health, poverty, etc. All these challenges not only are independently very important to address but also are interconnected and hence need to be addressed simultaneously. These challenges are braided with each other and all are related to energy directly or indirectly. Hence, energy is one of the very important sectors to deal with. The worldwide demand for the energy is increasing day by day and the planet's resources are exhausting rapidly. Thus, there is a need to manage the existing resources as well as to find out the new solutions to the problems of energy. More crucial and important issues are related to energy consumption, supply, storage, delivery and the economics management.

The polymers are the potential candidates for the energy systems on account of their numerous types and the presence of functionality (ies). The present work deals with the energy conversion, storage and conservation using different types of polymeric systems. Specifically, the work deals with synthesis and modification of polymeric systems for energy applications.

### **Objectives, Nature and the Scope of the Work Done:**

In this work, we have explored some easy ways for polymer synthesis and modification, and investigated their applications in the field of energy (viz. conversion, storage and conservation). One of the main features of our efforts is the development of simple synthetic routes for generating potentially applicable polymeric systems. This kind of study would lead to the easy access and different prospective to the materials engineering and design for the specific targeted applications. The thesis presentation is divided into three sections. Section I deals with energy conversion i. e. photovoltaic system: solar cell. The objective of this section is to demonstrate the modification of the conjugated polymer for its use in DSSC as a sensitizer. Section II is devoted to energy storage part in which the molecular engineering and the synthesis of the polystyrene derivative for the formation of porous carbon for its use in the supercapacitor and Li-HEC applications. Section III deals with the energy conservation sector, wherein the synthesis of conjugated polymer was carried out and the field emission performance was studied.

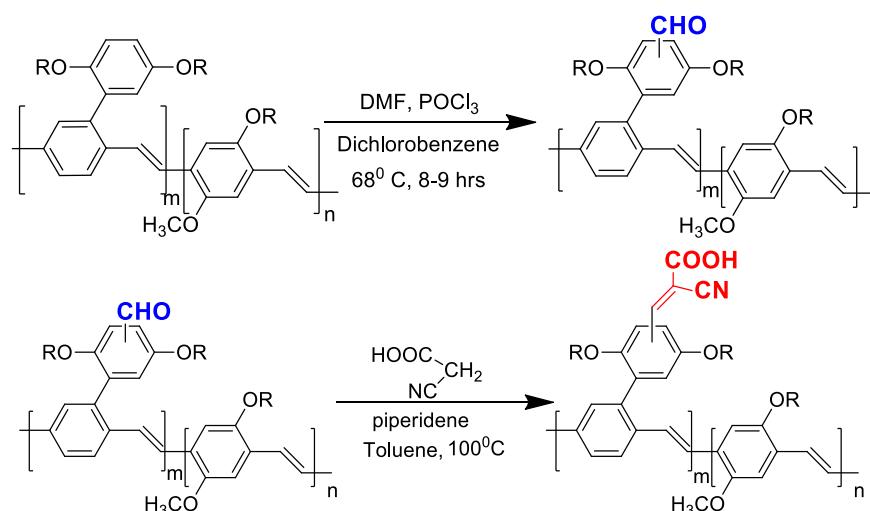
### **Section I: Energy Conversion: Solar Cell- DSSC**

#### **Carboxyl-modified conjugated polymer sensitizer for dye sensitized solar cells: significant efficiency enhancement**

This chapter describes a simple protocol for chemical modification of the conjugated polymer (**BEHP-co-MEH-PPV**) system for its application in DSSC as a sensitizer.

A simple two step strategy was developed to introduce carboxyl groups *via* Vilsmeier–Haack formylation on the commercially available conjugated polymer [(poly{[2-[2',5'-bis(2''-ethylhexyloxy)phenyl]1,4-phenylenevinylene]co-[2-methoxy-5-(2'-ethylhexyloxy)-1,4-phenylenevin-

ylene}}] (**BEHP-co-MEH PPV**) followed by Knoevenagel condensation with cyanoacrylic acid (**Scheme 1**).



**Scheme 1:** Modification of the conjugated polymer **BEHP-co-MEH PPV**

Adsorption of the carboxyl-modified polymer onto  $\text{TiO}_2$  film and J-V curves were studied for the dye sensitized solar cell (DSSC) and compared with the base polymer **BEHP-co-MEH PPV**. Carboxyl modification of **BEHP-co-MEH PPV** resulted in significant enhancement in the efficiency (3%), compared to the base polymer, which showed an efficiency of only 0.3% (**Figure 1**). The details of the synthetic procedure, characterization and the photovoltaic property measurements are presented and discussed.

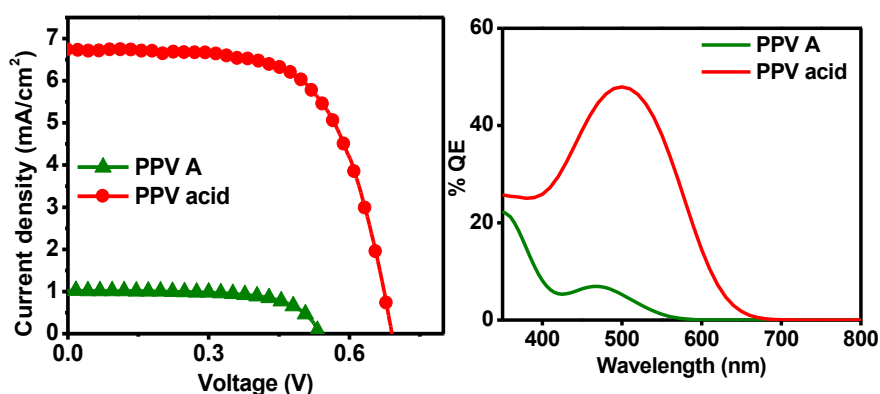


**Figure 1:** I-V and IPCE data of the modified polymer (**PPV acid**) and original polymer (**PPVA**)

In conclusion, we have successfully demonstrated a simple two-step strategy to introduce carboxylic acid groups on a conjugated polymer **PPV A**. The introduction of carboxyl groups clearly proved to be beneficial for charge injection through proper anchoring to TiO<sub>2</sub> film for its use in DSSCs. Modified polymer **PPV acid** gives considerably higher efficiency (3%) as compared with the unmodified counterpart. Also, importantly this polymer was found to be stable up to 200°C.

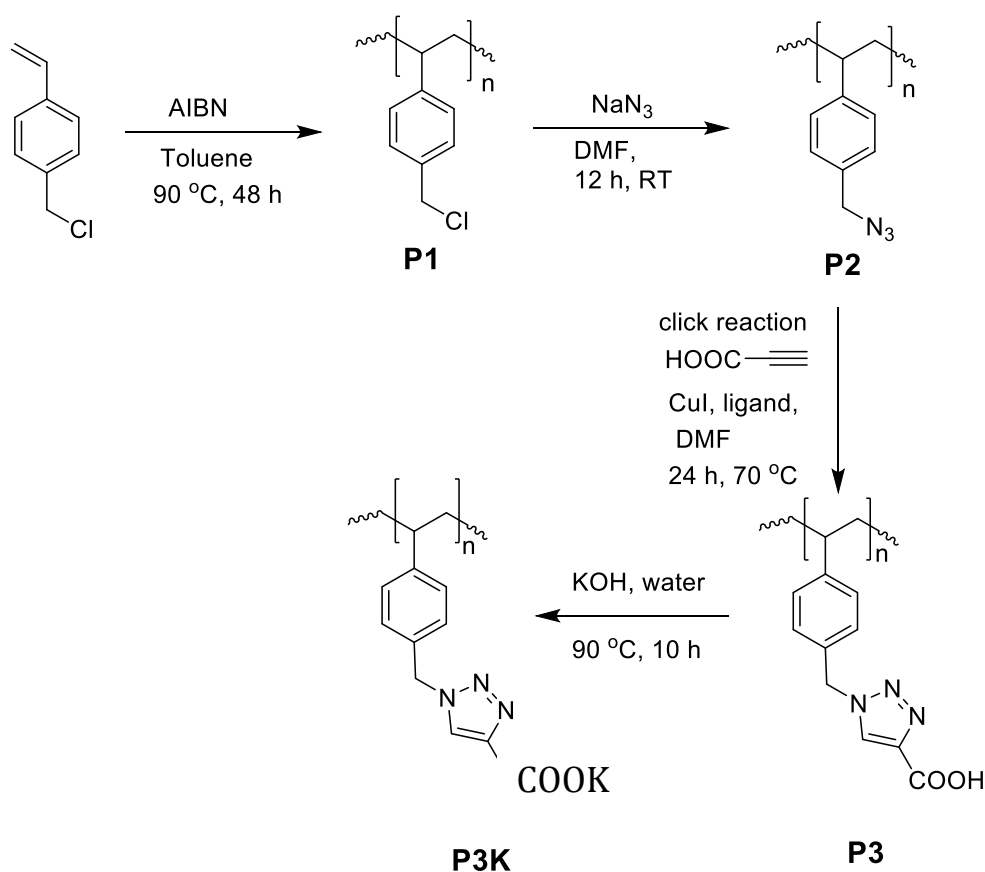
## **Section II: Energy Storage: Supercapacitor and Li-HEC applications**

### **High surface area porous carbon for ultracapacitor application by pyrolysis of polystyrene containing pendant carboxylic acid groups prepared *via* click chemistry**

This chapter describes a simple synthesis of the polystyrene derivative containing pendant carboxylic acid groups for the formation porous carbon and its use in supercapacitor and Li-HEC.

Strategic designing and synthesis of polystyrene derivative (**Scheme 2.**) was performed *via* click chemistry to achieve micro/meso-porous conducting carbon with high surface area (1860 m<sup>2</sup>g<sup>-1</sup>) by controlled pyrolysis.





**Scheme 2:** Synthesis of the polymer precursor for carbon: polystyrene derivative

The design was done with the objective to get graphene-like framework (by polystyrene backbone), nitrogen doping (by triazole ring) and high porosity (salt of carboxylic acid). Potassium hydroxide was reacted with the carboxylic acid groups of the polymer to achieve uniform *in-situ* molecular activation. From the FESEM, it is clear that the carbon formed is porous carbon (**Figure 2**).

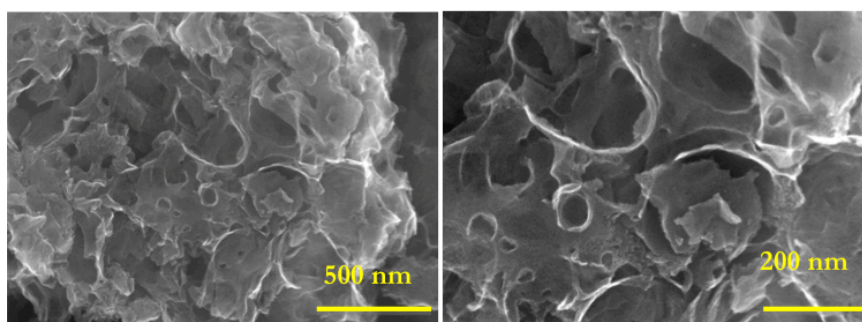


**Figure 2:** FESEM of the carbon formed by the pyrolysis of the polymer

The obtained hierarchically porous carbon was characterized and studied for the electric double layer capacitor in organic electrolyte as well as lithium ion

hybrid electrochemical capacitor (Li-HEC) performance. A specific capacitance of  $100 \text{ Fg}^{-1}$  was obtained for the applied current density of  $0.5 \text{ Ag}^{-1}$  using tetraethyl ammonium tetrafluoroborate in propylene carbonate as an electrolyte, in the potential range of 0-3V (**Figure 3.**). The Li-HEC cell (**Figure 4.**) was observed to deliver the maximum energy and power densities of  $61 \text{ Wh kg}^{-1}$  and  $10015 \text{ W kg}^{-1}$ , respectively, with  $\sim 70\%$  capacitance retention after 2000 charge-discharge cycles at the current density of  $2 \text{ Ag}^{-1}$ .

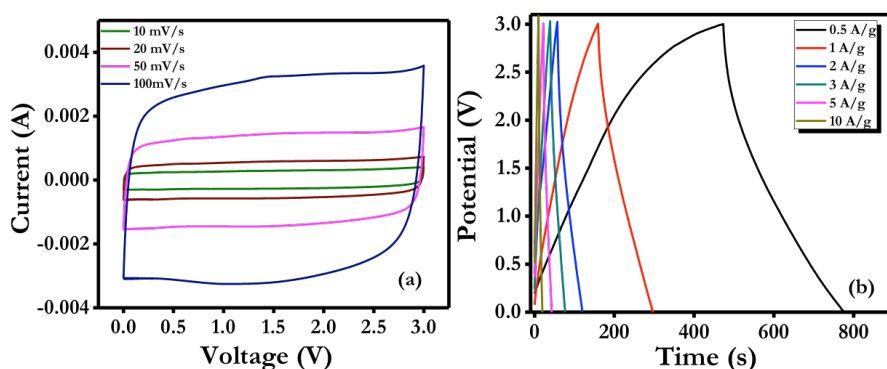


**Figure 3:** Supercapacitor measurements using 1M TBABF<sub>4</sub> in PC electrolyte: CV and galvanic charging–discharging data.

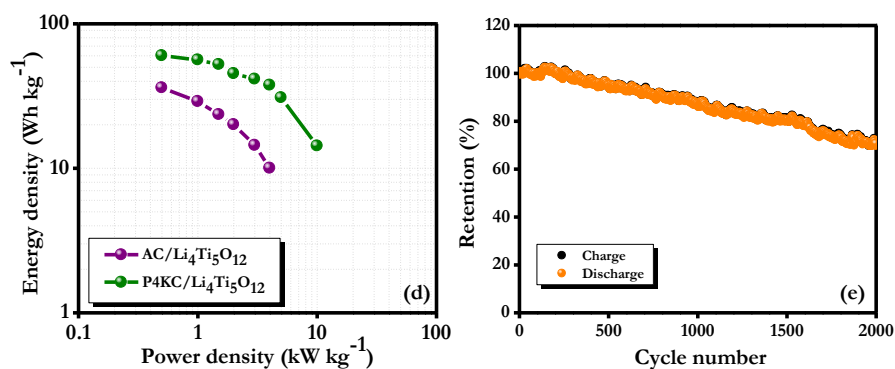


**Figure 4:** Ragone plot for Li-HEC performance and the cyclic stability of the full Li-HEC cell.

In conclusion, highly porous carbon was synthesized by the pyrolysis of a polymer precursor with in situ porogen presence for molecular activation, which shows BET specific surface area of  $1860 \text{ m}^2\text{g}^{-1}$ . The formed carbon contains good density of micro/meso-porous and shows high electrical conductivity. Supercapacitor measurements were performed in the organic electrolyte

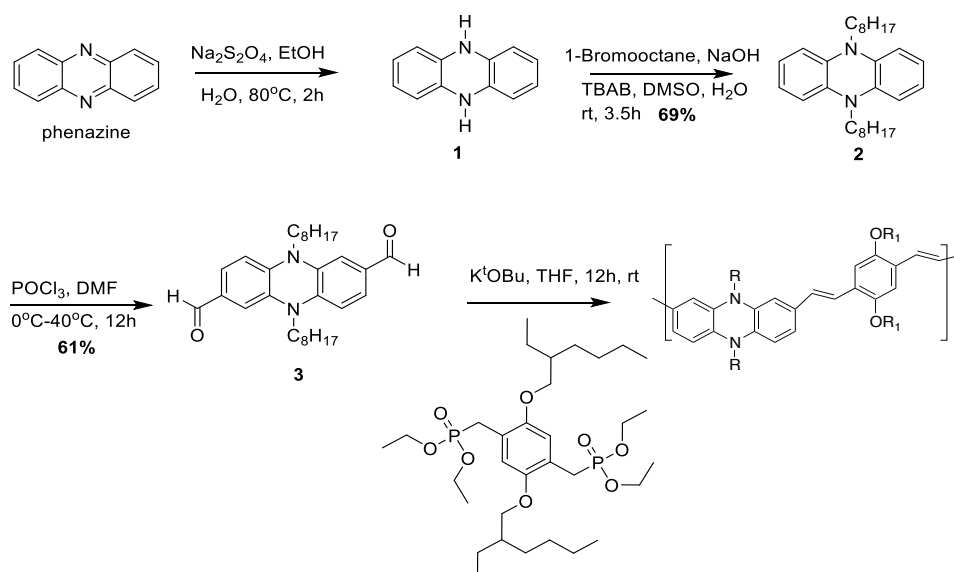
TEABF<sub>4</sub> in PC, which yielded the specific capacitance of 100 Fg<sup>-1</sup> at the applied current density of 0.5 Ag<sup>-1</sup>. The Li-HEC measurements performed using the 1M LiPF<sub>6</sub> as the electrolyte show that the maximum energy density and maximum power density values of 61 Wh kg<sup>-1</sup> and 10015 W kg<sup>-1</sup>, respectively, were obtained. After 2000 cycles 70 % capacitance retention was noted.

### **Section III: Energy Conservation: Field emission study**

#### **Synthesis of dihydro-phenazine containing conjugated polymer and its application for field emission**

This chapter deals with the synthesis of dihydrophenazine containing conjugated polymer and its application for the field emission.

The conjugated polymers are very important systems in solution processable optoelectronic and display devices. Polyphenylene vinylene systems are known to be applicable for a variety of applications like organic light emitting diodes (OLED), field effect transistors (FET) and also photovoltaics. 5,10-Dihydrophenazine system is attractive as it is electron rich and due to presence of two tertiary nitrogens, this system exhibits redox properties. Dihydrophenazine containing polyphenylene vinylene system was synthesized (**Scheme 3.**) and characterized (**PPV-PHN**). Based on the results of the basic characterization data such as UV, PL and conductivity measurements the polymer was considered to be a potential candidate for the field emission studies.



**Scheme 3:** Synthesis of dihydrophenazine-containing PPV

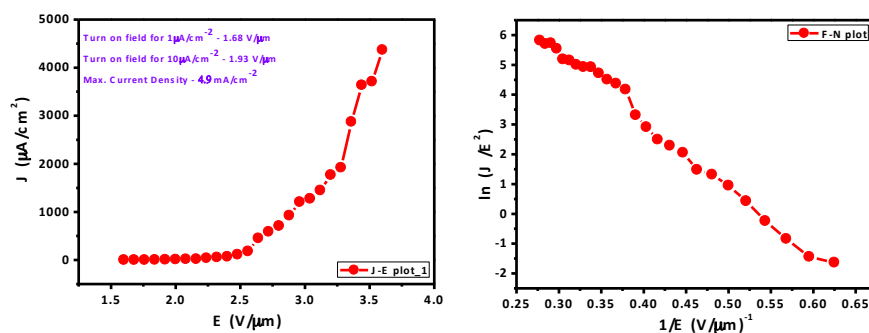


**Figure 5:** J-E plot and F-N plot for the dihydrophenazine-containing PPV

The turn-on and threshold field (field required to draw an emission current density of 1 and  $100\ \mu\text{A}/\text{cm}^2$ ) were observed to be  $1.68\ \text{V}/\mu\text{m}$  and  $2.56\ \text{V}/\mu\text{m}$  respectively (**Figure 5**). The emission current shows almost exponential growth with gradual increase in applied electric field indicating the emission due to tunneling of electrons through the deformed potential barrier, particularly post threshold field value, and reaches the maximum current density of  $4.9\ \text{mA}/\text{cm}^2$ . Because of such high current density **PHN-PPV** can be considered as a promising field emitter.

In conclusion, dihydro-phenazine containing polyphenylene vinylene has been synthesized and characterized. From J-E plot, the turn on and threshold field (field required to draw an emission current density of 1 and  $100\ \mu\text{A}/\text{cm}^2$ ) were  $1.68\ \text{V}/\mu\text{m}$  and  $2.56\ \text{V}/\mu\text{m}$  respectively with the maximum current density of  $4.9\ \text{mA}/\text{cm}^2$ .

The Salient features of the present work are listed below:

1. We report the chemical modification of the conjugated polymer (PPV) for DSSC application. The carboxy-modified polymer shows efficiency of 3% when used as sensitizer in DSSC.
2. Strategic design and synthesis of triazole ring with carboxylic acid containing polystyrene was achieved and used as the precursor for the formation of porous carbon. The specific capacitance of  $100 \text{ Fg}^{-1}$  at the applied current density of  $0.5 \text{ Ag}^{-1}$ . For Li-HEC, maximum energy and power densities values obtained were  $61 \text{ Wh kg}^{-1}$  and  $10015 \text{ W kg}^{-1}$ ,
3. Synthesis of dihydro-phenazine containing poly (phenylene vinylene) was achieved and the field emission studies were performed. The turn-on and threshold field were observed to be  $1.68 \text{ V}/\mu\text{m}$  and  $2.56 \text{ V}/\mu\text{m}$ , respectively.

### **References:**

- [1] <http://zezantam.com/2013/07/02/week-two/>
- [2] M.-R. Kim, W. Shin, W. Kim, H. Lee, S. Park, J. Lee and S. Jin, *Mol. Cryst. Liq. Cryst*, 2006, 462, 91–99.
- [3] H. Jiang, X. Zhao, A. H. Shelton, S. Ho Lee, J. R. Reynolds and K. S. Schanze, *ACS Appl. Mater. Interfaces*, 2009, 1, 381–387.
- [4] C. Kanimozhi, P. Balraju, G. D. Sharma and S. Patil, *J. Phys. Chem. C*, 2010, 114, 3287–3291.
- [5] X. Liu, R. Zhu, Y. Zhang, B. Liu and S. Ramakrishna, *Chem. Commun.* 2008, 3789.
- [6] X. Chen, C. Li, [Grätzel](#), R. Kostecki, S. S. Mao. *Chem Soc Rev* 2012, 41, 7909-7937.
- [7] A. S. Aricò, P. Bruc, B. Scrosati, J. M. Tarascon, W. Schalkwijk. *Nat Mater* 2005, 4, 366-377
- [8] J. Yan, Q. Wang, T. Wei, Z. Fan. *Adv Energy Mater* 2014, 4, 300816.
- [9] B. R. Chalamala, Y. Wei, B.E. Gnade, *IEEE Spectrum*, 1998, 35, 42–5.

- [10] I. Musa, D. A. I. Munindrasdasa, G. A. J. Amaratunga, W. Eccleston. *Nature*, 1998, 395, 24
- [11] S. S. Patil, S. P. Koiry, P. Veerender, D. K. Aswal, S. K. Gupta, D. S. Joaga, M. A. More. *RSC Advances*, 2012, 2, 5822–5827

**Shraddha Y. Chhatre**  
(Research Student)

**Dr. P. P. Wadgaonkar**  
(Research Guide)

**Dr. S. B. Ogale**  
(Research co-guide)

## List of Publications and Patents

### Publications:

1. **Shraddha Chhatre**, Shruti Agarkar, Vivek Dhas, Satyawan Nagane, Vishal Thakare, Satishchandra Ogale and Prakash Wadgaonkar. *Carboxyl-modified conjugated polymer sensitizer for dye sensitized solar cells: significant efficiency enhancement*, *J. Mater. Chem.*, 22, 2012, 23267-23271.
2. **Shraddha Chhatre**, Vanchiappan Aravindan, Dhanya Puthussery, Abhik Banerjee, Srinivasan Madhavi, Prakash P Wadgaonkar, Satishchandra Ogale. *High surface area porous carbon for ultracapacitor application by pyrolysis of polystyrene containing pendant carboxylic acid groups prepared via click chemistry*. *Materials Today Communications*, 4 (2015) 166–175.
3. **Shraddha Chhatre**, Amol Ichake, Kashmira Harpale, Mahendra More, Satishchandra Ogale and Prakash Wadgaonkar. *Phenazine containing poly(phenylene vinylene): Synthesis, Characterization and Application to Field Emission*. (Manuscript under preparation)
4. Miquel Planells, Luke X. Reynolds, Umesh Bansode, **Shraddha Chhatre**, Satishchandra Ogale, Neil Robertson and Saif A. Haque. *Synthesis and optical characterisation of triphenylamine-based hole extractor materials for CdSe quantum dots*. *Phys. Chem. Chem. Phys.*, 15, 2013, 7679-7684.
5. Satyawan Nagane, Umesh Bansode, Onkar Game, **Shraddha Chhatre** and Satishchandra Ogale. *CH<sub>3</sub>NH<sub>3</sub>PbI(3-x)(BF<sub>4</sub>)<sub>x</sub>: molecular ion substituted hybrid perovskite*. *Chem. Commun.*, 50, 2014, 9741-9744.
6. Dipti Dhakras, Yogesh Gawli, **Shraddha Chhatre**, Prakash Wadgaonkar and Satishchandra Ogale. *A high performance all-organic flexural piezo-FET and nanogenerator via nanoscale soft-interface strain modulation*. *Phys. Chem. Chem. Phys.*, 16, 2014, 22874-22881.

Patent Submitted

1. An organic flexural piezo-ferro-FET: 48-NF-2014: 2014-INV-0011 (complete specification)

Academic visits

- Three months visit under the Indo-UK APEX program (Advancing the Efficiency and Production Potential of Excitonic solar cells) to the Edinburgh University, Edinburgh, UK under Prof. Neil Robertson for the work of “Synthesis of small molecules as co-sensitizer and Fabrication of dye sensitized solar cells.”
- Five months visit to the laboratory of Prof. Andreas F. M. Kilbinger, Fribourg University, Switzerland for “Synthesis of monomers and synthesis conjugated polymers by ROMP.”

Workshops and Posters

- RSC Dalton Division Summer School" (June 18, 2012 to June 22 2012) Edinburgh University, UK
- Academic Paper Writing Course (10th May 2012) St. Andrews University, Edinburgh, UK.
- Poster at National Science Day (2014 and 2012), NCL, Pune
- Poster at International workshop on Nanotechnology and advance functionalized materials (NTAFM 2013 and 2009) in NCL, Pune.
- Attended Symposium on Nano materials and their Applications (SNMA 2009) in Fergusson College.